2013

Numerical Modeling and Characterization of Vertically Aligned Carbon Nanotube Arrays

Johnson Joseph
University of Kentucky, johnson.j9@gmail.com

STUDENT AGREEMENT:

I represent that my thesis or dissertation and abstract are my original work. Proper attribution has been given to all outside sources. I understand that I am solely responsible for obtaining any needed copyright permissions. I have obtained and attached hereto needed written permission statements(s) from the owner(s) of each third-party copyrighted matter to be included in my work, allowing electronic distribution (if such use is not permitted by the fair use doctrine).

I hereby grant to The University of Kentucky and its agents the non-exclusive license to archive and make accessible my work in whole or in part in all forms of media, now or hereafter known. I agree that the document mentioned above may be made available immediately for worldwide access unless a preapproved embargo applies.

I retain all other ownership rights to the copyright of my work. I also retain the right to use in future works (such as articles or books) all or part of my work. I understand that I am free to register the copyright to my work.

REVIEW, APPROVAL AND ACCEPTANCE

The document mentioned above has been reviewed and accepted by the student's advisor, on behalf of the advisory committee, and by the Director of Graduate Studies (DGS), on behalf of the program; we verify that this is the final, approved version of the student's dissertation including all changes required by the advisory committee. The undersigned agree to abide by the statements above.

Johnson Joseph, Student

Dr. Y. Charles Lu, Major Professor

Dr. James M.McDonough, Director of Graduate Studies

Numerical Modeling and Characterization of Vertically Aligned Carbon Nanotube Arrays

---

DISSERTATION

A dissertation submitted in partial fulfillment of the

requirements for the degree of Doctor of Philosophy in the
College of Engineering
at the University of Kentucky

By
Johnson Joseph

Lexington, Kentucky

Director: Dr. Y. Charles Lu, Associate Professor, Mechanical Engineering

Lexington, Kentucky

2013

ABSTRACT OF DISSERTATION

Since their discoveries, carbon nanotubes have been widely studied, but mostly in the forms of 1D individual carbon nanotube (CNT). From practical application point of view, it is highly desirable to produce carbon nanotubes in large scales. This has resulted in a new class of carbon nanotube material, called the vertically aligned carbon nanotube arrays (VA-CNTs). To date, our ability to design and model this complex material is still limited. The classical molecular mechanics methods used to model individual CNTs are not applicable to the modeling of VA-CNT structures due to the significant computational efforts required. This research is to develop efficient structural mechanics approaches to design, model and characterize the mechanical responses of the VA-CNTs. The structural beam and shell mechanics are generally applicable to the well aligned VA-CNTs prepared by template synthesis while the structural solid elements are more applicable to much complex, super-long VA-CNTs from template-free synthesis. VA-CNTs are also highly "tunable" from the structure standpoint. The architectures and geometric parameters of the VA-CNTs have been thoroughly examined, including tube configuration, tube diameter, tube height, nanotube array density, tube distribution pattern, among many other factors. Overall, the structural mechanics approaches are simple and robust methods for design and characterization of these novel carbon nanomaterials.

KEYWORDS:

CNT : Carbon nanotube

SWCNT : Single walled carbon nanotube

DWCNT: Double walled carbon nanotube

MWCNT : Multi walled carbon nanotube

VA-CNT : Vertically aligned carbon nanotube

Johnson Joseph

Nov 22, 2013

Numerical Modeling and Characterization
of Vertically Aligned Carbon Nanotube Arrays

By

Johnson Joseph

Dr. Y. Charles Lu
Co-Director of Dissertation

Dr. James M. McDonough
Director of Graduate Studies

NOV 22, 2013

To My beloved Parents Mrs. Pushpavathi Iris Mary, Mr. A. Joseph and to my wife Chandra Suma.

ACKNOWLEDGMENTS

It has been a great learning experience working under the guidance of Dr. Y Charles Lu, Associate Professor, Mechanical Engineering Department, University of Kentucky. His patient advice, mentorship and support have helped me to achieve my goal in a steady and progressive manner.

I thank my committee members Dr. Tingwen Wu , Dr. Vincent R. Capece, Dr. John Baker, Dr. Yang-Tse Cheng for their time and for providing valuable inputs and critical evaluations of my dissertation. I thank my external examiner Dr. Alberto Corso for his time.

I thank my colleagues Dr. Wei Lei and Dr. Limin Zhou for their valuable input during the course of my program.

I thank my brother Mr. William Joseph for his encouragement and support to pursue higher education.

In a special way I thank my friend Deacon Dennis Dever, for his support and timely advice during the course of my program.

Last but not the least; I thank everyone who has directly or indirectly influenced me, without which it would have been impossible for me to accomplish this job.

TABLE OF CONTENTS

LIST OF FIGURES

LIST OF TABLES

Chapter 1

1. Introduction

1.1 Overview of vertically aligned carbon nanotube arrays

1.1.1 Individual carbon nanotube (CNT)

Carbon nanotube (CNT) is a new class of material that was discovered during the late 90's by Iijima (Iijima 1991). Like diamond, graphene and graphite, carbon nanotube is an allotrope of carbon. One of the notable features of carbon nanotube is its enormous aspect ratio which can go up to 1.32e8:1.0. It has been realized that carbon nanotube has tremendous potential owing to its exceptional mechanical, electrical, magnetic, optical and thermal properties. From a mechanical stand point carbon nanotube has high tensile strength (of the order of 11 – 63 GPa) and very high Young's modulus (around 1TPa). From electrical viewpoint carbon nanotube has very high current carrying capacity (4e9 A/cm^2) which is 1000 times greater than that of copper (Lu 1997), high electron mobility (100,000 $cm^2/V/s$) as compared to silicon (1400 cm^2 /V/s) (Lu 1997) resulting in high electrical conductivity and also high thermal conductivity (3500 w/m/k, as against 385 w/m/k for copper) (Lu 1997) .

In its simplest form a carbon nanotube structure may be understood as a molecule with atoms connected by bonds in a hexagonal ring structure pattern. An individual CNT may be visualized as having formed from a graphene sheet with atoms that are interconnected by bonds in hexagonal chains and upon rolling this sheet forms into a tube structure as seen in Figure 1.1 below. The CNT can be single walled or multiwalled. The latter one can be either of the "Russian Doll" model type with several concentric layers or "Parchment" (scroll) model type with single unending layer rolled into spiral configuration.

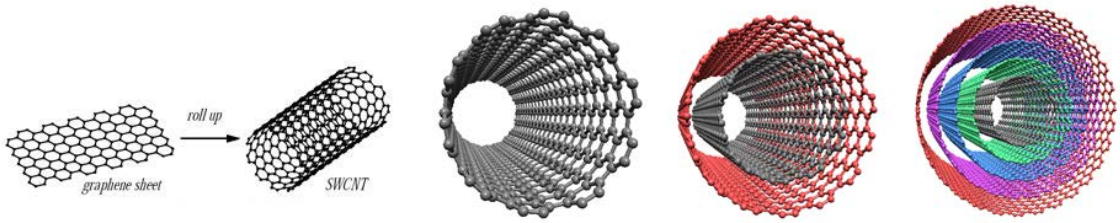

Figure 1.1. Graphene sheet rolled into nanotube, single walled, double walled and multi walled tubes (Shen et al. 2011)

CNTs are classified into three types based on their direction of rolling vector: (i) arm chair, (ii) zigzag, and (iii) chiral. Each of the three configurations of the nanotube may be realized by rolling the nanotube along the vectors as shown in Figure 1.2. Here n, m are the number of unit vectors along unit vectors a_1 and a_2 and C_h is the resultant vector.

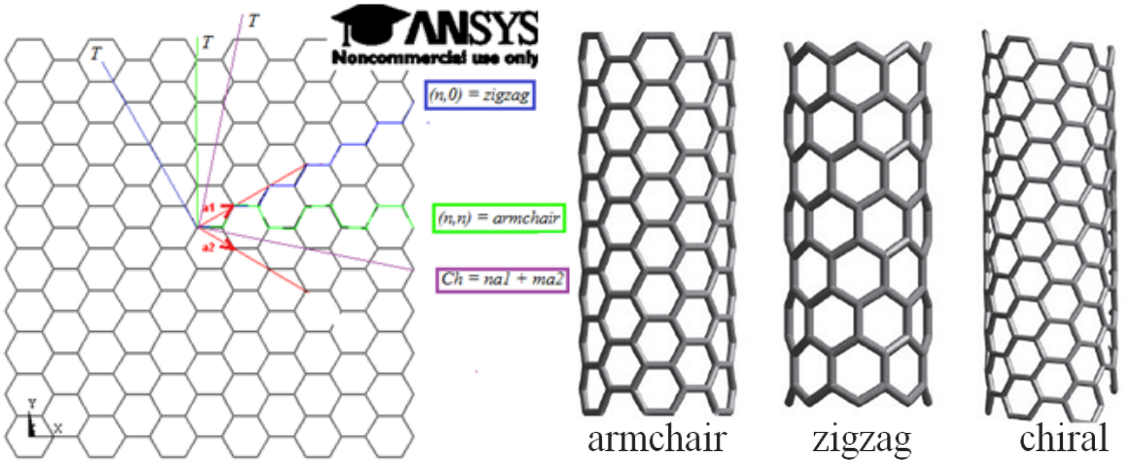

Figure 1.2. Graphene sheet with unit vectors a1, a2 showing the three CNT configurations.(Choudhary and Gupta 2011)

Resultant vector is given by "$Ch = n\overrightarrow{a_1} + m\overrightarrow{a_2}$" and T is the nanotube axis. With m = 0, the nanotube configuration realized is “zigzag”. With n = m, the nanotube configuration realized is “armchair”. With n ≠ m, the nanotube configuration realized is “chiral”. Carbon nanotubes can be either of metallic or semiconducting types. Specifically all armchair nanotubes (n, n) are metallic, (n, m) nanotubes with n-m = 3j

where j is an integer are again metallic and (n, m) nanotubes with n-m ≠ 3j are semiconductors. This classification is pictorially depicted in the Figure 1.3 below.

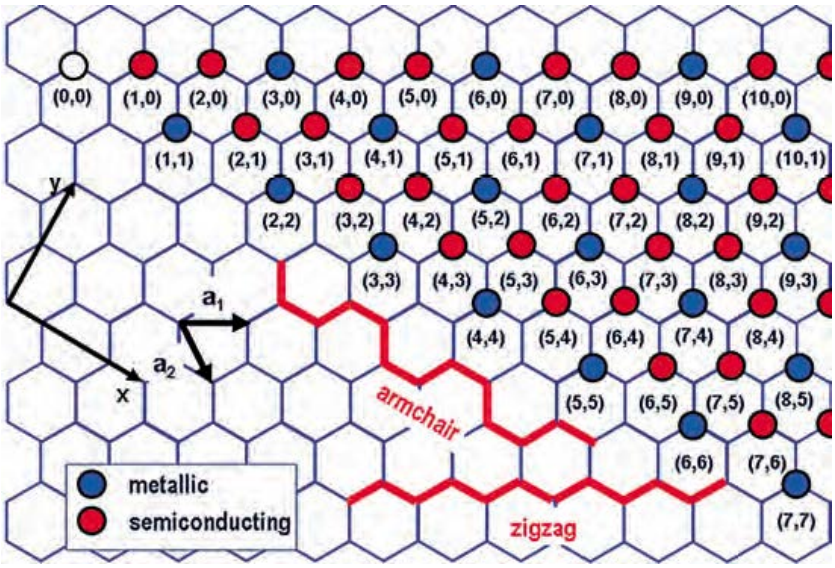

Figure 1.3. Figure showing metallic and semiconducting nanotube configurations (Kreupl et al. 2002)

Metallic nanotubes are used as ballistic nano-scale conductors while semiconducting nanotubes form the material for devices filling the main needs in the microelectronic industry for use in cooling elements, super capacitors, lithium-ion batteries, solar cells, nano-electromechanical systems (NEMS), sensors etc. In medicine, nanotechnology is used for improved drug delivery, new drugs and therapies, the developing of new biomaterials and active implants, imaging and diagnostics of diseases, etc. (Ismach 2008). Further it has been reported that MWCNTs almost always show metallic behavior making it highly suitable for use in interconnect applications in view of its strong metallic behavior(Kreupl et al. 2002)

1.1.2 Vertically aligned carbon nanotube arrays (VA-CNTs)

From practical application point of view, it is highly desirable to produce carbon nanotubes in large scales and on various substrates. This has resulted in a new class of carbon nanotube material, called the vertically aligned carbon nanotube arrays (VA-CNTs). Within literature, VA-CNTs is also referred as vertically aligned carbon nanotube forests, vertically aligned carbon nanotube turfs, vertically aligned carbon nanotube mats, vertically aligned carbon nanotube brushes, etc. The vertically aligned carbon nanotube arrays usually consists of a dense packing of individual CNT with densities as high as 1 x 10^8 tubes /cm^2 through 1x 10^{13} tubes /cm^2 (Figure 1.4).

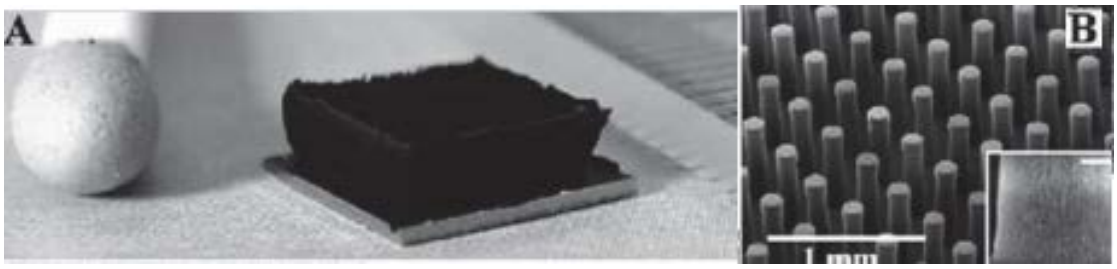

Figure 1.4. (A) Picture of a single-walled VA-CNT arrays. (B) SEM image of VA-CNT cylindrical pillars with 150 µm radius, 250 µm pitch, and 1mm height. The inset shows an SEM image of a root of a pillar, scale bar 50 µm (Ismach 2008).

The VA-CNTs materials can be mass produced through various new synthesis techniques, including (1) carbon arc discharge, (2) electric arc discharge, (3) laser ablation, and (4) chemical vapor deposition, etc. The VA-CNTs can also be grown on different substrates for a variety of applications as seen in in Figure 1.5. VA-CNTs grown on planar substrates, as shown in Figure 1.5(a) and have found widespread applications in areas such as the electrical interconnects (Kreupl et al. 2002), thermal interface materials(Xu and Fisher 2006, Dai 2010) , energy dissipation devices (Kreupl et al. 2002, Dai 2010) and microelectronic devices and micro-electromechanical systems (Treacy et al. 1996). VA-CNTs grown on rounded carbon fibers, as shown in Figure 1.5.(b), can be used for improving the fiber-matrix interfaces in composites (Ruoff and Lorents 1995, Kreupl et al. 2002, Cola et al. 2009, Chen et al. 2010), and as flow or

pressure sensors used on micro air vehicles (MAVs) (Wendy et al. 1995, Goze et al. 1999). VA-CNTs reinforced with matrix composites forms anisotropic conductive materials, while VA-CNTs grown on patterned substrates find applications in triode-type field emitters. In view of their large surface area and high thermal conductivity both of which ensure rapid heat transfer to the surroundings, VA-CNTs are important materials in the construction of solar cells. VA-CNTs are used in hydrogen storage in view of the interior and interstitial surfaces of open-ended CNTs possessing strong binding energy for adsorbing hydrogen gas molecules. Since VA-CNTs possess larger surface area and higher electrical conductivity over entangled CNTs they form an ideal electrode material for DNA biosensor, sensors for glucose, pH and NO_2. Super –aligned CNTs which has a greater nucleation density, lower CNT diameter distribution and better alignment compared to VA-CNT arrays in view of their excellent mechanical (strength > 460MPa) and electrical properties are further developed into a touch panel, liquid crystal display and transparent loudspeaker while still retaining their properties while being exposed to very high or low temperature. VA-CNTs are also used to draw transparent sheets which can further be employed to make organic light emitting diodes (LED). VA-CNTs are used in complementary metal oxide semiconductor (CMOS) IC that can overcome device-to-device variation when normal CNTs are used. VA-CNTs are also grown on spherical substrates. In view of their super compressible foam like behavior demonstrating quick recovery properties, the VA-CNT array is used in energy absorbing coatings.

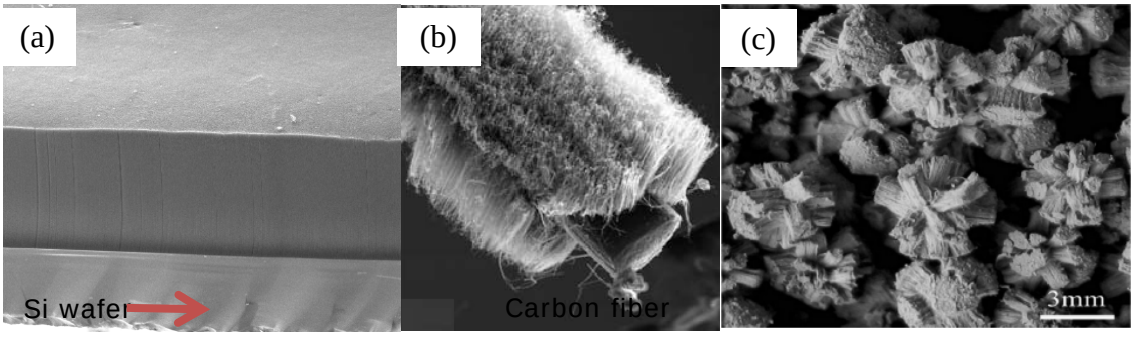

Figure 1.5. Vertically aligned carbon nanotube arrays grown on (a) Planar substrate and (b) Circular substrate (c) Spherical substrate (Ismach 2008)

1.2 Synthesis of vertically aligned carbon nanotube arrays

The vertically aligned carbon nanotube arrays are generally produced through the methods of (1) template synthesis and (2) template-free synthesis.

1.2.1 Growth of VA-CNTs by template synthesis

The commonly used template synthesis techniques include arc discharge and laser ablation. In one of the works by De-Heer et al (De Heer et al. 1995) , an ethanol dispersion of arc-produced nanotubes was passed through an aluminum oxide micropore filter. This in turn leads to perpendicular alignment of nanotubes on the filter surface. This was further transferred to a cathode substrate inside a field emitting device. In a similar way other porous membranes such as mesoporous silica and aluminium nanoholes have been used as templates for the template synthesis of VA-CNTs (Terrones et al. 1997). Terrones et al (Terrones et al. 1997) reported growth of aligned CNTs on cobalt coated silica plate by way of laser ablation and etching of cobalt on the silica plate generated the linear tracks in which there is no catalyst (cobalt) which upon subjecting to two stage pyrolysis lead to growth of well aligned CNTs with no growth observed in the linear tracks.

1.2.1.1 VA-CNT synthesis by arc discharge method

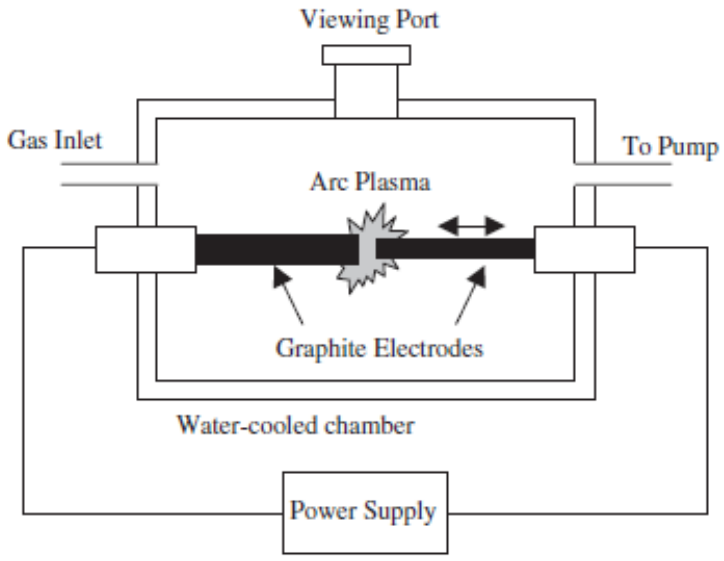

Figure 1.6. Schematic of plasma arc discharge method (Kingston and Simard 2003).

Carbon nanotubes were first observed as a byproduct during the fabrication of fullerenes using electric arc discharge between the graphite electrodes. MWCNTS were first reported following which it was discovered that addition of a catalyst to one of the electrodes produced deposits that were rich in SWCNTs. Arc discharge method is a high temperature (>1700°C) CNT synthesis method causing the CNT growth with fewer structural defects (Prasek et al. 2011). Both MWCNTs and SWCNTs are grown using this technique.

A schematic of the arc discharge method in its simplest form is as shown in figure above. In this method, a DC arc discharge between a pair of water cooled graphite electrodes (6 mm anode and 12 mm cathode in diameter) is created by applying a potential difference of 10V-35V in a chamber filled with an inert gas such as helium at sub atmospheric pressure .Hydrogen and Methane are also used in this process. Thin and long MWNTs have been synthesized under a CH_4 gas pressure of 50 - 500 Torr and an arc current of 20A-100A for the anode (Kingston and Simard 2003, Prasek et al. 2011). The high

temperature arc discharge between the electrodes leads to sublimation of material from the anode which is transferred to the cathode and surrounding walls of the apparatus. In the arc discharge method under controlled conditions of pressure and related parameters, pure nanotubes with high yield may be obtained. Yield of 20-100 mg/min have been reported. Since the consumption of the anode is faster than the growth of MWCNTs, the gap between the graphite electrodes is always maintained at 1 mm by way of constant feeding of one electrode leading to stable arc discharge between the electrodes and a high yield. Synthesis of MWCNTs with an outer diameter of 10-20nm having 5-15 walls and lengths up to 3µm are produced using this method. When the process is carried without the use of a catalyst, MWCNTS are formed as against using a catalyst in which case SWCNTs are produced. SWCNT growth in arc discharge makes use of a composite anode consisting of graphite and a metal such as Ni, Fe, Co, Pd, Ag, Pt or mixtures of elements such as Co, Fe, Ni, Cu, Ti etc. In the case of a metal catalyst and graphite, when introduced into a hole that is drilled in the carbon anode, the so formed nanotubes are found in the soot that is deposited in the chamber wall (Choudhary and Gupta 2011).

1.2.1.2 VA-CNT synthesis by laser ablation method

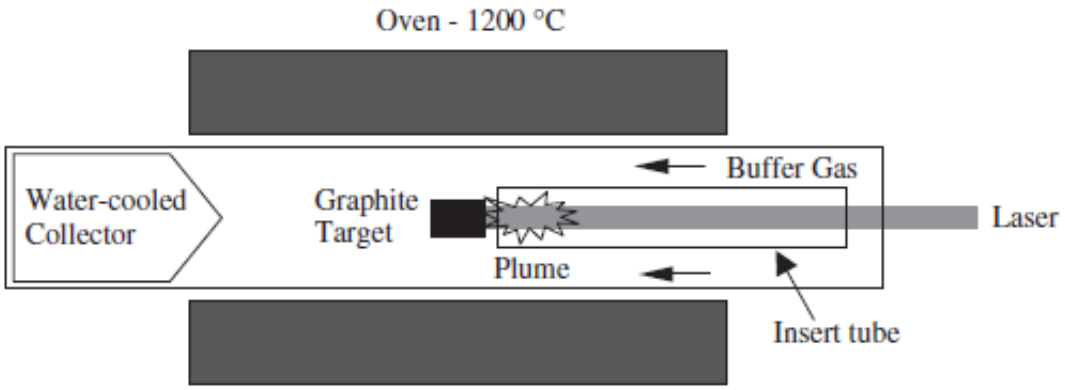

Figure 1.7. Schematic of CNT growth by laser ablation (Kingston and Simard 2003, Choudhary and Gupta 2011).

The laser ablation technique used for the growth of CNT is as shown in the figure above. In its simplest form the setup consists of a furnace, quartz reactor tube and a laser beam source. An intense laser pulse is focused onto the graphite rod target located inside the reactor tube which in turn vaporizes a carbon target containing small amounts of metals such as nickel and cobalt. The target is vaporized in a high temperature argon buffer gas. The entire setup is placed in a tube furnace that is maintained at a temperature of 1200°C. Upon ablation of the target by the laser and with the passage of an inert gas through the chamber, the grown nanotubes are carried to the copper collector that is cooled with water from where the nanotubes are collected. The deposit consists of both MWCNTs and SWCNTs. The main advantage of this method is the production of high quality SWCNT with minimal defects and contaminants such as amorphous carbon and catalytic metals. The diameter of the SWCNT produced can be controlled by changing the furnace temperature, catalytic metals and the flow rate. It has been observed that raising the furnace temperature results in SWCNTs with larger diameter (Koziol et al. 2010, Choudhary and Gupta 2011). Production rates observed in this method is around 80 mg/day up to 1g/24h (Kingston and Simard 2003). It has been observed that the properties of the CNTs so produced is largely dependent on the laser properties, the structural and chemical composition of the target material being ablated, the chamber pressure maintained, the chemical composition, flow as well as the pressure of the buffer gas, the substrate properties, ambient temperature and the distance between the target and the substrate.

In general, the template synthesis allows producing highly ordered VA-CNT structures. By controlling the design of the template, the resultant VA-CNTs can have various architectures and geometric parameters, including the tube height, tube diameter, tube array density, tube distribution pattern, inter-tube distance, and among many other factors as shown in figure below.

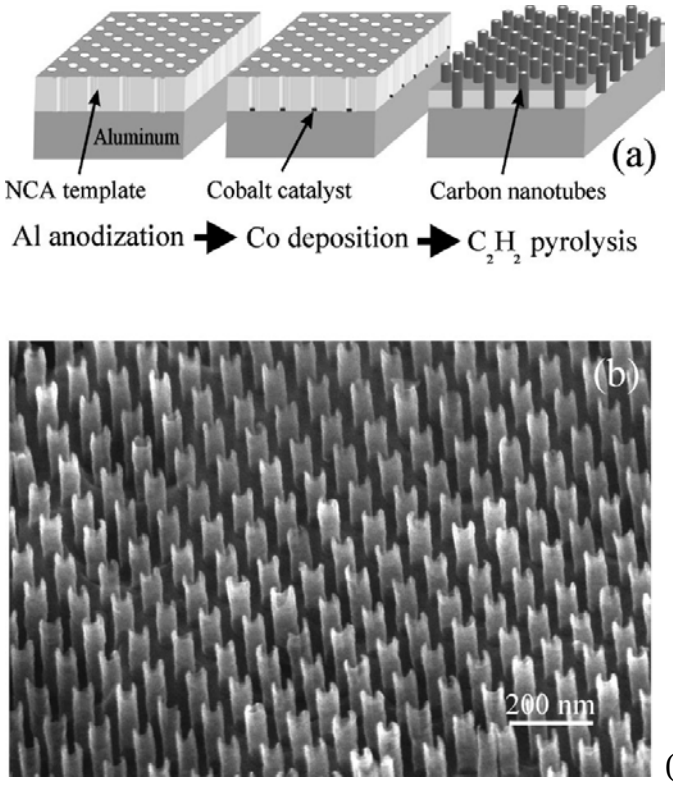

Figure 1.8. (a) Schematic showing the process of template synthesis for producing vertically aligned carbon nanotubes structure. (b) SEM image of aligned carbon nanotubes structure (Waters et al. 2005).

1.2.2 Growth of VA-CNT by template free synthesis

Unlike in the template synthesis method, the template free synthesis is a one step process in which there is no preparation of the catalyst nanoparticles on the substrate used for the nanotube growth. Further, there is no need for the use of template pores in the substrate as reported by several research groups. Among the several available methods, Chemical Vapor Deposition (CVD) has been recognized as the most promising as well as the most popular method for producing VA-CNT arrays. In this process thermal decomposition of a hydrocarbon vapor is achieved in the presence of a metal catalyst. Hence, it is also known as thermal CVD or catalytic CVD. Various types of CVD have been developed such as thermal CVD (T-CVD), plasma-enhanced CVD (PE-CVD) and floating catalyst CVD (FC-CVD). In comparison with electric arc-discharge and laser-ablation techniques,

CVD is the simplest and most economic technique for synthesizing CNTs at low temperatures and ambient pressure conditions. However in terms of crystallinity, arc discharge- and laser-grown CNTs are much superior to those grown by CVD. It may be noted that the crystallinity of SWCNTs grown by CVD is comparable to those grown by arc-discharge and laser ablation methods while slightly reduced crystallinity is observed in MWCNTs grown by CVD. CNTs grown by CVD have better yield, purity, structure control and architecture as compared to other techniques. The CVD technique is versatile with regards to harnessing several hydrocarbons in solid, liquid and gaseous states, makes use of substrates from varieties of materials allowing the CNT growth to take place in several forms as powder, thin or thick films, aligned, entangled, straight, coiled nanotubes or of a desired architecture on predefined sites of a patterned substrate. Further CVD technique offers better control of growth parameters (Kumar and Ando 2010).

1.2.2.1 VA-CNT synthesis by CVD

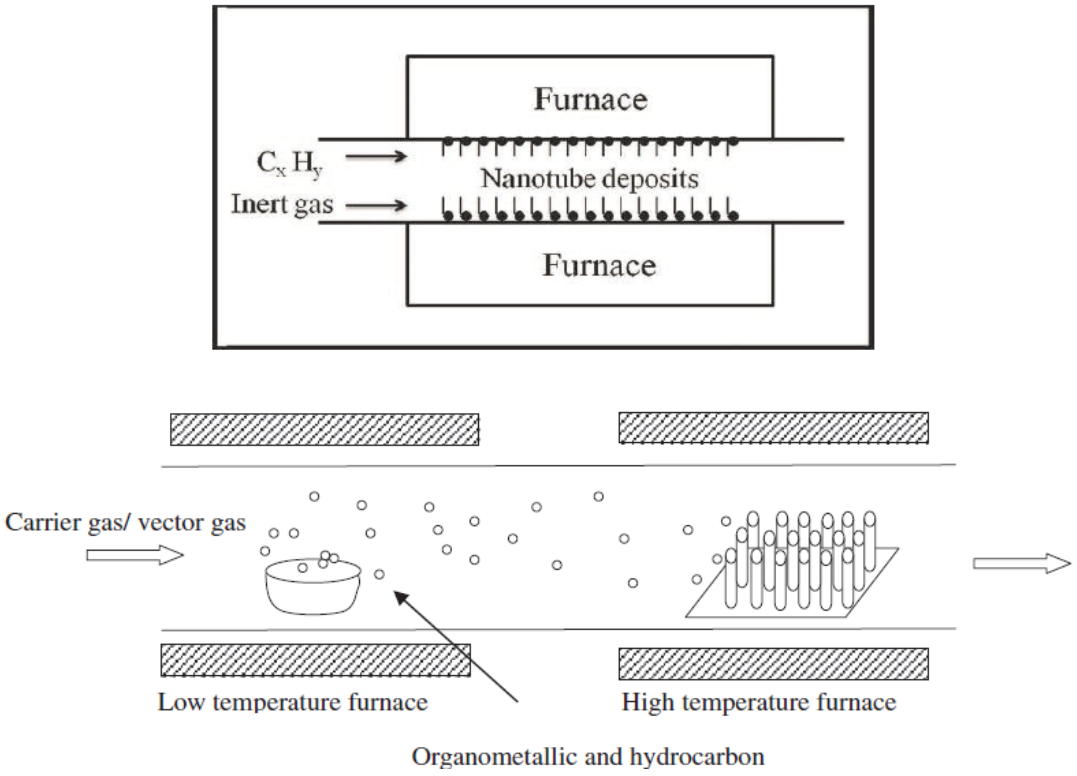

Figure 1.9. Schematic showing the process of template-free synthesis for producing vertically aligned carbon nanotubes structure (Choudhary and Gupta 2011)

Figure 1.9 shows the experimental setup for growth of CNTs by CVD technique in its simplest forms. Hydrocarbon vapor is passed through a tubular reactor /reaction chamber in which a catalyst material has been introduced on a substrate material and maintained at high temperatures of 600°C -1200°C. During this process decomposition of hydrocarbon takes place leading to formation /growth of nanotubes that are collected upon cooling the reactor to room temperature. The diameter of the nanotubes grown greatly depends on the size of the catalyst clusters and under carefully monitored conditions a closely uniform diameter with a very narrow band of diameter distribution may be obtained. Further high temperatures (900°C-1200°C) maintained in the reactor leads to coalescence of catalyst clusters resulting in higher diameter nanotubes as compared to small diameter nanotubes grown at slightly lesser temperatures (600°C – 900°C). Also, high temperature leads to

growth of SWCNTs (900°C -1200°C) as against MWCNTs that grow at lower temperatures (600°C -900°C). It has been observed that higher growth temperatures ensures straight and well aligned growth of VA-CNTs along with a greater degree of crystalline perfection and the VA-CNT yield is greatly dependent on the catalyst concentrations. A higher catalyst to hydrocarbon gas ratio results in a higher VA-CNT yield (Seah et al. 2011). Further, the growth of nanotubes is based on two models namely (i) Tip growth model and (ii) Base growth model. These growth models are as shown in the Figure 1.10 below.

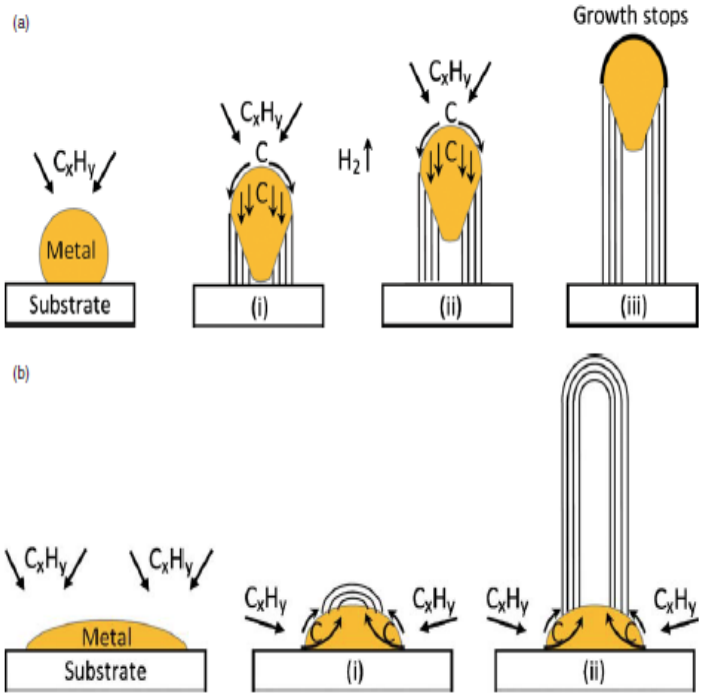

Figure 1.10. CNT growth models by CVD technique (Kumar and Ando 2010).

In the tip growth model the catalyst particles stay at the tip of the growing nanotube as the nanotube grows while in the base growth model the catalyst particles remain at the base of the nanotube and relies on the adhesion between the catalyst particle and the substrate.

The most commonly used CNT precursors are methane, ethylene, acetylene, benzene, xylene and carbon monoxide, while commonly used catalyst metals are Fe, Co, Ni, in

view of high solubility of carbon in these metals at high temperatures as well as high diffusion rate. In recent developments tree products such as turpentine and camphor are being used as sources of carbon for synthesizing VA-CNTs (Seah et al. 2011).The most commonly used substrates for CVD process are graphite, quartz, silicon, silicon carbide, silica, alumina, alumina-silicate (zeolite), $CaCO_3$, magnesium oxide, etc. The CVD technique offers greater control over the length and structure of the grown nanotubes in comparison with arc discharge and laser ablation methods. Further it is also observed that CVD technique is well suited to produce nanotubes in large quantities(Kumar and Ando 2010, Choudhary and Gupta 2011). Plasma enhanced hot filament CVD was first used by Ren and Huang (Ren et al. 1999) to obtain CNT growth at low temperatures (< 666°C). They used an electric field as an external force to ensure alignment of nanotubes. Position controlled growth of VA-CNT on porous and plain silicon substrates was introduced by Fan et al (Fan et al. 1999). The growth of Aligned Carbon Nanotubes (VA-CNTs) was first reported by Thess et al (Thess et al. 1996) in 1996. During the same year the Chinese Academy of Science reported the successful growth of a 50 mm thick film of highly aligned nanotubes by CVD method.

1.2.3 Super-long VA-CNT synthesis by CVD

In view of several recent advancements in CVD techniques, it has become possible to grow nanotubes having lengths in the ranges of millimeters or even centimeters. Compared to the VA-CNTs produced by template synthesis, the super-long VA-CNTs typically have much complex structure. Figure 1.11 shows the morphology of the super-long VA-CNT specimen examined by the scanning electron microscope (SEM). At lower magnifications, the nanotubes are seen to well-align perpendicularly to the substrate. At higher magnification, the individual nanotubes are somewhat zigzag-like along the nanotube length with some entanglements between the nanotubes. All those features are the direct result of the template-free growth process. The areal density of the VA-CNT arrays can be estimated as: $\rho=10^{10}\sim10^{11}$ tubes/cm^2 by counting the numbers of the carbon nanotubes on the substrate. The lengths of these super-long VA-CNTs are typically in the

range of a few hundred to several thousand microns, as achieved by controlling the deposition time and pressure.

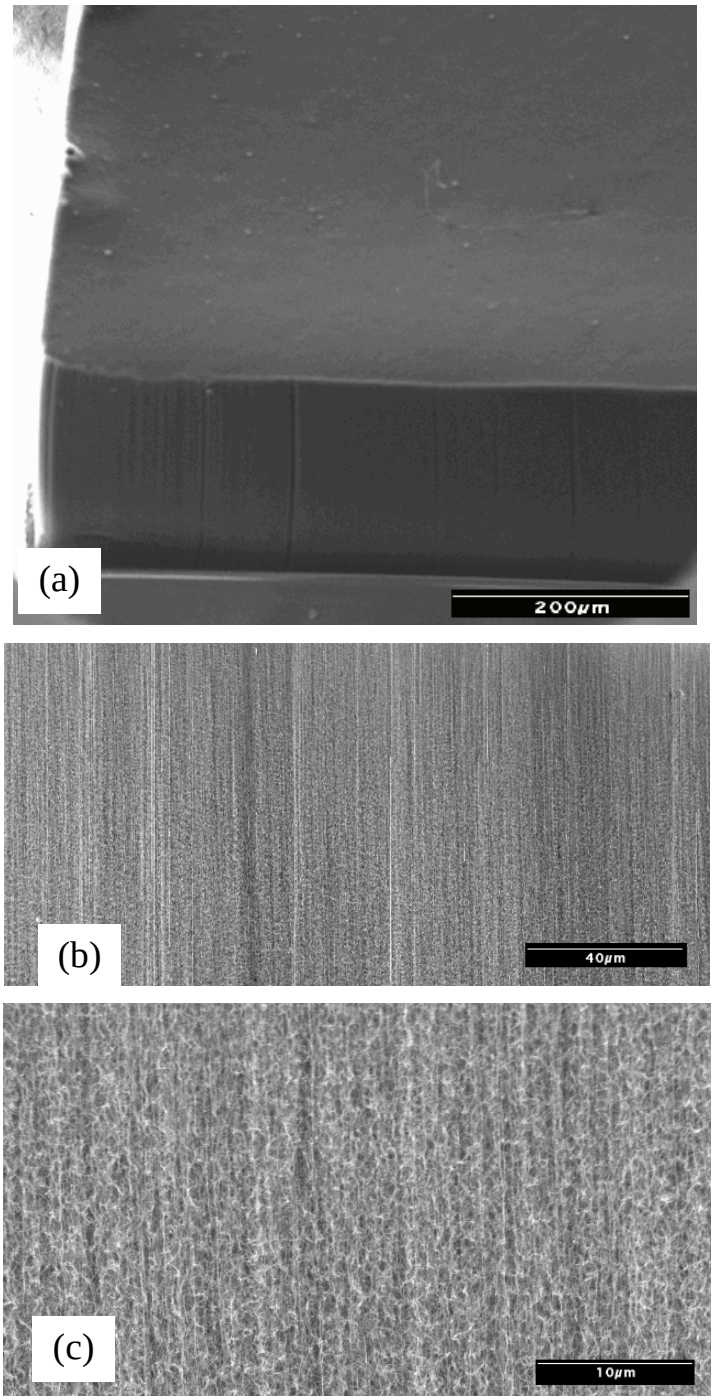

Figure 1.11. SEM images showing the morphology of the super-long vertically-aligned carbon nanotube arrays. The order of magnification increases from (a) to (c).

1.3 Experimental or physical characterization of vertically aligned carbon nanotube arrays

1.3.1 Characterizations of individual carbon nanotube

The diameter of a single CNT is usually in the range of a few nanometers while the length of CNT ranges anywhere from few micrometer to a few millimeters. This very unique nature of the CNTs wherein the aspect ratio, i.e., the ratio of length to diameter being the order of 1.32e8:1.0 or more, poses a difficulty in handling the CNTs for experimentation. Several experimental studies have been conducted in order to evaluate the elastic moduli of the single carbon nanotube. Treacy et al (Treacy et al. 1996) have reported Young's modulus values of 0.4 - 4.15 TPa from transmission electron microscopy by way of thermal vibrations of multiwalled CNT. Krishnan et al. (Krishnan et al. 1998) have conducted similar experiments on multiwalled CNT at room temperature and reported Young's modulus in the range 0.9 - 1.7 TPa. Wong et al., (Wong et al. 1997) have reported for multiwalled CNTs Young's Modulus values of 0.69 - 1.87 TPa by using an AFM to bend the CNT. Similar approach in the work by Salvet et al. (Salvetat et al. 1999) applied to ropes of SWCNT resulted in Young's Modulus value of around 0.6 TPa while with the work by Tombler et al. (Tombler et al. 2000) conducted on a single multiwalled CNT, the Young's Modulus observed is 1.2 TPa. Yu et al.(Yu et al. 2000, Yu et al. 2000) conducted nanoscale tensile test of a CNT by pulling the tip with an AFM and observing it under SEM and reported Young's modulus in the range 0.27 - 0.95 TPa. Studies by Pan et al., (Pan et al. 1999) involving direct measurement of Young's modulus from tensile tests of ropes of very long and aligned CNTs have recorded values between 0.22 – 0.68 TPa.

The experimental investigations of mechanical properties of individual CNTs are summarized in Table 1.1(Sears and Batra 2004). It is noticed that only the Young's modulus of the CNT has been reported. Other mechanical properties such as the shear modulus and Poisson's ratio have not been obtained through experimental means due to the limitations of the testing apparatus. In addition, there is a large scattering in the

Young's modulus values, ranging from 0.27 TPa to 3.6 TPa. This is because most tests used are not conventional mechanical tests, and there exist large variations in terms of testing procedures, data interpretations, etc.

Table 1.1. Material property of individual CNT obtained from experimental measurements (Sears and Batra 2004).

investigation	year	Young's modulus (TPa)	deviation (TPa)	test	tube
Treacy et al.[39]	'96	1.8	1.4	thermal vibrations	mwnt
Wong et al.[35]	'97	1.28	0.6	cantilever	mwnt
Krishnan et al.[41]	'98	1.3	0.5	thermal vibrations	swnt
Salvetat et al.[36]	'99	0.81	0.41	3 pt. bending	bundles
Salvetat et al.[36]	'99	1.28	0.59	3 pt. bending	mwnt
Tombler et al.[37, 42]	'00	1.2	na	3 pt. bending	swnt
Cooper and Young	'00	0.78 - 2.34		raman spect.	swnt
Yu et al.[3]	'00	0.27 - 0.95		tension	mwnt
Lourie et al.[43]	'98	2.8 - 3.6		raman spectroscopy	swnt
Lourie et al.[43]	'98	1.7 - 2.4		raman spectroscopy	mwnt
Yu et al.[38]	'00	0.32 - 1.47		tension	ropes
Poncharal et al.[44]	'99	~1	na	electric vibrations	mwnt

1.3.2 Characterizations of vertically aligned carbon nanotube arrays

The mechanical properties of these VA-CNTs have been investigated lately, mostly through the nanoindentation technique (McCarter et al. 2006, Mesarovic et al. 2007, Pathak et al. 2009, Patton et al. 2009, Zhang et al. 2010). The indenter used was either three-face pyramidal shape (Berkovich indenter), parabolic shape (spherical indenter), or flat shape (flat indenter). By driving the indenter into the specimen and then withdrawn from it, the indentation load-depth curves are obtained and then analyzed by following the standard Oliver-Pharr method (Oliver and Pharr 1992, Goze et al. 1999), from which the modulus and hardness of the VA-CNT arrays can be estimated .

The modulus of the VA-CNT structures determined from the experiments have been found to vary greatly, ranging from several Megapascals to several hundred of Gigapascals (Table 1.2). The reason for the lower modulus is primarily due to the high

porosity in the VA-CNT structures, since the interstitial space between nanotubes is only occupied by air. In a typical VA-CNT structure, the individual nanotubes are either completely separated from neighboring tubes or in weak contact with neighboring tubes through van der Waals attractions.

Table 1.2. Summary of Elastic modulus of VA-CNT structures determined through various nanoindentation experiments.

Indenter Shapes Used in Indentation Experiments	**CNT Height**	**CNT Diameter**	**Elastic Modulus**	**References**
Flat Indenter	35–650 μm	10-20 nm	20-35 MPa	(Maschmann et al. 2011, Lu et al. 2012)
Spherical Indenter	20μm, 500 μm	1-3 nm, 10 nm	18 GPa, 58 MPa	(Misra et al. 2009, Zhang et al. 2010)
3-Sided Pyramid Indenter	~600nm, 20μm	~50nm	0.9-1.2 TPa, 40-600 MPa, 0.1-0.8 GPa	(Mesarovic et al. 2007, Tong et al. 2008)

The deformation mechanisms of the VA-CNTs have also been examined. .Guduru and Waters (Waters et al. 2006) have used a flat indenter to perform compression tests on a VA-CNT arrays, from which the critical buckling load of the nanotube arrays are obtained (Figure 1.12). Cao et al (Cao et al. 2005) have conducted uniaxial compressive tests on CNT arrays up to a strain of 80%. The CNT array was found to behave as an open-cell foam-like material. The stress-strain curve displays three distinct stages: a short elastic region, followed by a prolonged plateau region, and finally a densification region as seen in Figure 1.12. Under compression, the CNT arrays folded themselves in wavelike pattern. It is needless to mention that the magnitude of values on the load-displacement curve for CNT array is much greater than that of the foams, by an order of 6.

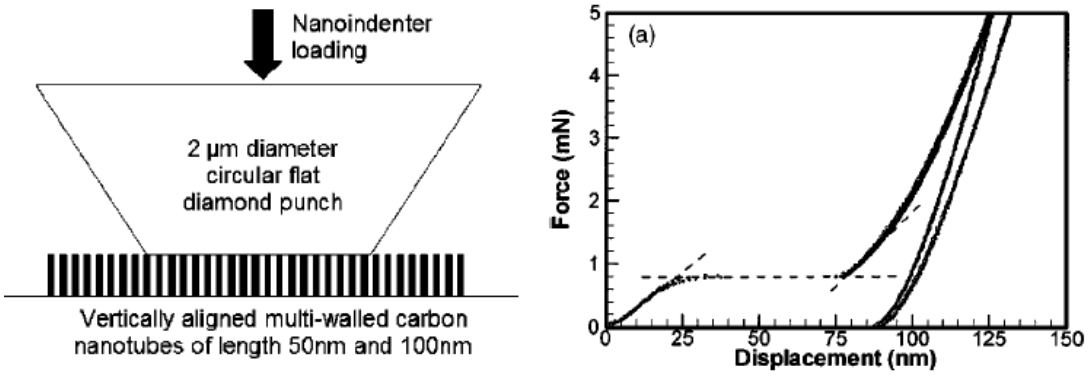

Figure 1.12. Deformation of VA-CNT array examined by a flat indenter(Waters et al. 2006) .

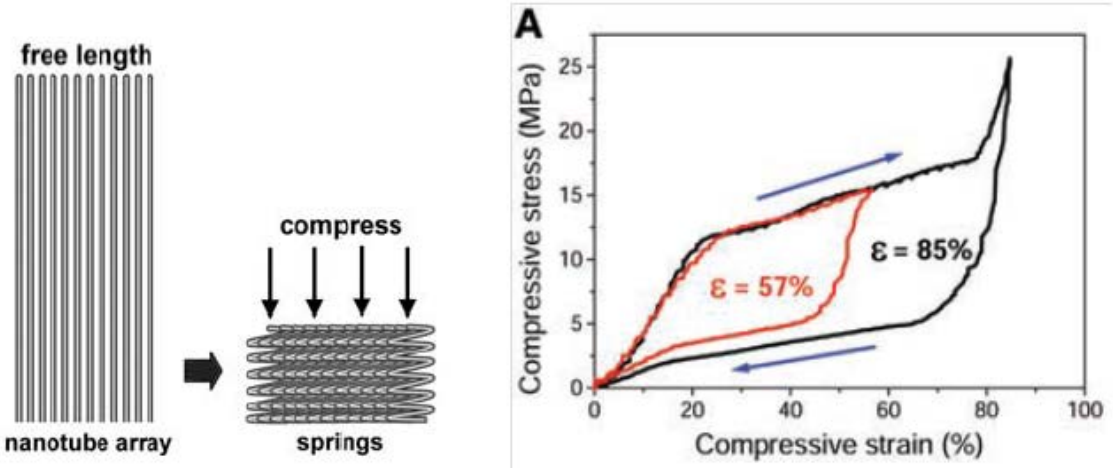

Figure 1.13. Deformation of VA-CNT array examined by uniaxial compression(Fan et al. 1999, Cao et al. 2005).

1.4 Analytical or theoretical modeling of vertically aligned carbon nanotube arrays

1.4.1 Overview of analytical / theoretical techniques

The class of nanotube materials belong to the group of materials that make use of multiscale modeling in which the modeling of materials, systems and phenomenon largely differ by many orders in time and length scales. In view of their nanometer level dimensions and the importance of their responses at this level when combined with other materials such as polymers or composites involving predictions at the macro level having close to 10 orders of size difference, methods that can bridge the gap between model and size scales are needed. To this direction a new research paradigm focusing on the research of materials at nanometer level and using multiscale modeling employing powerful computing resources is currently made available and is referred to as “Integrated Computational Materials Engineering” - ICME / “Computational Materials” (Gates et al. 2005, Sears 2006). With regards to the increasing level of magnification in both length and time scales for multiscale simulation, the available techniques may be grouped in the following order starting from Quantum Mechanics (dealing with atoms. nuclei and electrons), Molecular mechanics / Nano mechanics(dealing with molecular fragments, bond angles, force fields), Mesomechanics (dealing with surface interactions, orientation, crystal packing), Micromechanics(dealing with constituents, interphase, damage), macro and structural mechanics /continuum mechanics (Gates et al. 2005).

1.4.2 Modeling of individual carbon nanotube

The most commonly used analytical method for modeling the individual CNT has been the atomistic approach. The atomistic approaches include classical quantum mechanics, molecular dynamics, tight binding molecular dynamics and density functional theory.

1.4.2.1 Quantum mechanics: Density functional theory

The Density functional theory (DFT) is one of the quantum mechanics (other methods being molecular orbitals, ab initio and semi empirical) techniques also referred to as the first principles method that is applied in order to obtain all the chemical information and changes such as bond breaking of any nanostructure or to understand the physics of a system and provides the most detailed results as compared to any other techniques by way of solving the Schrödinger wave equation for all electrons in the system. The DFT method does not calculate the full wave function instead it calculates the electron density. This technique is computationally expensive and is mainly used when experimental data is unavailable due to difficulties in conducting experiments. An example application is the characterization of electronic properties of CNTs (Garg 2005, Maiti 2008). In principle the state of a particle is defined by a wave function to which the energy associated with each electron in an atom of the CNT system is added. This is followed by applying either the Hartree-Fock or Local density (LD) approximation or Tight-Binding (Semi-empirical) methods in order to obtain an approximate solution to the Schrödinger equation.

$$H\Psi = E\Psi \tag{1.1}$$

where ,

H = Hamiltonian operator of the quantum mechanical system

Ψ= Energy Eigen function corresponding to energy eigen value

Density Functional theory is based on the theorem developed by Hohenberg and Kohn (Hohenberg 1964)according to which all ground state properties are functions of the total electronic charge density ρ(r). In view of its better scaling options with the number of electrons, the density functional theory is becoming the first principle technique of choice for advanced and complicated problem solving.

1.4.2.2 Molecular dynamics (MD)

The MD analyses techniques is one of the most widely used in the theoretical studies applied in order to understand the physical behavior of the nanotubes. The MD techniques is computationally more efficient than the ab initio methods in that it can handle models with atoms up to $1x10^9$ atoms (Wang and Wang 2004) and with time step interval of $1x10^{-15}$ s (Lau et al. 2004). The MD technique treats the group of atoms as a single large molecule comprised of carbon atoms. In theory, Newton's second law of motion is applied for the solution of the governing equations with the law applied to each atom in the system. Referring to an arbitrary atom 'i' the equation of motion is written as

$$m_i a_i = m_i \frac{d^2 r_i}{dt^2} = F_i, \forall i = 1 \dots \dots N_{at} \quad (1.2)$$

where,

m_i = mass of atom i

a_i = acceleration of atom i

F_i = Force applied on the i^{th} atom that is created by all other atoms in the system and defined by interatomic potentials.

In MD technique, each atom having a predefined velocity and position, the acceleration is derived from the interatomic energy potentials. The MD techniques allow for a large range of structures to be analyzed as the system moves and vibrates. Also, temperatures may be prescribed for MD relating to the system's momenta. In general, MD simulations will tend to converge around a potential energy for the system as compared to its initial state. The structure will continue to move and vibrate past local minima thereby potentially sampling a large range of structures.

The various methods using which the interatomic potentials may be evaluated are broadly termed under Molecular Mechanics and are classified as below.

a) Force Field Methods
b) Bond order method

1.4.2.2.1 Force field method

In the force field method that provides a simple and effective approach for describing the atomic potential of interacting atoms in a system, the force field is calculated by summing the individual energy contributions from each degree of freedom (bond stretching, bond angle bending, bond torsion, and non-bonded interactions) of the individual carbon atoms in a CNT. The commonly used molecular mechanics force field potentials are MM2 and MM3 and can be used for both organic and inorganic systems involving polypeptides, proteins and DNA. The MM2 potential is based on bond stretching and bond angle bending while the MM3 potential has higher-order expansions consisting of quartic terms and cross-terms and is primarily used to model proteins. In view of similarities between carbon bonding in nanotube and aromatic protein structures the MM3 potential is very appropriate for CNTs. The MM3 potential is given by the following set of equations consisting of energy terms due to bond stretching (U_s), bond bending (U_θ), bond angle torsion (U_φ) constituting the primary bond deformation terms, non-bonded Vander Waals energy term (U_{vdw}) and terms representing cross interactions between the variables ($U_{s\theta}, U_{\varphi s}, U_{\theta\theta'}$) (Sears and Batra 2004, Garg 2005). The Figure 1.14 below shows the various variables involved in the MM3 potential.

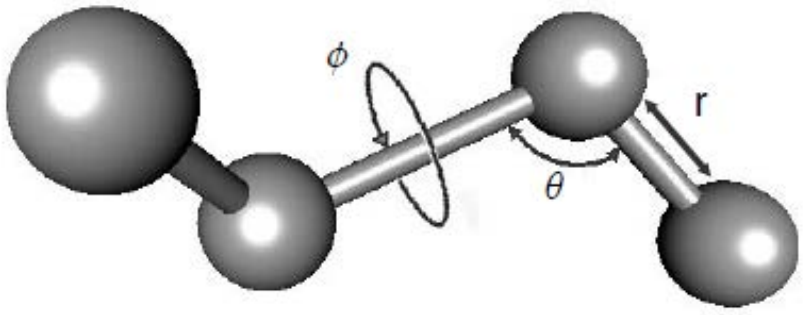

Figure 1.14. Variables used in MM3 potential (Sears and Batra 2004).

The total energy of the system U is given by

$$U = \sum_i \sum_j \left(U_s + U_\theta + U_\varphi + U_{s\theta} + U_{\varphi s} + U_{\theta\theta'}\right) + \sum_i \sum_j U_{vdw} \quad (1.3)$$

where,

$$U_s = 71.94K_s(r - r_0)^2 \left[1 - 2.55(r - r_0) + (\frac{7}{12})2.55(r - r_0)^2\right]$$

$$U_\theta = 0.02191K_\theta(\theta - \theta_0)^2\, X$$
$$[1 - (\theta - \theta_0) + 5.6(10^{-5})(\theta - \theta_0)^2 - 7.0(10^{-7})(\theta - \theta_0)^3 + 9.0(10^{-10})(\theta - \theta_0)^4]$$

$$U_\varphi = \left(\frac{V_1}{2}\right)(1 + cos\varphi) + \left(\frac{V_2}{2}\right)(1 - cos2\varphi) + \left(\frac{V_3}{2}\right)(1 + cos3\varphi)$$

$$U_{vdw} = \varepsilon_0 \left\{-2.25\left(\frac{r_v}{r}\right)^6 + 1.84(10)^5 e^{\left[-12(\frac{r}{r_v})\right]}\right\}$$

$$U_{s\theta} = 2.511K_{sb}[(r - r_0) + (r' - r_0')](\theta - \theta_0)$$

$$U_{\varphi s} = 11.995(\frac{K_{\varphi s}}{2})(r - r_0)(1 + cos3\varphi)$$

$U_{\theta\theta'} = -0.021914K_{\theta\theta'}(\theta - \theta_0)(\theta' - \theta_0')$(Sears and Batra 2004).

The constants $K_s, K_\theta, V_1, V_2, V_3, \varepsilon, \gamma_v, K_{sb}, K_{\varphi s}$ and $K_{\theta\theta'}$ are as per (Zhou et al. 2000).One of the works by Aaron & Sears have used this technique to study the torsion and bending behavior of (16, 0) SWCNT and torsion behavior of a (16, 0) (25, 0) DWNT shown in Figure 1.15.

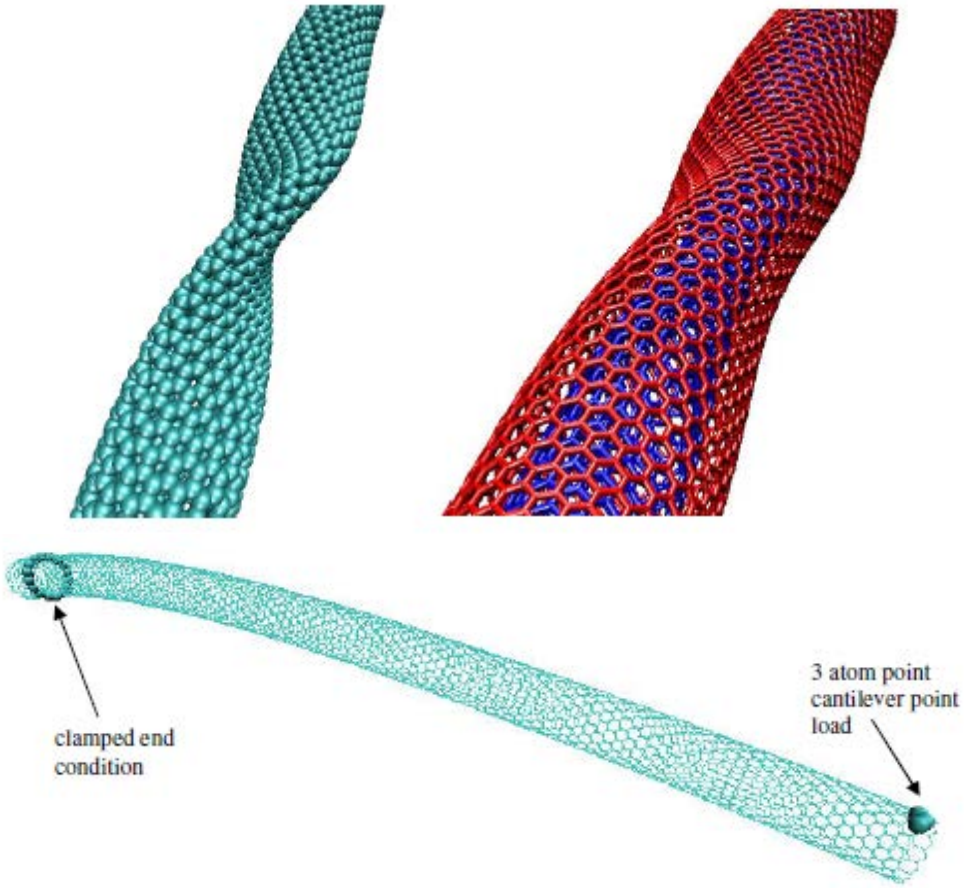

Figure 1.15. Deformation of SWCNT and DWCNT due to torsion and bending based on MM3 potential (Sears 2006).

1.4.2.2.2 Bond order method

Tersoff Brenner (TB) potential is an empirical bond-order potential that is specifically designed for diamond and graphite structures. In this method the bond strength is a pair-wise potential function of the atomic separation, angle and the number of neighboring bonds. TB potential uses exponential functions rather than using a polynomial function to define the bond strength.

The TB potential in its reduced form for purely c-c bonds is given below. The number of neighboring atoms within a prescribed distance determines the number of bonds for an atom and the number of bonds /bond order defines the bond strength of the pairwise bond

potential. The Tersoff-Brenner interatomic potential for carbon is given by the following equation (Zhang et al. 2002, Sears 2006).

$$U = \sum_i \sum_{j(>i)} V_R(r_{ij}) - \overline{B_{ij}} V_A(r_{ij}) \tag{1.4}$$

The above equation sums the energies between atoms i and j, where r_{ij} is the distance between atoms i and$j$, V_R and V_A are attractive and repulsive terms and B_{ij} is the bond order and are given as below

$$V_R(r_{ij}) = \frac{D_{ij}^e}{S_{ij} - 1} e^{-\sqrt{2S_{ij}}\beta_{ij}\left(r_{ij} - R_{ij}^e\right)} f_{ij}(r_{ij})$$

$$V_A(r_{ij}) = \frac{D_{ij}^e S_{ij}}{S_{ij} - 1} e^{-\sqrt{2S_{ij}}\beta_{ij}\left(r_{ij} - R_{ij}^e\right)} f_{ij}(r_{ij})$$

$$B_{ij} = \left[1 + \sum_{k(\neq ij)} G(\theta_{ijk}) f_{ik}(r_{ik})\right]^{-\delta}$$

$$G\left(\theta_{ijk}\right) = a_0 \left[1 + \frac{c_0^2}{d_0^2} - \frac{c_0^2}{d_0^2 + (1 + \cos\theta_{ijk})^2}\right]$$

where θ_{ijk} is the angle between the lines joining atoms $i, j$and k. $G\left(\theta_{ijk}\right)$ is the angle bond energy and functions $f_{ij}(r_{ij})$ and $f_{ik}(r_{ik})$ are linear cutoff functions ranging from 1 to 0.The values of other constants are as discussed by Brenner (Brenner 1990). One of the works by Liew et al (Liew et al. 2004) is based on the above potential and the morphological changes as observed for a (8, 0) SWCNT showing high strains concentrated at the kinks at strains of 0.13 ,0.15 and 0.17 is as shown in the Figure 1.16 below.

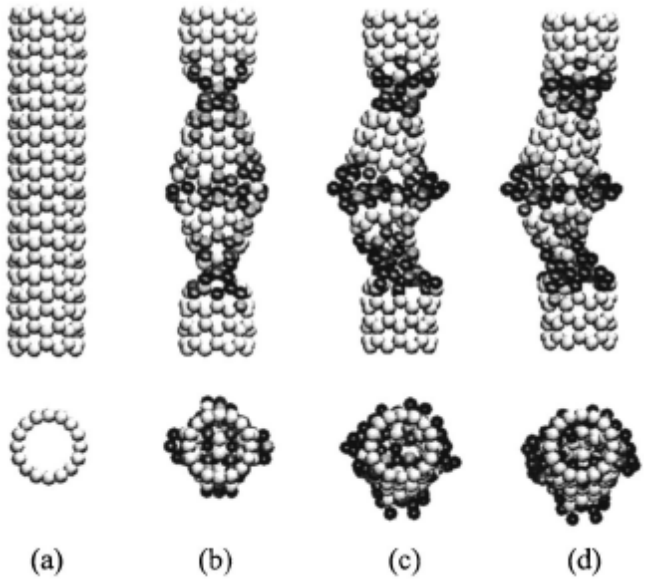

Figure 1.16. Deformation of a SWCNT based on TB potential(Liew et al. 2004) .

A number of researchers have used the molecular dynamics method to model the individual CNTs. Robertson et al (Robertson et al. 1992) reported a single walled CNT Young's modulus value of 1.02 TPa, Yakobson et al (Yakobson et al. 1996) reported a Young's modulus of 1.07TPa for single walled CNTs, Cornwell and Willie (Cornwell and Wille 1997) reported 0.8TPa for Young's Modulus of single walled CNT, Halicioglu (Halicioglu 1998) reported for single walled CNTs a Young's Modulus in the range between 0.44 - 0.50 TPa . All these work employed Tersoff Brenner (TB) Potential (Tersoff 1988, Brenner 1990). The other potentials stated above are used in the work by Overney et al (Overney et al. 1993) who reported a Young's modulus value of 1.5 TPa, Lu (Lu 1997) who reported a Young's modulus of 0.97 TPa and Prylutskyy et al (Prylutskyy et al. 2000) who reported Young's modulus between 1.1 – 1.2 TPa respectively for single walled CNTs. Lu (Lu 1997) obtained a slightly larger value of Young's modulus in the range between 0.97-1.11 TPa for multiwalled CNTs, while Popov et.al (Popov and Van Doren 2000) reported 1 TPa as the elastic modulus of single walled CNT.

The Tight Binding method is employed by Hernandez et al. (Hernandez et al. 1998, 1999) who reported Young's modulus value of 1.26 TPa for single walled CNT and 0.67 TPa in the work reported by Molina et al. (Molina 1996). Sanchez-Portal et al. (Sanchez-Portal et al. 1999) based their work on density functional theory and reported that the Young's Moduli of single walled CNT varied in the range between 0.95 - 1.1 TPa. Van Lier et al. (Van Lier et al. 2000) based their work on ab initio multiplicative integral approach and reported Young's modulus values for single walled CNT in the range of 0.75 – 1.18 TPa. Zhou et al. (Zhou et al. 2001) in their work have reported a Young's modulus value of 0.76 TPa for single walled CNT.

In addition to having several advantages, one of the main disadvantages of atomistic modeling is the need for huge computational resources for handling large sized models having enormous number of atoms & molecules. Hence this approach is limited to analysis of single walled CNT with considerably less number of atoms. Recently, the continuum mechanics approach has been used to model the individual CNTs. The continuum mechanics or the structural mechanics approach considers analyzing the CNT as geometrical space frame structures. Stiffness matrix calculation approach is followed to evaluate the Young's modulus of CNT using either truss or beam elements.

Among the fewer works based on continuum modeling, Liu et al (Liu et al. 2001) have used beam elements while truss elements have been used in the work by Odegard (Odegard et al. 2001). In both work critical buckling strains and buckling modes are evaluated which are in close agreements with the work based on molecular dynamics by Iijima et al. (Iijima et al. 1996) and Yakobson et al.(Yakobson et al. 1996) . Yakobson et al (Yakobson et al. 1996) and Ru et al. (Ru 2000a, 2000b, 2001) have further modeled nanotube using cylindrical shell elements.

Li and Chou (Li and Chou 2003) have used this approach in order to evaluate the Young's modulus and shear modulus of CNT for Armchair, Zigzag and Chiral configurations. The carbon nanotube is modeled considering it to be a geometrical space frame structure with primary bonds acting as load carrying beam members while the

individual atom acts as joints for these beam members. The sectional property parameters for these beam elements are evaluated by establishing a linkage between structural mechanics & molecular mechanics approach. Further, they have verified the results of their method by applying similar technique to graphite sheet and comparing with the results since CNTs belong to the family of graphene. From their findings they have concluded that the Young's moduli of CNT are affected by the tube diameter and their helicity. Accordingly, the Young's moduli of both armchair & zigzag carbon nanotube increase monotonically and approach the value of Young's modulus of graphite.

To (To 2006) has conducted a closely similar work as above, wherein he has modified the method presented by Li and Chou so as to include the effect of Poisson's ratio for evaluation of Young's modulus and shear modulus of single walled carbon nanotubes. To concluded that within linear regime the Young's and Shear modulus are estimated to be constant. The stresses used for evaluation of Young's and shear modulus in this work is based on Cauchy or true stress as against second Piola Kirchhoff's stress used by Li and Chou (Li and Chou 2003).

Tserpes & Papanikos (Tserpes and Papanikos 2005) have modeled a SWCNT with all three configurations Armchair, Zigzag & Chiral having varying thickness and diameter. They have modeled nanotube considering it as a geometrical space frame structure with the bonds being modeled as beam members and connected by joints which are the atoms. Equivalence of energies between molecular and structural mechanics has been used to obtain the sectional properties of the beam which further is used to set up the FE model of the CNT structure. They have conducted tensile and torsion tests to obtain the Young's & Shear modulus of the nanotube

In the continuum shell modeling approach the CNT walls are modeled using shell elements**.** In either of the methods the inclusion and consideration of the atomic interaction forces is questionable. However the computational time with handling of large sized CNT array using discrete modeling approach becomes a matter of concern. The

following table summarizes the modulus and thickness of the carbon nanotube as reported by several researchers using atomistic /molecular simulation techniques.

Table 1.3. CNT Young's modulus and thickness predictions based on molecular methods (Sears and Batra 2004, Sears 2006).

Author(s)	Year	Modulus (TPa)	Thickness (Å)	Poisson's ratio ν	Potential / Method	Trend
Robertson *et al.* (Ref. 15)	1992	1.06	3.4		Brenner & LDF[a]	$1/r^2$, helicity
Yakobson *et al.* (Ref. 1)	1995	5.5	0.66		Brenner	na
Yakobson *et al.* (Ref. 1)	1996	1.07	3.4	0.19	Brenner	
Cornwell and Wille (Ref. 16)	1997	1	3.4		Brenner	$1/r^2$
Halicioglu (Ref. 2)	1997	0.5	6.8		Brenner	Radial
Lu (MWNT) (Ref. 17)	1997	1.11	3.4		Universal force field	Number of walls
Lu (SWNT) (Ref. 17)	1997	0.97	3.4		Universal Force field	None
Hernandez *et al.* (Ref. 18)	1998	1.24[a]	3.4		Density-functional theory[a]	None
Yao and Lordi (Ref. 19)	1998	1	3.4		Universal force field	$1/r^2$
Ozaki *et al.* (Ref. 20)	2000	0.98	3.4		Tight binding O(N)	None
Van Lier *et al.* (Ref. 21)	2000	1.09	3.4	0.11	Hartree-Fock[a]	Helicity (small)
Zhou *et al.* (Ref. 3)	2000	5.1	0.71		Electronic band theory	$1/r^2$
Belytschko *et al.* (Ref. 22)	2002	0.94	3.4	0.29	Modified Morse	

[a]Quantum-mechanical method.

1.4.2.3 Modeling of vertically aligned carbon nanotube arrays

While major research work in the characterization of carbon nanotubes lie in the modeling of individual carbon nanotube (CNT), the modeling of nanotubes in the form of a dense vertically aligned array (VA-CNTs) have been relatively scarce in the literature (Goze et al. 1999, Hutchens et al. 2011, Wang et al. 2011).

Wang et al (Wang et al. 2011) has conducted discrete modeling of VA-CNT arrays by treating each individual CNT in the array as a solid beam. The distribution patterns of the tube arrays (square pattern and random pattern) have been analyzed. The effects of tube density, tube height, and tube tilt angle on elastic modulus have been investigated. Hutchens et al (Hutchens et al. 2011) and Lu et al (Lu et al. 2012) have modeled the VA-CNTs as continuum solid. The VA-CNTs were treated as a dense foam materials and the deformation under uniaxial compression (Hutchens et al. 2011) and indentation (Lu et al. 2012) analyzed.

1.5 Research objectives and methodologies

Since their discoveries, carbon nanotubes have been widely studied, but mostly in the forms of 1D "individual carbon nanotube (CNT)". To date, work on the complex vertically aligned carbon nanotube arrays (VA-CNTs) is still limited. The actual fabrications of such materials seems still facing many technical difficulties. Therefore, new material development models are needed to accelerate the realization of such novel and important materials. Unlike traditional materials (metals, ceramics and polymers) whose microstructures are relatively "fixed", vertically aligned carbon nanotube array materials are highly "tunable" from the structure standpoint. The optimal performance of the VA-CNTs highly depends upon their architectures and geometric parameters, including: tube height, tube diameter, tube array density, tube distribution pattern, inter-tube distance, among many other factors. Thus, it is crucial to have a rational strategy to design and evaluate the architectures and geometric factors to help process the optimal materials.

The overall objective of this research project is to develop effective numerical modeling procedures to design, model and characterize the mechanical responses of the VA-CNTs. The work in this research has been organized into three stages of analysis:

1) Structural Beam Modeling of Vertically Aligned Carbon Nanotube Arrays

2) Continuum Shell Modeling of Vertically Aligned Carbon Nanotube Arrays

3) Continuum Solid Modeling of Vertically Aligned Carbon Nanotube Arrays

Figure 1.17 below depicts these stages of work.

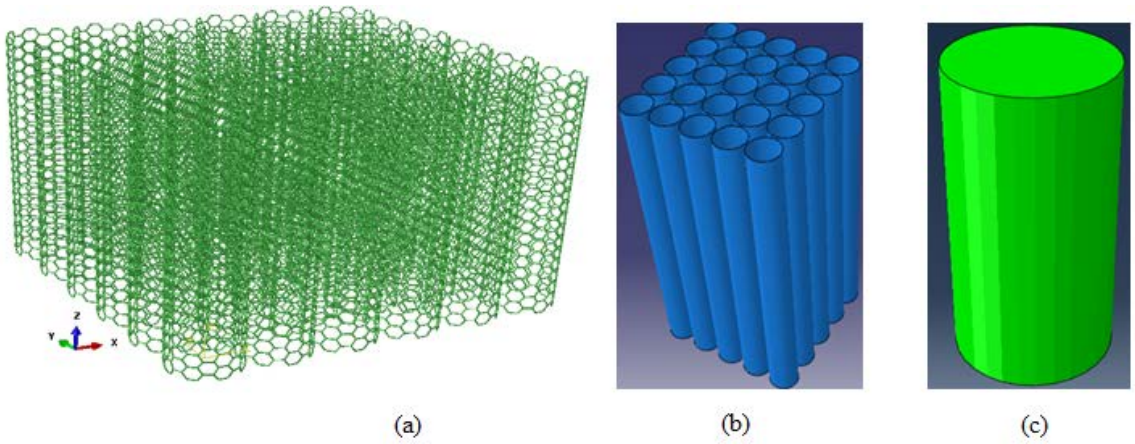

Figure 1.17. Development of numerical modeling frame work for vertically aligned carbon nanotube arrays (VA-CNTs): (a) Structural beam modeling of VA- CNT arrays, (b) Continuum shell modeling of VA-CNT arrays, and (c) Continuum solid modeling of VA-CNT arrays.

The first stage of analysis, as presented in Chapter 2 and Chapter 3, is to evaluate the elastic moduli of an individual CNT and VA-CNTs by way of FE modeling and analysis of the nanotube as a space frame structure using beam elements. The approach in this stage is based on Classical / Structural Mechanics principles. Carbon nanotube may be understood as geometrical space frame structures with primary bonds between any two neighboring atoms acting as load bearing members and the atoms may be visualized as joints for these load bearing members. Suitable section properties are obtained by establishing appropriate linkage between structural mechanics & the constant force field in the atomic system. In this stage, the effect of nanotube thickness, diameter, length, number of walls on the elastic modulus and stiffness is studied.

This is followed, as presented in Chapter 4 and Chapter 5, by FE modeling and analysis of individual CNT (SW-CNT, MW-CNT) and VA-CNT array using continuum shell modeling. In both the stages above, the VA-CNT array is modeled and analyzed to

understand the effects of several design parameters on the Young's modulus and stiffness of the arrays. These are: (1) Density of nanotube packing .i.e. aerial density which is the number of tubes per unit cross sectional area, (2) Type of nanotube packing configuration: FCC and SQUARE packed configuration, and (3) Length / height of carbon nanotubes in the array. Additionally, VA-CNT arrays modeled using shell elements as in stage 2 above allows studying the effect of additional parameters on the Young's modulus and stiffness as: (1) Effect of nanotube diameter and (2) Effect of number of walls in a MW VA-CNT.

The third stage of analysis, as presented in Chapter 6, covers the FE modeling and analysis of a VA-CNT array based on continuum solid modeling approach. Several works in the VA-CNT arrays have reported that the behavior of VA-CNT array resembles close to that of low density foam. Proceeding with this understanding, the VA-CNTs are modeled using Hyperelastic and Crushable foam material models having a low density that are available in ABAQUS FE software. The behavior of VA-CNTs is analyzed with regards to several parameters (including axisymmetric model). Parameters such as critical buckling load, plastic deformation etc. are studied.

Chapter 2

2. Design and Modeling of Vertically Aligned Carbon Nanotubes Using Structural Beam Modeling: Individual Carbon Nanotubes

2.1 Introduction

Carbon nanomaterials such as vertically aligned carbon nanotubes arrays are emerging new materials that have demonstrated superior mechanical, thermal, and electrical properties. The carbon nanomaterials have the huge potential for a wide range of vehicular applications, including lightweight and multifunctional composites, high-efficiency batteries and ultra-capacitors, durable thermal coatings, etc. In order to design the carbon nanomaterials for various applications, it is very important to develop effective computational methods to model such materials and structures. In contrast with traditional materials whose microstructures are relatively "fixed", the aligned carbon nanotube materials have highly "tunable" structures. Therefore, it is crucial to have a rational strategy to design and evaluate the architectures and geometric factors to help process the optimal nanotube materials. A structural mechanics based computational modeling is used for designing the aligned carbon nanotubes structures. The present work presents a structural mechanics approach to effectively model the mechanical behavior of vertically aligned carbon nanotube arrays. As the fundamental building block of the aligned nanotube structures, the variations of geometric parameters of the individual nanotube on its mechanical properties are thoroughly examined.

The carbon nanotube may be viewed as a geometrical space frame structure with primary bonds between any two neighboring atoms and thus can be modeled using three-dimensional beam elements. Effects of tube geometric factors (wall thickness and tube diameter) and material properties (Poisson's ratio) on mechanical properties of the nanotube structure were examined. Results show that the Young's modulus is inversely proportional to the nanotube wall thickness and Poisson's ratio. On the other hand, the Young's modulus and shear modulus exhibit nonlinear relationships with the nanotube

diameter, i.e., both moduli increase rapidly at smaller diameters but become stabilized at larger diameters. Compression test conducted on VA-CNT array shows linear behavior for the values of applied strains in the present case.

Since its discovery in the early 90's by Iijima (1991, 1993), carbon nanotube (CNT) has continued to attract great interest due to its superior structure and properties. An individual single-walled CNT may be visualized as originating from a single layer sheet of graphene rolled up to form a tube structure. Depending on the directions of rolling vectors, the CNT can be in different configurations, i.e., arm chair, zigzag, and chiral. Carbon nanotube can also be in multi-walled structure, which consists of a group of coaxial single-walled carbon nanotubes. Like diamond, carbon nanotube is also allotrope of carbon. A carbon atom in a CNT has six electrons with two of them filling the 1s orbital and the other four filling the sp^2 orbital. The rolled structure of CNT causes σ-π rehybridization in which the three σ bonds are slightly out of plane, which makes the π orbital more delocalized outside the nanotube. This has resulted in extremely strong carbon nanotubes, with possibly the highest Young's modulus and tensile strength. There have been numerous theoretical studies on the mechanical properties of an individual carbon nanotube (Lu 1997, Wong et al. 1997, Krishnan et al. 1998, Popov and Van Doren 2000, Qi et al. 2003) and the Young's modulus and shear modulus of a CNT have been predicted to be as high as 1.25 TPa and 0.45 TPa, respectively. Due to the small dimensions, the actual measurements on the properties of an individual CNT has proven to be difficult. Treacy et al. have carried out the first successful measurement of the Young's modulus of individual CNT. By thermally inducing a vibration on a CNT cantilever inside a transmission electron microscope, they have reported the Young's modulus of a multi-walled CNT as 1.8 TPa (Treacy et al. 1996). Wong et al. (1997) have reported for multiwalled CNTs Young's Modulus values of 0.69 - 1.87 TPa by using an AFM to bend the CNT. Yu et al. (2000) have conducted nanoscale tensile test of a CNT by pulling the tip with an AFM and observing it under SEM and reported Young's modulus in the range 0.27 - 0.95 TPa.

Due to its small sizes (the tube diameter is only a few nanometers), a single carbon nanotube has very limited applications. Most devices would require that the carbon nanotube be produced in large scales and at oriented forms. This has resulted in a new form of carbon nanotubes: the aligned carbon nanotubes (VA-CNTs) structures. As sketched in Figure 2.1(a), a VA-CNT structure is consisted of numerous individual CNTs adhered vertically to a flat substrate. The aligned CNTs was first grown by Terrones. (Terrones et al. 1997) through the method of laser ablation. Latest technologies such as the chemical vapor deposition (CVD) method have made it possible to produce the aligned CNTs at large scales. The vertically aligned CNTs have found a wide range of applications in areas such as electrical interconnects (Kreupl et al. 2002), thermal interfaces (Cola et al. 2009), energy dissipation devices (Liu et al. 2008), and microelectronic devices (Fan et al. 1999), and flow sensors on micro air vehicles (Zhang et al. 2010), etc.

Unlike traditional materials (metals, ceramics and polymers) whose microstructures are relatively “fixed”, the aligned carbon nanotube materials have highly “tunable” structures. The optimal performance (thermal, electrical and mechanical) of the VA-CNTs highly depend upon their architectures and geometric parameters, including the tube height, tube diameter, tube array density, tube distribution pattern, inter-tube distance, tube-tube junction structure, and among many other factors. Therefore, it is crucial to have a rational strategy to design and evaluate the architectures and geometric factors to help process the optimal nanotube materials. A review of literature on carbon nanotubes has revealed that extensive works available so far are on modeling and characterization of individual CNT as against fewer works available / published on modeling and characterization of the VA-CNT structures. The most commonly used method for modeling the individual CNT is the atomistic approach, which includes the classical molecular dynamics, tight binding molecular dynamics and density functional theory. Although the atomistic approach is successful for handling an individual nanotube, it is too computational expensive for modeling an aligned CNT structure that is consisted of millions of individual tubes. Here we present a frame work for designing and modeling the aligned carbon nanotubes structures by using the structural beam modeling.

In specific, Chapter 2 presents the theory and the modeling of an individual nanotube, the fundamental building block of the aligned nanotube structures while Chapter 3 presents the detailed design and modeling of the aligned carbon nanotube structures.

2.2 Modeling procedures for individual carbon nanotubes

2.2.1 Finite element formulation

The approach in this work is based on the principle of structural mechanics (finite element method (FEM)). As illustrated in Figure 2.1(a), an aligned carbon nanotubes structure is consisted of numerous individual nanotubes that are packed vertically on flat substrates. Each individual carbon nanotube may be understood as geometrical space frame structure with primary bonds between any two neighboring atoms acting as load bearing members and the atoms may be visualized as joints for these load bearing members (Figure 2.1 (b)). Therefore, the 3D space beam elements were deemed to be appropriate and effective for modeling these bonds and hence the carbon nanotube structures (Figure 2.1 (c)). Suitable section properties are obtained by establishing appropriate linkage between structural mechanics and the constant force field in the atomic system.

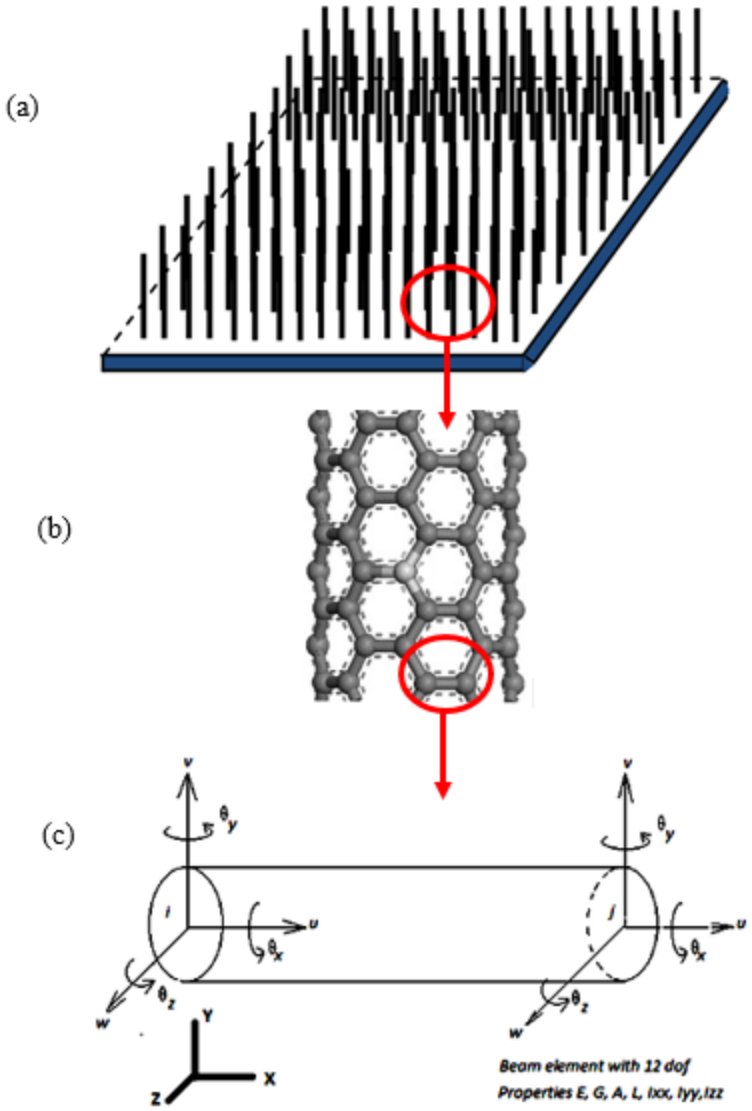

Figure 2.1. (a) A sketch for aligned carbon nanotube array structure (not to scale) (b) A sketch for an individual carbon nanotube; and (c) a 3D beam element in space.

The general idea of finite element formulation of a structural problem lies in obtaining the solution for a system of simultaneous algebraic equations. This is different from the solution obtained to differential equations while solving analytical mathematical equations that pose difficulty with increasing complexities of geometry, material & loading. Thus, the numerical methods yield very close approximations of the values of the unknowns at discrete number of points in the continuum. The process involves modeling the structure by dividing it into equivalent system of smaller bodies referred to as finite elements and interconnected at points that are common to two or more elements

referred to as discretization. The essence of the finite element method lies in that instead of solving the problem for the entire body in one operation the equations for each of the finite element is formulated and then is combined to obtain the solution to the whole body. In general, the solution for structural problems involves determining displacement at each node and the stress within each element of the structure subject to applied loads.

The general purpose finite element programs are often based on displacement or stiffness based finite element formulation, wherein the governing equations are expressed in terms of nodal displacements using equations of equilibrium describing the behavior of an element in matrix form and represented as below (Logan 2004).

.

$$\{\mathbf{f}\}^{\mathbf{e}} = [\mathbf{k}]^{\mathbf{e}} \{\mathbf{q}\}^{\mathbf{e}} \tag{2.1}$$

where $[k]^e$ = Element stiffness matrix

$\{q\}^e$ = Element displacement vector

$\{f\}^e$ = Element force vector

The system of simultaneous linear equations can then be solved by applying boundary conditions to obtain the nodal displacements.

2.2.2 Finite element formulation of beam element

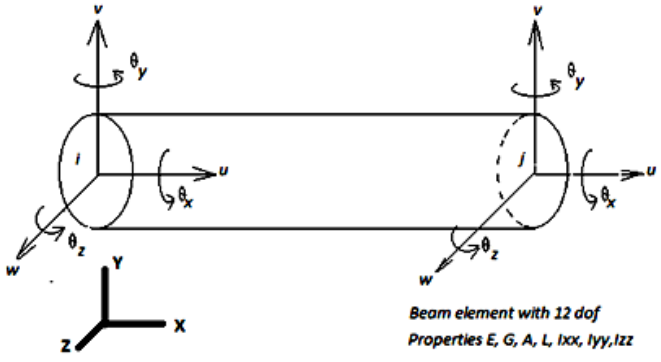

Figure 2.2. 3D beam element in space.

For a beam element that is arbitrarily oriented in space as shown in Figure 2.2 the stiffness matrices considering bending about two axes viz. $\hat{y}$ (for bending in $\hat{x}-\hat{z}$ plane) and $\hat{z}$ (for bending in $\hat{x}-\hat{y}$ plane), upon direct superposition with the axial stiffness matrix & the torsional stiffness matrix yields the element stiffness matrix $[k]^e$ for the beam element in 3-D space as below.

$$[\mathbf{k}]^{\mathbf{e}} = \begin{bmatrix} \mathbf{k_{ii}} & \mathbf{k_{ij}} \\ \mathbf{k_{ji}} & \mathbf{k_{jj}} \end{bmatrix} \tag{2.2}$$

where,

$$k_{ii} = \begin{bmatrix} \frac{EA}{l} & & & & & \\ 0 & \frac{12EI_{zz}}{l^3} & & & symmetric & \\ 0 & 0 & \frac{12EI_{yy}}{l^3} & & & \\ 0 & 0 & 0 & \frac{GJ}{l} & & \\ 0 & 0 & \frac{-6EI_{yy}}{l^2} & 0 & \frac{4EI_{yy}}{l} & \\ 0 & \frac{6EI_{zz}}{l^2} & 0 & 0 & 0 & \frac{4EI_{zz}}{l} \end{bmatrix}$$

$$k_{jj} = \begin{bmatrix} \frac{EA}{l} & & & & & \\ 0 & \frac{12EI_{zz}}{l^3} & & & symmetric & \\ 0 & 0 & \frac{12EI_{yy}}{l^3} & & & \\ 0 & 0 & 0 & \frac{GJ}{l} & & \\ 0 & 0 & \frac{6EI_{yy}}{l^2} & 0 & \frac{4EI_{yy}}{l} & \\ 0 & \frac{-6EI_{zz}}{l^2} & 0 & 0 & 0 & \frac{4EI_{zz}}{l} \end{bmatrix}$$

$$k_{ij} = \begin{bmatrix} \frac{-EA}{l} & 0 & 0 & 0 & 0 & 0 \\ 0 & \frac{-12EI_{zz}}{l^3} & 0 & 0 & 0 & \frac{6EI_{zz}}{l^2} \\ 0 & 0 & \frac{-12EI_{yy}}{l^3} & 0 & \frac{-6EI_{yy}}{l^2} & 0 \\ 0 & 0 & 0 & \frac{-GJ}{l} & 0 & 0 \\ 0 & 0 & \frac{6EI_{yy}}{l^2} & 0 & \frac{2EI_{yy}}{l} & 0 \\ 0 & \frac{-6EI_{zz}}{l^2} & 0 & 0 & 0 & \frac{2EI_{zz}}{l} \end{bmatrix}$$

and $$k_{ji} = k_{ij}{}^{T}$$

The corresponding element displacement and force vectors are

$$\{\mathbf{q}\}^{\mathbf{e}} = \left[\mathbf{u_i}, \mathbf{v_i}, \mathbf{w_i}, \theta_{\mathbf{xi}}, \theta_{\mathbf{yi}}, \theta_{\mathbf{zi}}, \mathbf{u_j}, \mathbf{v_j}, \mathbf{w_j}, \theta_{\mathbf{xj}}, \theta_{\mathbf{yj}}, \theta_{\mathbf{zj}} \right]^{\mathbf{T}}$$

$$\{\mathbf{f}\}^{\mathbf{e}} = \left[\mathbf{f_{xi}}, \mathbf{f_{yi}}, \mathbf{f_{zi}}, \mathbf{m_{xi}}, \mathbf{m_{yi}}, \mathbf{m_{zi}}, \mathbf{f_{xj}}, \mathbf{f_{yj}}, \mathbf{f_{zj}}, \mathbf{m_{xj}}, \mathbf{m_{yj}}, \mathbf{m_{zj}} \right]^{\mathbf{T}}$$

The element stiffness equation is established for each of the beam element in the space frame followed by appropriate transformation of reference frame from local to global coordinate system and solution to nodal displacement. The individual element equations are then added together using a method of superposition referred to as direct stiffness method in order to obtain the global equations for the whole VA-CNT structure with the final assembled / global equation written in the form as below

$$\{\mathbf{F}\} = [\mathbf{K}]\{\mathbf{Q}\} \qquad (2.3)$$

where, [K] = Structure global stiffness matrix

{Q} = Vector of generalized displacements

{F} = Vector of global nodal forces

The system of simultaneous linear equations can then be solved by applying boundary conditions to obtain the nodal displacements, element strains, element stresses and nodal forces.

In the above equations, the tensile resistanceEA, flexural rigidity EI_{yy} and EI_{zz}, torsional rigidity GJ are related to the bond axial stretching force constant, bond bending constant & torsional resistance of the bond as described in the following sections.

2.2.3 Estimation of total potential energy from molecular mechanics

Considering molecular mechanics approach, a carbon nanotube may be regarded as a large molecule comprising of carbon atoms with material points at the atomic nuclei. The force fields causing the motion and generated by electron-nucleus & nucleus-nucleus interaction (Machida 1999) is expressed in the form of steric potential energy. At stable equilibrium state the total potential energy resulting from the valence or bonded & non-bonded interactions may be expressed as (Rappe et al. 1992).

$$\mathbf{U} = \sum_{\mathbf{r}} \left(\mathbf{U}_{\mathbf{a}}^{\mathbf{r}} + \mathbf{U}_{\boldsymbol{\theta}}^{\mathbf{r}} + \mathbf{U}_{\boldsymbol{\varphi}}^{\mathbf{r}} + \mathbf{U}_{\boldsymbol{\omega}}^{\mathbf{r}} + \mathbf{U}_{\boldsymbol{\vartheta}}^{\mathbf{r}} + \mathbf{U}_{\mathbf{e}}^{\mathbf{r}} \right) \tag{2.4}$$

where,

U_a^r : Energy due to bond axial stretching

U_θ^r : Energy due to bond angle bending

U_φ^r : Energy due to dihedral angle torsion

U_ω^r : Energy due to out of plane torsion

U_ϑ^r : Energy due to nonbonded Vander Waals interaction

U_e^r : Energy due to electrostatic interaction and r is the bond number.

In general for covalent systems the main contribution to the total potential energy arises from the first four terms. Under the assumptions of small deformations and for simplicity,

upon merging the dihedral angle torsion and out of plane torsion we can represent each of the above energy terms in harmonic approximation as below.

$$U_a^r = \frac{1}{2}k_a(\Delta u)^2 \quad (2.5)$$

$$U_\theta^r = \frac{1}{2}k_\theta(\Delta\theta)^2 \quad (2.6)$$

$$U_\tau^r = \left(U_\varphi^r + U_\omega^r\right) = \frac{1}{2}k_\tau(\Delta\varphi)^2 \quad (2.7)$$

where,

k_a : Bond Stretching force constant

k_θ : Bond Bending force constant

k_τ : Bond torsional resistance constant

2.2.4 Relationship between molecular mechanics and structural mechanics parameters

As described earlier, a nanotube may be considered as a space frame structure, which upon subject to external forces the displacement of individual atoms are constrained by bonds between these atoms. A very close analogy between molecular & structural mechanics may be established by considering the bonds at the molecular level as equivalent beams forming space frame structures.

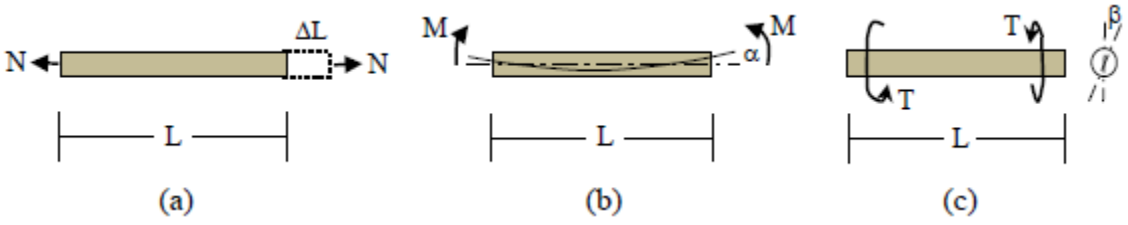

Figure 2.3. Beam under (a) pure tension, (b) bending and (c) torsion.

As considered by several researchers in their work (Li and Chou 2003) and from theory of structural mechanics, equivalence may be established between the structural stiffness

parameters and molecular force constants shown above. It is assumed that the C-C bonds are circular in cross section. From structural mechanics principles, the expression for strain energy of a uniform beam subjected to a pure axial force 'N' as shown in Figure 2.3(a) above is given by

$$U_N = \frac{1}{2}\iiint \sigma_x \varepsilon_x \, dV = \frac{1}{2}\int_0^L \left(\frac{N^2}{EA}\right) dx = \frac{1}{2}\left(\frac{N^2 L}{EA}\right)$$

$$= \mathbf{\frac{1}{2}\left(\frac{EA}{L}\right)(\Delta L)^2} \tag{2.8}$$

where 'ΔL' is the axial deformation due to stretching.

Similarly, the strain energy of a beam subject to pure bending moment 'M' as shown in Figure 2.3 (b) above is given by

$$U_M = \frac{1}{2}\iiint \sigma_b \varepsilon_b \, dV = \frac{1}{2}\int_0^L \left(\frac{M^2}{EI}\right) dx = 2\left(\frac{EI}{L}\alpha^2\right)$$

$$= \mathbf{\frac{1}{2}\left(\frac{EI}{L}\right)(2\alpha)^2} \tag{2.9}$$

where 'α ' is the rotation due to bending.

Further, the strain energy of a beam subject to pure torsional moment 'T'as shown in Figure 2.3 (c) above, developing circumferential shear stress 'τ' and corresponding shear strain 'γ' is given by

$$U_T = \frac{1}{2}\iiint \tau \gamma \, dV = \frac{1}{2}\int_0^L \left(\frac{T^2}{GJ}\right) dx = \frac{1}{2}\left(\frac{T^2 L}{GJ}\right)$$

$$= \mathbf{\frac{1}{2}\left(\frac{GJ}{L}\right)(\Delta\beta)^2} \tag{2.10}$$

where, '$\Delta\beta$' is the torsional rotation.

A close observation of the above two sets of equations (2.5, 2.6, 2.7, 2.8, 2.9, 2.10) shows that

$$\Delta \mathbf{u} = \Delta \mathbf{L}\,; \quad \Delta \boldsymbol{\theta} = \mathbf{2}\boldsymbol{\alpha}\,; \quad \Delta \boldsymbol{\varphi} = \Delta \boldsymbol{\beta} \tag{2.11}$$

And the molecular force constants may be related to structural stiffness parameters as below

$$\mathbf{k_a} = \frac{\mathbf{EA}}{\mathbf{L}} \quad ; \quad \mathbf{k_\theta} = \frac{\mathbf{EI}}{\mathbf{L}} \quad ; \quad \mathbf{k_\tau} = \frac{\mathbf{GJ}}{\mathbf{L}}. \tag{2.12}$$

The force constants values selected are k_a = 938 Kcal mol^{-1} Å^{-2}, k_θ = 126 Kcal mol^{-1}rad^{-2} and k_τ = 40 Kcal mol^{-1}rad^{-2} (Jorgensen 1990, Wendy et al. 1995)

2.2.5 FE modeling of individual carbon nanotubes

The CNTs are classified into three types: (i) arm chair, (ii) zigzag, and (iii) chiral. It is noticed that when the chiral angles become 0^o and 30^o, the chiral CNT essentially becomes the zigzag and armchair tubes, respectively. Therefore, the CNTs with zigzag and arm chair configurations were the primary concern in the present study. First, individual carbon nanotube in zigzag and arm chair configurations were geometrically modeled using the modeling capability of ANSYS FEA software. The nanotube model is imported into ABAQUS FEA software where the nanotube geometric model is then taken through the stages of FE modeling. FE mesh is generated using the 3D Beam element. Both linear (B31) and quadratic (B32) formulation beam elements are used in several analysis trials to ensure mesh convergence along with mesh refinement. Suitable loading and boundary conditions are applied leading to complete FEA model set up. All nodes at the bottom edge of the nanotube are fixed with a displacement applied to the top end. Appropriate beam section orientation, geometric sectional properties (L=0.1421 nm), and material properties (E=1.02 TPa, ν=0.16) obtained from the molecular-structural correlation were implemented. Based on literature review several values of nanotube

thickness are identified in the range from 0.066nm (Ci et al. 2008) to 0.69 nm (Odegard et al. 2002). These values are used as thickness values based on which several trials of analysis are conducted. Among these, a thickness value of 0.34nm which is the interspatial distance between layers of graphite sheet is chosen for further analysis in this work. The combination of modulus and thickness chosen agrees very well with the in-plane stiffness value of 360 J/m^2 for graphene. The beam element is modeled assuming a circular cross section for which the diameter is assigned equivalent to the values of the above thickness identified. The diameter of the nanotube was varied between 0.5 nm - 2.5 nm for both armchair and zigzag configuration nanotubes. The Figure 2.4 below shows the geometric model of one of the armchair nanotube (8, 8) with diameter of 1.086 nm that is modeled for the analysis.

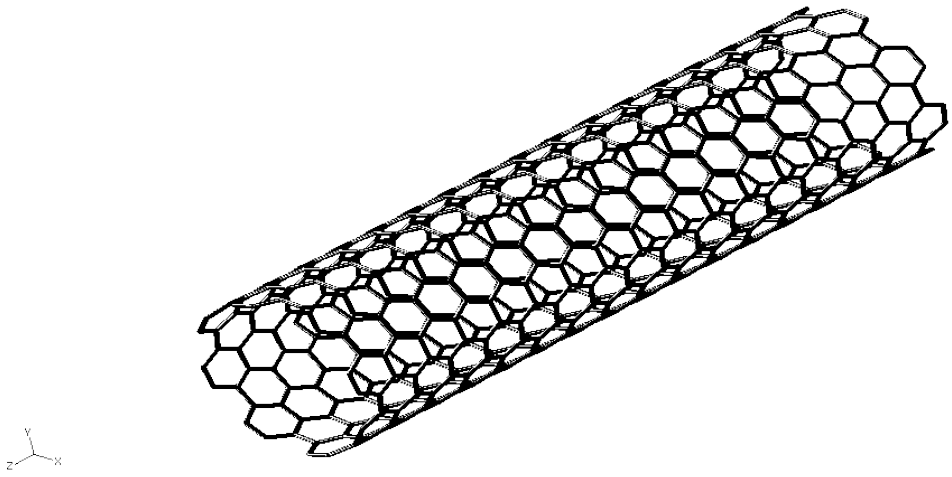

Figure 2.4. FE model of armchair (8, 8) CNT.

A linear elastic analysis with NLGEOM = OFF is conducted with several trials of analysis runs by varying the mesh size i.e. by varying the number of elements and the order of the elements used in the nanotube FE model. Thus a convergence study is conducted before arriving at the final results. The nanotube is subjected to tensile loading by way of imposing a displacement at the free end and with the other end of the nanotube constrained in all the six degrees of freedom. The application of load & boundary conditions for both zigzag and armchair nanotube configurations is shown in Figure 2.5 below.

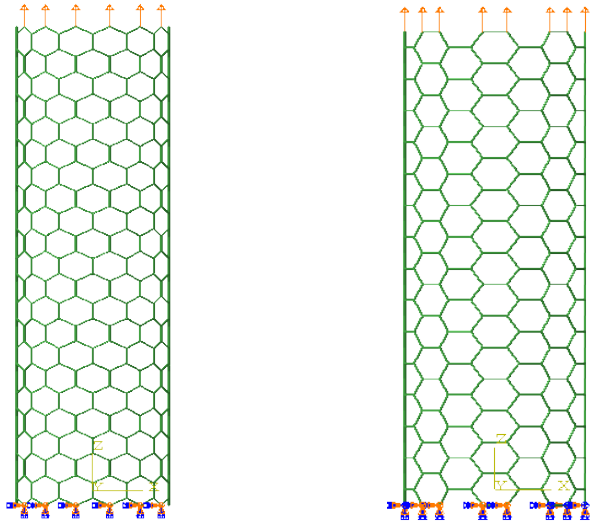

(a) (b)

Figure 2.5. FE models for (a) CNT zigzag (14, 0) configuration and (b) CNT armchair (8, 8) configuration model showing loads and boundary conditions.

The model setup and analysis runs are conducted using 3D beam elements having six degrees of freedom U_x, U_y, U_z, R_x, R_y, R_z.. In all these analyses a poisson's ratio of 0.16 is implemented based on the work by Chang and Gao (Chang and Gao 2003)..

2.3 Results and discussion

2.3.1 Variation of nanotube Young's modulus with nanotube thickness

The individual nanotube is the fundamental building block of the aligned nanotube structures, therefore, the structure and properties of the individual nanotube were first analyzed. The complete FE model for the individual nanotube was setup in the FE software ABAQUS with appropriately calculated beam properties for the C-C bonds of the nanotubes. Studies such as effect of variation of nanotube thickness, nanotube diameter, nanotube Poisson's ratio and nanotube aspect ratio on the Young's modulus 'E' ,stiffness and Shear modulus 'G' of nanotubes are conducted. Resulting Poisson's ratio assuming linear behavior of nanotube are computed as functions of nanotube diameter.

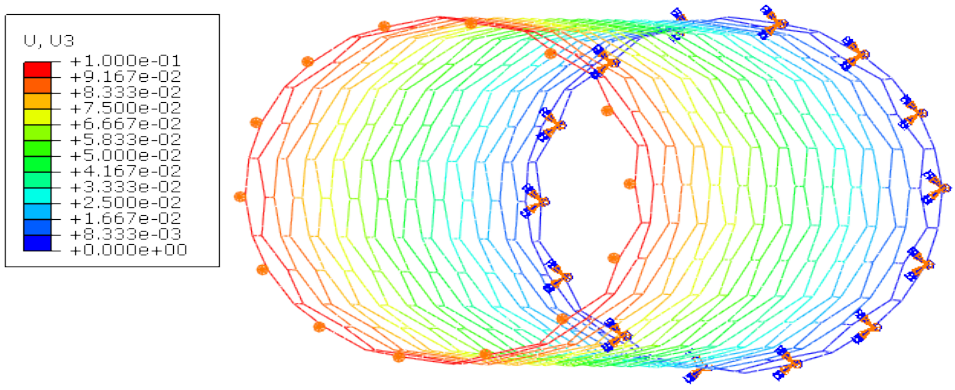

Figure 2.6. Displacement contour of a (14, 0) nanotube subject to tensile loading

A convergence study is made using linear beam elements B31 having linear displacement function as well as using quadratic beam elements B32 having 3 nodes having quadratic displacement function and by varying the mesh size. Figure 2.6 above shows the displacement contour of a (14, 0) nanotube subject to tensile loading. Figure 2.7 below shows the plot of convergence of "E' for a (14, 0) nanotube with increase in number of nodes.

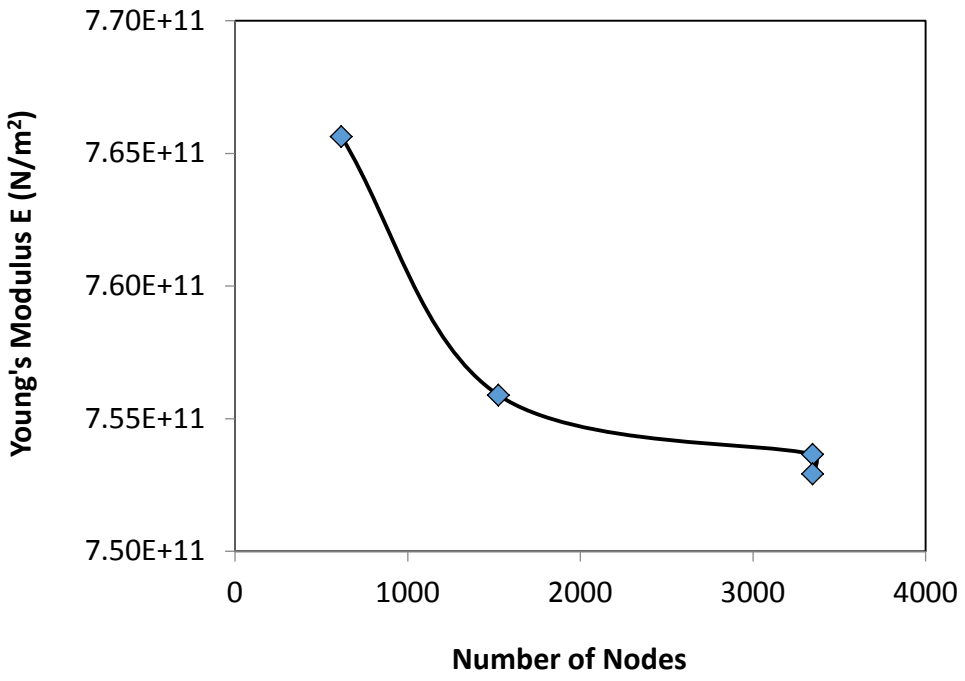

Figure 2.7. Convergence of Young's modulus of nanotube with number of nodes. The nanotube used is the zigzag (14, 0) structure.

Following this, the nanotube is modeled with a quadratic 3D beam element B32 having quadratic displacement function in order to ensure the accuracy of the results obtained. The following sections discuss the various studies carried out.

Several values of nanotube thickness have been reported in the literature that are evaluated experimentally and have been widely accepted (Iijima 1991, Iijima et al. 1996, Lu 1997, Hernandez et al. 1998, 1999, Popov and Van Doren 2000, Prylutskyy et al. 2000). In this analysis, the commonly reported values of thickness viz. 0.066 nm (Yakobson et al. 1996), 0.075 nm, (Tu and Ou-Yang 2002)0.147 nm (Tserpes and Papanikos 2005), 0.154 nm (which is the diameter of carbon atom), and 0.34 nm (which is the inter-wall spacing of graphite) have been used for modeling the nanotube.

Table 2.1 below summarizes the different analysis trials conducted for evaluation of Young's Modulus 'E' of CNT with varying thickness and element order. Two CNT models viz. zigzag (14, 0) with diameter of 1.097 nm and armchair (8, 8) with diameter

of 1.086 are modeled and analyzed to study the effect of increasing the CNT thickness on the CNT Young's Modulus in stages. Resulting stress-strain plots are obtained by considering the force resisting area which is equal to $\pi * d_t * t$ where 'd_t' is the nanotube diameter and 't' is the diameter of the beam element (bond). The resulting value of Young's modulus of the nanotube structure was then evaluated using the relation.

$$E = \frac{PL}{A\delta} \tag{2.13}$$

where P = Applied load / Reaction force developed

δ = Elongation of the nanotube

L = Length of the nanotube

A = Cross sectional area of the nanotube

Since a quadratic approximation is always more appropriate than a linear approximation, the nanotube model meshed with quadratic beam elements B32 yields values of Young's modulus closer to those modeled with linear beam elements B31 with higher number of elements as again seen from Table 2.1 in the following page.

Table 2.1. Table showing dependency of 'E' on CNT wall thickness

CNT FE Model Details			**CNT Zigzag (14, 0)**	**CNT Armchair (8, 8)**
			nu=0.16	
Thickness (nm)	**Beam Element**	**# Elements per hex arm**	**Computed E N/m^2**	
0.066	B31(Linear)	1	2.22299E+12	2.35609E+12
		2	1.92E+12	2.04035E+12
		4	1.85746E+12	1.97294E+12
	B32(Quadratic)	2	1.83728E+12	1.95164E+12
0.075	B31(Linear)	1	2.17038E+12	2.29182E+12
		2	1.91876E+12	2.02273E+12
		4	1.86393E+12	1.96415E+12
	B32(Quadratic)	2	1.84602E+12	1.94549E+12
0.147	B31(Linear)	1	1.55563E+12	1.5974E+12
		2	1.48641E+12	1.52387E+12
		4	1.46912E+12	1.50649E+12
	B32(Quadratic)	2	1.46336E+12	1.50079E+12
0.154	B31(Linear)	1	1.50264E+12	1.54251E+12
		2	1.44099E+12	1.47679E+12
		4	1.42542E+12	1.46118E+12
	B32(Quadratic)	2	1.42023E+12	1.45604E+12
	B31(Linear)	1	7.65632E+11	7.72471E+11
0.34		2	7.55887E+11	7.64684E+11
		4	7.53653E+11	7.6276E+11
	B32(Quadratic)	2	7.52912E+11	7.62124E+11

It is observed from the above results that an increase in the CNT thickness leads to a decrease in the value of the Young's modulus of CNT. The Young's modulus of armchair

CNT is slightly higher than that of zigzag CNT. This trend is in close agreement with results that are already reported in several works seen from literature and the values of the Young's modulus obtained here are within the published range of values from the literature. The plot below in Figure 2.8 show the dependency of the nanotube Young's modulus for both (14, 0) zigzag and (8, 8) armchair nanotube configurations on the nanotube thickness while the number of elements per hexagonal arm are varied to observe the effect of mesh convergence on the Young's Modulus.

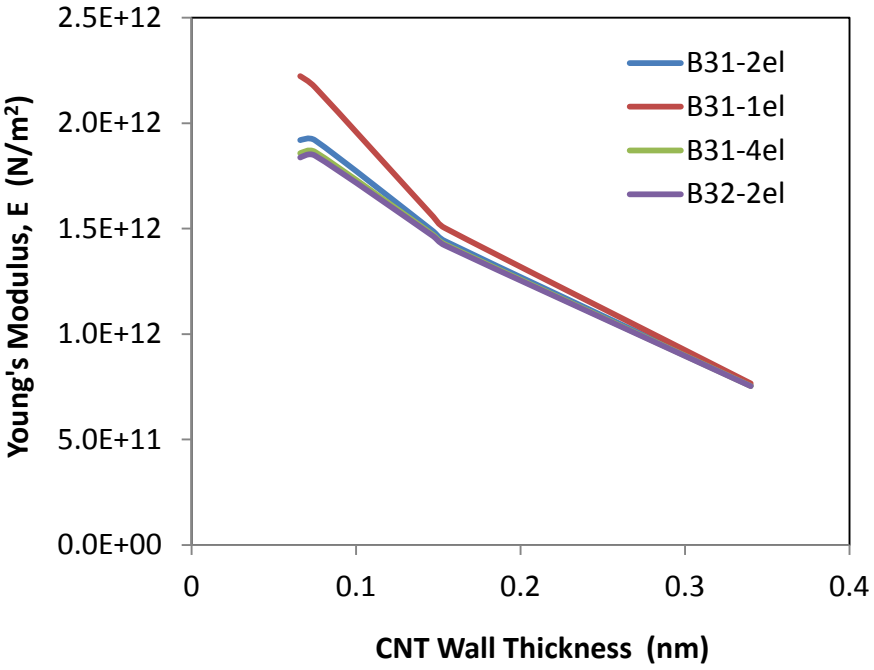

(a)

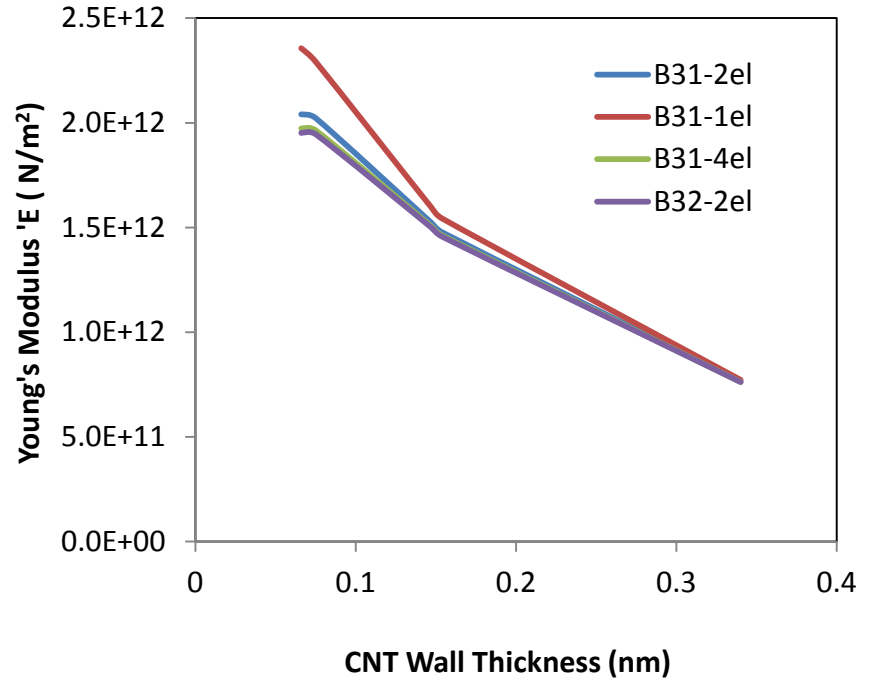

(b)

Figure 2.8. Variation of Young's modulus as a function of nanotube wall thickness for (a) zigzag (14, 0) CNT and (b) armchair (8, 8) CNT.

Further, Figure 2.9 shows the comparison of Young's modulus variation with nanotube thickness for the two nanotube configurations. Upon observation it may be concluded

that the Young's Modulus of armchair nanotubes is slightly higher than that of zigzag nanotubes for small values of thickness and converge as the thickness of nanotube approaches 0.34 nm.

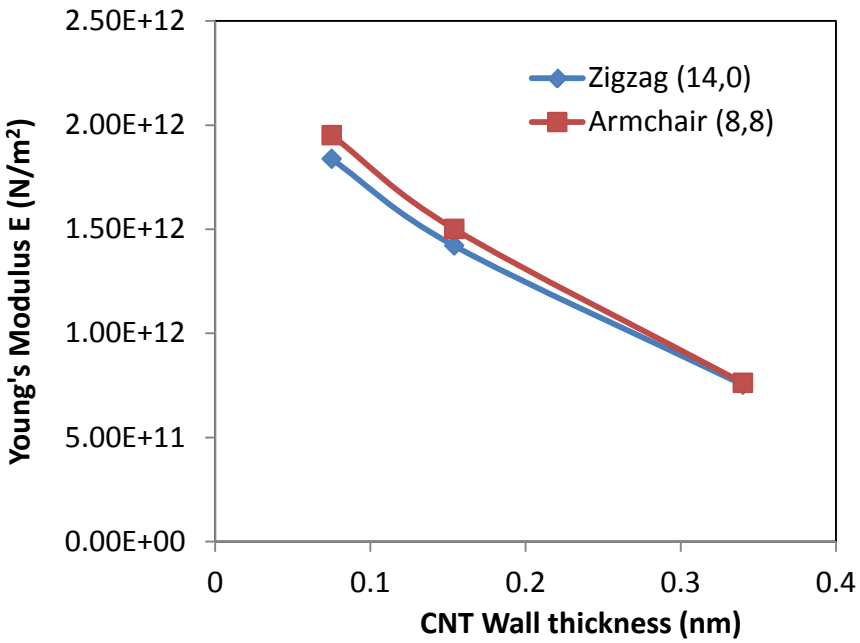

Figure 2.9. Comparison of Young's modulus from two different CNT configurations. Results are obtained by using 3-node, quadratic beam elements (B32).

Thus it can be concluded that the Young's modulus of the nanotube is sensitive to the wall thickness, consistent with the works reported in the literature (Lu 1997, Hernandez et al. 1998, 1999, Popov and Van Doren 2000, Prylutskyy et al. 2000, Chang and Gao 2003)

2.3.2 Variation of 'E' of nanotube with Poisson's ratio

The effect of variation of Poisson's ratio on the Young's Modulus of the nanotube was further studied. The plots below show the effect of variation of Poisson's ratio on the Young's modulus of the nanotube.

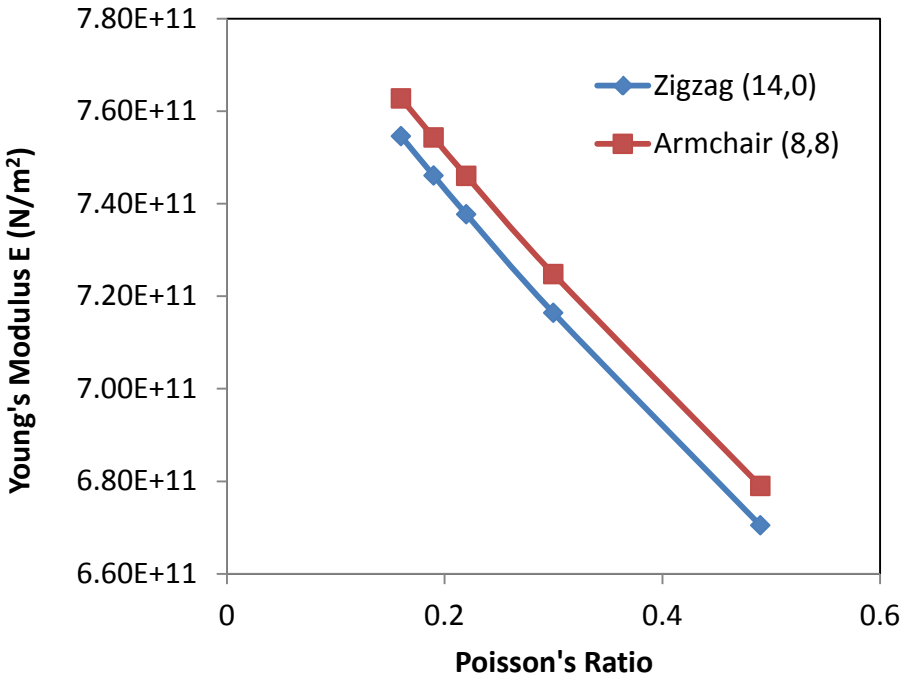

Figure 2.10. Variation of Young's modulus as a function of nanotube Poisson's ratio for (14, 0) zigzag and (8, 8) armchair CNT.

Similar to the several values of thickness reported in the literature an equally good number of values of Poisson's ratio have been reported as well (Lu 1997, Chang and Gao 2003). Values of Poisson's ratio viz. 0.16, 0.19, 0.22, 0.30 and 0.49 have been commonly observed. For the same (14, 0) zigzag and (8, 8) armchair nanotube modeled as above and with Poisson's ratio values listed as above the nanotube Young's modulus E is evaluated. The thickness of the nanotube is fixed at 0.34 nm which is most widely accepted as seen from the literature, while the Poisson's ratio is varied. The resulting graph for both the (14, 0) zigzag and (8, 8) armchair configuration are as shown in above Figure 2.10 above wherein the 'E' of nanotube decreases with increasing values of Poisson's ratio.

2.3.3 Variation of 'E' of nanotube with nanotube diameter

Nanotubes in the diameter range from 0.392 nm to 2.351 nm with zigzag and armchair configurations are considered in order to evaluate the variation of Young's modulus 'E'

with the nanotube diameter. The thickness of these nanotubes is fixed at 0.34nm which is one of the widely accepted values in the literature. It may be noted that the value of this thickness assigned to small diameter nanotubes is contradictory since the thickness is close to the diameter as already has been pointed out by several researchers in the nanotube community. However this scenario is still included for the analyses in this work. The zigzag CNT FE models with diameter variation from 0.392 nm until 2.351 nm are set up for tensile loading experiment in ABAQUS. The material properties for the beam material simulating the bond is based on the initial evaluated values that is obtained upon equivalence of molecular and structural mechanics parameters. Appropriate boundary conditions are imposed and mesh convergence is ensured with several trials of mesh refinement as well as use of higher order elements. As earlier, beam element B32 with quadratic interpolation having three displacement and three rotation degrees of freedom at each node is used. The nanotube is subjected to an axial displacement and a linear static analysis with NLGEOM= OFF is conducted and the resulting reaction forces are evaluated. Figure 2.11(a) below shows the displacement contour along the length for a zigzag (14, 0) nanotube upon subjecting it to an axial displacement. The evaluated values of Young's modulus of several zigzag nanotubes are plotted as seen Figure 2.11(b). The Young's modulus of the beam is based on the bond's axial stiffness (K_a) that is computed from the equivalences of molecular mechanics and structural mechanics parameters. Poisson's ratio value of 0.16 is applied as in previous analysis. This is applied to all of the zigzag configuration nanotubes that are evaluated.

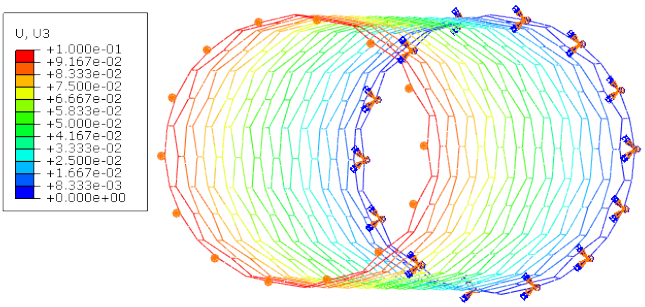

(a)

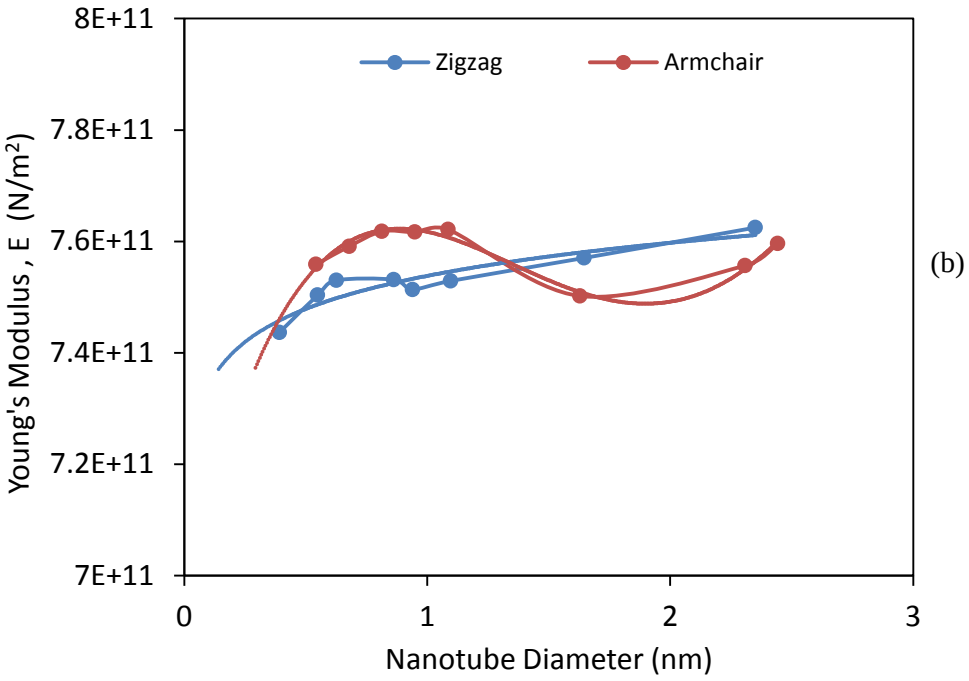

(b)

Figure 2.11. (a) Deformation contour of a zigzag CNT under tension; (b) Variation of Young's modulus as a function of nanotube diameter for a zigzag CNT.

As seen in Figure 2.11(b) above, the 'E' values of the armchair nanotube is slightly higher than those of the zigzag nanotubes up to around a nanotube diameter of 1.3 nm beyond which the trend is seen to reverse. This is observed in several results reported in the literature and is attributed to orientation of the nanotube bonds within a small radius of curvature for small diameter. The bonds oriented are perpendicular (90°) to and are at an angle of ± 60° and ± 120° to the nanotube axis in the armchair configuration which displays higher stiffness than those oriented parallel (0°) to and at an angle of ± 30° and

±150° to the nanotube axis in the zigzag configuration nanotubes. With increasing radius of curvature the number of bonds that are parallel to (0°) and oriented at angles of ± 30° and ± 150° to the nanotube axis in the zigzag configuration increase that add more resistance to deformation and resulting in 'E' values higher than those of armchair nanotube configuration. A drop in the 'E' value of armchair nanotube between (8, 8) of diameter 1.086 nm and (12, 12) of diameter 1.629 nm seen in the graph plotted in the figure above. This may attributed to a decrease in the stiffness of the arm chair CNT models with increase in radius of curvature. Further, it may be observed that the 'E' values of most of the nanotubes that are modeled above with both armchair & zigzag configurations vary between 0.74 TPa and 0.76 TPa for a thickness value of 0.34nm. These values are in good agreement with earlier research findings that are reported based on experimental & theoretical methods by several researchers. In all of the analyses reported here the most widely accepted nanotube thickness value of 0.34 nm has been used.

2.3.4 Variation of 'G' of nanotube with nanotube diameter

Continuing with a similar analysis as above, the shear modulus 'G' of carbon nanotube for zigzag and armchair nanotube configurations is evaluated. Zigzag CNT FE models with diameters from 0.392 nm – (5, 0) until 2.351 nm – (30, 0) as well as armchair CNT with diameters from 0.543 nm – (4, 4) until 2.443 (18, 18) are set up for torsion experiment in ABAQUS CAE virtual environment. The material properties for the beam material simulating the bond is based on the initial evaluated values that is obtained upon equivalence of molecular and structural mechanics parameters. The thickness of the nanotubes considered here is 0.34 nm which is the interspatial thickness of graphite. Appropriate boundary conditions are imposed and mesh convergence is ensured with several trials of element refinement as well as use of higher order elements. 3D beam element B32 with quadratic interpolation function having three displacements and three rotation dof at each node is used. The nanotube is subject to a torsional moment and the resulting twist angle parameter is evaluated. Figure 2.12 below shows the contour plot of torsional displacement.

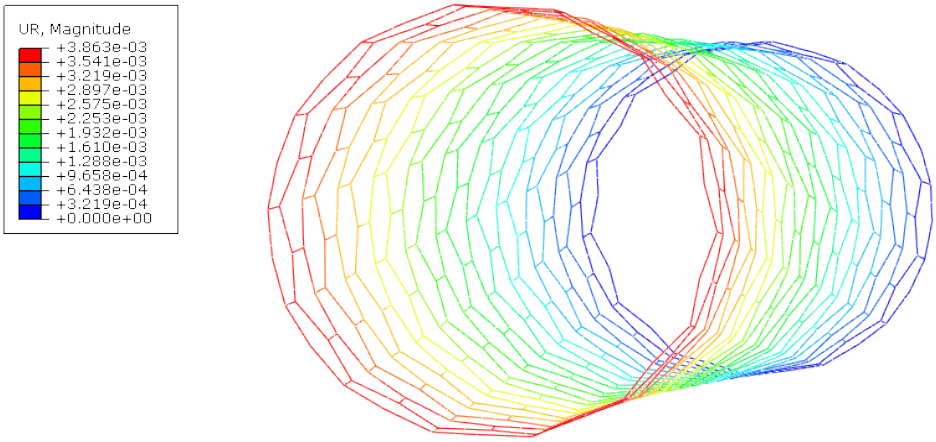

Figure 2.12. Displacement contour of a (14, 0) nanotube subject to torsional load.

A linear static analysis is conducted and shear modulus 'G' of the nanotube is evaluated as per the equation

$$G = \frac{TL}{J\theta} \tag{2.14}$$

where T = Torque applied to the nanotube

L = Length of the nanotube

J = Polar Moment of Inertia of nanotube

θ = Angle of twist of the Nanotube

A plot of variation of 'G' with diameter of nanotube for both Armchair and Zigzag nanotube is as shown in Figure 2.13 below.

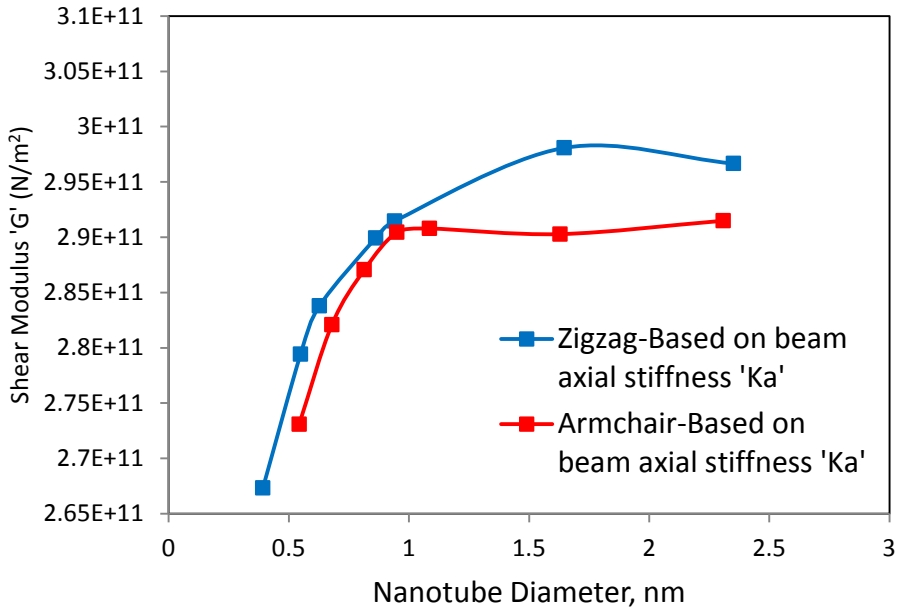

Figure 2.13. Variation of CNT 'G' with varying nanotube diameter –armchair and zigzag for t = 0.34nm.

The evaluated values of shear modulus of several zigzag nanotubes are plotted as seen in Figure 2.13. The shear modulus of the beam is based on bond's axial stiffness (K_a) that is computed from the equivalences of molecular mechanics and structural mechanics parameters. Poisson's ratio of 0.16 as earlier is applied. As may be observed from the graph, the shear modulus starts with 0.267 TPa for the (5, 0) zigzag, 0.273 TPa for the (4, 4) configuration and increases almost linearly until 0.304 TPa for the (14, 0) zigzag, 0.290 TPa for the (7, 7) configuration beyond which the value of shear modulus almost stabilizes at around 0.30 TPa for nanotube diameters up to 2.5 nm for both the armchair and zigzag CNT configurations , approaching close to that of shear modulus of graphite. It may be observed that the shear modulus for both the zigzag and armchair configuration nanotubes increases with diameter for small diameter nanotubes and tends to become constant for large diameter nanotubes. The shear modulus of zigzag configuration is slightly higher than that of the armchair due to bonds parallel to the axis offering greater resistance to shear/torsion compared to armchair configuration that has bonds non

parallel to the nanotube axis This trend has been observed in several of the works reported earlier (Hernandez et al. 1998, Goze et al. 1999, Hernandez et al. 1999, Popov and Van Doren 2000, Wang et al. 2011).

.

2.3.5 Variation of the computed nanotube Poisson's ratio with nanotube diameter.

Considering the behavior of the nanotube to be linear elastic, the Poisson's ratio of the nanotube is computed using the computed values of Young's modulus and Shear modulus of the nanotubes. It is to be noted here that this computed Poisson's ratio is different from the Poisson's ratio (υ=0.16 as per (Chang and Gao 2003)) that is used for modeling the bonds of the carbon nanotube using the beam element which are the building blocks of the nanotube structure. The computed values of the Poisson's ratio falls in the range between 0.39 and 0.28 as shown in the plot in Figure 2.14. Initially for small diameters though the values appear to drastically drop (within a small range) with increase in the nanotube diameter the values of the Poisson's ratio stabilizes at around 0.28. Also it may be seen that the Poisson's ratio of the armchair nanotube is slightly higher than that of the zigzag nanotube. This may be attributed to the nanotube configurations whereby the bonds that are parallel to the nanotube axis in zigzag configuration have greater resistance to lateral deformation and hence a lesser values of Poisson's ratio compared to armchair configuration in which case there is lesser resistance to lateral deformation. It is clear that the Poisson's ratio of both zigzag and armchair nanotubes are very sensitive for small nanotube diameters up to 1.6nm. For higher diameter nanotubes the effect on Poisson's ratio is weak. This trend has been observed in several of the works from literature (Hernandez et al. 1998, Goze et al. 1999, Hernandez et al. 1999, Popov and Van Doren 2000, Wang et al. 2011) whereby the Poisson's ratio of both achiral (armchair, zigzag) and chiral nanotubes have been reported using experimental as well as molecular dynamics approach using Tersoff-brenner potential. Hence there is a very good agreement between the results.

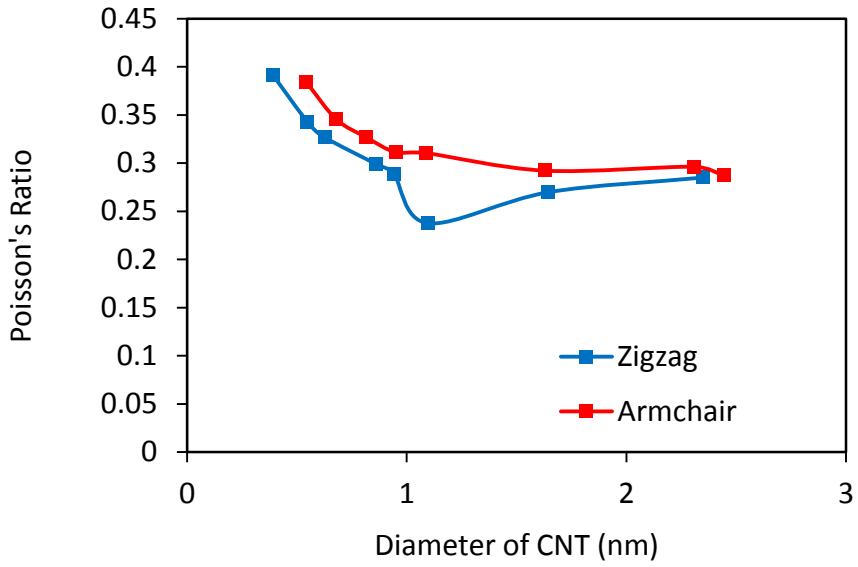

Figure 2.14. Calculated values of Poisson's ratio from E and G of nanotubes.

2.3.6 Variation of 'E' of nanotube with varying aspect ratio

A key parameter in designing a carbon nanotube is its length or height. Experimentally, the length of the carbon nanotubes can be adjusted by controlling the growth conditions such as temperature, time, and pressure. It is interesting to know the effect of nanotube length on the resultant properties of the nanotube structures. In this study, the FE models for nanotubes with various lengths (heights) were constructed and the elastic moduli were evaluated. The nanotubes used were in zigzag configuration with a fixed wall thickness of 0.34 nm.

In order to study the effect of nanotube aspect ratio on the young's modulus and on the stiffness, a (14, 0) zigzag model nanotube that is modeled as earlier is considered. Nanotube models with varying aspect ratio varying from 4 to 11 are considered. The nanotube is meshed with B32 beam elements having quadratic displacement function and a thickness of 0.34nm consistent with previous analyses is used. The lower end of the nanotube is fixed in all 6 degrees of freedom while the top end of the nanotube is subject to an axial displacement. Strain up to 5% is applied for each of the nanotube model. The nanotube is subject to both tensile and compression tests and is observed that the results

obtained are identical from both the tests cases. Plots of nanotube Young's modulus and stiffness against the nanotube aspect ratio are obtained.

Figure 2.15 below shows variation of nanotube Young's modulus with aspect ratio. Values are plotted for two cases (i) Considering nanotube wall thickness area, as in individual nanotube, (ii) Considering nanotube as part of an array in which case the nanotube's diametrically enclosed area is considered. The Young's modulus value in case (ii) is lower than that of case (i) as seen in the plot in Figure 2.15 below. Computation of Young's Modulus in the above two ways gives an understanding of the magnitude by which one differs the other. It is seen that the nanotube Young's modulus considered as part of an array is 0.72 (ratio between Young's modulus between two cases) times the Young's modulus considered as individual tube. The plot shows that the nanotube Young's modulus remains constant and is unaffected by the variation in the aspect ratio.

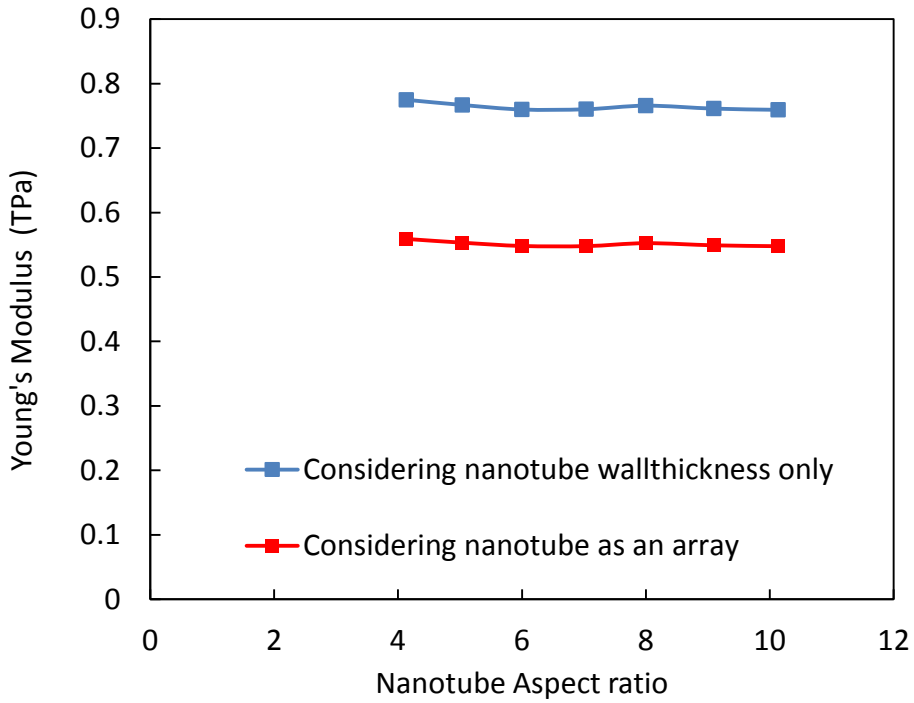

Figure 2.15. Variation of (14, 0) nanotube young's modulus with aspect ratio.

Figure 2.16 below shows the variation of nanotube stiffness with varying nanotube aspect ratio. A gradual drop in the stiffness of the nanotube with increasing aspect ratio is observed. This behavior of the nanotubes was as expected.

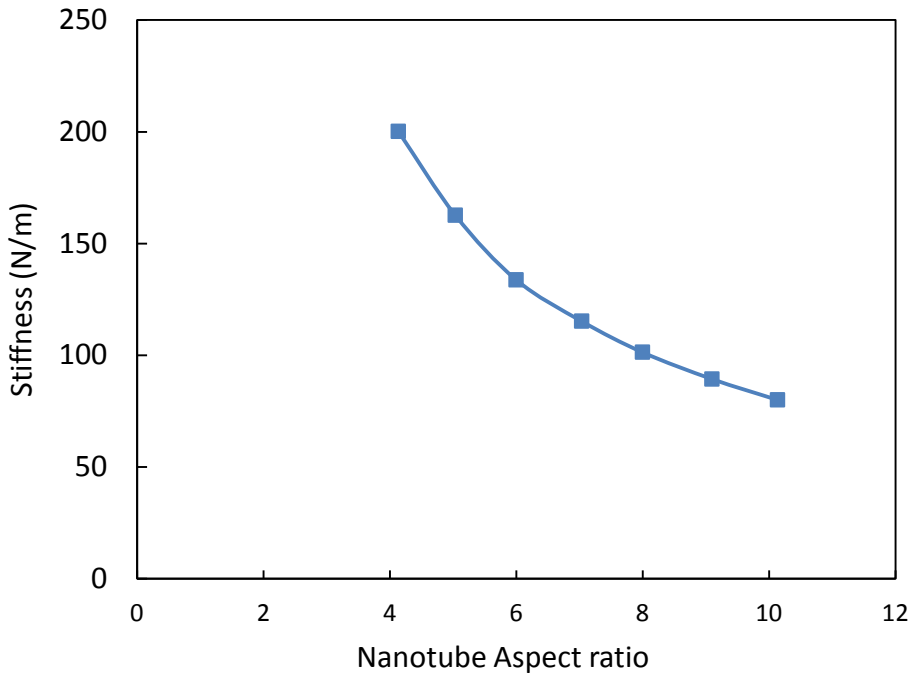

Figure 2.16. Variation of (14, 0) nanotube stiffness with aspect ratio.

2.4 Conclusions

The structural mechanics based computational modeling has been used to design and characterize the individual carbon nanotubes, which are the fundamental building block of aligned carbon nanotubes structures. Based on an understanding of carbon nanotubes at the atomic/molecular level, the equivalent truss structure models of the CNTs were constructed by using space beam elements. The geometric parameters of the individual nanotube on its mechanical properties are thoroughly examined. The modulus of the nanotubes is largely affected by the overall tube diameter. It is observed that the Young's modulus and shear modulus of the nanotube are sensitive to the atomic structure of the tubes, whereby the CNTs in armchair configuration exhibit higher young's modulus than the CNTs in zigzag one with increasing diameter whereas for the shear modulus the

zigzag configuration exhibits higher than that of the armchair with increasing nanotube diameter. Both Young's modulus and Shear modulus generally increases at a much steeper rate with diameter for small diameter nanotubes and then becomes stabilized for large diameter nanotubes. The Poisson's ratio computed from the values of Young's and shear moduli show that the Poisson's ratio of armchair nanotubes is higher than that of the zigzag and is sensitive for small diameters of nanotubes. This trend is seen in the work by Popov (Popov and Van Doren 2000) and others. The strength of the CNTs further depends upon the diameter of the C-C bonds (tube wall thickness). As the wall thickness increases, the Young's modulus of the nanotubes decreases. Also the Young's Modulus is sensitive to the value of the Poisson's ratio chosen for the C-C bond whereby a decreasing trend of modulus with increasing Poisson's ratio is seen. Finally, the modulus of the nanotubes is unaffected by the tube length whereas the stiffness is inversely proportional to the tube length.

Chapter 3

3. Design and Modeling of Aligned Carbon Nanotubes Using Structural Beam Modeling - Aligned Carbon Nanotubes Structures

3.1 Introduction

The aligned carbon nanotube (VA-CNT) structure is composed of arrays of individual CNTs grown vertically on a flat substrate. The overall structure and properties of VA-CNTs are highly dependent upon the designs of various architectures and geometric parameters. In Part 2, the detailed designs and modeling of various aligned carbon nanotube structures is presented. It is found the VA-CNT structures generally have much lower modulus than an individual CNT. The reason is due to the high porosity and low density of the VA-CNT structures, since the interstitial space between nanotubes is mostly occupied by air. Increasing the nanotube array density is seen to have significantly improved the modulus of VA-CNT structures. The mechanical property of the VA-CNT structure can be affected by the individual nanotube atomic structure, but only at small wall thickness. As a material, the elastic modulus of the VA-CNT is not affected by the size (height) of testing specimen.

Practical applications often require that the carbon nanotubes be produced in large scales and at oriented forms. These have resulted in a novel carbon nanotube material: the aligned carbon nanotube (VA-CNTs) structures. The VA-CNTs was first grown by Terrones et al. (Terrones et al. 1997) through the method of laser ablation. In this experiment, a thin film of cobalt (~10–100 nm) was deposited on a silica plate. The coated plate was subsequently etched with a laser pulse to create linear tracks. Through the use of a patterned catalyst the aligned carbon nanotubes were formed. The aligned CNTs produced can have a length up to about 50 μm and a fairly uniform diameter of 30–50 nm. Since then, various techniques have been used to synthesize this novel material. Li et al.(Li et al. 1999) have reported the growth of aligned carbon nanotubes by the pyrolysis of acetylene on an alumina template. In this method, the cobalt or nickel

catalyst particles were pre-deposited at the bottom of the alumina membrane pores, followed by deposition of carbon nanotubes in the pores. The diameter, packing density, and length of carbon nanotube arrays could be tuned by altering the designs of the alumina templates. Recently, the chemical vapor deposition (CVD) method has been used to produce aligned CNTs. Dai and co-workers (Dai et al. 2003)have prepared large-scale, aligned carbon nanotubes on the substrate surfaces by the pyrolysis of iron phthalocyanine (FePc). Rao et al.(C. N. R. Rao 1998) and Wei et al (Wei et al. 2003) have synthesized well-aligned CNTs from ferrocene in xylene solution.(Qu et al. 2008)) have successfully produced aligned, single-walled carbon nanotube arrays by using the combined plasma-enhanced CVD and fast heating method (Qu et al. 2008). The single-walled VA-CNTs are much lighter and more efficient than the multi-walled VA-CNTs. A typical growth process for aligned carbon nanotube structures is shown in Figure 3.1.

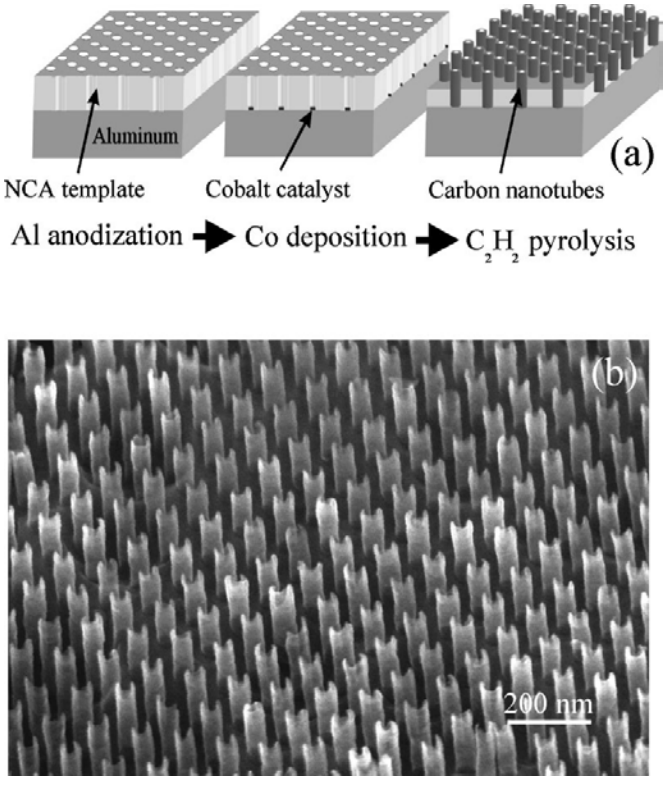

Figure 3.1. (a) Schematic showing the process of growing aligned carbon nanotubes structure. (b) SEM image of aligned carbon nanotubes structure (Li et al. 1999)

As illustrated in Figure 3.1, a VA-CNT structure is composed of arrays of individual CNTs grown vertically on a flat substrate. The overall structure of an VA-CNTs highly depend upon the designs of various architectures and geometric parameters, including the tube height, tube diameter, tube array density, tube distribution pattern, inter-tube distance, tube-tube junction structure, and among many other factors. A small variation in each parameter would have great impact on the optimal performance of the VA-CNT structure. Therefore, it is crucial to have a rational strategy to design and evaluate the architectures and geometric factors to help process the optimal nanotube materials. The traditional material development has relied on the experimental "trial-and-error" method, thus is a very slow and expensive process. The National Materials Advisory Board of the National Academy has recently recommended a brand new material development model to the entire material science community, i.e., the "Integrated Computational Materials Engineering (ICME)" (National Research Council, 2008). The objective of the ICME approach is to integrate computational materials science tools into a holistic system that can accelerate materials development process. The most commonly used computational method for designing nanomaterials has been the atomistic approach, i.e., the classical molecular dynamics (MD), which has been very successful for modeling an individual nanotube. However, for a VA-CNT structure that consists of millions or even billions of individual nanotubes, the atomistic approach is simply too computationally expensive. We propose to use the structural beam mechanics for designing and modeling the aligned carbon nanotubes structures. In chapter2, the fundamentals of the structural mechanics method are presented and modeling of the individual nanotube - the fundamental building block of the aligned nanotube structures has been covered. In chapter 3, the detailed design and modeling of the aligned carbon nanotubes structures will be presented.

3.2 Modeling of VA-CNT array with (14, 0) zigzag SWCNT using beam elements

3.2.1 VA-CNT array layout design for Square and FCC patterns

VA-CNT arrays are grown with square, FCC, HCP, Square and random distribution patterns of the nanotubes. In this analysis, square and FCC distribution patterns are designed and modeled in order to study the effect of nanotube distribution pattern, nanotube density on the Young's Modulus 'E' and stiffness of the VA-CNT material. The VA-CNTs are grown with several different packing densities commonly referred to as areal densities. The most commonly grown areal densities being $1x10^8$ tubes/cm^2, $1x10^9$ tubes /cm^2, $1x10^{10}$tubes/cm^2, $1x10^{11}$ tubes /cm^2, $1x10^{12}$ tubes /cm^2 and $1x10^{13}$ tubes /cm^2.

The layout and the modeling details of Square and FCC distribution pattern for the VA-CNT array considered are shown in Figure 3.2 below.

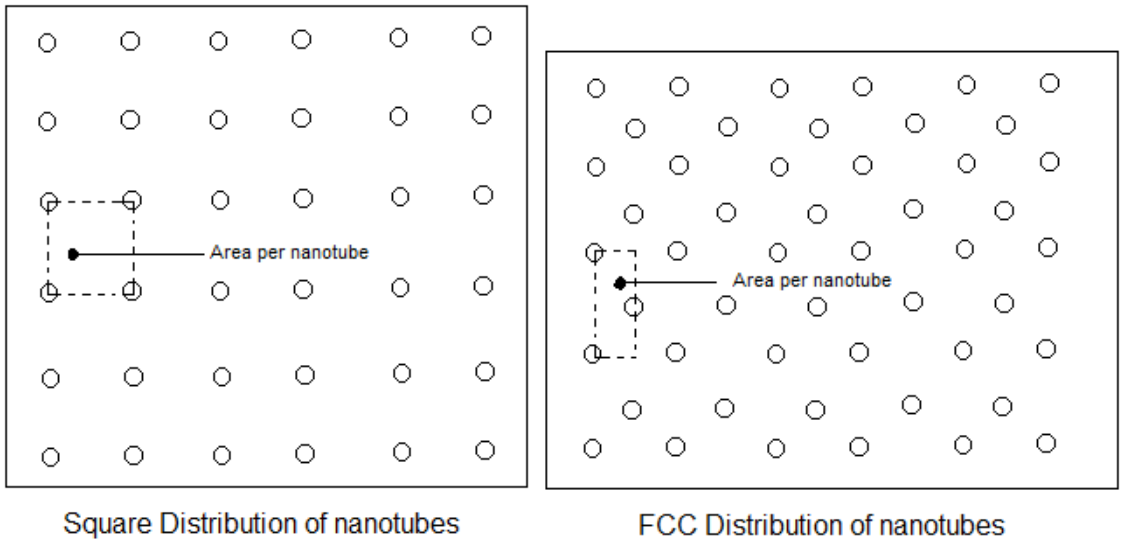

Figure 3.2. Layout of Square and FCC distributions of nanotubes.

The area occupied by an individual nanotube for square and FCC distribution of nanotubes is highlighted. The final design parameters which are the nanotube interspacing distance and the maximum diameter of the nanotube that can be accommodated for a given areal density without nanotube overlap/interference as observed in a grown VA-CNT and with well aligned nanotubes for both square and FCC configurations with reference to Figure 3.3 is given in Table 3.1 and Table 3.2 as below.

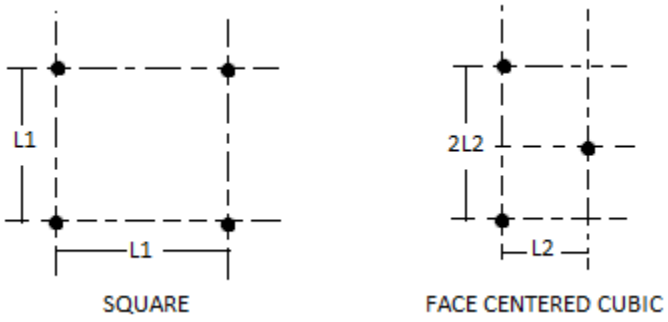

Figure 3.3. Unit cell layout for SQUARE and FCC design.

With L_1^2 as the area per nanotube in a square configuration and L_2*2*L_2 as the area per nanotube in a FCC configuration, for identical unit cell area in both configurations we obtain $L_2 = 0.707\ L_1$. It is to be noted here that $L_1 \neq 2L_2$. Table 3.1 and Table 3.2 shows the intertube distances L_1 and L_2 for both Square and FCC distribution and the maximum diameter of the nanotubes that could be accommodated for each density distribution.

Table 3.1. L_1 and nanotube diameter values for different areal densities-Square configuration.

Areal Density (tubes/cm$^{2)}$	**L_1 (m)**	**CNTs with diameter < than (nm)**
1.00E+08	1.00E-06	**1000**
1.00E+09	3.16E-07	**316.2**
1.00E+10	1.00E-07	**100**
1.00E+11	3.16E-08	**31.62**
1.00E+12	1.00E-08	**10**
1.00E+13	3.16E-09	**3.162**

Table 3.2. L_2 and nanotube diameter values for different areal densities-FCC configuration.

Areal Density (tubes/cm$^{2)}$	L_2 (m)	CNTs with diameter < than (nm)
1.00E+08	7.07E-07	**999**
1.00E+09	2.24E-07	**316**
1.00E+10	7.07E-08	**99.9**
1.00E+11	2.24E-08	**31.62**
1.00E+12	7.07E-09	**9.899**
1.00E+13	2.24E-09	**3.15**

A representative comparison of VA-CNT distribution for different densities and a fixed number of tubes for Square distribution of nanotubes modeled in ABAQUS is shown in Figure 3.5 below. Also Figure 3.6 shows the FCC distribution pattern for an areal density of 1e13 tubes/cm^2. The square and FCC distribution VA-CNT arrays are designed such that the area occupied by a predefined number of tubes (16, 36, 64, 100) in square configuration for a given aerial density is maintained the same in FCC configuration for the corresponding areal density by way of calculation of a new set of number of tubes (13, 32, 61, 98) in view of the difference in the tube distribution patterns. Hence the design is for a "Fixed number" of tubes. This implies that for a predefined number of tubes (for example 100) the total area occupied by this predefined number of tubes diminishes with increasing areal density. Greater areal density indicating close packing of

nanotubes as compared to smaller areal densities indicating loose packing of the nanotubes. The tube-tube distance varies accordingly. Figure 3.4 below shows this diminishing trend of VA-CNT area for a fixed number of nanotubes and with increasing tube areal/ packing density. The calculated intertube distances for each of the areal densities and for both Square and FCC configurations is as given in Table 3.1 and Table 3.2. Figure 3.5 shows pictorially the actual area occupied by each of the areal densities for a fixed number of tubes-100 tubes in this case for square configuration. This design approach will help to compare the characteristics of VA-CNT for both Square and FCC distribution for various densities. The VA-CNT area for an areal density of $1X10^{13}$ tubes/cm^2 for 98 tubes and FCC configuration is shown in Figure 3.6.

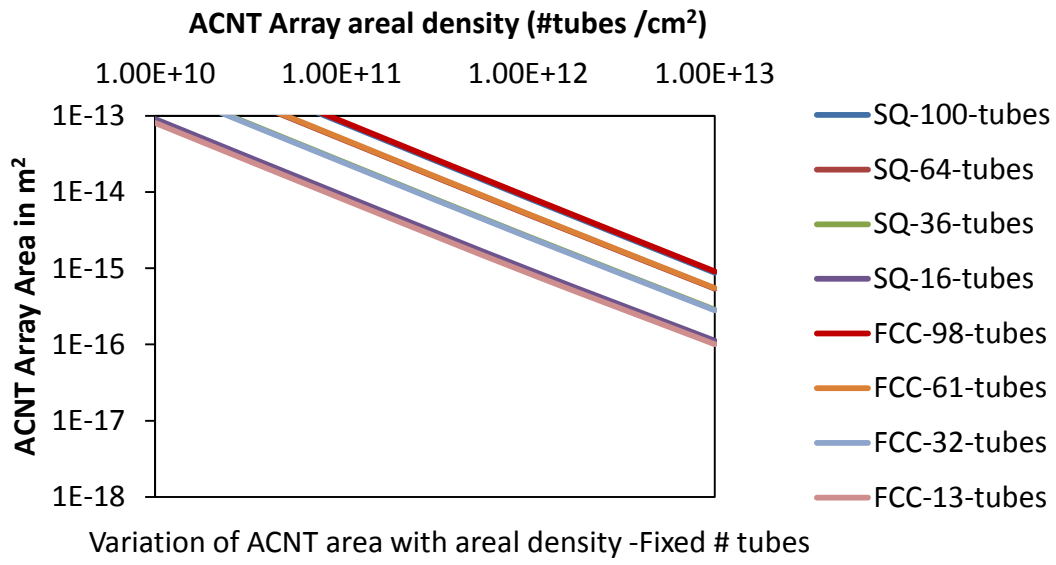

Figure 3.4. Diminishing trend of the VA-CNT area with increasing packing density for a fixed number of tubes.

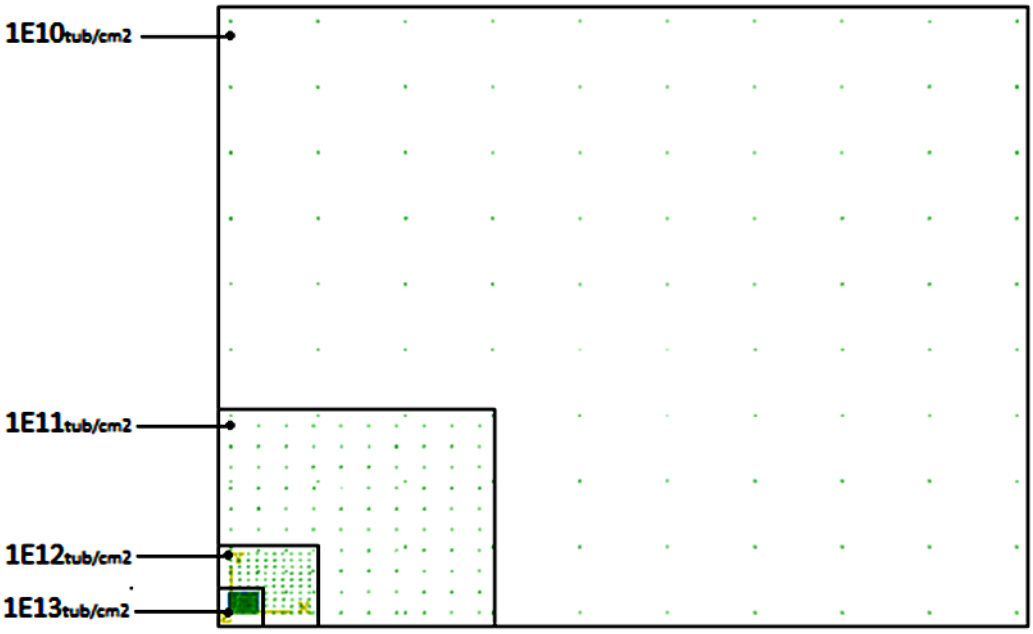

Figure 3.5. Overview of VA-CNT area for different areal densities for a fixed no. of tubes- 100 tubes for square configuration.

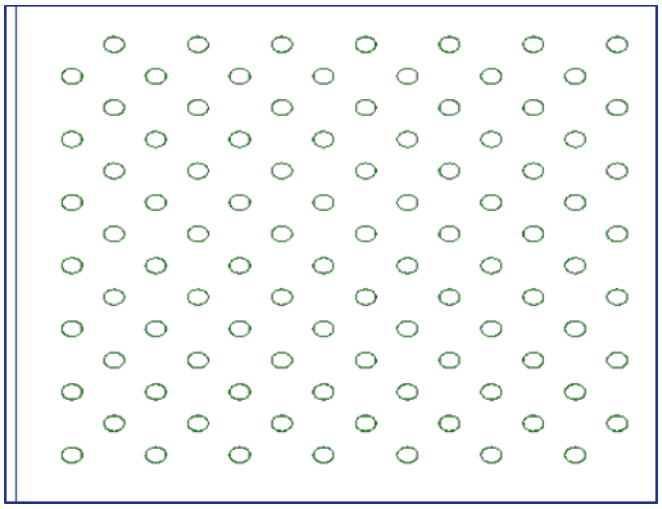

Figure 3.6. FCC distribution of nanotubes for $1X10^{13}$ tubes/cm^2 for 98 tubes

3.2.2 Modeling procedure for VA-CNT structures

The aligned carbon nanotubes structures are consisted of individual nanotubes that are packed vertically on flat substrates. The overall structures depend upon numerous geometric parameters, including tube array density, tube distribution pattern, inter-tube distance, tube-tube junction structure, among many others. To construct the VA-CNT structures, the solid models for individual carbon nanotubes in zigzag and arm chair configurations were geometrically modeled using the modeling capability of ANSYS software and then imported into ABAQUS CAE for FE modeling. The 3-node beam elements (B32) with a quadratic displacement function were used. Appropriate beam section orientation, geometric sectional properties, and material properties were assigned following the procedures described in chapter 2.

The VA-CNT structures at various densities were constructed, ranging from $1x10^{10}$ tubes/cm^2 to $1x10^{13}$ tubes/cm^2. FE models of various sizes, from 16-tube structure to 100 tube structure, were constructed for both Square and FCC configurations. The heights of the VA-CNT structures were varied, from 4.54 nm to 8.67 nm. To conduct compression experiments, the compression heads (as represented by analytical rigid surfaces) were subjected to a displacement in the downward direction. The bottom ends of the nanotubes were constrained in all directions to simulate the fixity of the nanotubes to the substrate material. Suitable contact interactions were defined between the nanotube top surfaces and the compression head surfaces with an assumed coefficient of friction of 0.1. Examples of the FE models for the vertically aligned carbon nanotubes structures are shown in Figure 3.7 and Figure 3.8 below.

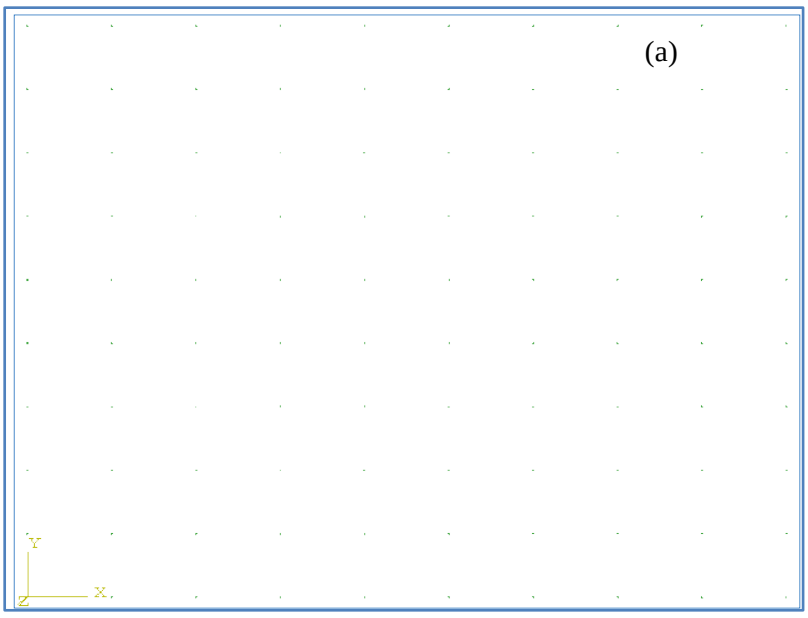
(a)
Y
Z
X

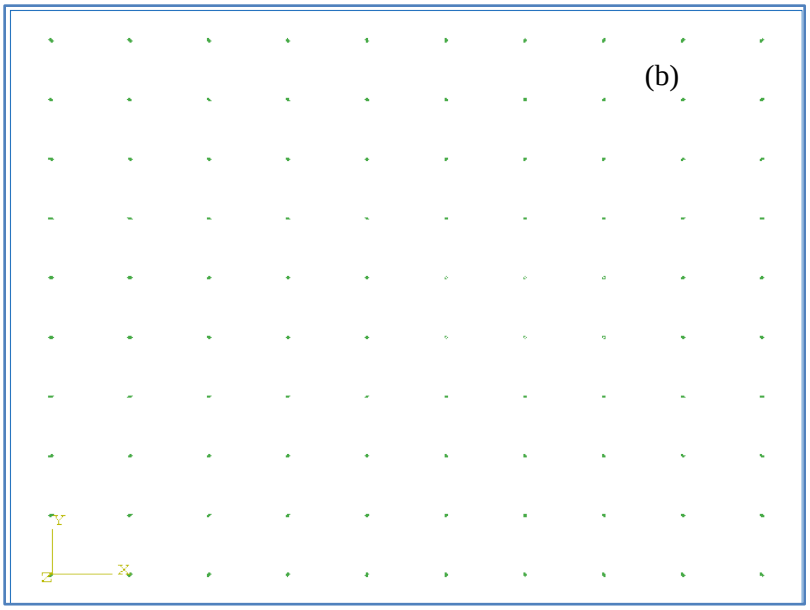
(b)
Y
Z
X

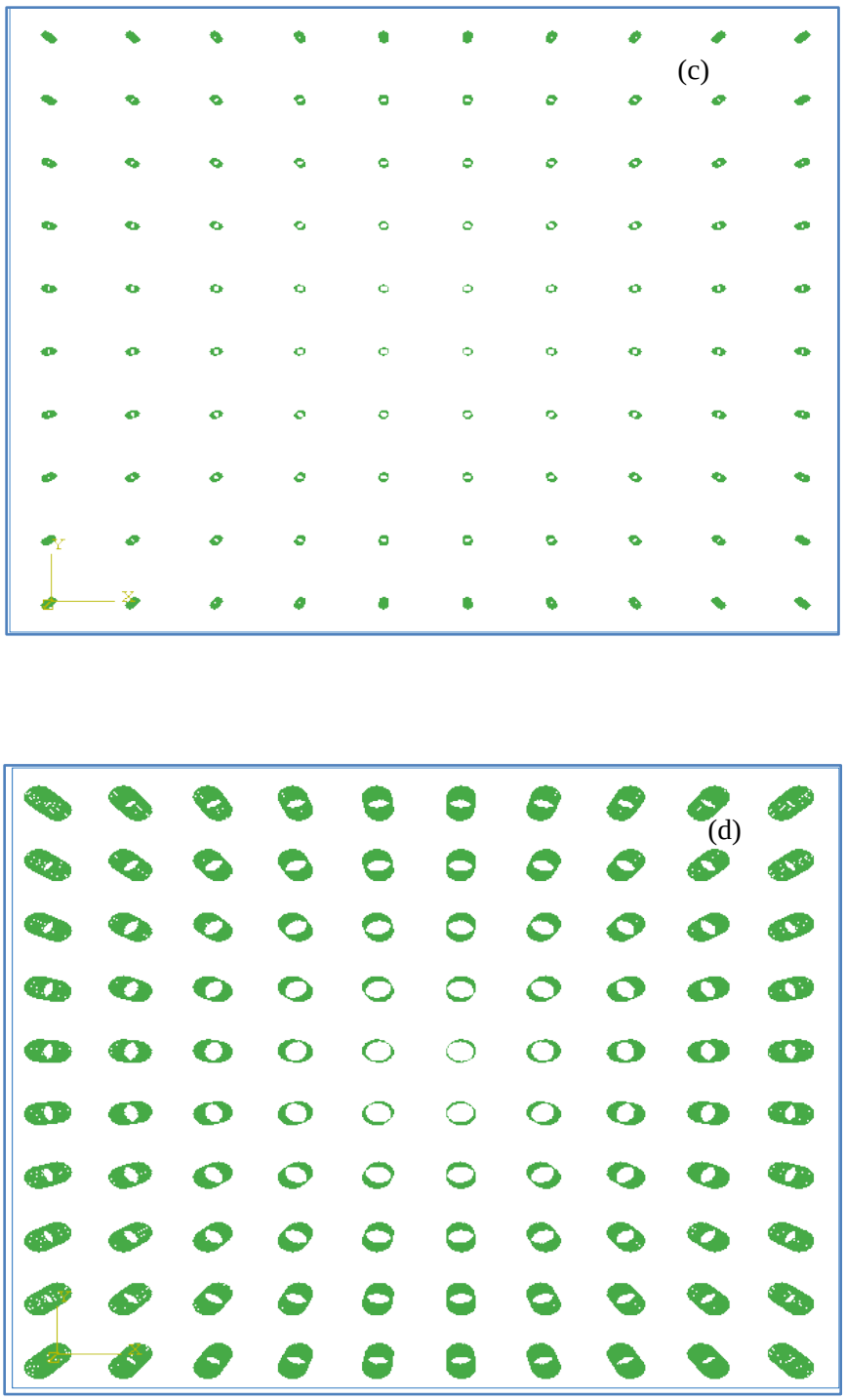

Figure 3.7. FE models of aligned carbon nanotubes structures at various tube densities; (a)$1x10^{10}$ tubes/cm^2, (b) $1x10^{11}$ tubes/cm^2, (c) $1x10^{12}$ tubes/cm^2, (d) $1x10^{13}$.The number of tubes in the structure is 100 and height is 4.54nm

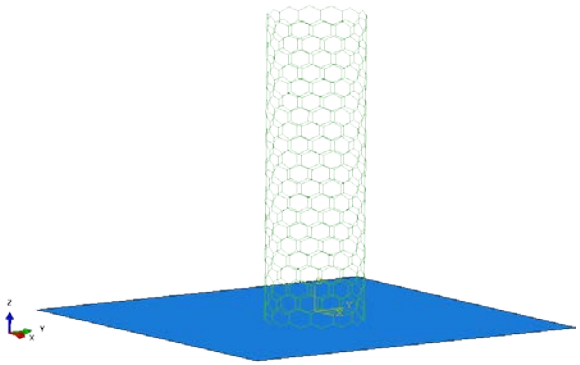

(a)

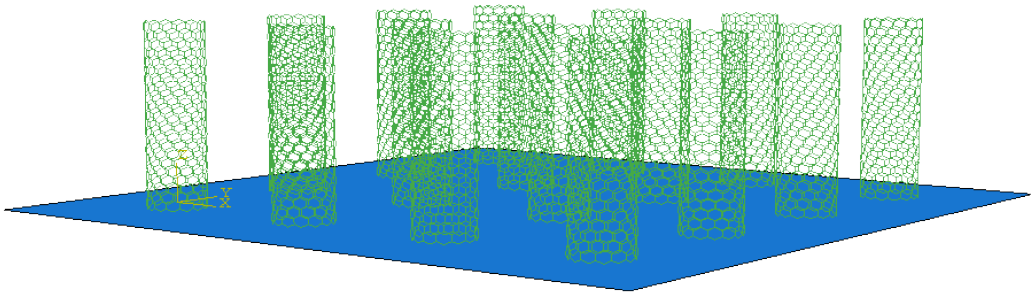

(b)

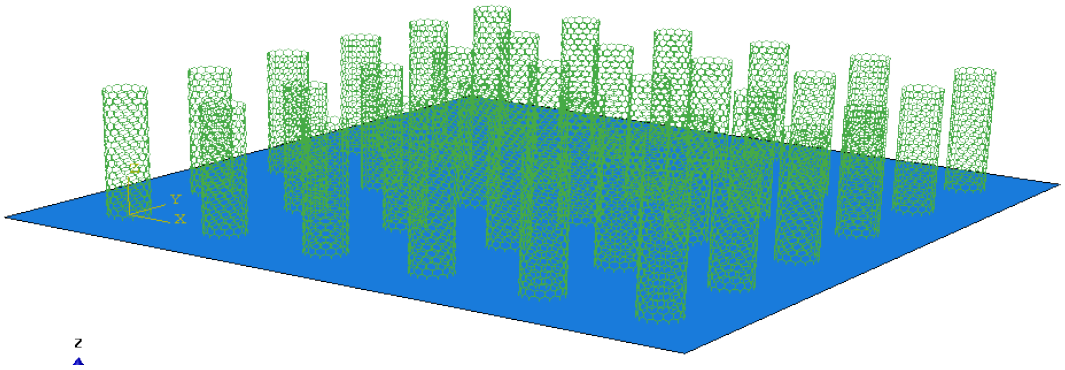

(c)

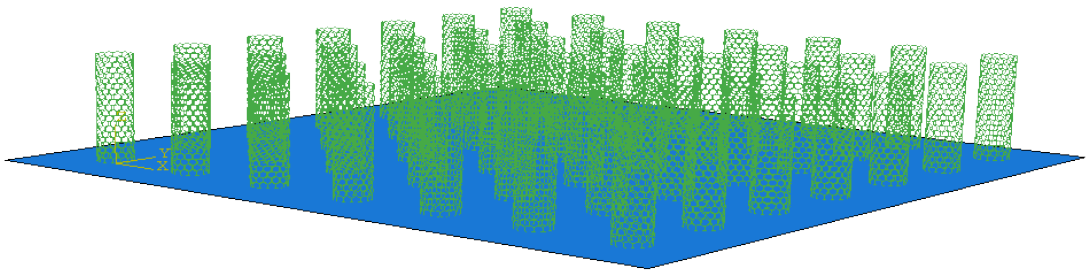

(d)

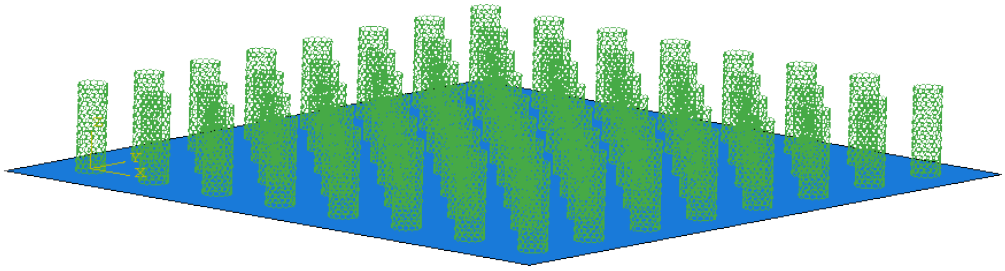

(e)

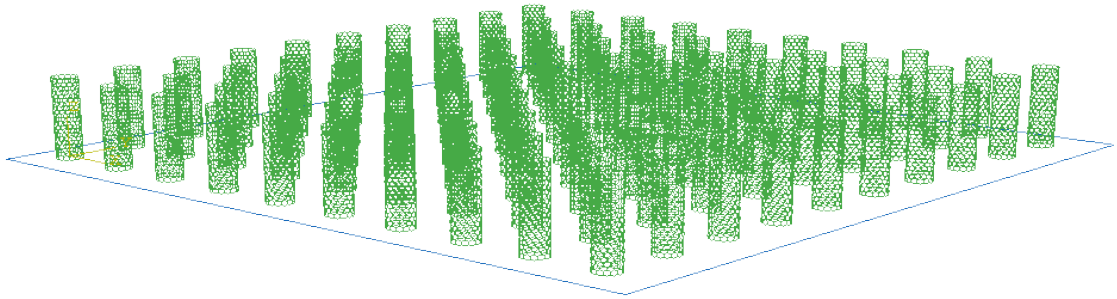

(f)

Figure 3.8. FE models of vertically aligned carbon nanotube arrays containing different number of tubes: (a) 1 tube, (b) 16 tubes, (c) 36 tube, (d) 49 tubes, and (e) 64 tubes (f)100 tubes. The height of the tube is 4.54 nm –Square configuration.

3.3 Results and discussion

3.3.1 Modulus of the VA-CNT structures

An individual carbon nanotube is believed to possess exceptionally high modulus and strength, with a Young's modulus as high as 1 TPa and a strength over 100 times of a steel (Lu 1997, Wong et al. 1997, Krishnan et al. 1998, Popov et al. 2000). However, the aligned nanotube array structures have been found to exhibit rather weak properties. The mechanical properties of the VA-CNT structures have been experimentally investigated, mostly through the nanoindentation technique (McCarter et al. 2006, Mesarovic et al. 2007, Pathak et al. 2009, Patton et al. 2009, Zhang et al. 2010). The indenter used was either three-face pyramidal shape (Berkovich indenter), parabolic shape (spherical indenter), or flat shape (flat indenter). By driving the indenter into the specimen and then withdrawn from it, the indentation load-depth curves are obtained and then analyzed by following the standard Oliver-Pharr method (Oliver and Pharr 1992). The modulus of the VA-CNT structures so determined have been found to vary greatly, ranging from several Megapascals to several hundred of Gigapascals (Table 3.3). The reason for the lower modulus is primarily due to the high porosity in the VA-CNT structures, since the interstitial space between nanotubes is only occupied by air. In a typical VA-CNT structure, the individual nanotubes are either completely separated from neighboring tubes or in weak contact with neighboring tubes through van der Waals attractions.

Table 3.3. Summary of Elastic modulus of VA-CNT structures determined through various nanoindentation experiments.

Indenter Shapes Used in Indentation Experiments	**CNT Height**	**CNT Diameter**	**Elastic Modulus**	**References**
Flat Indenter	35–650 μm	10-20 nm	20-35 MPa	(Maschmann et al. 2011, Lu et al. 2012)
Spherical Indenter	20μm, 500 μm	1-3 nm, 10 nm	18 GPa; 58 MPa	(Misra et al. 2009, Zhang et al. 2010)
3-Sided Pyramid Indenter	~600nm, 20μm	~50nm	0.9-1.2 TPa; 40-600 MPa; 0.1-0.8 GPa	(Mesarovic et al. 2007, Tong et al. 2008)

In this study, the moduli of the VA-CNT structures are evaluated through computational method. The construction and modeling of individual CNT have been discussed in detail in Part 1 of the paper. Assuming the same geometry and properties, those individual CNTs were arranged in various patterns and densities to construct the aligned carbon nanotube structures. Figure 3.9 shows the deformation of a VA-CNT structure, in which the individual CNTs were arranged in an ordered square distribution in a small representative area (8.6E-4μm^2). The structure has an areal density of 10^{13} tubes/cm^2. Figure 3.10 shows the stress-strain response of this VA-CNT structure. For comparison, the stress-strain response of a single CNT is also included. It is seen that the VA-CNT array has a noticeably lower stress-strain response, due to the open space between the tubes. The Young's modulus of the VA-CNT structure is evaluated using Equation (3.1). The resulting Young's modulus of the VA-CNT array is approximately 0.103 TPa, which is about 12% of the modulus of a single CNT (0.79 TPa).

$$\mathrm{E} = \frac{\mathrm{PL}}{\mathrm{A}\delta} \tag{3.1}$$

where P = Total applied load

δ = Elongation of the VA-CNT structure

L = Length of the VA-CNT structure

A = Cross sectional area of the VA-CNT structure

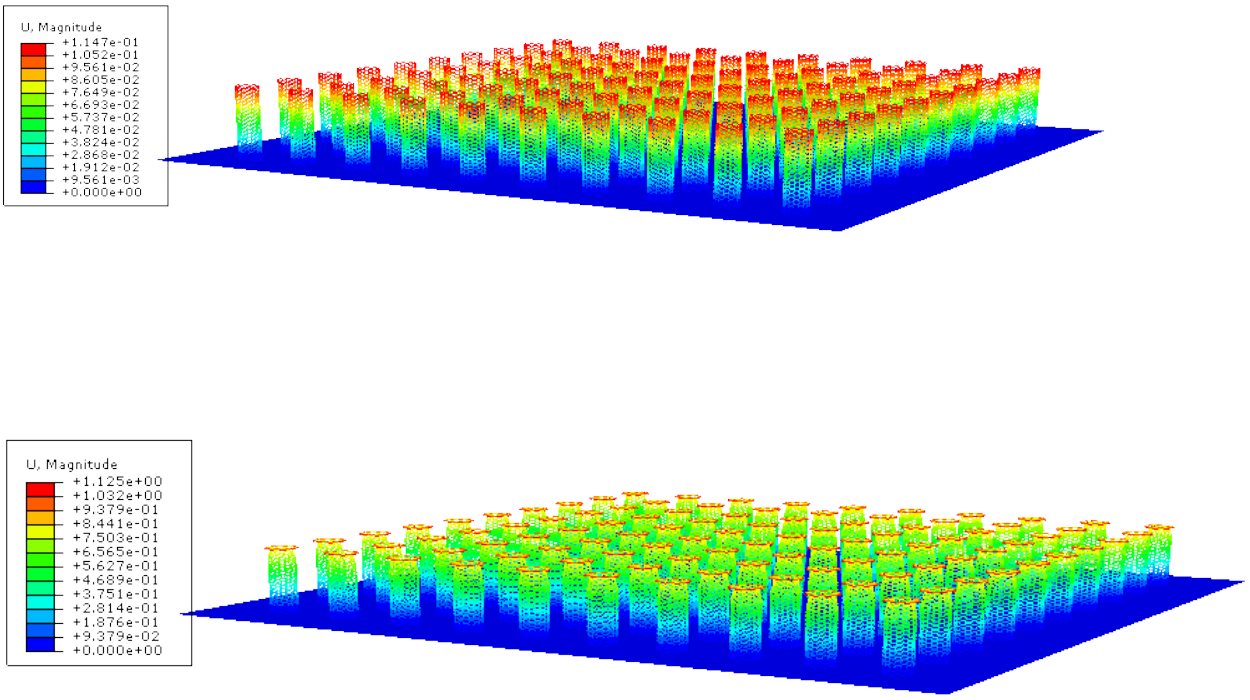

Figure 3.9. Deformation Contour of an aligned nanotube structure under compressions.

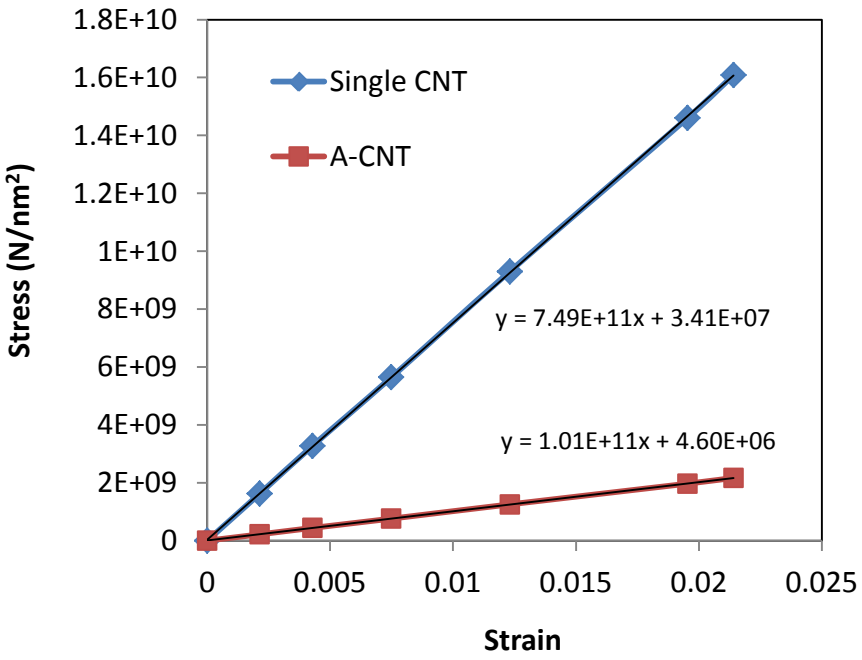

Figure 3.10. Stress-strain response of the vertically aligned nanotube arrays and single CNT under compression.

The effect of tube atomic structure on modulus of the VA-CNT structures was further examined. Figure 3.11shows the stress-strain responses of the VA-CNT structures with zigzag and armchair configurations. It is observed that at thinner tube wall thickness (t=0.066 nm), there exists a noticeable difference in stress-strain curves between the two VA-CNTs. The VA-CNT in armchair configuration is much stiffer and has approximately 13% higher modulus than the VA-CNT in zigzag configuration. When the tube wall thickness become larger (t=0.35 nm), the stress-strain curves of the two structures are almost indistinguishable and the Young's moduli of the two structures are essentially the same. The dependence of modulus on tube wall thickness is consistent with results observed earlier on single CNTs (Figure 2.9 in chapter 2).

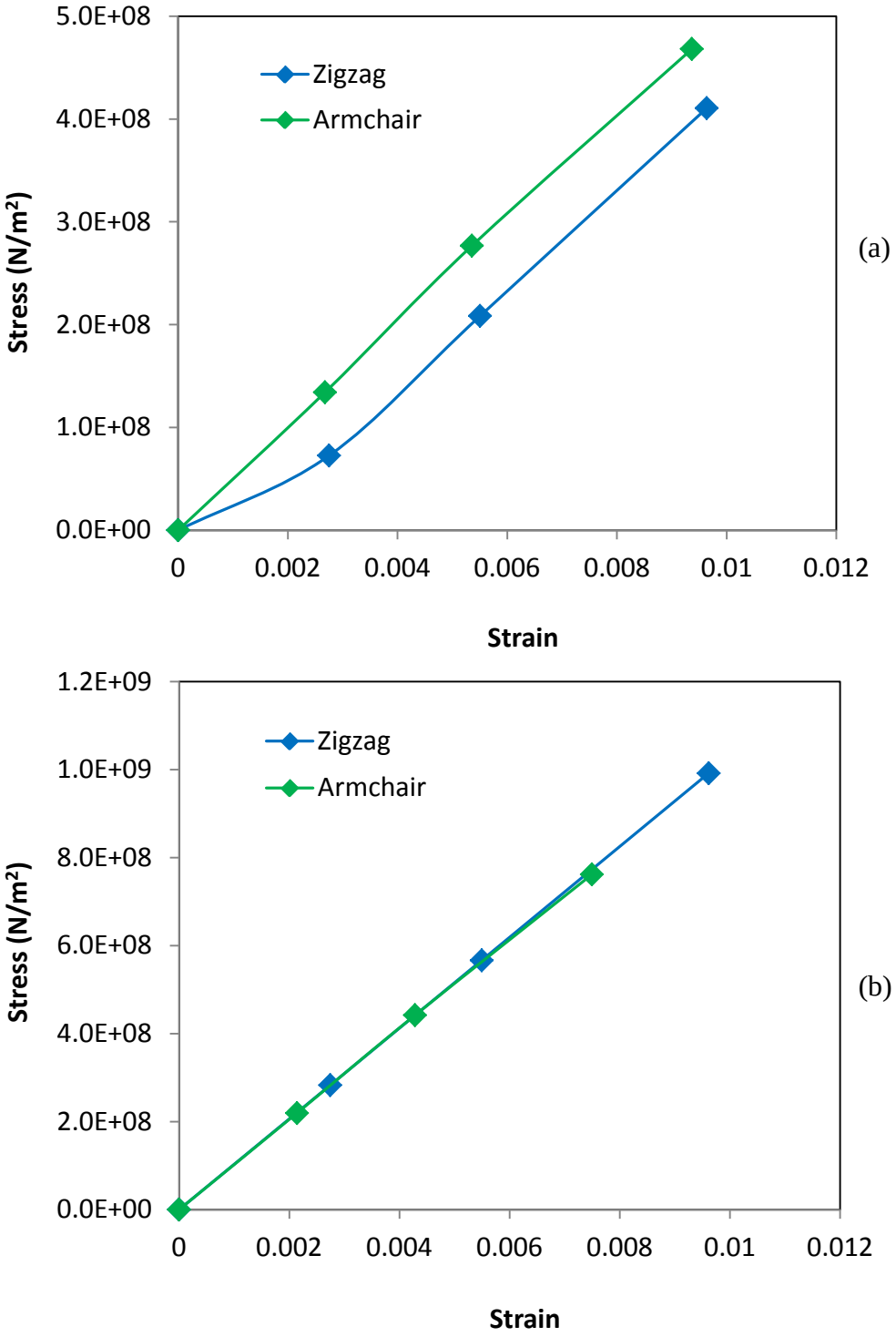

Figure 3.11. Comparison of stress-strain responses of two VA-CNT structures with different atomic configurations. (a) The wall thickness of all individual tubes in the structure is 0.066 nm, and (b) The wall thickness of all individual tubes in the structure is 0.34nm.

3.3.2 Effect of FE model size on stiffness and modulus of VA-CNT array

An aligned CNT structure is comprised of millions of individual tubes per one square centimeter; therefore it is computationally impractical to consider all the tubes in the structure. Here the CNT structure with different tube number was constructed and studied, from 16 tubes to 100 tubes. Figure 3.12 shows the variations of stiffness and elastic modulus of the VA-CNT structures as a function of the number of nanotubes. As expected, as the number of tubes increases the stiffness increases. That is because there are more load-carrying members in the array. However, the modulus of the structures is seen to remain relatively constant as number of tubes increases. Thus, from design point of view, a modest size FE model (>36 and 32 tubes for Square and FCC) is sufficient for achieving accurate results while maintaining good computational efficiency.

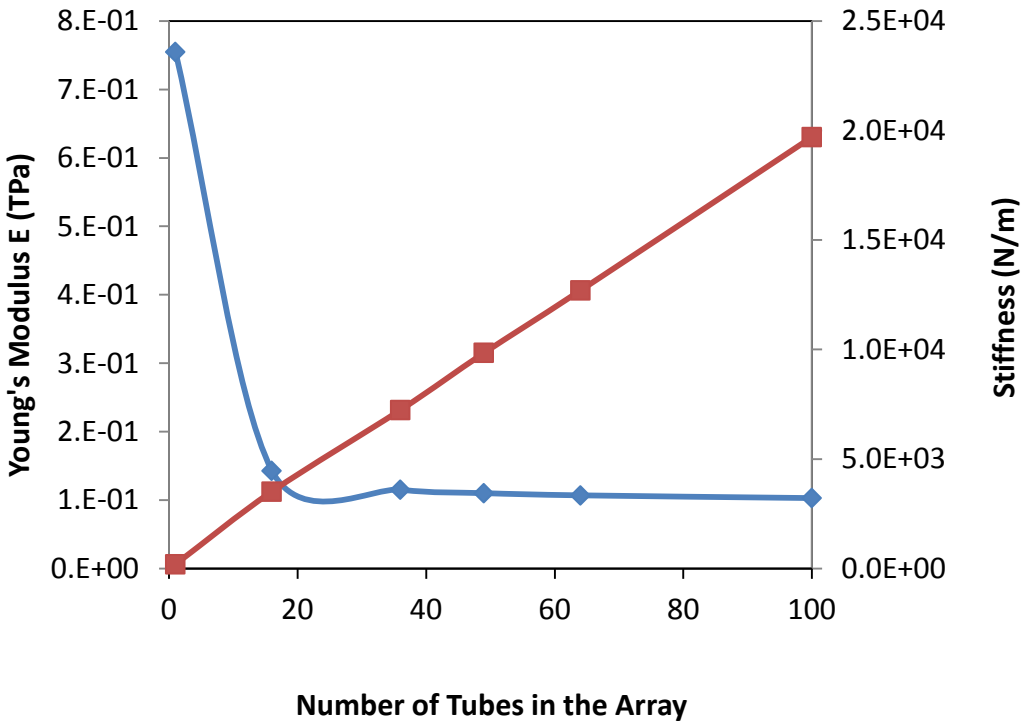

Figure 3.12. Effect of FE model size on properties of the VA-CNT structure.

3.3.3 Effect of tube / array density on stiffness and modulus of VA-CNT array

The VA-CNT array may be conceptually viewed as a complex structure consisted of nominally aligned tubes; between the tubes are unfilled open spaces that have no load-carrying capability. Therefore, the mechanical behaviors of the VA-CNT structure are highly dependent upon the "density" of the nanotube arrays. A more densely packed nanotube array would have more load-carrying capability and fewer geometric freedoms for tube movements Recent experimental study has shown that there exists a linear relationship between the elastic modulus of the VA-CNT structure and its density. When the density of the VA-CNT array is doubled, the modulus can be increased by 50% (Wardle et al. 2008).

In the present study, the VA-CNT structures at various densities were constructed, ranging from $1x10^{10}$ tubes/cm^2 through $1x10^{13}$ tubes/cm^2. Figure 3.13 and Figure 3.14

show the results of these VA-CNT arrays obtained with FE models containing 16 tubes to 100 tubes for SQ and 13tubes to 98tubes for FCC distribution. In each model, it is seen that as the density increases, the stiffness remains relatively constant. This is because the overall number of the load-carrying structural members (tubes) remains the same in each array model (16 tubes, 32 tubes, 64 tubes or 100 tubes). However, the modulus is seen to increase linearly with the increase of the array density.

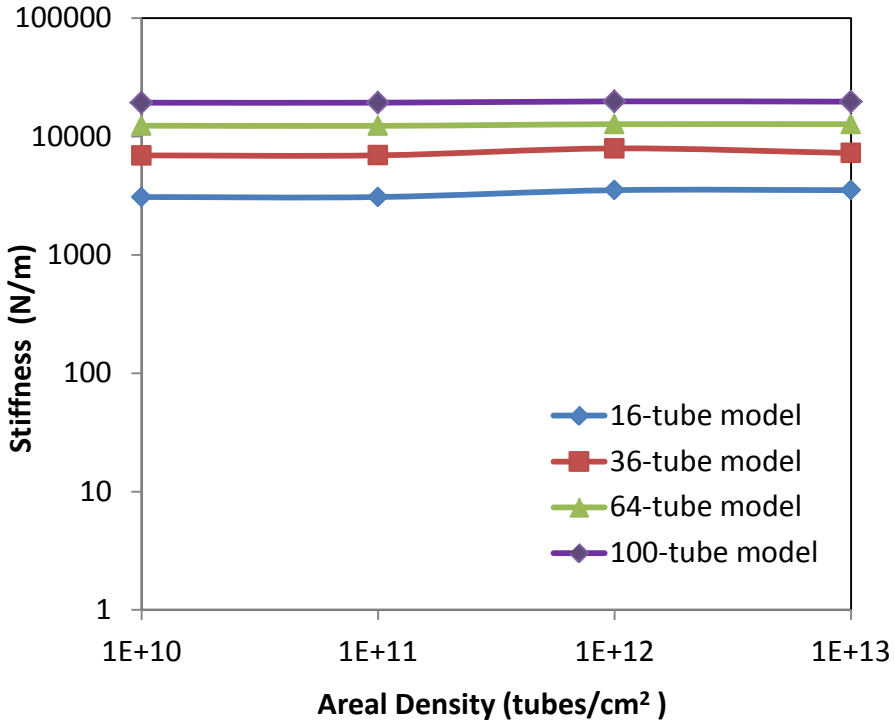

Figure 3.13. Effect of nanotube areal density on stiffness of the VA-CNT structure with Square configuration

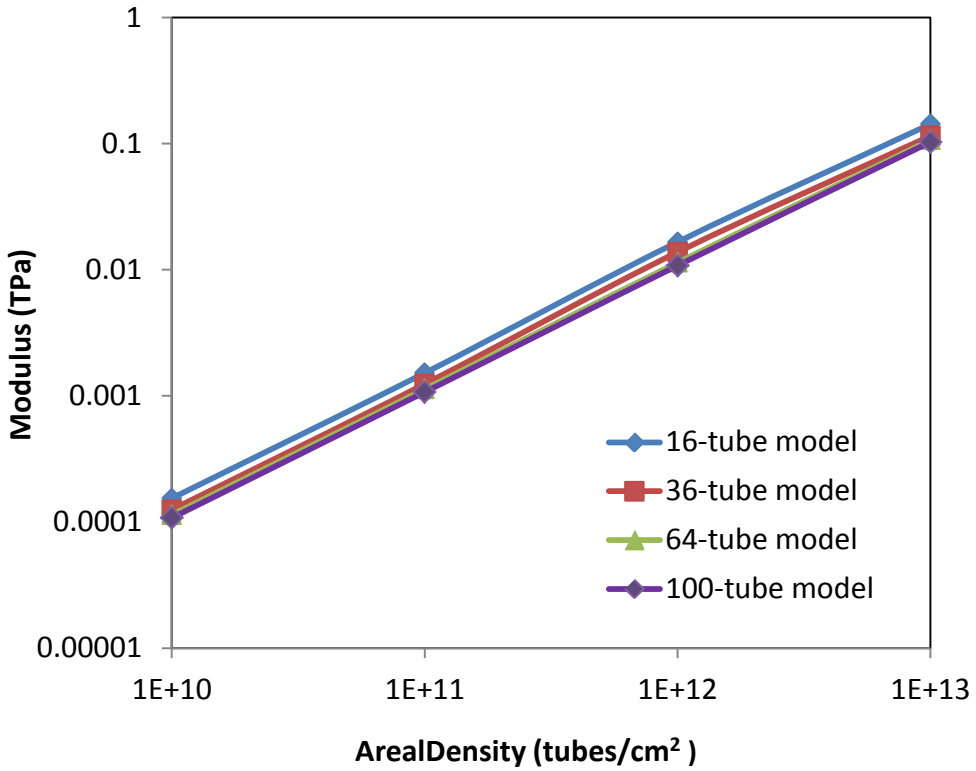

Figure 3.14. Effect of nanotube areal density on modulus of the VA-CNT structure with Square configuration

3.3.4 Effect of VA-CNT height on modulus and stiffness

Although the aligned carbon nanotube arrays are initially grown on various substrates, they are able to retain their structural integrities after their removal from the substrates. Therefore, it has been widely accepted that an aligned carbon nanotube array is indeed a type of material (McCarter et al. 2006, Mesarovic et al. 2007). As a material, the VA-CNT will have its unique mechanical property (modulus), which should be independent upon the geometries of the testing specimens. Several researchers have examined the influence of nanotube length (height) on mechanical properties of the aligned carbon nanotube arrays, and have found that the elastic modulus remains relatively unchanged when the tube height varies (Tong et al. 2008, Maschmann et al. 2010).

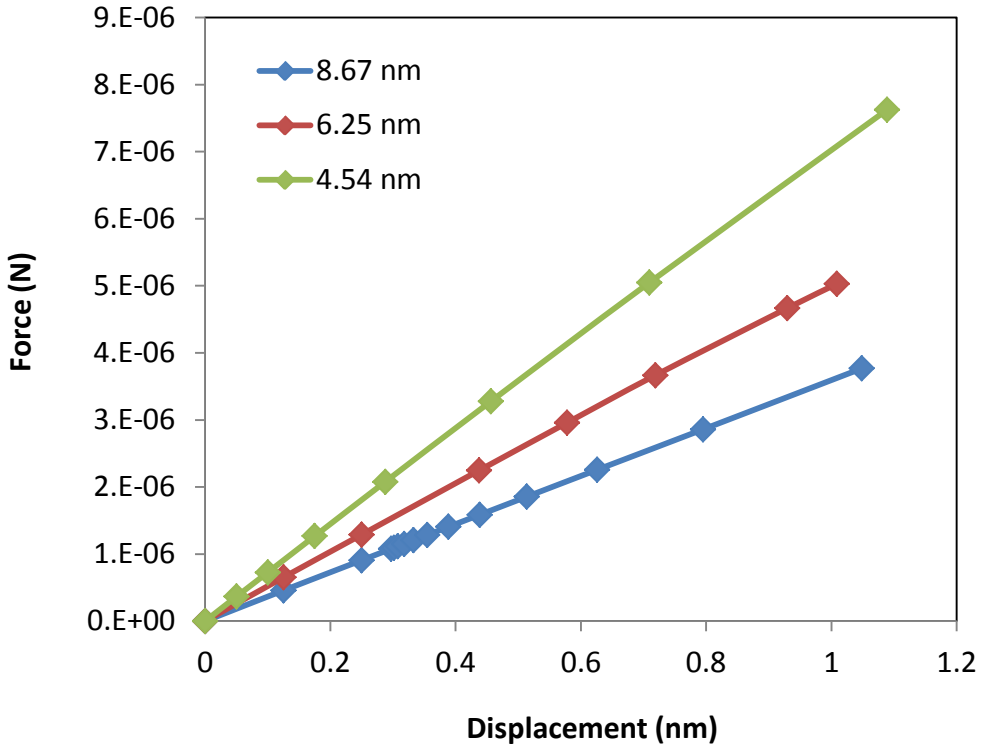

Figure 3.15. Load-displacement responses of the VA-CNT structures at different heights. Results are obtained from the 36-tube VA-CNT structure.

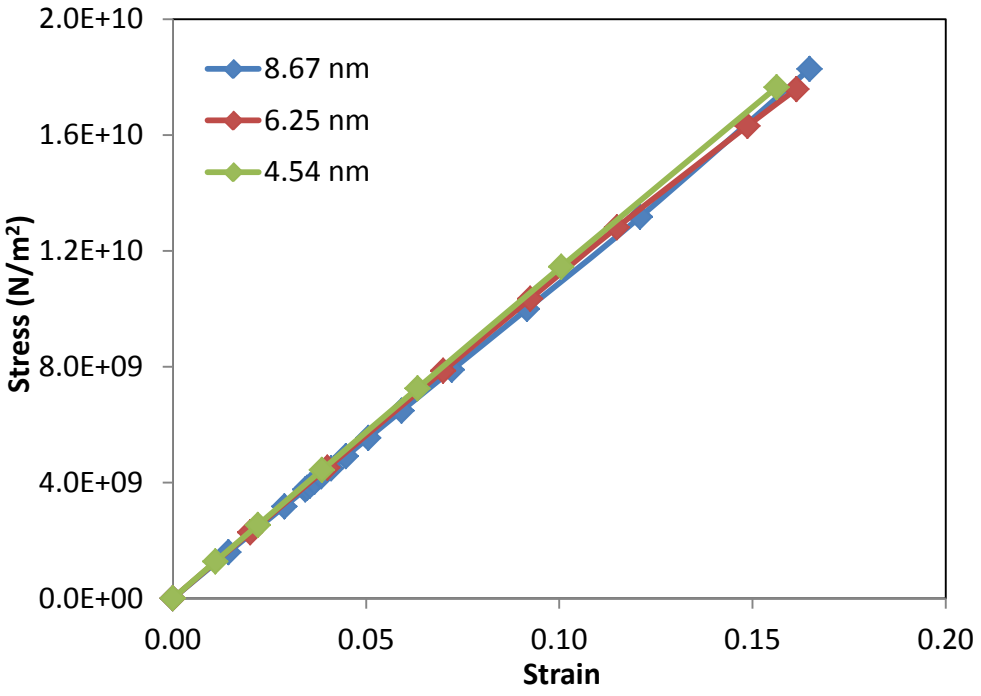

Figure 3.16. Stress-strain responses of the VA-CNT structures at different heights.

In this study, the VA-CNTs with various lengths (heights) were modeled and the elastic moduli were evaluated. The nanotubes were all assumed in zigzag configuration with a fixed wall thickness of 0.34 nm. Figure 3.15 displays the resulting load-displacement curves for these VA-CNT materials. As expected, the load-displacement responses clearly depend upon the specimen geometries. As the length of the VA-CNT material is increased (from 4.54 nm to 8.67nm), the stiffness of the material has been reduced, from 7.1 N/mm to 3.5 N/mm.

The stress-strain curves of these VA-CNT materials are shown in Figure 3.16. It is seen that the stress-strain responses of these materials are essentially indistinguishable. The modulus are computed, ranging from 110 GPa to 113 GPa, a merely 3% difference.

In an another trial of VA-CNT array with 100 tubes and square configuration for heights of 4.54nm, 6.25nm and 8.81 nm, the VA-CNT modulus and stiffness variation is plotted as shown in Figure 3.17 and Figure 3.18 below. It may be observed that for a given fixed number of nanotubes, the Young's modulus of the VA-CNT array is independent of the array height however the VA-CNT modulus increases with increasing areal density. Further, for a fixed given number of tubes, the stiffness of the VA-CNT array greatly depends on the VA-CNT height and is independent of the VA-CNT areal density since the number of load carrying members are the same for every areal density. The VA-CNT stiffness is inversely proportional to the VA-CNT height. The results are very consistent with those previously observed and from the literature.

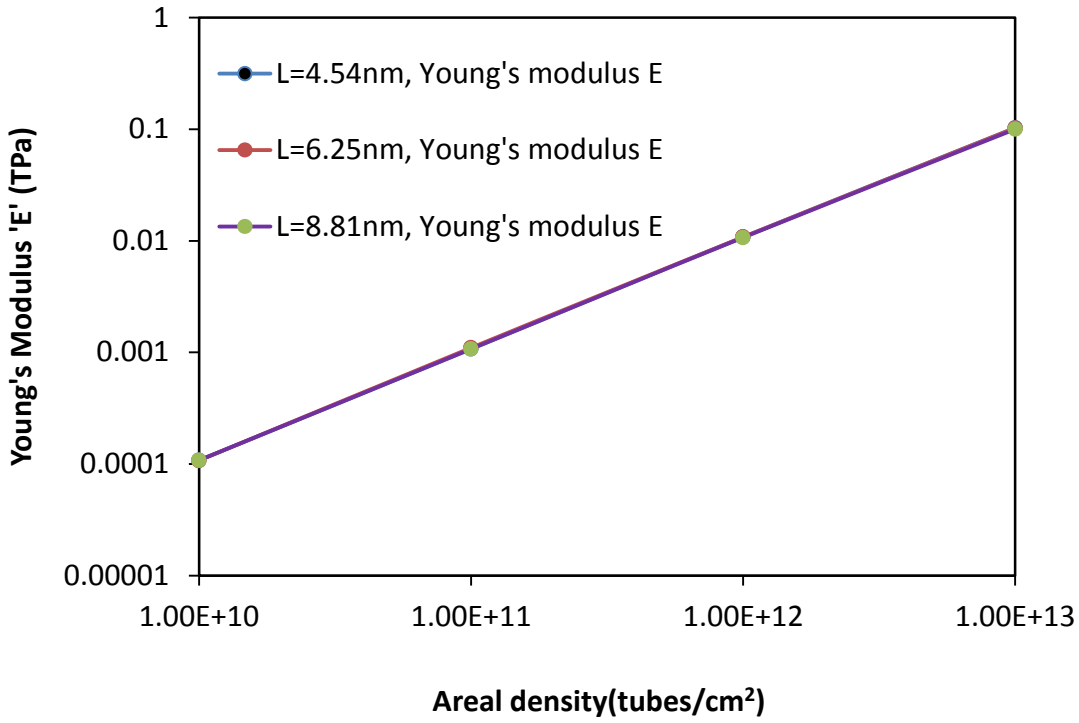

Figure 3.17. Variation of array modulus with areal density for different heights for fixed 100 tubes –square configuration.

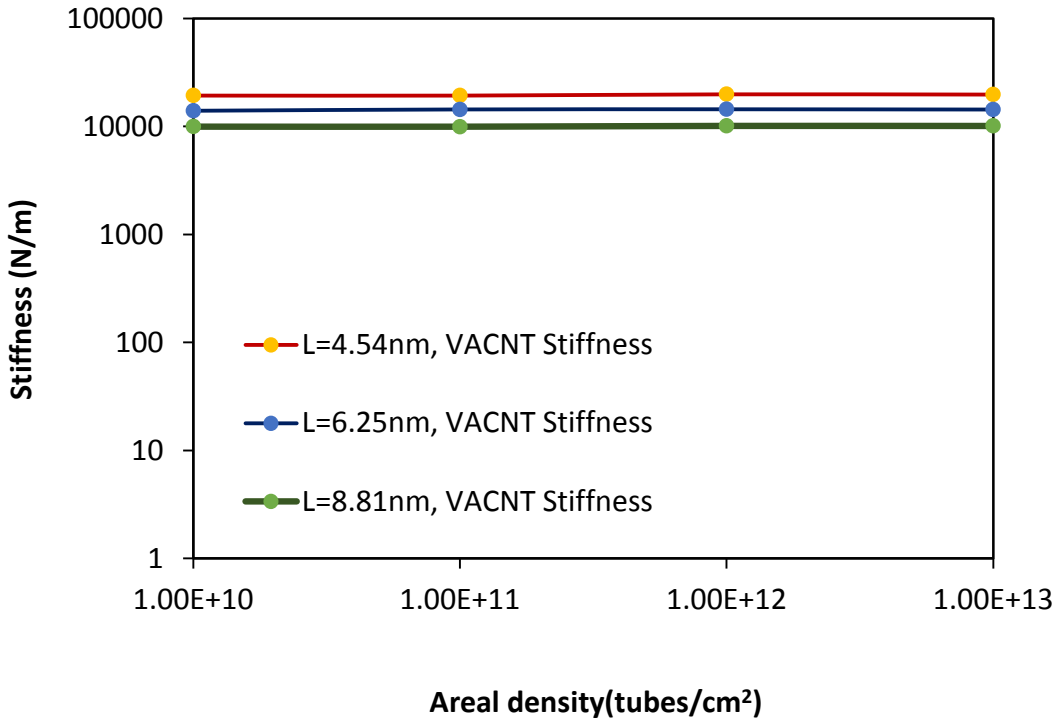

Figure 3.18. Variation of array stiffness with areal density for different heights for fixed 100 tubes-square configuration.

3.3.5 Effect of tube distribution pattern on stiffness and Young's modulus of VA-CNT

In another trial, the effect of tube distribution pattern /configuration on the modulus and stiffness of the VA-CNT array is studied. For this, a fixed number of tubes that occupy nearly identical area for both Square and FCC configurations is modeled. It is seen that the area occupied by 100 tubes in the VA-CNT array with Square configuration is closely identical to the area occupied by 98 tubes in FCC configuration with around 5% variation between the two areas; the area occupied by FCC configuration leading the area occupied by the Square configuration. This behavior may be also seen from Figure 3.19 seen earlier. The modulus of the VA-CNT array is closely identical for both Square and FCC configurations and increases with areal density as may be seen in the figure below. The minute variation in modulus between the two configurations is due to the small variation

in area discussed above and the modulus of VA-CNT with Square configuration leads that of the FCC configuration by a very small magnitude and is almost unnoticeable.

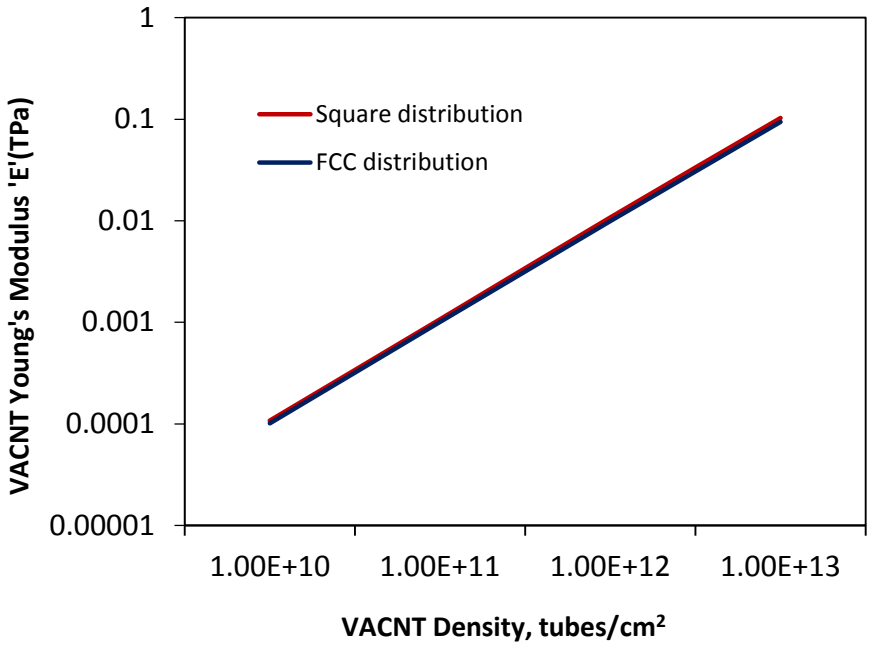

Figure 3.19. Effect of VA-CNT configuration on modulus.

The stiffness of the VA-CNT array as seen earlier is unaffected by the areal density for a given number of tubes. The stiffness of VA-CNT with Square configuration is slightly higher than that of the FCC configuration as seen in Figure 3.20. This is because the number of load carrying members i.e. nanotubes in Square configuration (100) is slightly higher than that of FCC configuration (98) occupying identically same area in both configurations

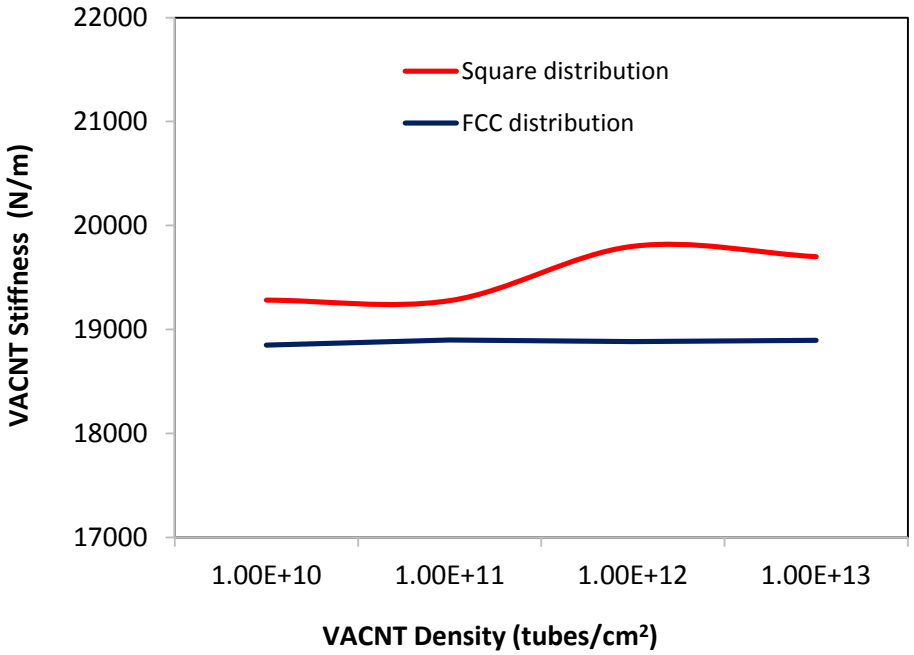

Figure 3.20. Effect of A-CNT configuration on stiffness.

3.4 Conclusions

An attempt is made in this work to design and characterize the material properties of aligned carbon nanotube arrays by using structural-based finite element method. VA-CNT structures with various densities and configurations have been constructed. Overall, the VA-CNT structures exhibit much lower modulus than the individual CNT, due to their high porosities and low densities. By increasing the nanotube array density, the modulus of VA-CNT structures are significantly improved. The individual nanotube atomic structure, i.e., zigzag versus armchair, can affect the mechanical property of the VA-CNT structure, but only at small wall thickness. The elastic modulus of the VA-CNT is not affected by the size (height) of testing specimen. The modeling approach serves as a computational tool to design and evaluate the architectures and geometric factors of the VA-CNTs for further widespread applications in the automotive, aerospace, space and related industries and thus help process the optimal nanotube materials.

Chapter 4

4. Design and Modeling of Aligned Carbon Nanotubes Structure Using Structural Shell Modeling: Single-walled VA-CNTs.

4.1 Introduction

An individual single-walled CNT may be visualized as originating from a single layer (Lu 1997) sheet of graphene rolled up to form a tube structure. Depending on the directions of rolling vectors, the CNT can be in different structures, i.e., armchair, zigzag, and chiral. The structures and resultant mechanical properties of an individual CNT have been extensively studied. However, practical applications often require that the carbon nanotube be produced in large scales and at oriented forms. These have resulted in a novel carbon nanotube material: the aligned carbon nanotube (VA-CNTs) structures.

A VA-CNT structure is composed of arrays of individual CNTs grown vertically through the use of a template (Figure 4.1). By controlling the design of the template, the resultant VA-CNTs can have various architectures and geometric parameters, including the tube height, tube diameter, tube array density, tube distribution pattern, inter-tube distance, and among many other factors. Any variation in each parameter may have great impact on the optimal performance of the VA-CNT structure. Therefore, it is crucial to have a rational strategy to design and evaluate the architectures and geometric factors to help process the optimal nanotube materials. The traditional material development has relied on the experimental "trial-and-error" method, thus is a very slow and expensive process. The National Materials Advisory Board of the National Academy has recently recommended a brand new material development model to the entire material science community, i.e., the "Integrated Computational Materials Engineering (ICME)" (National Research Council, 2008). The objective of the ICME approach is to integrate computational materials science tools into a holistic system that can accelerate materials development process.

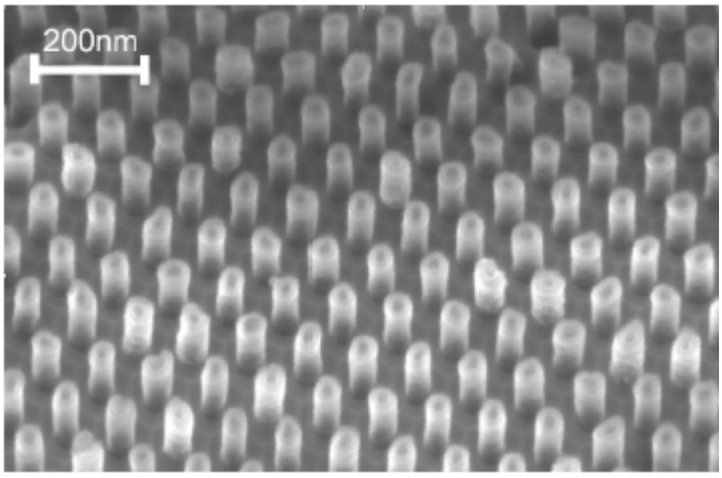

Figure 4.1. SEM micrographs of aligned carbon nanotubes(Li et al. 1999)

The most commonly used computational method for designing nanomaterials has been the atomistic approach, i.e., the classical molecular dynamics and ab initio techniques. The molecular simulations often require huge computational resources and are limited to simulating 10^6–10^8 atoms for a few nanoseconds (Qian et al., 2002, Wang et al., 2004). Therefore, although the atomistic method has been very successful for modeling an individual nanotube, it would not be a suitable feasible approach for modeling the aligned nanotube arrays.

Continuum mechanics techniques have gained great popularity recently due to their abilities to handle larger size carbon nanotube models. The previous chapter has presented the use of discrete beam elements for the aligned carbon nanotubes structures. The structural beam elements are more computational efficient in comparison with the traditional molecular simulations. However, for a VA-CNT structure that consists of millions or even billions of individual nanotubes, the preparations of a beam based finite element model is still quite an effort. In addition, the discrete beam elements would not be able to handle the contact between the interior walls in a multi-walled nanotube or the contacts between neighboring tubes in a nanotube arrays. In this chapter, we will attempt to use the continuum shell elements to design and model the aligned carbon nanotubes structures.

4.2 Modeling procedures

4.2.1 Finite element formulation

The approach in this work is based on the principle of structural mechanics (finite element method (FEM)). As illustrated in Figure 4.2(a), an aligned carbon nanotubes structure is composed of numerous individual nanotubes that are packed vertically on a flat substrate. Each individual single-walled carbon nanotube may be thought of as one graphene layer of a hexagonal lattice structure that has been wrapped into a seamless cylinder as seen in Figure 4.2(b), therefore, the continuum shell seems to be a natural representation of the nanotube structure. The force and moment diagram of a plate element further extended to shell element is shown in Figure 4.2(c).

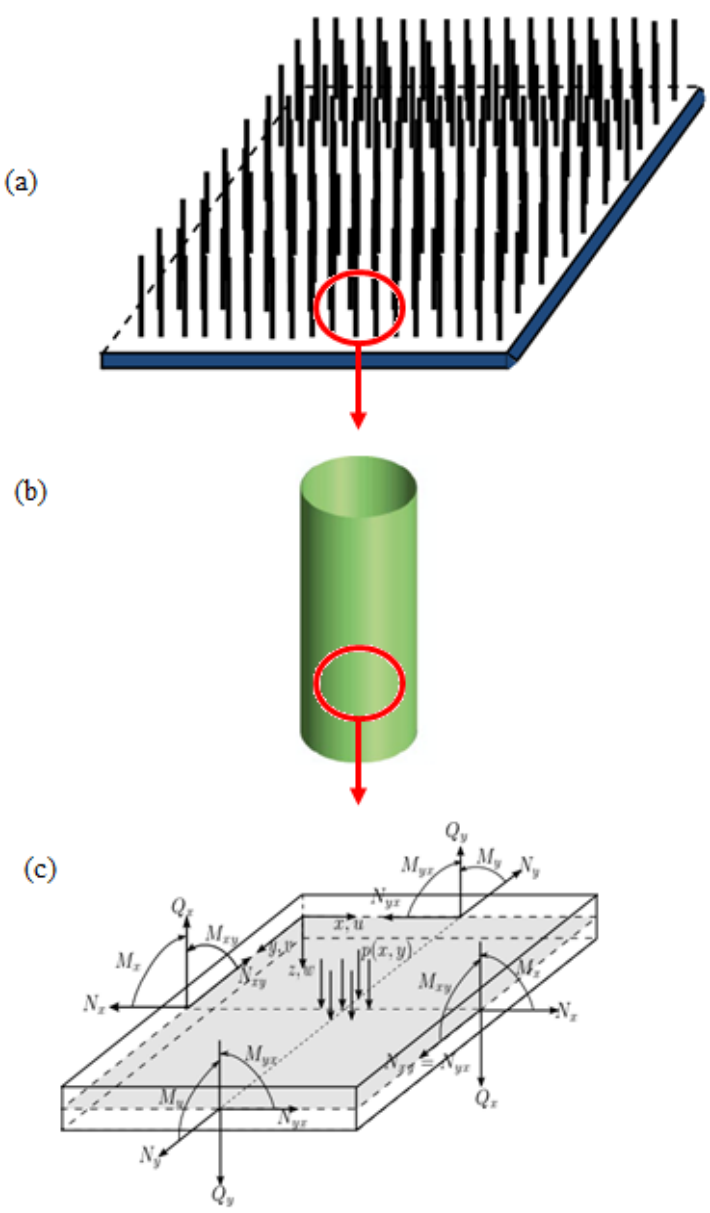

Figure 4.2. (a) A sketch for align carbon nanotubes structure (not to scale); (b) A sketch for an individual carbon nanotube; and (c) Forces and moments in a plate element.

According to Yakobson (Yakobson et al. 1996), there exists a close resemblance between the fullerenes (molecules of carbon in hollow structures such as tubes, spheres and ellipsoids) with densely packed atoms along a closed surface and the macroscopic objects of continuum, i.e. shells. Although a single-wall carbon nanotube (SWCNT) may be

treated as thin shells, the thickness and Young's modulus of the shell will have to be established.

It is shown that based on simulation of axial compression of nanotube that is modeled using Tersoff-Brenner potential at small strains, the total energy grows as $E(e) = \frac{1}{2}E"e^2$, where $E"$=59ev/atom. Further noting that the intrinsic symmetry of a graphite sheet is hexagonal with the elastic properties of a two-dimensional hexagonal structure being isotropic, the properties can be approximated by a uniform shell with only two elastic parameters, flexural rigidity D, and the shell's resistance to an in plane stretching, the in-plane stiffness C (Yakobson et al. 1996) . Also, it is seen that the energy of a shell is given by a surface integral of quadratic form and is derived as below.

Referring to Figure 4.2(c), above, the strain energy stored in a plate element is the sum of the strain energy due to bending moment and the strain energy due to twisting moment:

Strain energy = workdone by edge moments in bending and in twisting i.e workdone by

$$\left(M_x dy + M_y dx\right) + \left(M_{xy} dy + M_{yx} dx\right) \quad (4.1)$$

It is seen that the equation **(**4.1**)** above neglects the work done by the shearing forces and by stretching of the middle plane of the plate and is similar to beam theory, i.e., strain energy due to compression or tension along the axis or due to shear distortion is normally ignored.

Therefore work done by bending moments is $\frac{1}{2}$ x moment x angle between sides of the element after bending. The energy stored due to bending is given by

$$du_b = -\frac{1}{2}\left(M_x \frac{\partial^2 w}{\partial x^2} + M_y \frac{\partial^2 w}{\partial y^2}\right) dxdy \quad (4.2)$$

With the relative rotations of the element faces due to twist as $\frac{\partial^2 w}{\partial x \partial y} dx$ & $\frac{\partial^2 w}{\partial x \partial y} dy$, $M_{xy} dy$ and $M_{yx} dx$ the twisting moments and with $M_{xy} = M_{yx}$, the total energy due to twisting is given by

$$du_t = M_{xy} \frac{\partial^2 w}{\partial x \partial y} dx dy \tag{4.3}$$

Further, using $M_x = -D\left(\frac{\partial^2 w}{\partial x^2} + \vartheta \frac{\partial^2 w}{\partial y^2}\right)$ & $M_y = -D\left(\frac{\partial^2 w}{\partial y^2} + \vartheta \frac{\partial^2 w}{\partial x^2}\right)$ (4.4)

where, $D = \left\lfloor \frac{Et^3}{12}(1 - \vartheta^2) \right\rfloor$ the flexural rigidity and adding Equations (4.2) and (4.3) gives

$$du_b + du_t = \frac{1}{2} D \left[\left(\frac{\partial^2 w}{\partial x^2} + \frac{\partial^2 w}{\partial y^2} \right)^2 - 2(1 - \vartheta) \left(\frac{\partial^2 w}{\partial x^2} \frac{\partial^2 w}{\partial y^2} - \left(\frac{\partial^2 w}{\partial x \partial y} \right)^2 \right) \right] dx dy \tag{4.5}$$

The strain energy stored in the complete plate is given by integrating the above equation over the entire surface, i.e.

$$u = \frac{1}{2} D \iint \left[\left(\frac{\partial^2 w}{\partial x^2} + \frac{\partial^2 w}{\partial y^2} \right)^2 - 2(1 - \vartheta) \left(\frac{\partial^2 w}{\partial x^2} \frac{\partial^2 w}{\partial y^2} - \left(\frac{\partial^2 w}{\partial x \partial y} \right)^2 \right) \right] dx dy \tag{4.6}$$

Extending the above to thin shells as in Figure 4.3, the strain energy due to bending only with no middle surface stretching is given by Equation (4.6) above.

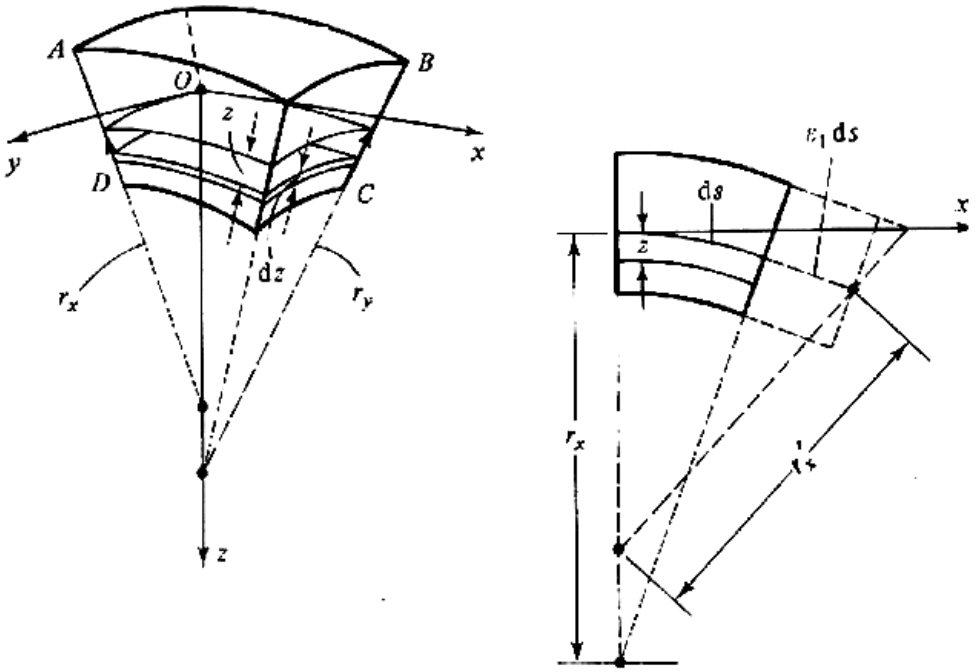

Figure 4.3. Shell Element (Allen and Bulson.P.S. 1980).

The strains in the x and y directions for a lamina in the shell element, as seen in Figure 4.3, at a distance 'z' from the middle surface in terms of middle surface strains and curvatures is given by

$$\varepsilon_x = \varepsilon_1 - z\frac{\partial^2 w}{\partial x^2} \text{ and } \varepsilon_y = \varepsilon_2 - z\frac{\partial^2 w}{\partial y^2} \tag{4.7}$$

The components of stress are then given by

$$\sigma_x = \frac{Ez}{(1-\vartheta^2)}[\varepsilon_1 - z\beta_x + \vartheta(\varepsilon_2 - z\beta_y)] \tag{4.8a}$$

$$\sigma_y = \frac{Ez}{(1-\vartheta^2)}[\varepsilon_2 - z\beta_y + \vartheta(\varepsilon_1 - z\beta_x) \tag{4.8b}$$

where $\beta_x = \frac{\partial^2 w}{\partial x^2}$ and are the change of curvatures

Components of edge forces are then given by

$$N_x = \int_{-t/2}^{+t/2} \sigma_x dz = \frac{Et}{(1-\vartheta^2)}(\varepsilon_1 + \vartheta\varepsilon_2) \quad (4.9a)$$

$$N_y = \int_{-t/2}^{+t/2} \sigma_y dz = \frac{Et}{(1-\vartheta^2)}(\varepsilon_2 + \vartheta\varepsilon_1) \quad (4.9b)$$

$$N_{xy} = \int_{-t/2}^{+t/2} \tau_{xy} dz = \frac{Et}{2(1+\vartheta)}\gamma_{xy} \quad (4.9c)$$

where γ_{xy} is the component of shear strain in the middle surface of the shell. The energy due to stretching of the middle surface *Us*, is given by,

$Us = \iint \frac{1}{2}\left(N_x\varepsilon_1 + N_y\varepsilon_2 + N_{xy}\gamma_{xy}\right)dA$, which can be written as

$$\boldsymbol{Us = \frac{C}{2(1-\vartheta^2)} \iint \left[(\varepsilon_1 + \varepsilon_2)^2 - 2(1-\vartheta)(\varepsilon_1\varepsilon_2 - \frac{\gamma_{xy}^2}{4})\right] dA} \quad (4.10)$$

where $C = Et$ is the shell in-plane stiffness.

The total energy of a shell combining the above two strain energies namely strain energy due to bending (Equation (4.6)) and strain energy due to stretching (Equation (4.10)) are defined as (Yakobson et al. 1996)

$$u = \frac{1}{2}\iint \left[D\left[\left(\frac{\partial^2 w}{\partial x^2} + \frac{\partial^2 w}{\partial y^2}\right)^2 - 2(1-\vartheta)\left(\frac{\partial^2 w}{\partial x^2}\frac{\partial^2 w}{\partial y^2} - \left(\frac{\partial^2 w}{\partial x \partial y}\right)^2\right)\right] + \frac{C}{(1-\vartheta^2)}\iint \left[(\varepsilon_1 + \varepsilon_2)^2 - 2(1-\vartheta)(\varepsilon_1\varepsilon_2 - \frac{\gamma_{xy}^2}{4})\right] dxdy\right] \quad (4.11)$$

The bending/flexural rigidity 'D' and the in-plane stiffness 'C' from the preceding continuum mechanics approach are compared with detailed *ab initio* and semi-empirical studies. The magnitudes of these properties are determined as: C = 59eV/atom = 360 J/m^2 and D=0.85eV (Yakobson et al. 1996). Using the standard relations from classical theory of elasticity (Yakobson et al. 1996) the thickness (h) and the modulus of elasticity (E) of the shell can be extracted.

$$D = \frac{Eh^3}{12(1-\vartheta^2)} \tag{4.12}$$

$$C = Eh \tag{4.13}$$

The thickness of shell is determined as, h=0.066 nm and the modulus of elasticity of the shell, E= 5.5 TPa. These values are used in the subsequent finite element models for the analysis of nanotubes.

4.2.2 Modeling of VACNT array with SWCNT using shell elements

4.2.2.1 VA-CNT array layout designs for Square and FCC patterns

VA-CNT arrays are grown with square, FCC, HCP, Square and random distribution patterns of the nanotubes. In this analysis, square and FCC distribution patterns are designed and modeled in order to study the effect of nanotube distribution pattern, nanotube density on the Young's Modulus 'E' and stiffness of the VA-CNT material. The VA-CNTs are grown with several different packing densities commonly referred to as areal densities. The most commonly grown areal densities being $1x10^8$ tubes/cm^2, $1\ x10^9$ tubes /cm^2, $1\ x10^{10}$ tubes/cm^2, $1\ x10^{11}$ tubes /cm^2, $1\ x10^{12}$ tubes /cm^2, $1\ x10^{13}$ tubes /cm^2. The layout and the modeling details of Square and FCC distribution pattern for the VA-CNT array considered are shown in Figure 4.4 below.

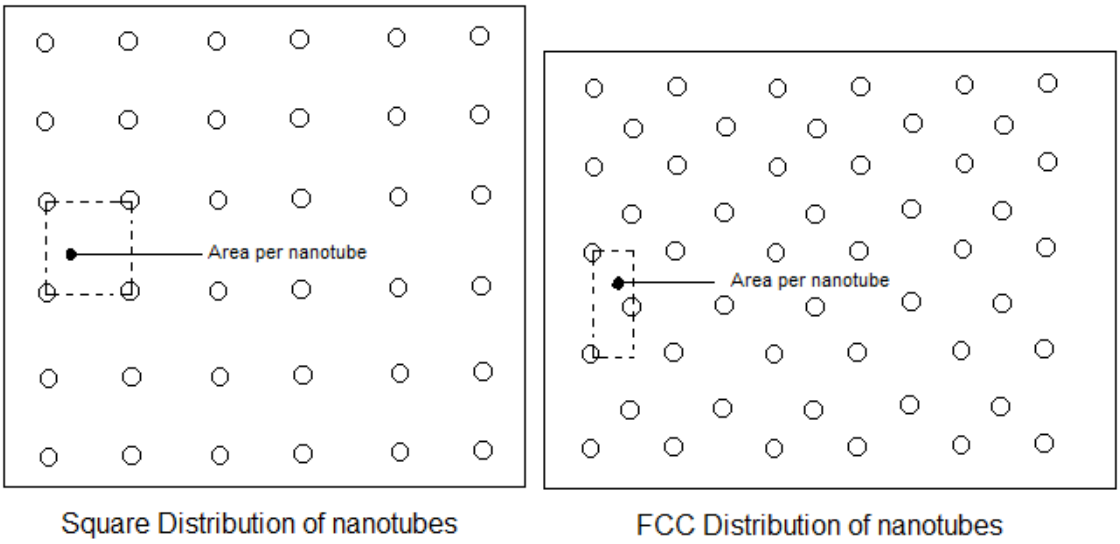

Figure 4.4. Layout of Square and FCC distribution of nanotubes.

The area occupied by an individual nanotube for square and FCC distribution of nanotubes is highlighted. The final design parameters which are the nanotube interspacing distance and the maximum diameter of the nanotube that can be accommodated for a given areal density without nanotube overlap/interference as observed in a grown VA-CNT and with well aligned nanotubes for both square and FCC configurations with reference to Figure 4.5 is given in Table 4.1 and Table 4.2 as below

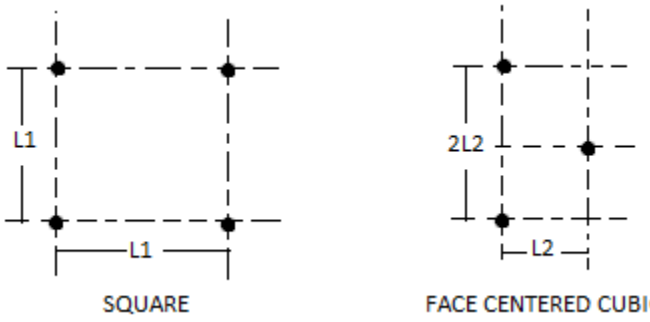

Figure 4.5. Unit cell layout for SQUARE and FCC design.

With $(L_1)^2$ as the area per nanotube in a square configuration and (L_2*2*L_2) as the area per nanotube in a FCC configuration, for identical unit cell area in both configurations we

obtain $L_2 = 0.707\ L_1$. It is to be noted here that $L_1 \neq 2L_2$. Table 4.1 and Table 4.2 shows intertube distances L_1 and L_2 for both Square and FCC distribution and the maximum diameter of the nanotubes that could be accommodated for each density distribution.

Table 4.1. L_1 and nanotube diameter values for different areal densities-Square configuration.

Areal Density (tubes/cm^2)	**L_1 (m)**	**CNTs with diameter < than (nm)**
1.00E+08	1.00E-06	**1000**
1.00E+09	3.16E-07	**316.2**
1.00E+10	1.00E-07	**100**
1.00E+11	3.16E-08	**31.62**
1.00E+12	1.00E-08	**10**
1.00E+13	3.16E-09	**3.162**

Table 4.2. L_2 and nanotube diameter values for different areal densities-FCC configuration.

Areal Density (tubes/cm^2)	L_2 (m)	CNTs with diameter < than (nm)
1.00E+08	7.07E-07	**999**
1.00E+09	2.24E-07	**316**
1.00E+10	7.07E-08	**99.9**
1.00E+11	2.24E-08	**31.62**
1.00E+12	7.07E-09	**9.899**
1.00E+13	2.24E-09	**3.15**

A representative comparison of VA-CNT distribution for different densities and a fixed number of tubes for Square distribution of nanotubes modeled in ABAQUS is shown in Figure 4.7 below. Also Figure 4.8 shows the FCC distribution pattern for an areal density of $1x10^{10}$ tubes/cm^2. The square and FCC distribution VA-CNT arrays are designed such that the area occupied by a predefined number of tubes (49) in square configuration for a given areal density is maintained the same in FCC configuration for the corresponding areal density by way of calculation of a new set of number of tubes (50) in view of the difference in the tube distribution patterns.. Hence the design is for a “Fixed number” of tubes. This implies that for a predefined numbers of tubes (for example, 50) the total area occupied by this predefined number of tubes diminishes with increasing areal density. Greater areal density indicating close packing of nanotubes as compared to smaller areal

densities indicating loose packing of the nanotubes. The tube-tube distance varies accordingly. Figure 4.6 below show this diminishing trend of VA-CNT area for a fixed number of nanotubes and with increasing tube areal/ packing density. The calculated intertube distances for each of the areal densities and for both Square and FCC configurations is as given in Table 4.1 and Table 4.2. Figure 4.7 shows pictorially the actual area occupied by each of the areal densities for a fixed number of tubes-100 tubes in this case for square configuration. This design approach will help to compare the characteristics of VA-CNT for both Square and FCC distribution for various densities. The VA-CNT area for an areal density of $1x10^{10}$ tubes/cm^2 for 50 tubes and FCC configuration is shown in Figure 4.8.

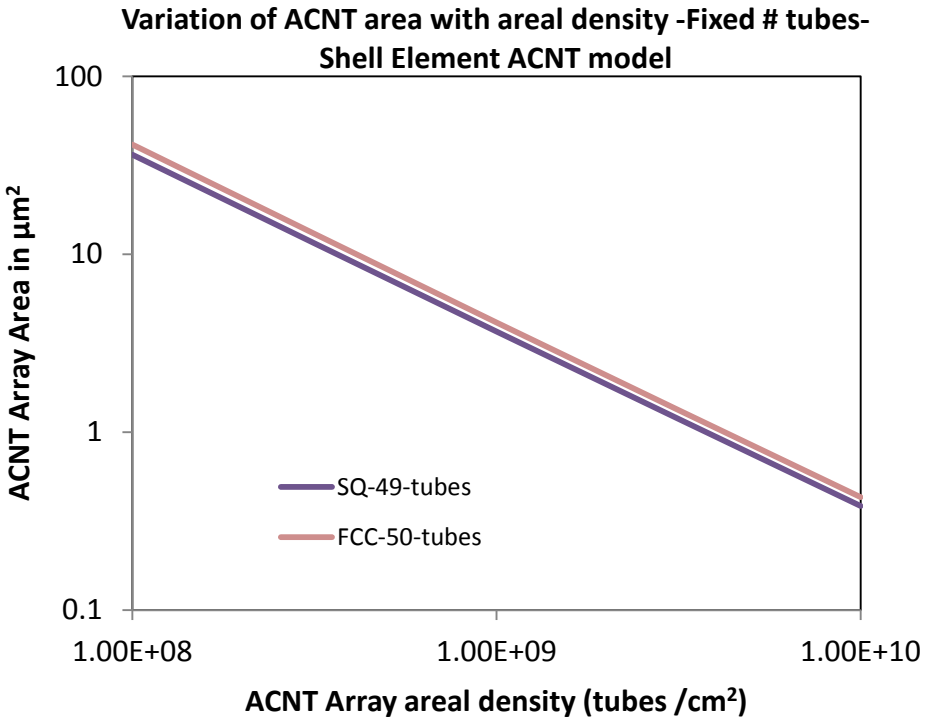

Figure 4.6. Diminishing trend of the VA-CNT area with increasing packing density for a fixed number of tubes.

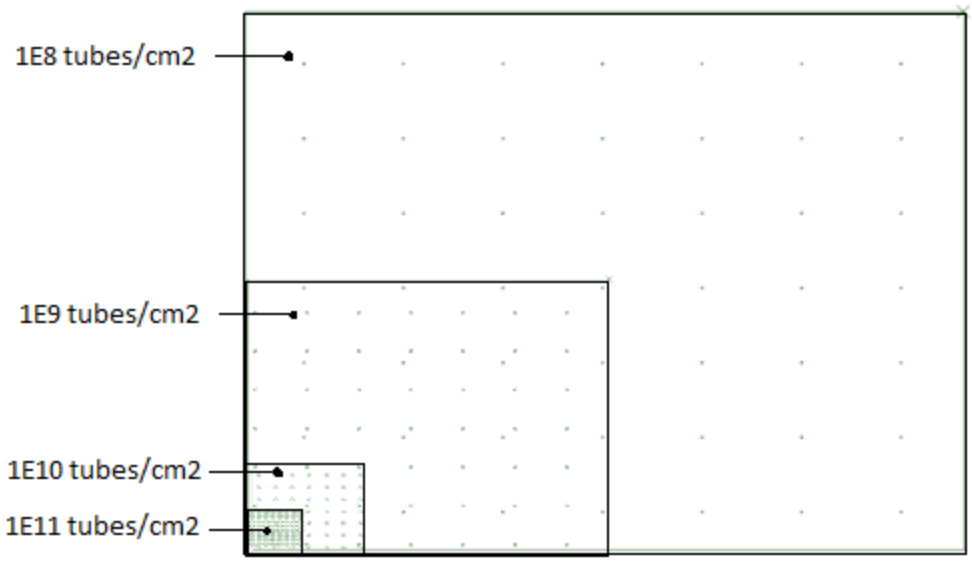

Figure 4.7. Overview of VA-CNT area for different areal densities for a fixed no. of tubes- 49 tubes for square configuration.

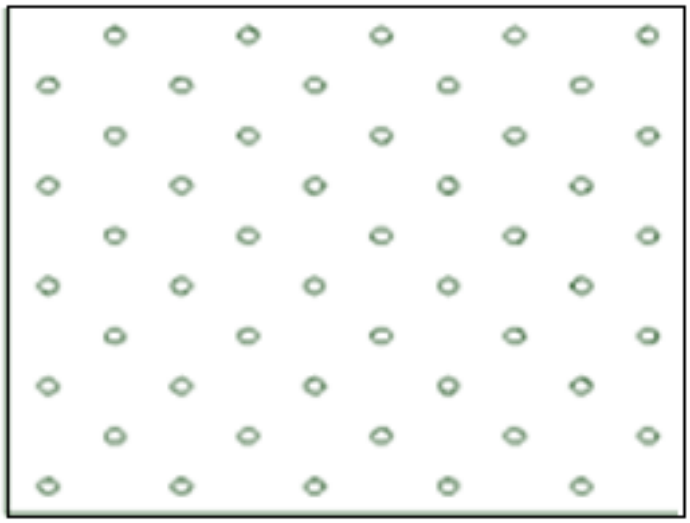

Figure 4.8. FCC distribution of nanotubes for $1x10^{10}$ tubes/cm^2 for 50 tubes.

4.2.2.2 Modeling procedure for VA-CNT structures

The aligned carbon nanotubes structures are consisted of individual nanotubes that are packed vertically on flat substrates. The overall structures depend upon numerous geometric parameters, including tube array density, tube distribution pattern, inter-tube distance, tube-tube junction structure, among many others. To construct the VA-CNT structures, the solid models for individual carbon nanotubes. 8 noded shell elements (S8R) with a quadratic displacement function were used. Appropriate geometric sectional properties (0.066nm thick), and material properties (E=5.5 TPa, υ= 0.19) were assigned following the procedures described in Chapter2.

The VA-CNT structures at various densities were constructed, ranging from $1x10^8$ tubes/cm^2 to $1x10^{11}$ tubes/cm^2.For the present case the number of tubes is fixed at 49 tubes for Square configuration and 50 tubes for FCC configuration for various VA-CNT-array areal densities. The array area decreases as the density increases due to decreasing intertube distance as shown in Figure 4.6 above The heights of the VA-CNT structures were varied, from 100 nm to 1000 nm having aspect ratios 5, 10 and 50. To conduct compression experiments, the compression heads (as represented by analytical rigid surfaces) were subjected to a displacement in the downward direction. The bottom ends of the nanotubes were constrained in all directions to simulate the fixity of the nanotubes to the substrate material. Suitable contact interactions were defined between the nanotube top surfaces and the compression head surfaces with an assumed coefficient of friction of 0.1. Examples of the FE models for the vertically aligned carbon nanotubes structures are shown in Figure 4.9 below.

4.2.3 FE models of carbon nanotubes

The aligned carbon nanotube arrays were modeled using ABAQUS CAE where the individual nanotube was meshed using shell elements (Figure 4.9). Both linear (S4R, S8R) and quadratic (S4R) formulation shell elements were used in the analyses. The diameter of the individual nanotube was varied between 10-100 nm and the length of the nanotube varied between 100-1000 nm. The nanotubes were subjected to compressive loading by way of imposing displacements at the free ends and with the other ends of the nanotubes constrained in all the degrees of freedom (Figure 4.10). The compression loading were applied for strains of up to 2.5%. Analyses were run by varying the mesh size, i.e., by varying the number of elements in the nanotube FE models. The nanotubes are studied using an element size starting from 10.472 nm until 2.5133 nm. An aspect ratio equal to 1 is maintained with the total number of elements varying from 60 to 1000 for the S4R element with linear formulation. The nanotube is then modeled with S8R element with quadratic formulation and the numbers of elements are varied from 60 to 228 for the same element size. Figure 4.9 below shows the models of nanotube with shell element modeled from coarse to fine mesh with decreasing mesh size. Hence a convergence study was conducted before arriving at the final results.

The aligned carbon nanotubes (VA-CNT) structures are consisted of individual nanotubes that are packed vertically on flat substrates. In this study, the VA-CNT arrays with a dimension of 2020 nm x 2020 nm were constructed. The diameter of the nanotube was fixed as 20 nm and the length was varied. The resultant length/diameter aspect ratios are 5 to 50. The distribution of the nanotubes in the arrays was arranged in square and face-centered cube (FCC) modes. To conduct compression experiments, the compression heads (as represented by analytical rigid surfaces) were subjected to various displacements in the downward direction. The bottom ends of the nanotubes were constrained in all directions to simulate the fixity of the nanotubes to the substrate material. Suitable contact interactions were defined between the nanotube top surfaces and the compression head surfaces with an assumed coefficient of friction of 0.1.

Examples of the FE models for the vertically aligned carbon nanotubes structures with SQUARE and FCC distributions are shown in Figure 4.11 and Figure 4.12.

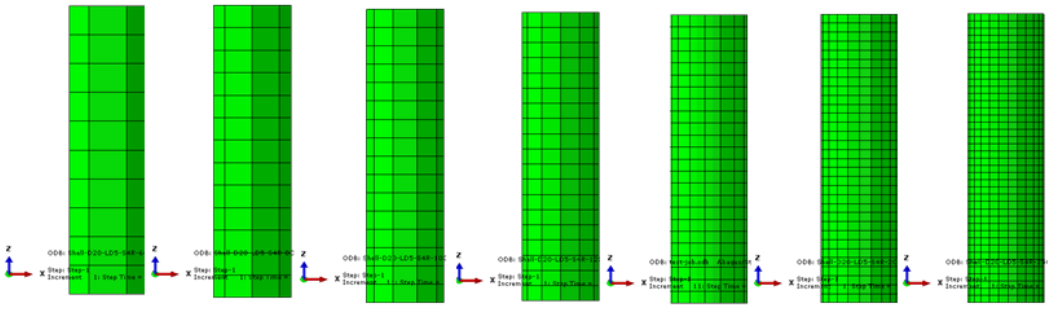

Figure 4.9. FE models showing mesh refinement of nanotube from coarse mesh model to fine mesh model for convergence studies.

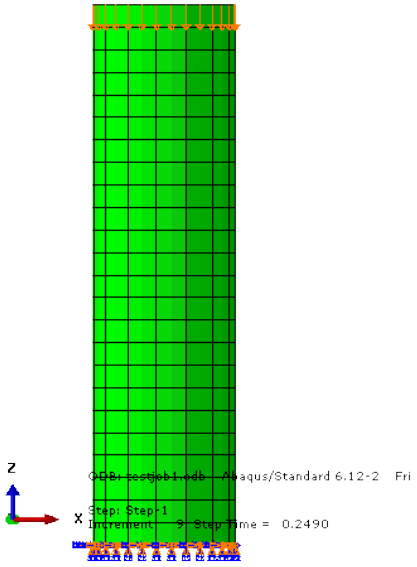

Figure 4.10. The load and boundary condition applied in an individual nanotube shell model.

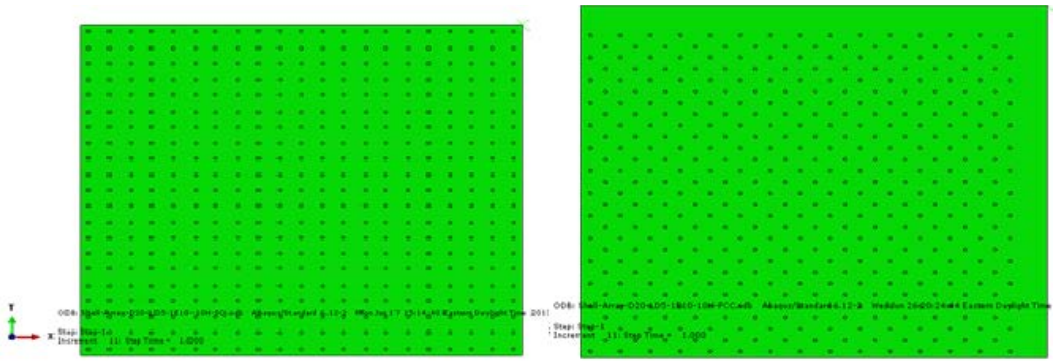

Figure 4.11. FE models showing the aligned carbon nanotube arrays: (a) Square configuration and (b) FCC configurations.

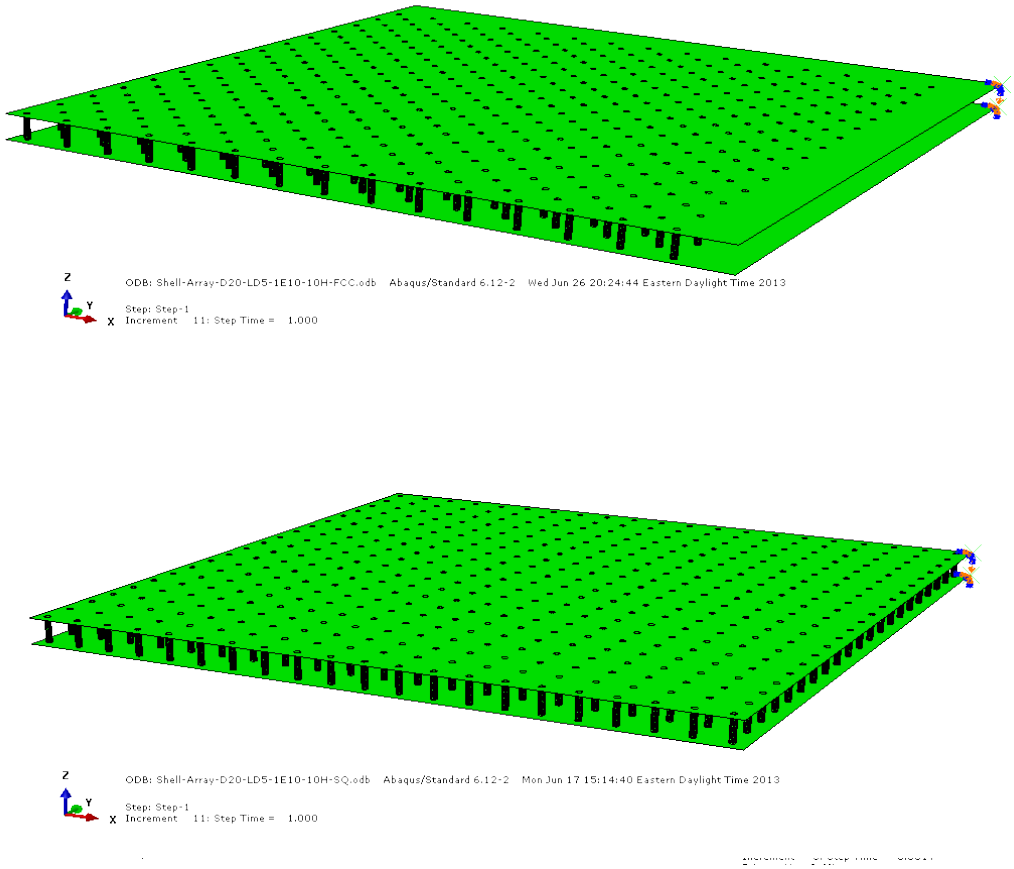

Figure 4.12. The load and boundary condition applied in the aligned carbon nanotube arrays models: (a) FCC configuration and (b) Square configuration.

4.3 Results and discussion

4.3.1 Convergences of FE models (effect of number of nodes, effect of element sizes)

In finite element simulations, the size and type of the element chosen in the model plays an important role in determining the accuracy of the results. A convergence study was first conducted by using shell elements (S4R, S8R) having linear displacement function(S4R) as well as using quadratic shell elements (S8R) having quadratic displacement function and by varying the mesh size (Figure 4.9 above). The Young's modulus of the nanotube structure is evaluated using the relation

$$\mathrm{E} = \frac{\mathrm{PL}}{\mathrm{A}\delta} \tag{4.14}$$

where $P =$ Applied load

$\delta =$ Elongation of the nanotube

$L =$ Length of the nanotube

$A =$ Cross sectional area of the nanotube

Figure 4.13 and Figure 4.14 show the plots of convergence of Young's modulus with the increases in numbers of nodes and elements, respectively. It is seen that there are significant variations in E when the 4-node elements were used (linear and nonlinear analysis). The coarse FE models (fewer nodes and elements) would yield very inaccurate results. In contrast, the results obtained from the 8-node element (S8R) are found to be consistent and a linear analysis using S8R elements converges very well with fewer numbers of nodes and elements. Hence convergence with a second order element results in smaller size of the model and more close approximation of the results. The plots below in Figure 4.13, Figure 4.14 and Figure 4.15 shows the results of mesh convergence for a nanotube model that is considered individual as well as for nanotube considered as part of an array. The Young's modulus of the nanotube calculated by considering it as a stand-alone entity is 5.48 TPa while it is 0.73 TPa or 730GPa considering it as part of an array

as seen in Figure 4.14 and Figure 4.15. The deformation contours of nanotubes from coarse mesh model to fine mesh for this study are as shown in Figure 4.16 below. It may be seen that the displacement contour plot is a smooth distribution contour plot for fine mesh as compared to that of coarse mesh.

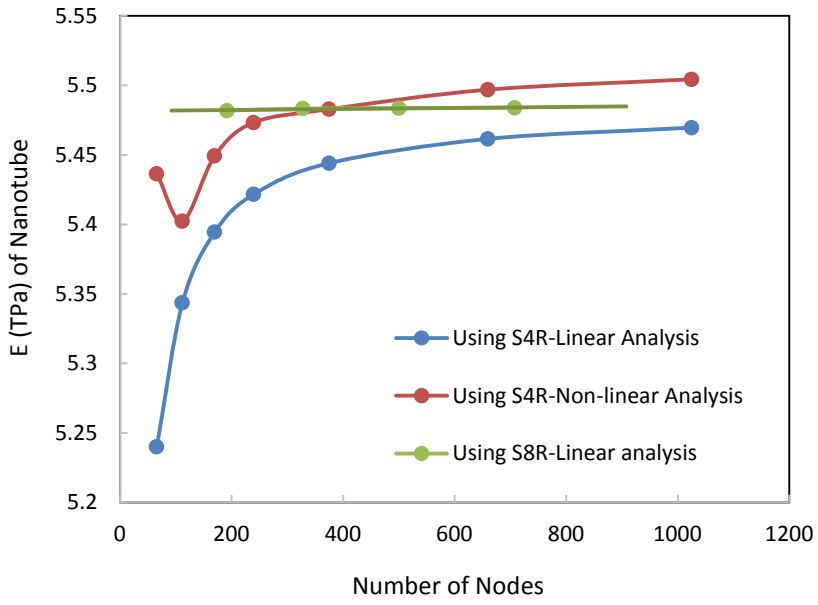

Figure 4.13. Convergence of Young's modulus of the nanotube with the number of nodes. 'E' is for nanotube.

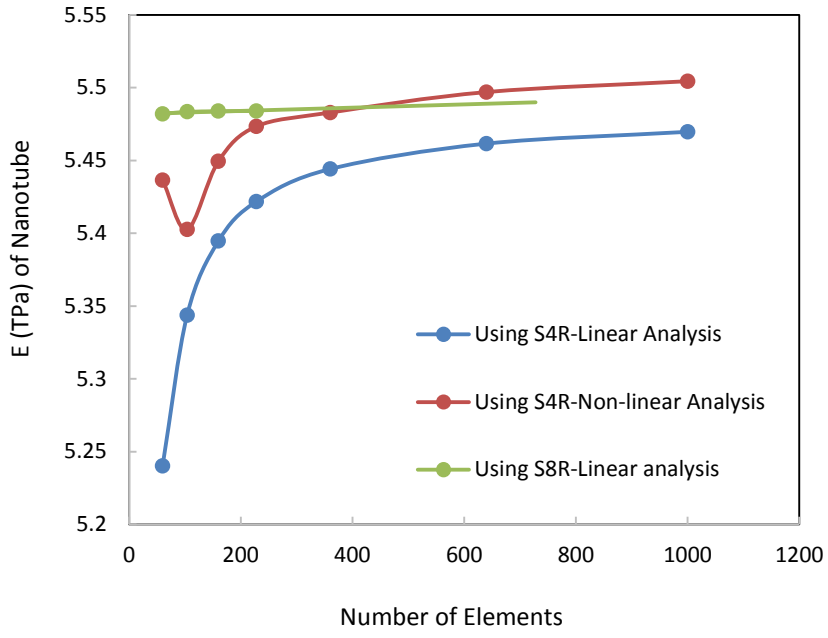

Figure 4.14. Convergence of Young's modulus of the nanotube with the number of elements. 'E' is for nanotube.

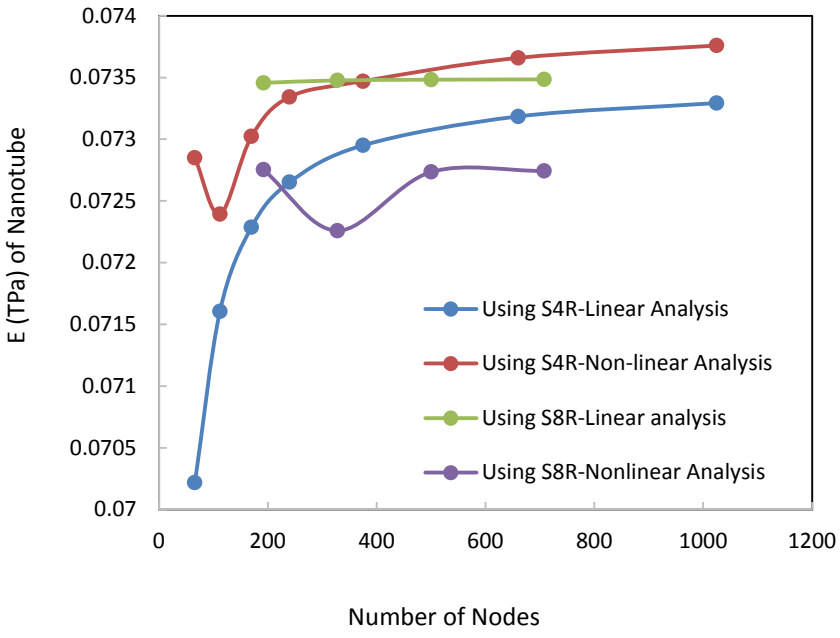

Figure 4.15. Convergence of Young's modulus of the nanotube with the number of elements. 'E' for nanotube considered as part of an array.

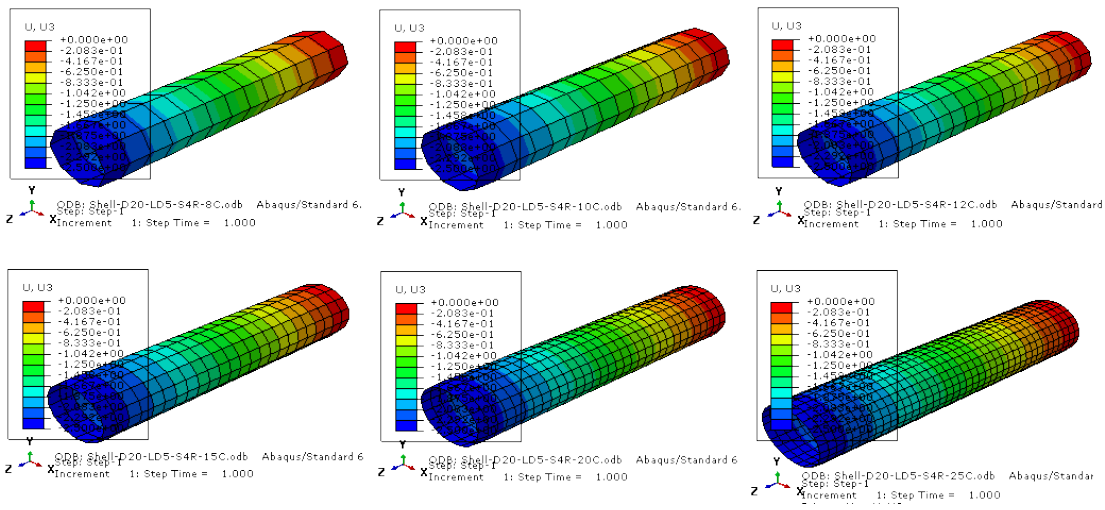

Figure 4.16. Deformation contours of nanotubes from coarse mesh model to fine mesh model for convergence studies.

4.3.2 Modeling of individual nanotubes

4.3.2.1 Variation of nanotube Young's modulus with nanotube diameter

Some key parameters in designing a carbon nanotube are the tube diameter and the tube height. Experimentally, the diameter and height of the carbon nanotubes can be adjusted by controlling the growth conditions such as temperature, time, and pressure. It is interesting to know these geometric parameters would affect the mechanical properties of the nanotubes. In present study, nanotubes in the diameter range from 10 nm to 100 nm were first considered in order to evaluate the variation of elastic modulus with the nanotube diameter. In those models, the height of these nanotubes was fixed at 200 nm. Secondly, the FE models for nanotubes were constructed at varying heights, from 100 to 1000 nm to evaluate the variation of elastic modulus with the nanotube height. In those models, the diameter of the tubes was fixed at 20 nm. In all cases, the nanotubes were

subjected to an axial displacement and linear static analyses with NLGEOM= OFF were conducted. The resulting reaction forces were evaluated, from which the Young's modulus (E) of the nanotubes at various nanotube diameters and heights were evaluated by using Equation 4.14.

Figure 4.17 shows the von Mises stress contours of the nanotubes upon subjecting to axial compressions. It may be observed from the contour plots that for a given amount of applied axial compression and hence for a given applied axial strain, the stress magnitude and the stress distribution is identically same for all of the tubes with increasing diameters as per the equation 4.14 above. The stiffness and Young's modulus of the nanotubes for a fixed nanotube length (L=200) are calculated and plotted in Figure 4.18 and Figure 4.19 respectively. As may be observed from the graph, the stiffness increases linearly with the increase of tube diameter. The Young's modulus is seen to remain relatively constant with the tube diameters. The variation of Young's Modulus of nanotube considering it as part of an array is plotted in Figure 4.20. The magnitude of 'E' of the nanotube in this case drops exponentially with increasing diameter values as may be seen which is a representation of higher modulus for smaller diameter nanotubes and lower modulus for larger diameter nanotubes. This is consistent with open cell foam behavior wherein foams with larger cells have a lesser modulus compared to foams with smaller cells having larger modulus (Kuncir et al. 1990).

Further, results for variation of Young's Modulus of nanotube with diameter for a fixed aspect ratio (L/D =10) wherein the diameter of the nanotube is varied from 10 to 100 in combination with length variation revealed identical behavior as that obtained for the fixed nanotube length L=200 case (Figure 4.22 and Figure 4.23). The variation of stiffness of nanotube with nanotube diameter for the fixed aspect ratio(L/D = 10) shows an initial rise followed by almost stagnation at around a particular value of stiffness indicating unlimited possibilities of tailoring / customizing the nanotube stiffness values by varying the combinations of nanotube diameter and length. This forms a very important /crucial understanding that guides the design of components and devices based

on VA-CNT arrays. In all of these cases the nanotubes strains were limited for linear range with strains upto around 0.8%

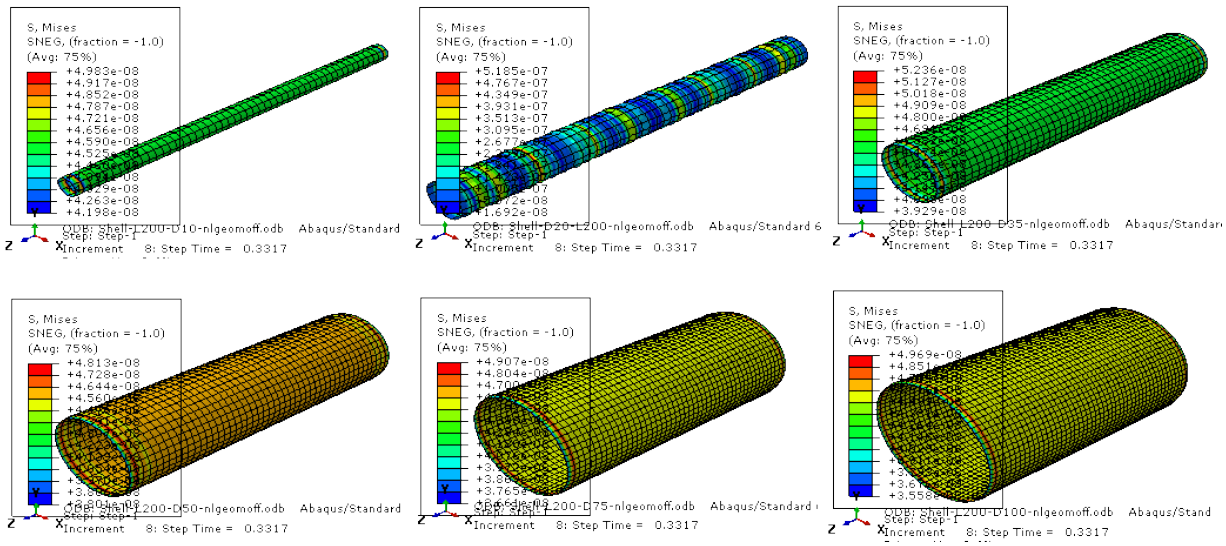

Figure 4.17. von Mises stress contours for all 6 tubes.

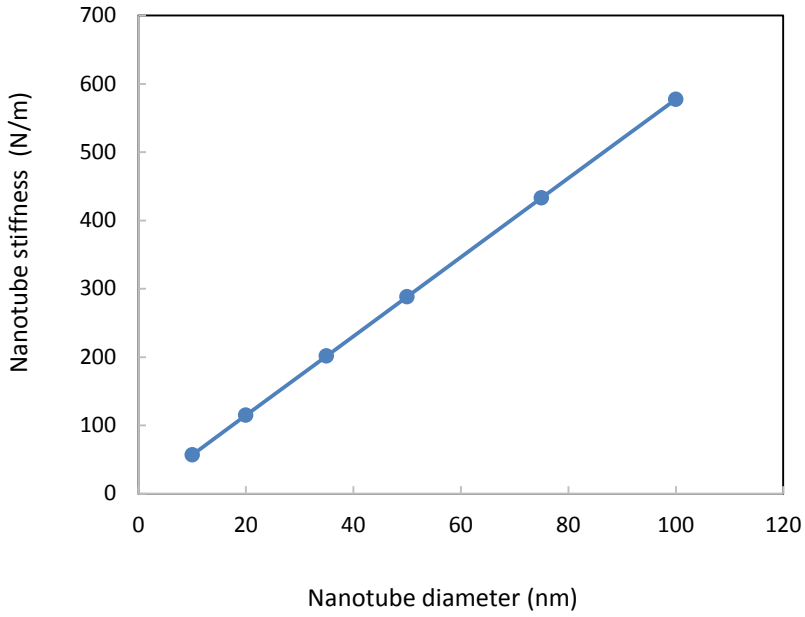

Figure 4.18. Variation of stiffness as a function of nanotube diameter. The length of nanotube was 200 nm.

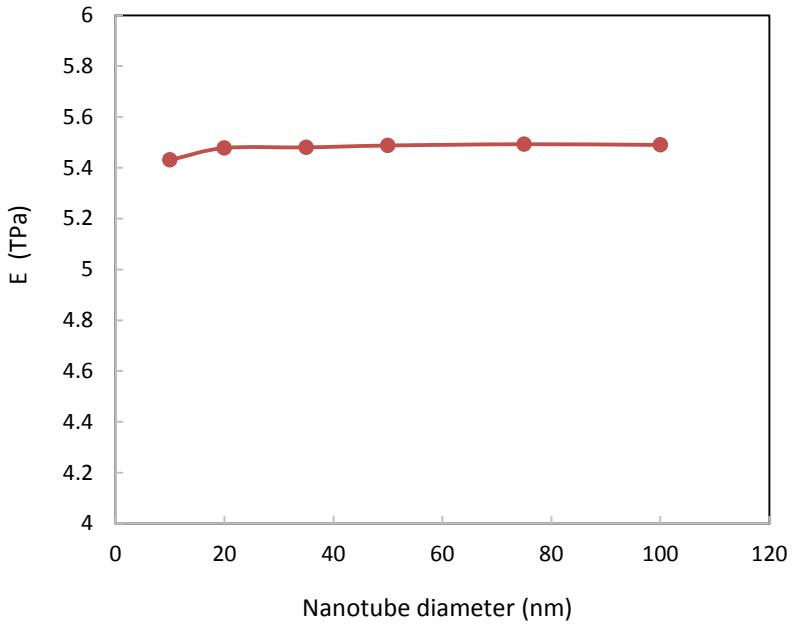

Figure 4.19. Variation of Young's modulus as a function of nanotube diameter. The length of nanotube was 200 nm.

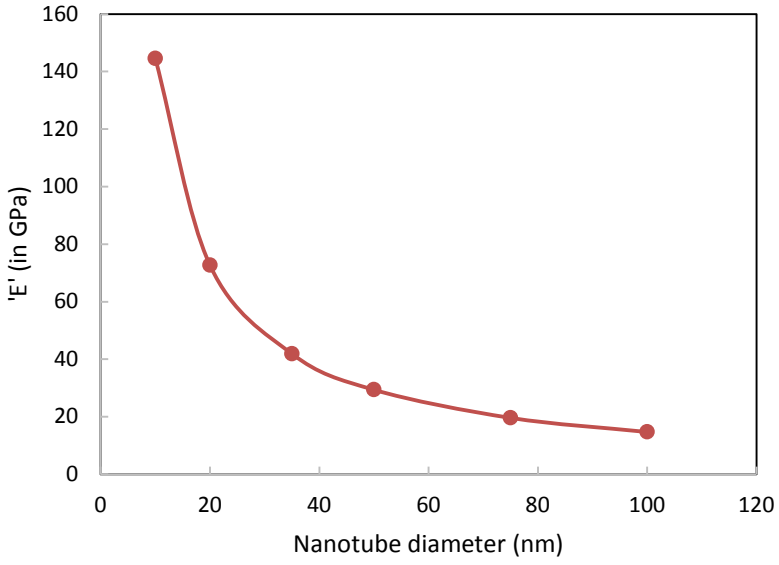

Figure 4.20. Variation of Young's modulus as a function of nanotube diameter considering the nanotube as part of an array. The length of nanotube was 200 nm.

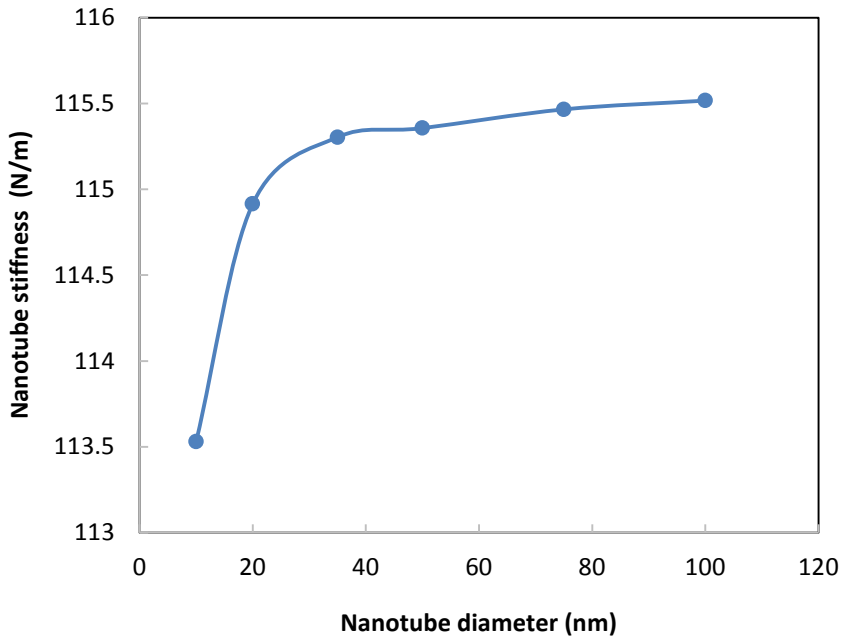

Figure 4.21. Variation of stiffness as a function of nanotube diameter. The nanotube aspect ratio is fixed at 10 with the nanotube diameter being varied.

4.3.2.2 Variation of nanotube Young's modulus with nanotube heights

The effects of nanotube height on stiffness and Young's modulus for a fixed nanotube diameter (d=20 nm) are depicted in Figure 4.22 and Figure 4.23. The stiffness is seen to decrease with the increase of tube height or aspect ratio. The modulus again is seen to remain relatively constant with the increase of tube height or aspect ratio. This again agrees with the equation 4.14 above, wherein with increasing nanotube height and for a constant applied displacement the applied strain decreases with increasing height and hence the stresses decrease linearly while the young's modulus remains relatively constant. The results are plotted for the linear range strains of the nanotubes recorded for strains for up to around 0.8%.

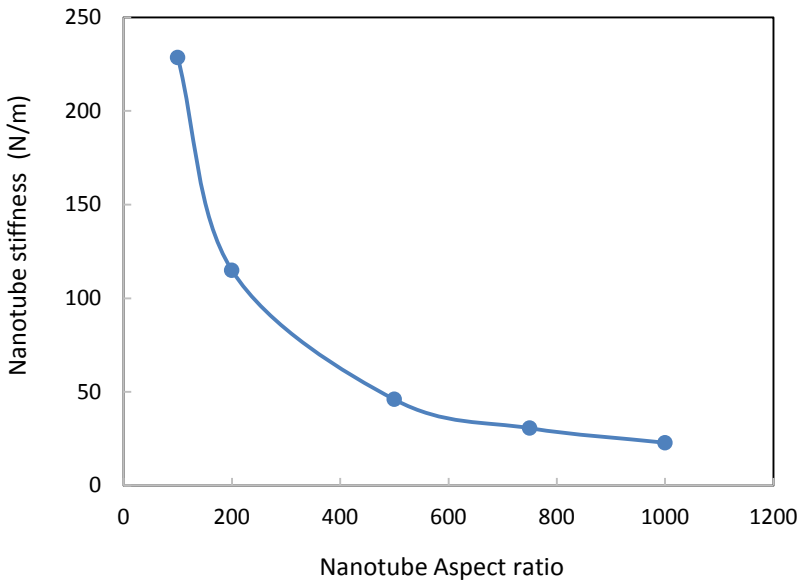

Figure 4.22. Variation of nanotube stiffness as a function of nanotube aspect ratio.

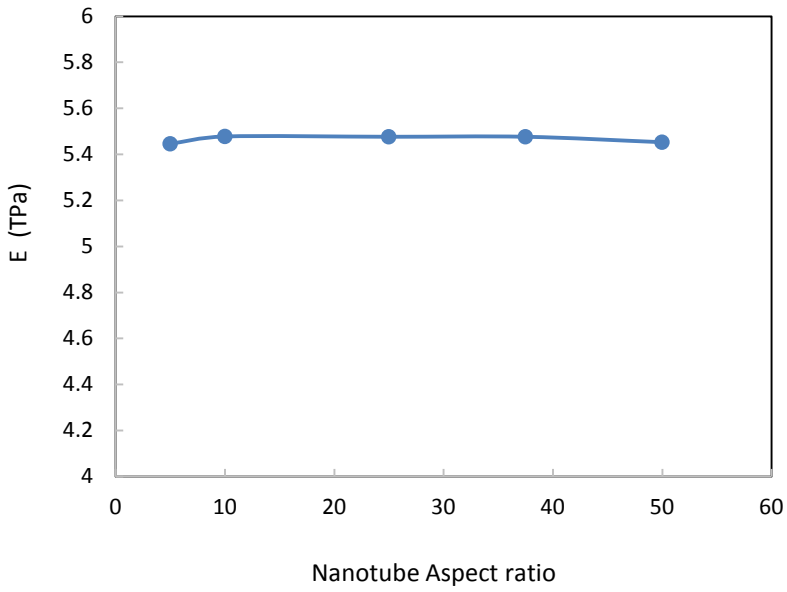

Figure 4.23. Variation of Young's modulus as a function of nanotube aspect ratio.

4.3.3 Modeling of vertically aligned, single-walled carbon nanotube arrays

4.3.3.1 Effect of tube aspect ratio

In this study, the mechanical performances of the VA-CNT structures are evaluated through computational method. Assuming the same geometry and properties, those individual CNTs were arranged in various patterns and densities to construct the aligned carbon nanotube structures. Mainly square and FCC configurations for areal densities ranging from $1X10^{8}$ tubes/cm^2 to $1X10^{10}$ tubes/cm^2. Nanotube of diameter 20 nm and with varying height/aspect ratios from 5 through 50 is considered. Figure 4.24, Figure 4.25, Figure 4.26 and Figure 4.27, Figure 4.28 and Figure 4.29 shows the displacement contour plots and von-mises stress plots for VA-CNT with areal density 1E8tubes/cm^2 and with aspect ratios varying through 5, 10 and 50 for VA-CNT with square configuration. The contour plots shown below correspond to an applied compressive strains of 0.1%. From Figure 4.27 it may be seen that the von-mises stress for VA-CNT with smaller aspect ratio (L/D = 5) is high (1.926e-7 N/nm^2) as compared to that of VA-CNT with higher aspect ratios shown in Figure 4.29 (L/D = 10 and 50) that are slightly lesser (1.018 N/nm^2 and 1.052 N/nm^2) for the same amount of strain indicating greater load carrying capacities for VA-CNTs with short lengths as compared to VA-CNTs that are taller. Hence a decreasing trend is observed in the VA-CNT stiffness with increasing aspect ratio as seen in Figure 4.30.

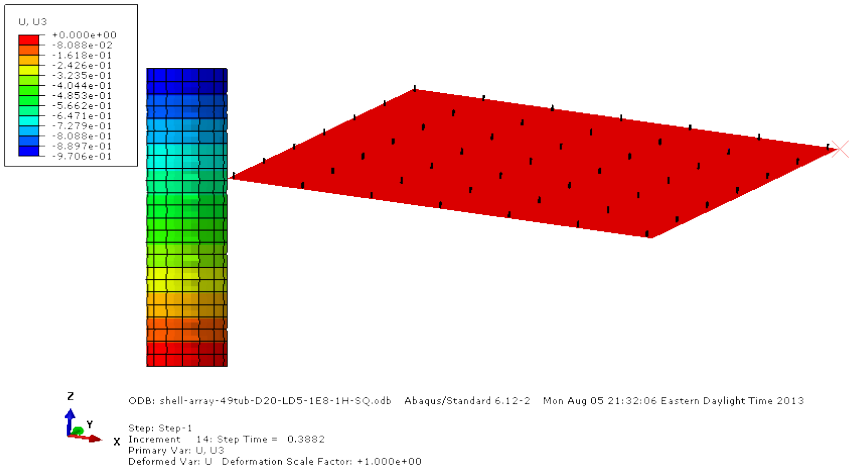

Figure 4.24. Deformation contours of aligned carbon nanotube structure under identical strains for L/D=5.

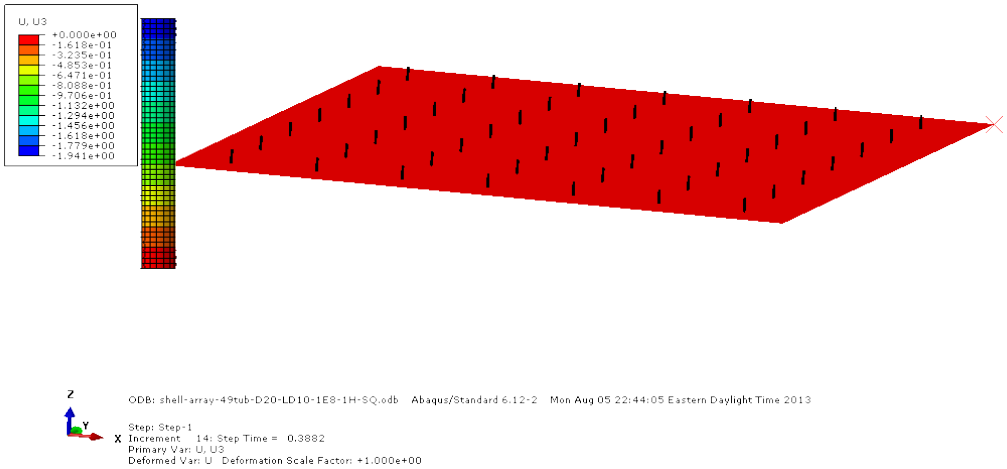

Figure 4.25. Deformation contours of aligned carbon nanotube structure under identical strains for L/D=10.

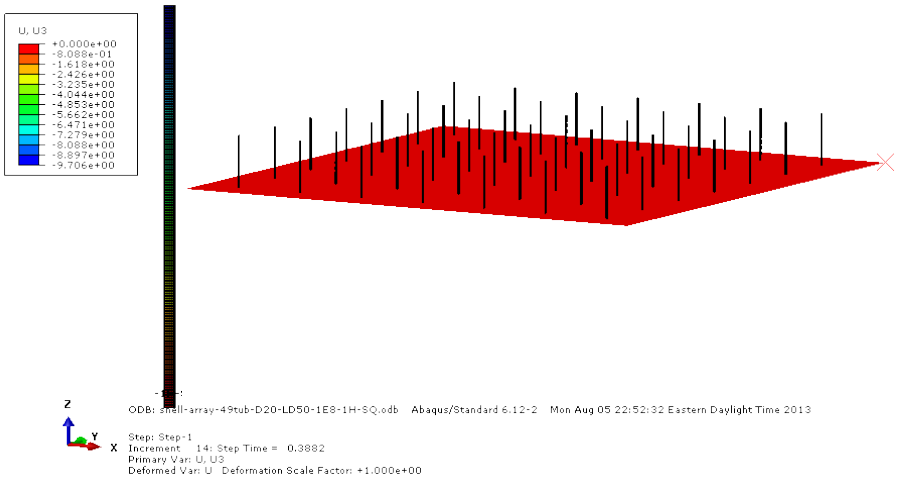

Figure 4.26. Deformation contours of aligned carbon nanotube structure under identical strains for L/D=50.

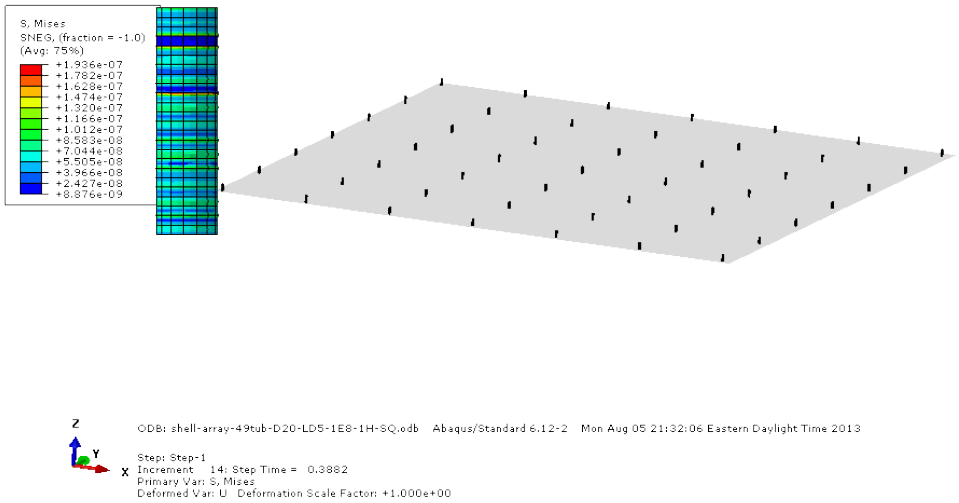

Figure 4.27. Mises stress contours of aligned carbon nanotube structure under compressions for L/D=5.

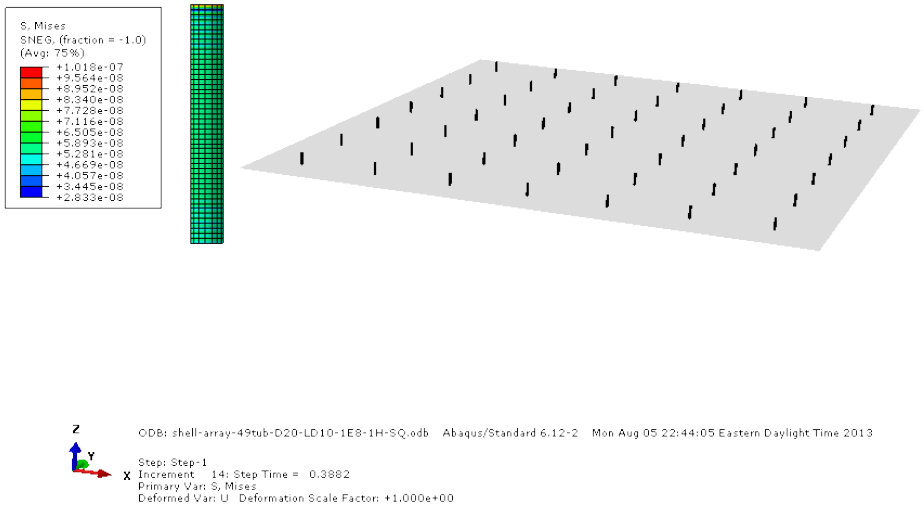

Figure 4.28. Mises stress contours of aligned carbon nanotube structure under compressions for L/D=10.

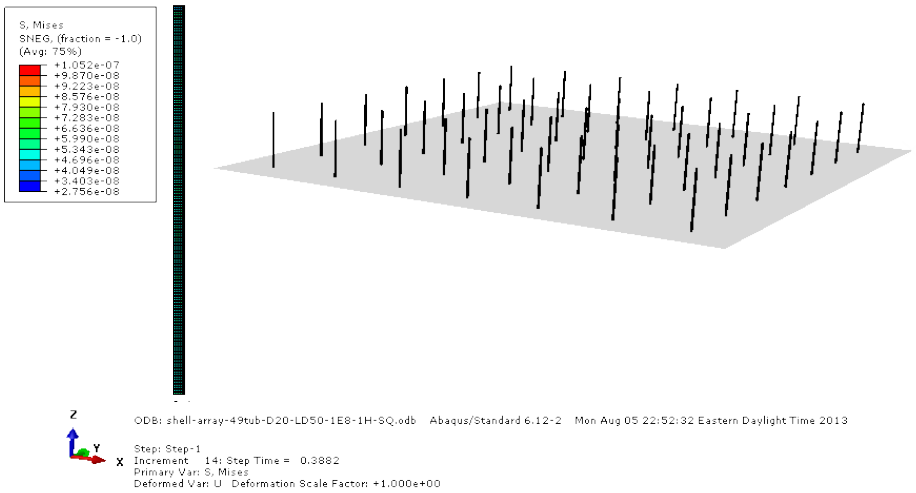

Figure 4.29. Mises stress contours of aligned carbon nanotube structure under compressions for L/D=50.

Figure 4.30 and Figure 4.31 show the stiffness and modulus of the VA-CNT structures at various aspect ratios, L/D=5, 10, 50. The stiffness is seen to decrease with the increase of tube height or aspect ratio, the same trend as seen from individual CNTs. It may be notice d that since the number of tubes is fixed at 49 for the square structure and 50 for the FCC structure, the array stiffness remains the same for all densities while the modulus increase

with density due to reducing array area with increasing density. The modulus again is seen to remain relatively constant with the increase of tube height or aspect ratio.

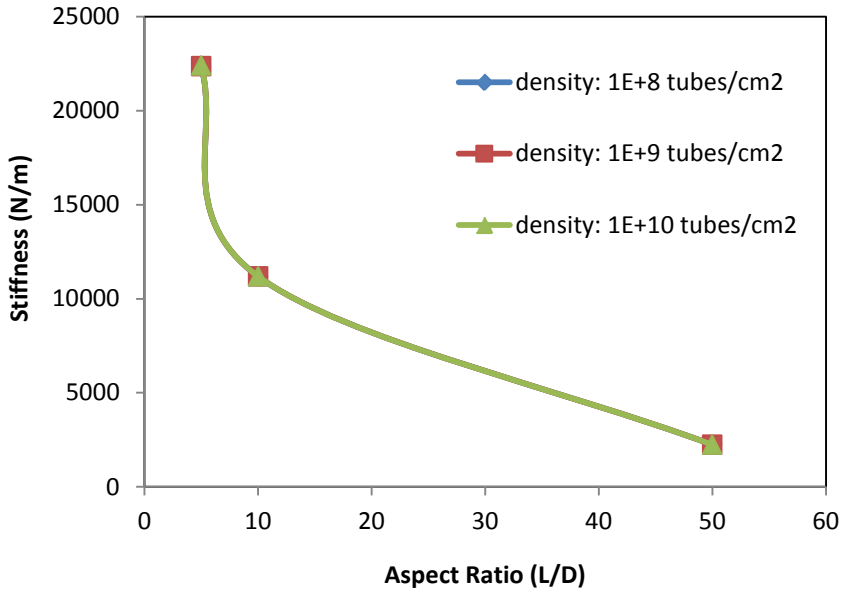

Figure 4.30. Variation of stiffness of VA-CNT structure as a function of nanotube aspect ratio.

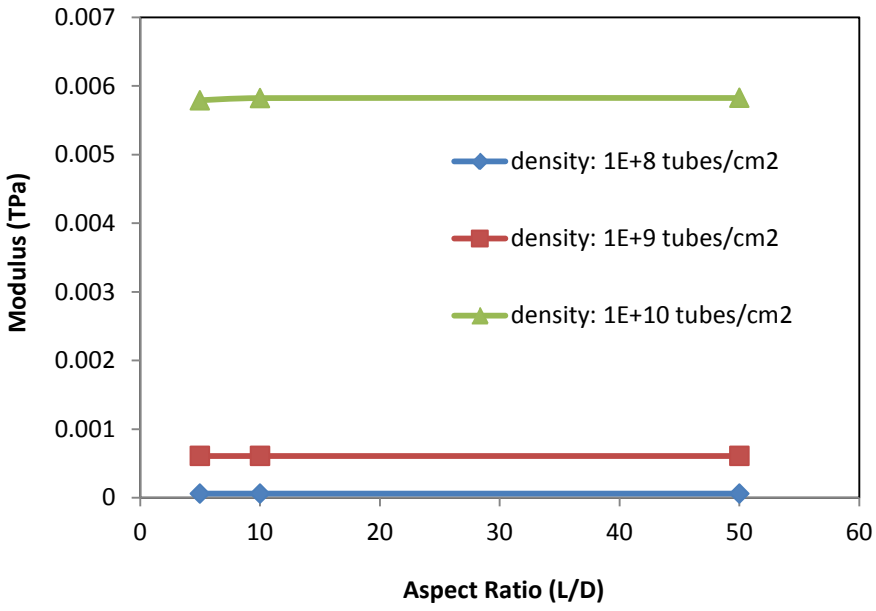

Figure 4.31. Variation of Young's modulus of VA-CNT structure as a function of nanotube aspect ratio.

4.3.3.2 Effect of VACNT array / tube areal density

The VA-CNTs may be conceptually viewed as a complex structure consisting of nominally aligned tubes; between the tubes are unfilled open spaces that have no load-carrying capability. Therefore, the mechanical behaviors of the VA-CNT structure are highly dependent upon the "density" of the nanotube arrays. A more densely packed nanotube array would have more load-carrying capability and fewer geometric freedoms for tube movements. Recent experimental study has shown that there exists a linear relationship between the elastic modulus of the VA-CNT structure and its density. When the density of the VA-CNT array is doubled, the modulus can be increased by 50% (Wardle et al. 2008).

In present study, the VA-CNT structures at various densities were constructed, ranging from $1x10^8$ tubes/cm^2 to $1x10^{10}$ tubes/cm^2. Figures 16 and 17 show the results of these VA-CNT arrays obtained with FE models constructed with fixed number of tubes (50 for FCC and 49 for square)) in a 36 μm^2 for $1x10^8$ tubes/cm^2 to 0.384 μm^2 for $1x10^{10}$ tubes/cm^2 areal density for square configuration array and 0.4μm^2 to 41.3μm^2 for FCC array for densities of $1x10^8$ tubes/cm^2 to $1x10^{10}$ tubes/cm^2 areal density. In each model, it is seen that as the tube density increases, the stiffness remains relatively constant. This is because the overall number of the load-carrying structural members (tubes) remains the same in each array model. However, the modulus is seen to increase linearly with the increase of the array density. The same observations have been seen earlier through the beam modeling for VA-CNT structures.

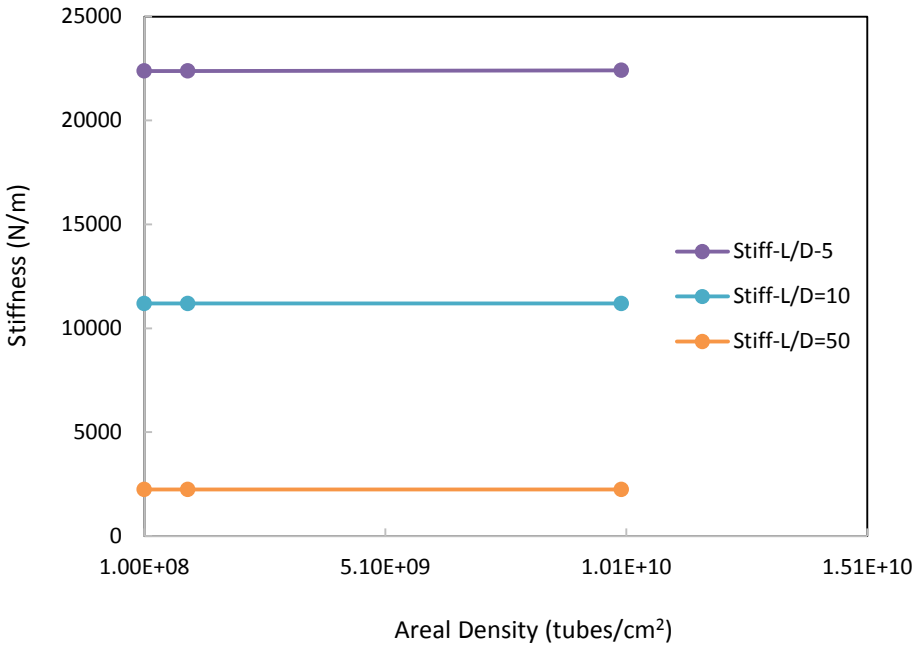

Figure 4.32. Effect of nanotube areal density on stiffness of the square patterned VA-CNT structures.

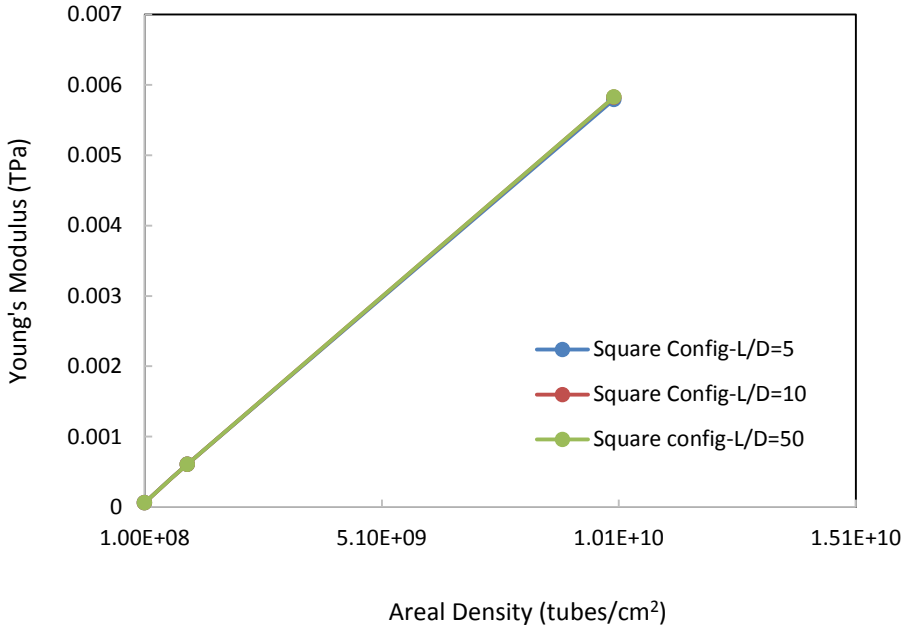

Figure 4.33. Effect of nanotube areal density on modulus of the square patterned VA-CNT structures.

4.3.3.3 Effect of tube / array distribution pattern

Figure 4.34 and Figure 4.35 show the effect of nanotube distribution patterns on mechanical properties of the arrays. In this study, the nanotubes in the arrays were arranged in the configurations of square and face centered cube (FCC). The stiffness of VA-CNT array with FCC configuration is higher than that of Square due to greater number of load carrying members in FCC (50 tubes) than in square configuration (49 tubes). The modulus of the square shaped arrays is slightly higher than that of the FCC shaped one. This trend is also seen in VA-CNT array with beam modeling.

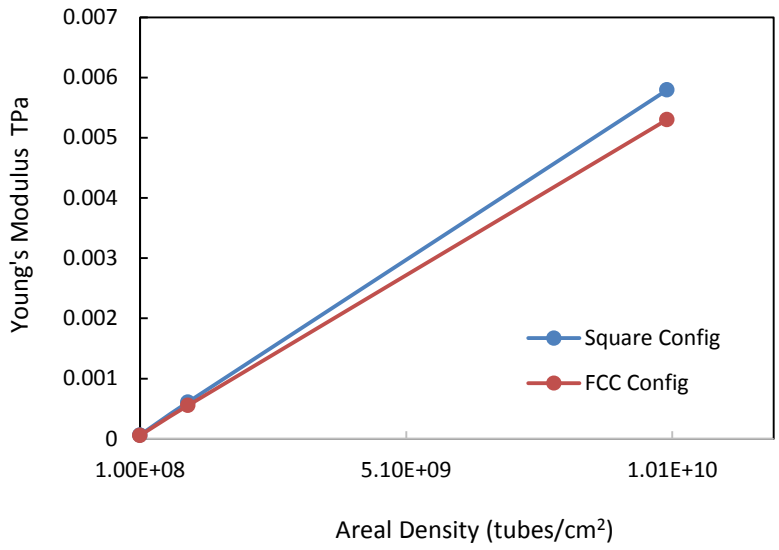

Figure 4.34. Effect of nanotube array configuration on modulus of the VA-CNT structures.

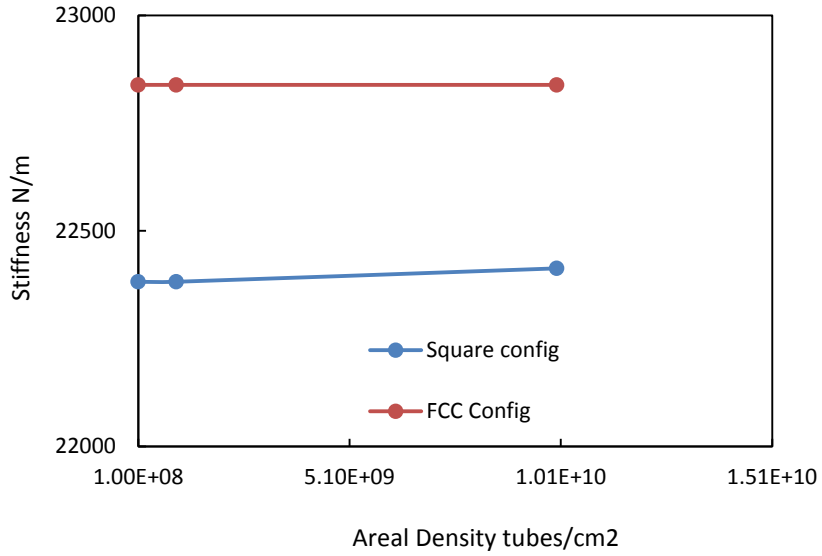

Figure 4.35. Effect of nanotube array configuration on stiffness of the VA-CNT structures.

4.4 Conclusions

The structural shell modeling has been used to design and characterize the individual carbon nanotubes and aligned carbon nanotube arrays. Based on an understanding of carbon nanotubes at the atomic/molecular level, the equivalent shell thickness and modulus in a single walled CNTs were estimated. The geometric parameters of the individual nanotube on its mechanical properties are thoroughly examined. The Young's modulus generally increases at a much steeper rate with diameter for small diameter nanotubes and then becomes stabilized for large diameter nanotubes. Finally, the modulus of the nanotubes is inversely proportional to the tube length. In the aligned nanotube arrays, the modulus is strongly dependent upon the tube areal density. The higher the density, the higher the modulus. In addition, the mechanical performance is also sensitive to the tube pattern in an array. The modulus from a square packed array has a slightly higher than that from a FCC packed one.

Chapter 5

5. Design and Modeling of Aligned Carbon Nanotubes Structures Using Structural Shell Modeling: Multi-walled VA-CNTs

5.1 Introduction

An individual CNT may be visualized a tube structure that is rolled up from a 2-dimensional graphene sheet. The actual wall structure of the tube can be either single layered, the single-walled carbon nanotube (SWCNT), or multi-layered, the multi-walled carbon nanotube (SWCNT). Figure 5.1 and Figure 5.2 show examples of SWCNT and MWCNT obtained from atomic simulation and physical experiment, respectively. The SWNTs are exactly one atom thick while the MWNTs are essentially concentrically nested SWNTs. The walls of individual tubes in a MWCNT only interact through the weak non-bonded van der Waals forces. Since they are not bonded together, the walls remain free to slide and rotate independently with only small resistive forces.

Figure 5.1. Atomic simulation of single walled, double walled and multi walled carbon nanotubes(Shen et al. 2011) .

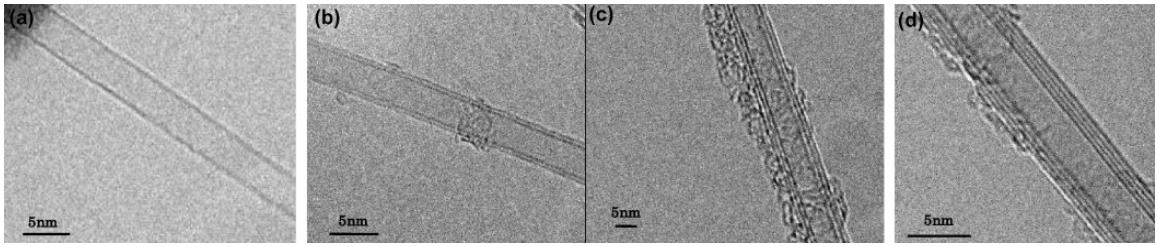

Figure 5.2. TEM images of single walled, double walled and multi walled carbon nanotubes (Hayashia and Endo 2011)

Although discovered first, multi-walled carbon nanotubes (MWNTs) have not been studied as thoroughly as single-walled carbon nanotubes (SWNTs). This could partly be due to the limitations in current atomic computations in a MWNT. It is seen that the solver computational time needed to run a multi-walled nanotube is higher than the time taken for a single-walled nanotube mainly due to huge size of the finite element model. Further, in order to solve the problem involving arrays, huge and expensive computational resources are needed. A 20nm diameter 15 walled MWCNT has an FE model size of 12427 shell elements of second order and 37855 nodes as against an equivalent SWCNT that has 360 shell elements and 1110 nodes array. Hence, in order to keep the computational cost lower and be able to solve the MWCNT, it became essential to reduce the size of the model by way of arriving at an equivalent SWCNT nanotube model that will have identical geometric properties viz. mean nanotube diameter, moment of inertia and cross sectional area . Continuum mechanics techniques have gained great popularity recently due to their abilities to handle larger size carbon nanotube models. The previous chapter has presented the use of discrete beam elements for the aligned carbon nanotubes structures made of single-walled CNTs. In this chapter, we will attempt to use the continuum shell elements to design and model the aligned carbon nanotubes structures made of multi-walled CNTs

5.2 Modeling procedures

5.2.1 Modeling of VACNT array with MWCNT using several shell elements and an equivalent SWCNT

The approach in this work is based on the principle of structural mechanics (finite element method (FEM)). As illustrated in Figure 5.3(a), an aligned carbon nanotubes structure is composed of numerous multi-walled nanotubes that are packed vertically on a flat substrate. Each individual multi-walled carbon nanotube may be thought of as a multi-layered cylinder (Figure 5.3(b)). To effectively and efficiently model the MWCNTs, an equivalent thickness SWCNT nanotube model is arrived at(Figure 5.3(c)),

which would have identical geometric properties viz. mean nanotube diameter, moment of inertia and cross sectional area. The use of equivalent SWCNT would become more efficient especially while solving VACNT arrays.

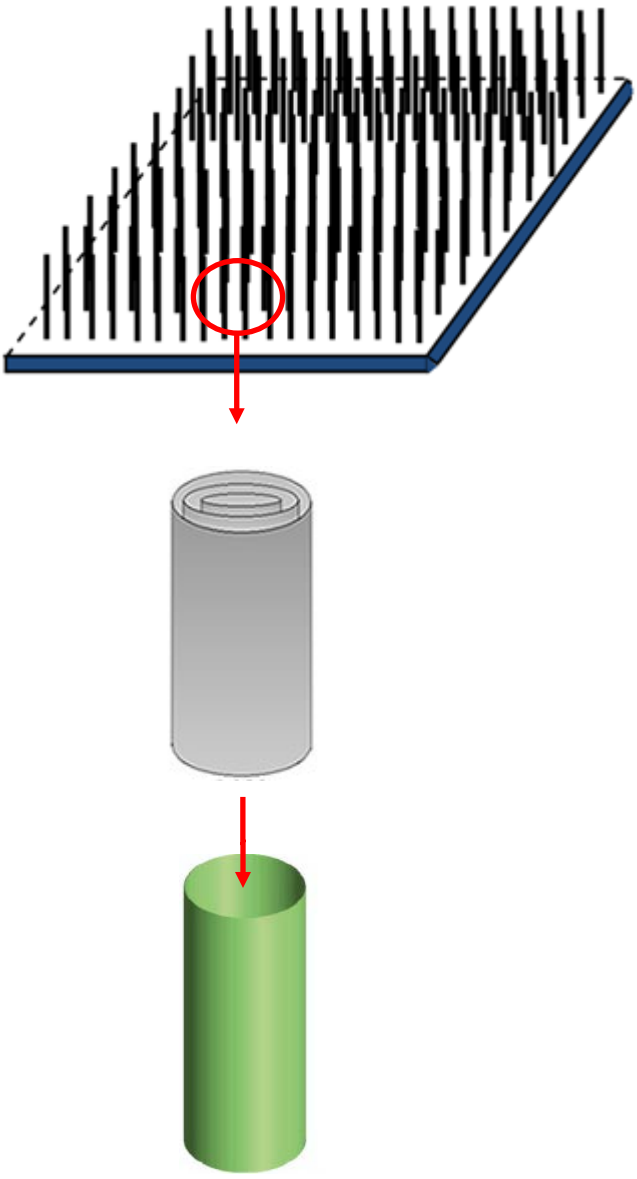

Figure 5.3. (a) A sketch for vertically aligned carbon nanotubes structure (not to scale); (b) A sketch for an individual multi-walled carbon nanotube; and (c) A sketch for the equivalent thickness, single-walled carbon nanotube.

For the MWCNTs, the wall thickness for each of the walls is assumed as 0.067 nm and the inter-wall distance as 0.34 nm. A schematic of a MWCNT with 3 walls showing the geometrical details is as in Figure 5.4(a) below. The outer diameter, inner diameter and wall thickness of the MWCNT are denoted as 'd_o' and 'd_i ', and 't' respectively (Figure 5.4(a)). A MWCNT with 5 walls and its equivalent SWCNT model having identical mean diameter, moment of inertia and cross sectional area of the tubes is as shown in Figure 5.4(b).

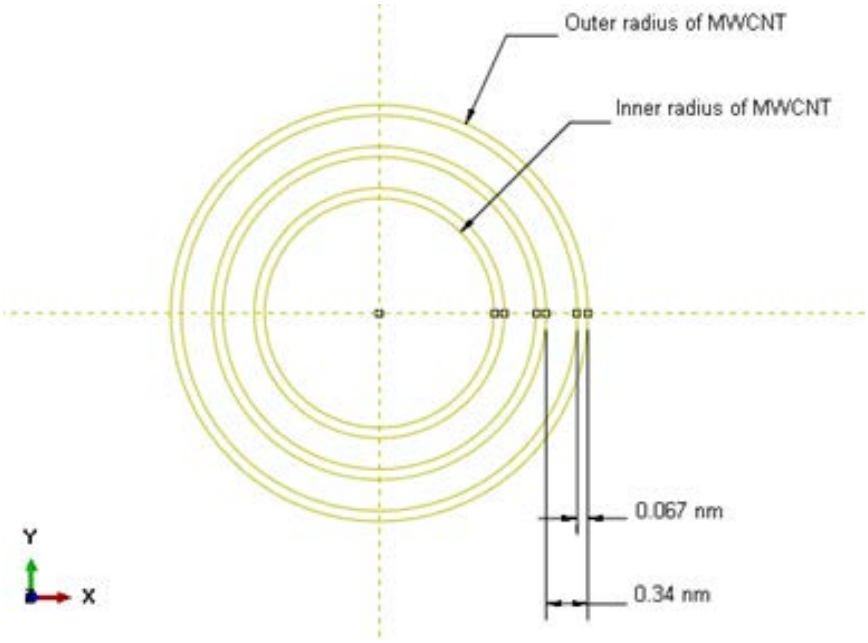

(a)

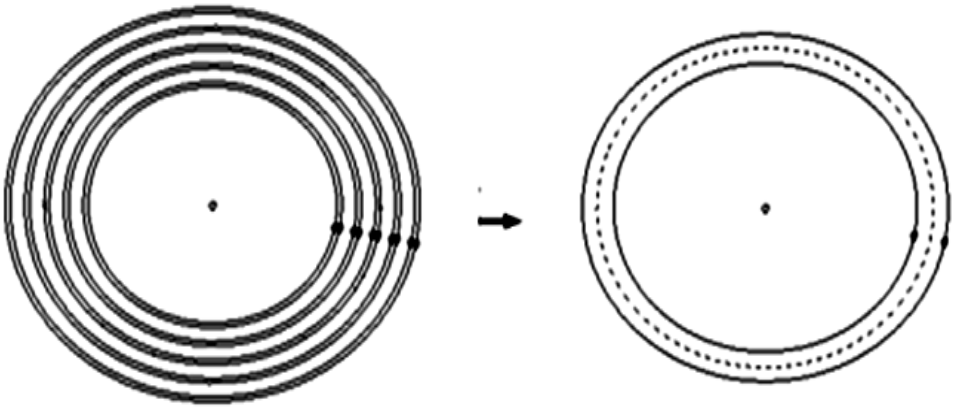

(b)

Figure 5.4. Schematic of a MWCNT and its SWCNT equivalent nanotube.

The geometric properties of the equivalent SWCNT that is identical to the MWCNT is calculated as below.

The total moment of inertia of a MWCNT is given by

$$I_{total} = \sum_{j=1}^{n} i_j \tag{5.1}$$

where $i_j$is the moment of inertia of the j th nanotube.

The total cross-sectional area of the MWCNT is given by

$$A_{total} = \sum_{j=1}^{n} a_j \tag{5.2}$$

where $a_j$is the cross sectional area of the j th nanotube.

Assuming the mean diameter as 'd_{mean}' and thickness as 't_{new}'of the 'to be computed' equivalent SWCNT and keeping the mean diameter, cross sectional area and moment of inertia of the 'to be computed' equivalent SWCNT, identical to the mean diameter, cross sectional area and moment of inertia of the MWCNT, the thickness 't_{new}' of the equivalent SWCNT is computed using I_{total} and A_{total} of MWCNT as below.

Moment of inertia of the equivalent SWCNT nanotube is given by

$$I_{new} = I_{total} = \frac{\pi}{64} \{(d_{mean} + t_{new})^4 + (d_{mean} - t_{new})^4 \} \tag{5.3}$$

Cross sectional area of the equivalent SWCNT nanotube is given by

$$A_{new} = A_{total} = \pi * d_{mean} * t_{new} \tag{5.4}$$

And with $(d_{mean})_{\text{MWCNT}} = (d_{mean})_{\text{EQ. SWCNT}}$ results in value of the thickness, t_{new}.for the equivalent SWCNT.

Table 5.1 below shows the mean diameter value for each of the walls of MWCNT for MWCNT with 2 and 5 walls for nanotube diameters of 10nm through 100nm in increments of 10 nm. The wall thickness for each of the wall is 0.067nm with an interwall spacing of 0.34nm.

Table 5.1.Mean diameter for each wall of MWCNT

Outer Dia. (nm)	Number of walls						
	2		5				
	Mean Dia. of wall(nm)		Mean Dia. of wall(nm)				
	D1	D2	D1	D2	D3	D4	D5
10	9.9	9.3	9.9	9.3	8.6	7.9	7.2
20	19.9	19.3	19.9	19.3	18.6	17.9	17.2
30	29.9	29.3	29.9	29.3	28.6	27.9	27.2
40	39.9	39.3	39.9	39.3	38.6	37.9	37.2
50	49.9	49.3	49.9	49.3	48.6	47.9	47.2
60	59.9	59.3	59.9	59.3	58.6	57.9	57.2
70	69.9	69.3	69.9	69.3	68.6	67.9	67.2
80	79.9	79.3	79.9	79.3	78.6	77.9	77.2
90	89.9	89.3	89.9	89.3	88.6	87.9	87.2
100	99.9	99.3	99.9	99.3	98.6	97.9	97.2

Table 5.2 below shows the inner diameter, overall mean diameter 'd_{mean}' and moment of inertia of the multi-walled carbon nanotubes for 1, 2, 5, 10 and 15 walls.

Table 5.2. Geometric properties of the multi-walled carbon nanotubes (MWCNTs).

Number of walls									
1				2			5		
Outer Dia. (nm)	Inner Dia. (nm)	Mean Dia. (nm)	Moment (nm^4)	Inner Dia. (nm)	Mean Dia. (nm)	Moment (nm^4)	Inner Dia. (nm)	Mean Dia. (nm)	Moment (nm^4)
10	9.9	9.9	25.8	9.2	9.6	46.6	7.1	8.6	86.0
20	19.9	19.9	208.4	19.2	19.6	396.2	17.1	18.6	849.6
30	29.9	29.9	705.6	29.2	29.6	1364.3	27.1	28.6	3079.3
40	39.9	39.9	1675.5	39.2	39.6	3266.8	37.1	38.6	7564.2
50	49.9	49.9	3275.7	49.2	49.6	6419.3	47.1	48.6	15093.9
60	59.9	59.9	5664.1	59.2	59.6	11137.6	57.1	58.6	26457.5
70	69.9	69.9	8998.7	69.2	69.6	17737.5	67.1	68.6	42444.4
80	79.9	79.9	13437.3	79.2	79.6	26534.7	77.1	78.6	63844.0
90	89.9	89.9	19137.8	89.2	89.6	37844.8	87.1	88.6	91445.5
100	99.9	99.9	26258.0	99.2	99.6	51983.6	97.1	98.6	126038.4

Number of walls						
10				15		
Outer Dia. (nm)	Inner Dia. (nm)	Mean Dia. (nm)	Moment (nm^4)	Inner Dia. (nm)	Mean Dia. (nm)	Moment (nm^4)
10	3.7	6.9	106.1	0.3	5.2	107.5
20	13.7	16.9	1314.7	10.3	15.2	1533.7
30	23.7	26.9	5187.0	20.3	25.2	6552.8
40	33.7	36.9	13301.5	30.3	35.2	17532.8
50	43.7	46.9	27237.1	40.3	45.2	36841.7
60	53.7	56.9	48572.2	50.3	55.2	66847.5
70	63.7	66.9	78885.6	60.3	65.2	109918.1
80	73.7	76.9	119755.9	70.3	75.2	168421.5
90	83.7	86.9	172761.7	80.3	85.2	244725.6
100	93.7	96.9	239481.8	90.3	95.2	341198.6

Table 5.3 below shows the equivalent thickness' t_{new}' ,mean diameter 'd_{mean}' moment of inertia and cross sectional area for equivalent single-walled carbon nanotubes for nanotube diameters of 10nm through 100nm in increments of 10nm.

Table 5.3. Geometric properties of the equivalent single-walled carbon nanotubes (SWCNTs).

	Number of walls							
	1				2			
Outer Dia.	t_{new}	D_{mean}	I_{new}	A_{new}	t_{new}	D_{mean}	I_{new}	A_{new}
(nm)	nm	nm	nm^4	nm^2	nm	nm	nm^4	nm^2
10	0.07	9.93	25.79	2.09	0.13	9.61	46.60	4.04
20	0.07	19.93	208.38	4.20	0.13	19.59	395.81	8.25
30	0.07	29.93	705.65	6.30	0.13	29.44	1349.63	12.46
40	0.07	39.93	1675.45	8.41	0.13	39.59	3266.07	16.67
50	0.07	49.93	3275.66	10.51	0.13	49.59	6418.43	20.88
60	0.07	59.93	5664.13	12.62	0.13	59.59	11136.60	25.09
70	0.07	69.93	8998.74	14.72	0.13	69.59	17736.30	29.30
80	0.07	79.93	13437.34	16.82	0.13	79.59	26533.26	33.51
90	0.07	89.93	19137.81	18.93	0.13	89.59	37843.20	37.72
100	0.07	99.93	26258.00	21.03	0.13	99.59	51981.87	41.93

	Number of walls							
	5				10			
Outer Dia.	t_{new}	D_{mean}	I_{new}	A_{new}	t_{new}	D_{mean}	I_{new}	A_{new}
(nm)	nm	nm	nm^4	nm^2	nm	nm	nm^4	nm^2
10	0.33	8.73	86.01	9.02	0.60	7.64	106.12	14.47
20	0.33	18.65	849.70	19.55	0.66	17.20	1314.73	35.52
30	0.33	28.62	3078.43	30.07	0.67	27.08	5186.23	56.56
40	0.33	38.61	7564.25	40.60	0.67	37.02	13301.74	77.61
50	0.33	48.60	15094.85	51.12	0.67	46.99	27239.39	98.66
60	0.33	58.59	26452.74	61.64	0.67	56.97	48566.88	119.71
70	0.33	68.59	42445.71	72.17	0.67	66.95	78880.24	140.76
80	0.33	78.60	63854.56	82.69	0.67	76.94	119747.72	161.81
90	0.33	88.60	91469.07	93.22	0.67	86.94	172768.02	182.86
100	0.34	98.57	126003.80	103.74	0.67	96.93	239487.24	203.90

Table 5.3 (Continued)

	Number of walls			
	15			
Outer Dia. (nm)	t_{new} nm	D_{mean} nm	I_{new} nm^4	A_{new} nm^2
10	0.72	7.22	107.50	16.33
20	0.95	15.98	1533.80	47.91
30	0.99	25.66	6552.78	79.48
40	1.00	35.53	17533.99	111.05
50	1.00	45.45	36843.47	142.62
60	1.00	55.40	66849.51	174.20
70	1.00	65.36	109911.00	205.77
80	1.00	75.34	168419.36	237.34
90	1.00	85.32	244715.98	268.92
100	1.00	95.31	341213.49	300.49

Individual multi-walled carbon nanotubes were first modeled in the forms of (1) multi-layer walls and (2) single-layer equivalent SWCNT. Quadratic (S4R) formulation shell elements were used in the analyses. The nanotubes were subjected to compressive loading by way of imposing displacements at the free ends and with the other ends of the nanotubes constrained in all the degrees of freedom. Figure 5.5 below shows the multi-walled carbon nanotube models with 1, 2, 5, 10 and 15 walls.

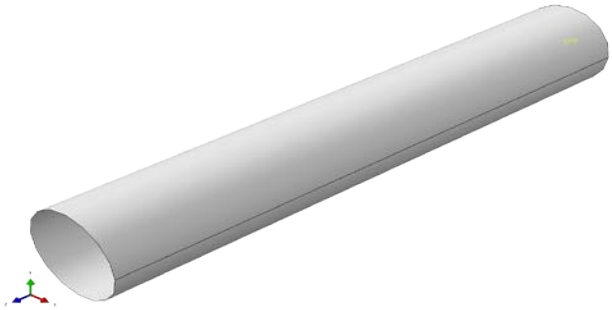

(a)

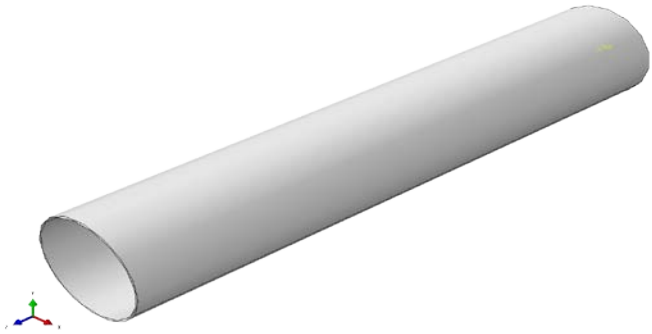

(b)

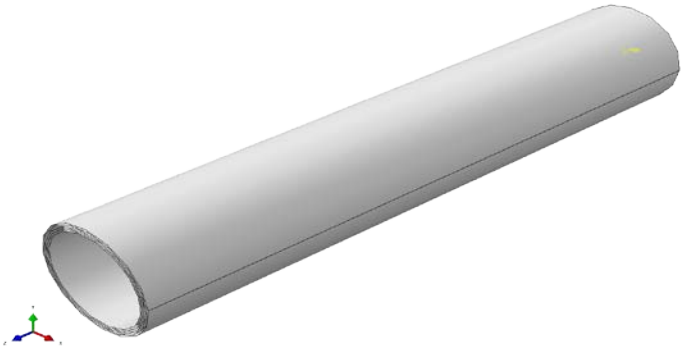

(c)

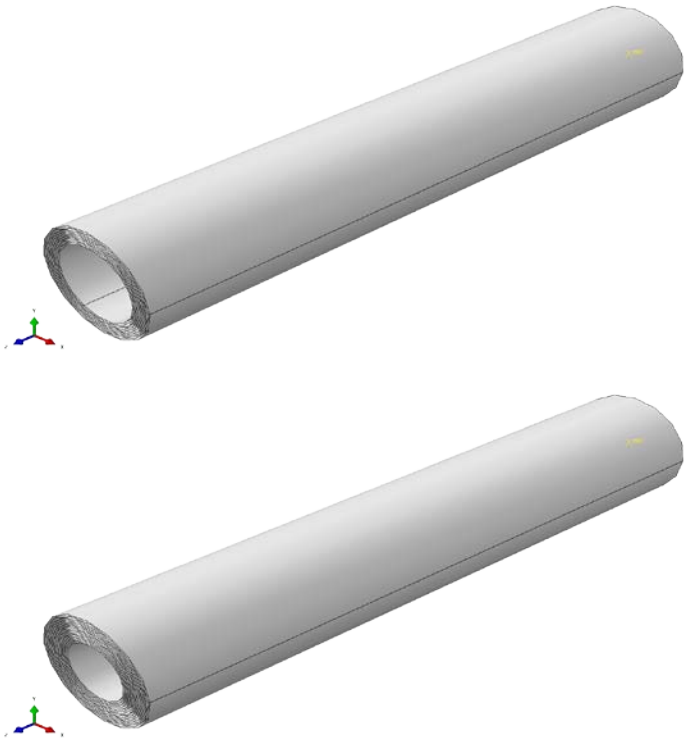

Figure 5.5. Individual multi-walled carbon nanotube : (a) 1-walled CNT, (b) 2-walled CNT, (c) 5-walled CNT, (d) 10-walled CNT, and (e) 15-walled CNT.

Secondly, the aligned carbon nanotubes (VA-CNT) structures made of individual multi-walled nanotubes were modeled by using the calculated equivalent SWCNT having single wall. The VA-CNT arrays with a dimension of 2020 nm x 2020 nm (4.13μm^2.) were constructed. The numbers of nanotubes in the arrays were varied from 9 to 4096 for square configuration and 8 to 4141 for FCC configuration, constructed with areal densities ranging from 1x10^8 tubes/cm^2 to 1x10^{11} tubes/cm^2. Hence the number of tubes were different for different areal densities for a given area. i.e., the number of tubes increased as the areal density increased as shown in the plot in Figure 5.6 below.

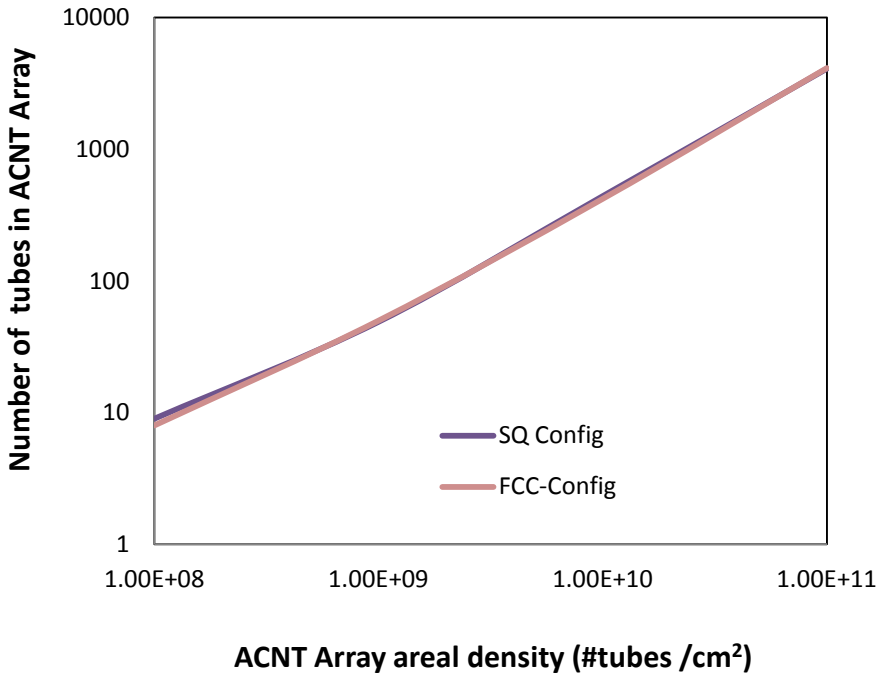

Figure 5.6. Variation of VACNT array area with areal density - Fixed area.

For modeling and analysis, identical VA-CNT array area was constructed for both FCC and Square configuration for various densities. Figure 5.7 through Figure 5.10 below shows the VA-CNT array modeled for square configuration for different areal densities. The VA-CNT array layout design for square and FCC configurations is the same as discussed in chapter 4.

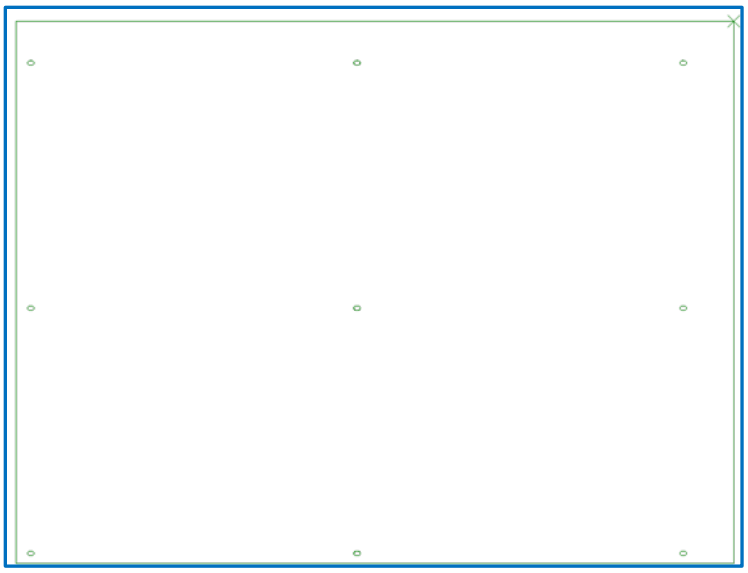

Figure 5.7. VA-CNT array with 9 tubes at an areal density of $1x10^8$ tubes/cm^2 for a fixed array area and square configuration

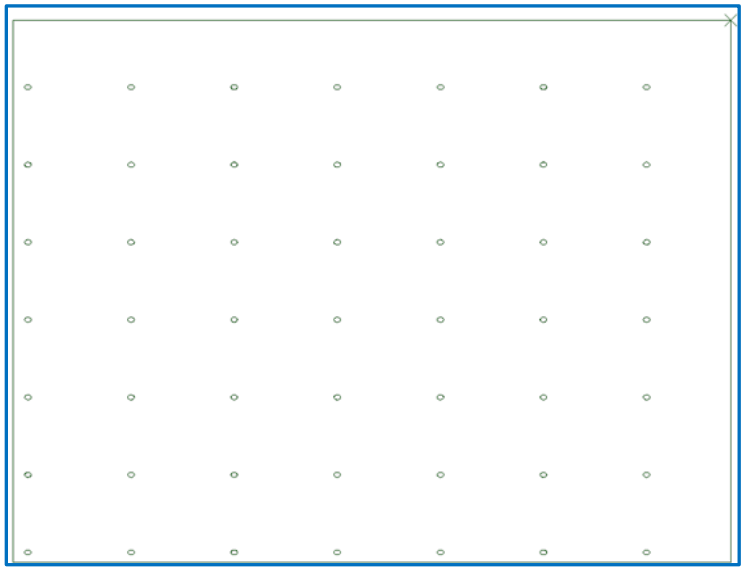

Figure 5.8. VA-CNT array with 49 tubes at an areal density of $1x10^9$ tubes/cm^2 for a fixed array area and square configuration

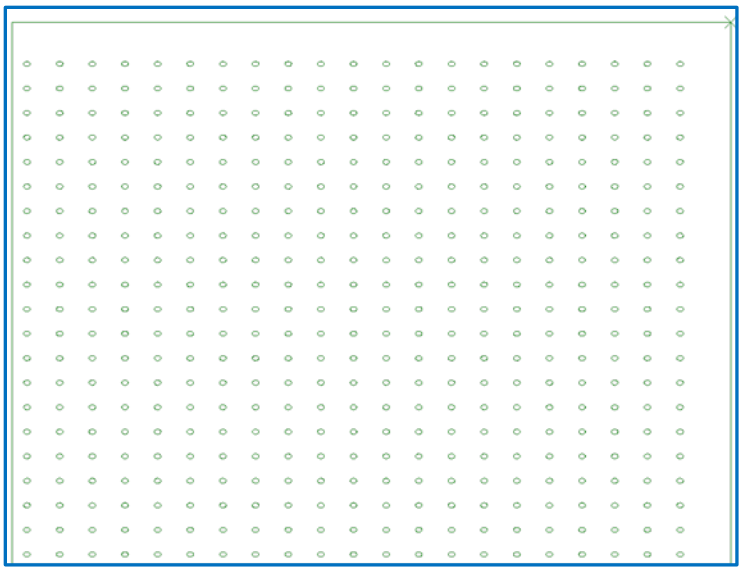

Figure 5.9. VA-CNT array with 441 tubes at an areal density of $1x10^{10}$ tubes/cm^2 for a fixed array area and square configuration

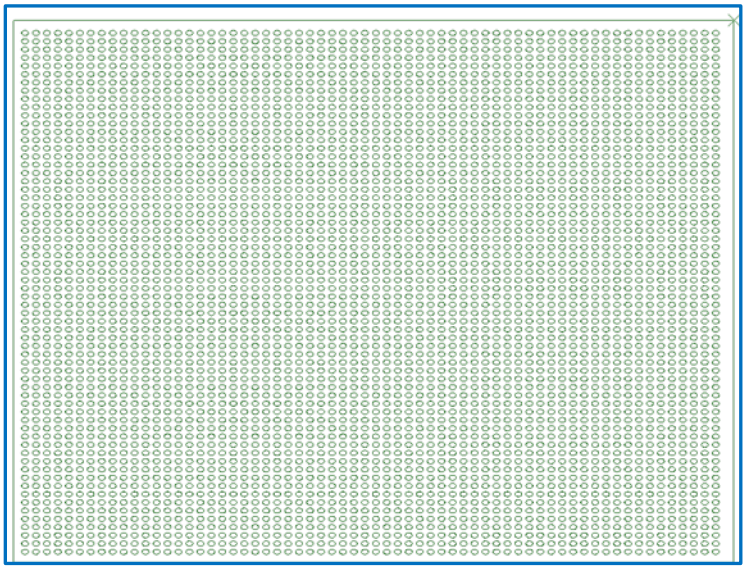

Figure 5.10. VA-CNT array with 4096 tubes at an areal density of $1x10^{11}$ tubes/cm^2 for a fixed array area and square configuration

VA-CNT arrays were modeled for a fixed area of the array for densities of $1x10^8$ tubes/cm^2, $1\ x10^9$ tubes/cm^2, $1\ x10^{10}$ tubes/cm^2, $1\ x10^{11}$ tubes/cm^2. The diameter of the nanotube was chosen as 20 nm and the length was varied. The resultant length/diameter aspect ratios are 5 to 50. The distributions of the nanotubes in the arrays were arranged in square and face-centered cube (FCC) modes. To conduct compression experiments, the compression heads (as represented by analytical rigid surfaces) were subjected to various displacements in the downward direction. The bottom ends of the nanotubes were constrained in all directions to simulate the fixity of the nanotubes to the substrate material. Suitable contact interactions were defined between the nanotube top surfaces and the compression head surfaces with an assumed coefficient of friction of 0.1. FE models constructed for the vertically aligned carbon nanotubes structures are shown in Figure 5.11 below.

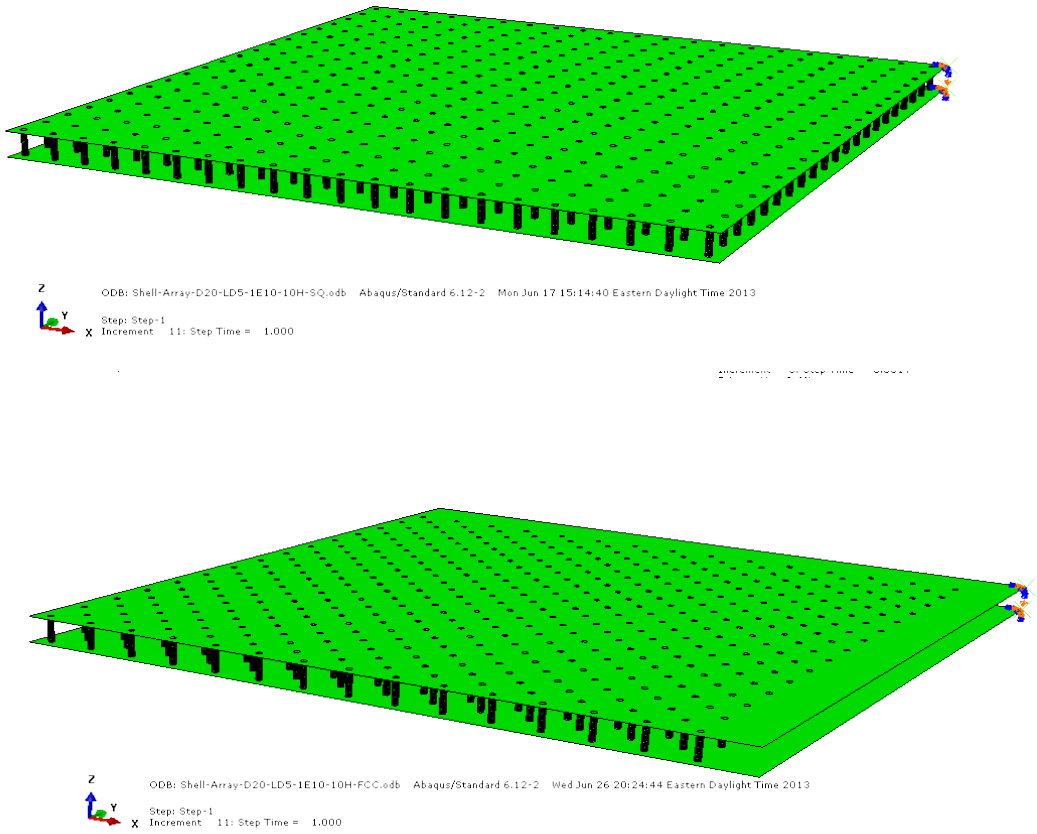

Figure 5.11. FE models showing the aligned carbon nanotube arrays made of multi-walled CNTs: (a) Square configuration and (b) FCC Configurations.

5.3 Results and discussion

5.3.1 Comparisons of multi-walled approach and equivalent thickness single-walled approach

The multi-walled carbon nanotubes have been modeled as multi-walled structures and also as equivalent thickness single-walled structure. Figure 5.12 through Figure 5.16 show the deformation contours of these CNTs under compression. It is seen that both methods have predicted identical results.

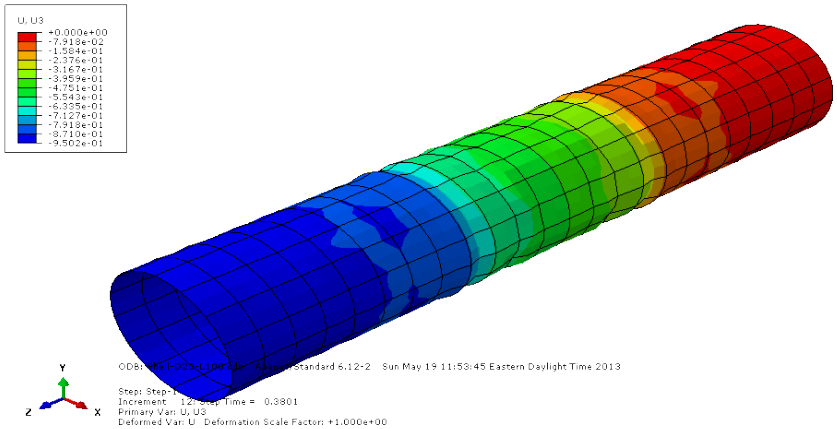

Figure 5.12. Deformation contours of 1-walled carbon nanotube structure under compressions.

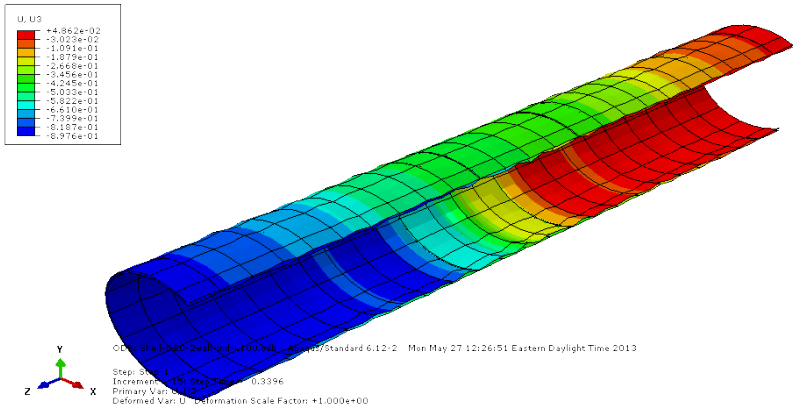

(1)

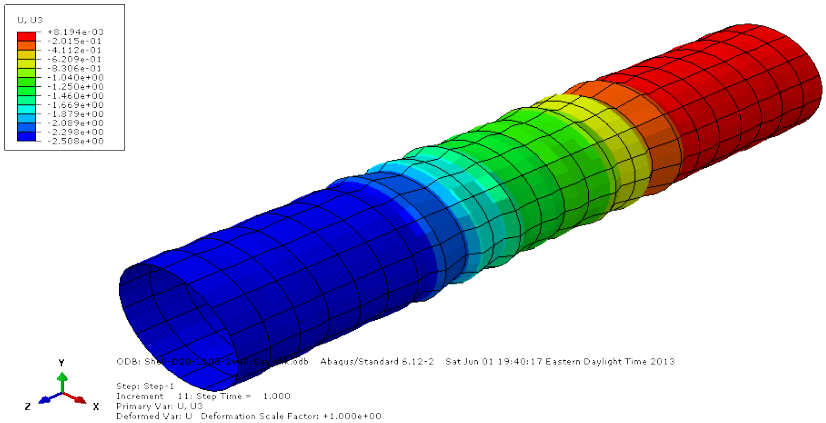

(2)

Figure 5.13. Deformation contours of 2-walled carbon nanotube structure under compressions. (1) multiple walls and (2) equivalent thickness single wall.

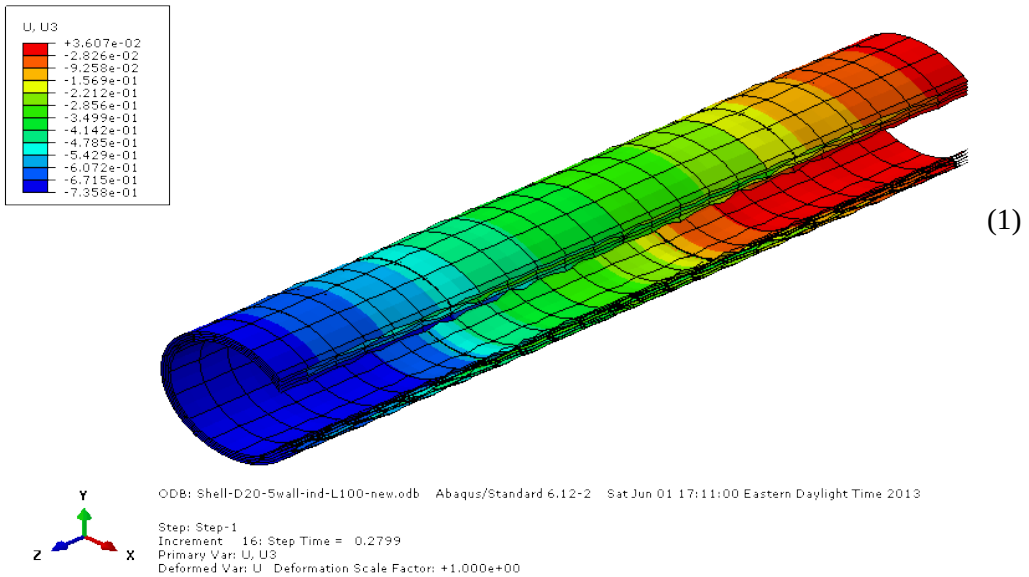

(1)

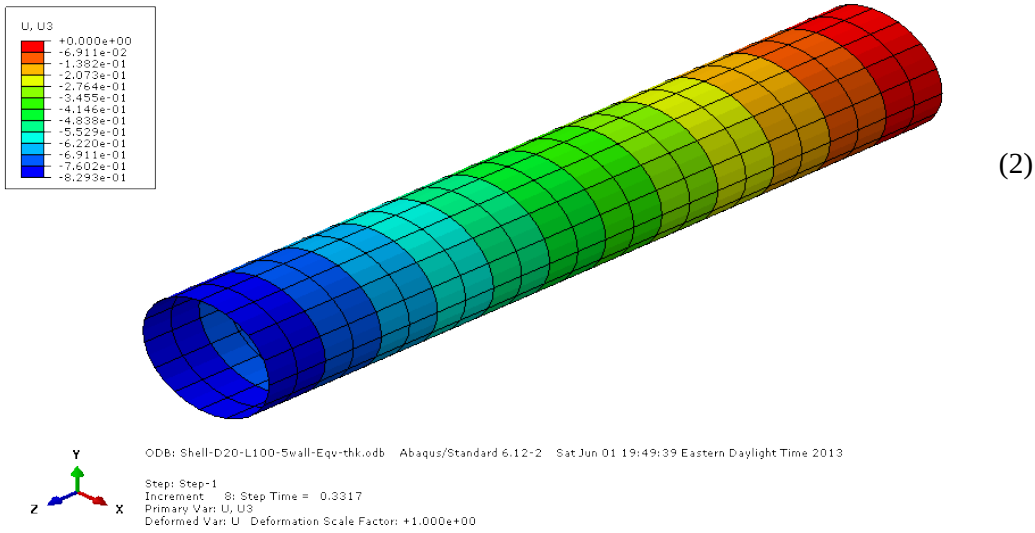

(2)

Figure 5.14. Deformation contours of 5-walled carbon nanotube structure under compressions. (1) multiple walls and (2) equivalent thickness single wall.

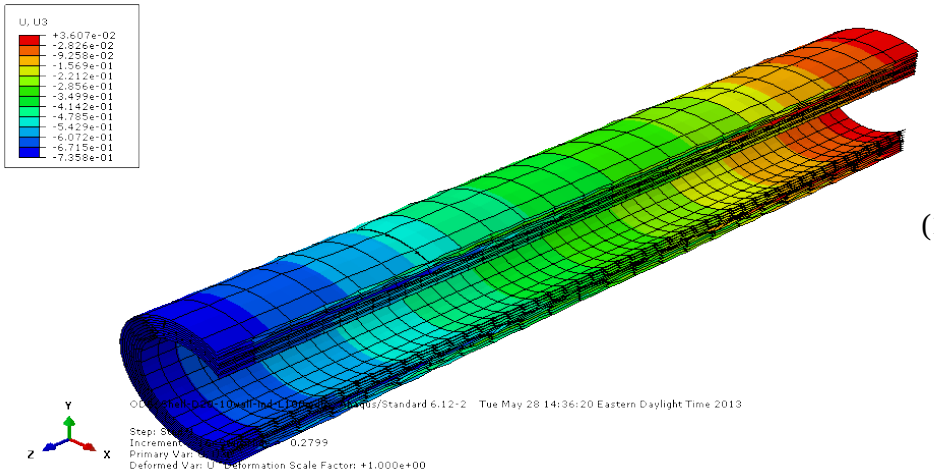

(1)

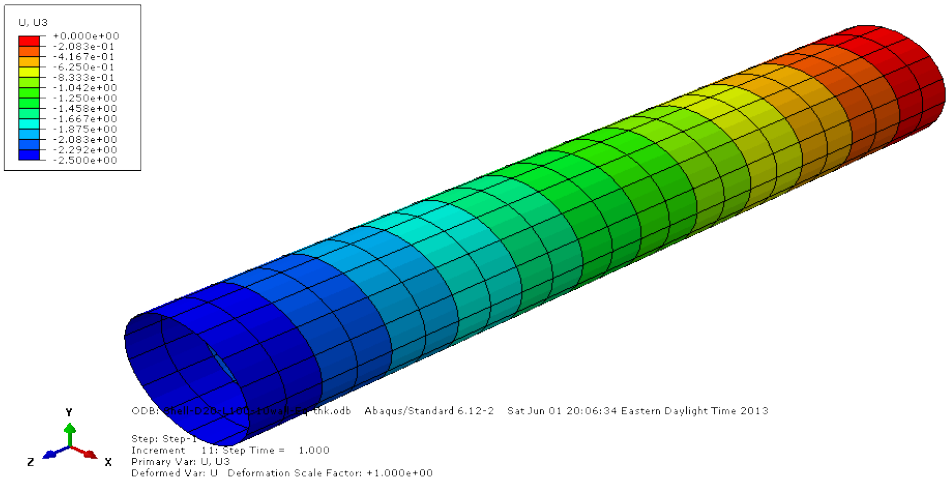

(2)

Figure 5.15. Deformation contours of 10-walled carbon nanotube structure under compressions. (1) multiple walls and (2) equivalent thickness single wall.

.

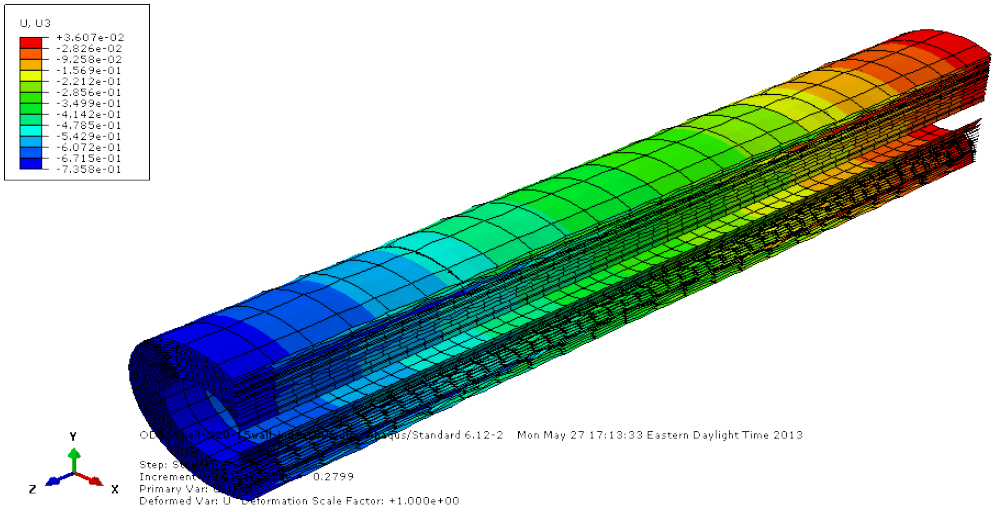

(1)

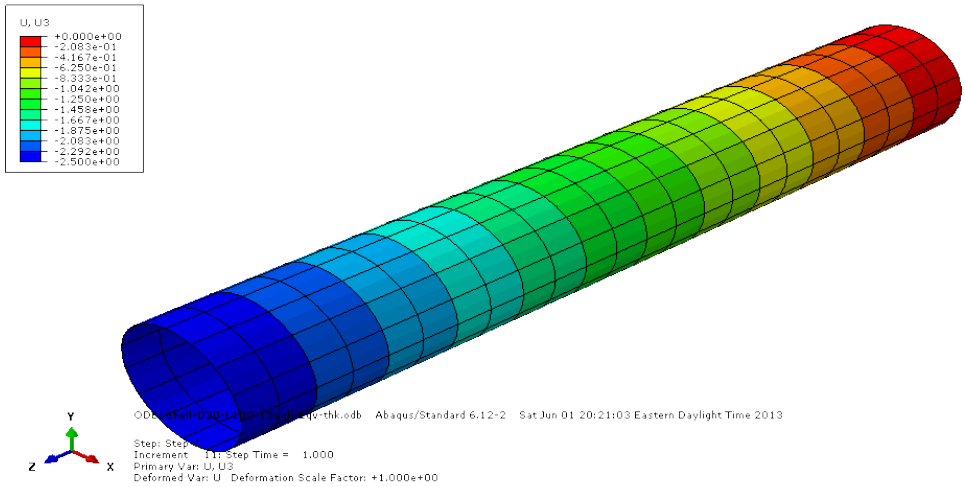

(2)

Figure 5.16. Deformation contours of 15-walled carbon nanotube structure under compressions. (1) multiple walls and (2) equivalent thickness single wall.

Figure 5.17 and Figure 5.18 show the mechanical properties of the multi-walled, individual carbon nanotubes modeled with the two different methods. It is seen that the results (stiffness and modulus) obtained from the two methods are identical, indicating

that the equivalent thickness approach have the same accuracy as the multiple wall approach and yet is much more efficient in terms of computational efforts (model construction, computational time, etc.). From the same plots, it can also be inferred that the number of walls in a nanotube has a significant effect on the mechanical properties. As the number of walls increases, the stiffness and modulus of the nanotube increase linearly.

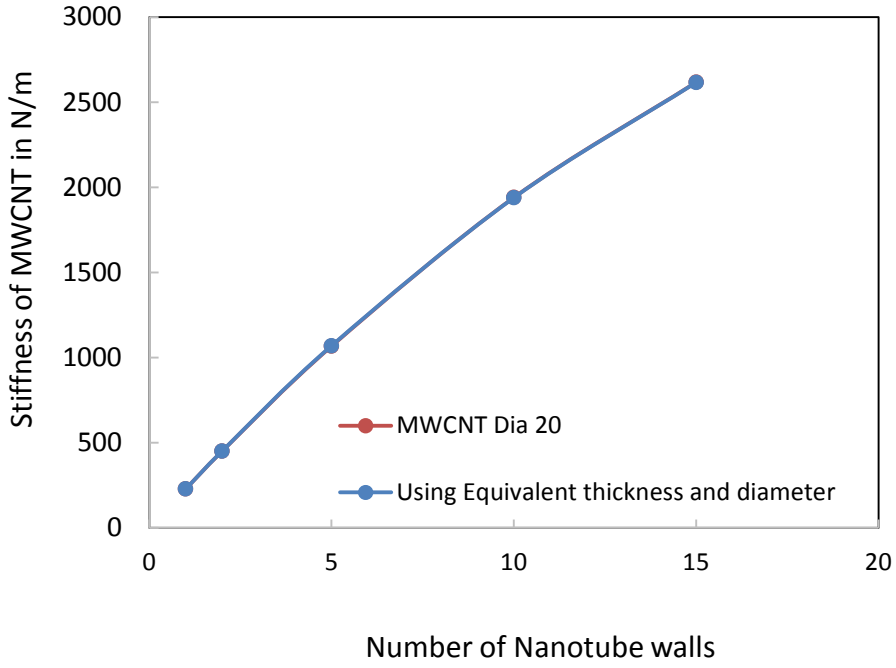

Figure 5.17. Comparison of multiple wall method and equivalent thickness method based on the modeling of individual CNT: stiffness results.

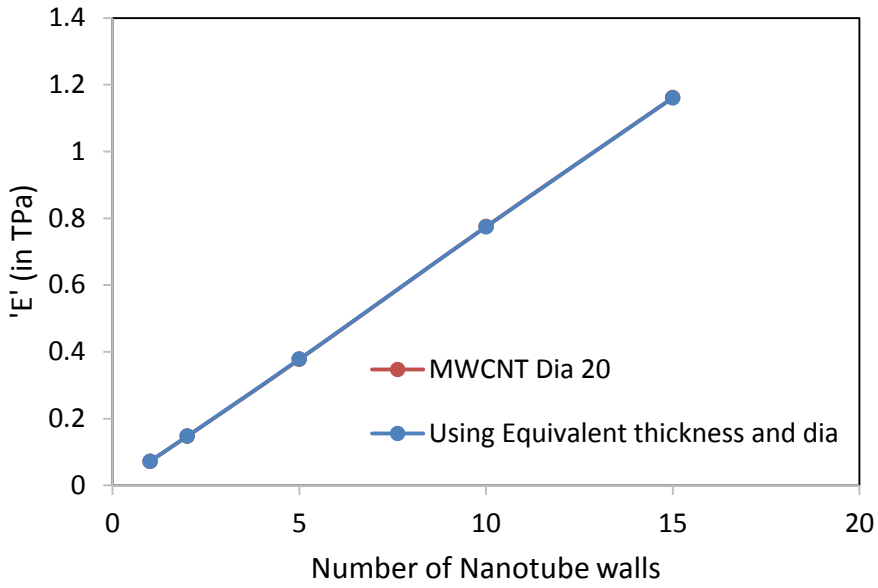

Figure 5.18. Comparison of multiple wall method and equivalent thickness method based on the modeling of individual CNT: modulus results.

5.3.2 Modeling of vertically aligned, multi-walled carbon nanotube arrays

5.3.2.1 Effect of number of walls and VACNT array / tube areal density

The aligned carbon nanotube arrays made of multi-walled nanotube using equivalent thickness have been modeled, and the results are depicted in Figure 5.19 and Figure 5.20. It is seen that as the number of walls increases, both the stiffness and modulus of the structures have increased. This is because the VA-CNT structures are constructed for a fixed area for different areal densities hence the number of tubes increases with increasing densities for a given area. Since the number of load carrying members are increasing the stiffness of the structure increases unlike in previous cases-i.e. fixed number of tubes case where the stiffness remains constant .Also, the Young's modulus increases with increasing densities which is the same as seen in Fixed number of tubes cases in Chapters 3 and 4. Both stiffness and modulus further increase with increase in number of walls as also seen in previous section.

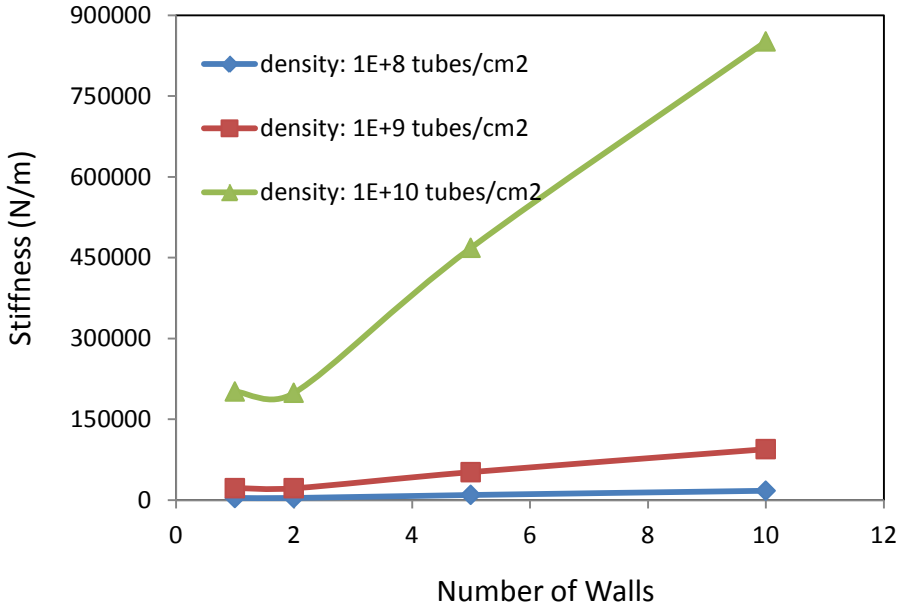

Figure 5.19. Effect of number of walls on stiffness of the VA-CNT structures.

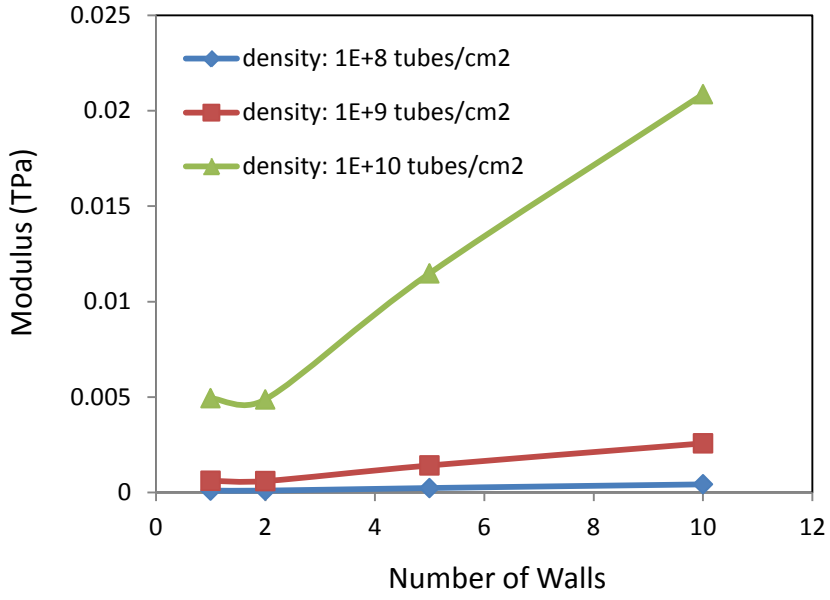

Figure 5.20. Effect of number of walls on modulus of the VA-CNT structures.

5.3.2.2 Effect of tube distribution pattern

Figure 5.21 and Figure 5.22 below show the effect of nanotube distribution patterns on mechanical properties of the arrays. In this study, the nanotubes in the arrays were arranged in the configurations of square and face centered cube (FCC) as earlier. The stiffness and modulus of the VA-CNT array display increasing trend with increasing array areal densities. The stiffness of VA-CNT array with square configuration leads that of FCC configuration in proportion to the number of load carrying members. The number of tubes in square configuration is 9, 49, 441 and 4096 and 8, 50, 421 and 4141 for FCC configuration for array densities $1x10^{8}$ tubes/cm^2, $1x10^{9}$ tubes/cm^2, $1x10^{10}$ tubes/cm^2, $1x10^{11}$ tubes/cm^2 for a fixed area. These trends have also been observed in VA-CNT array with beam modeling.

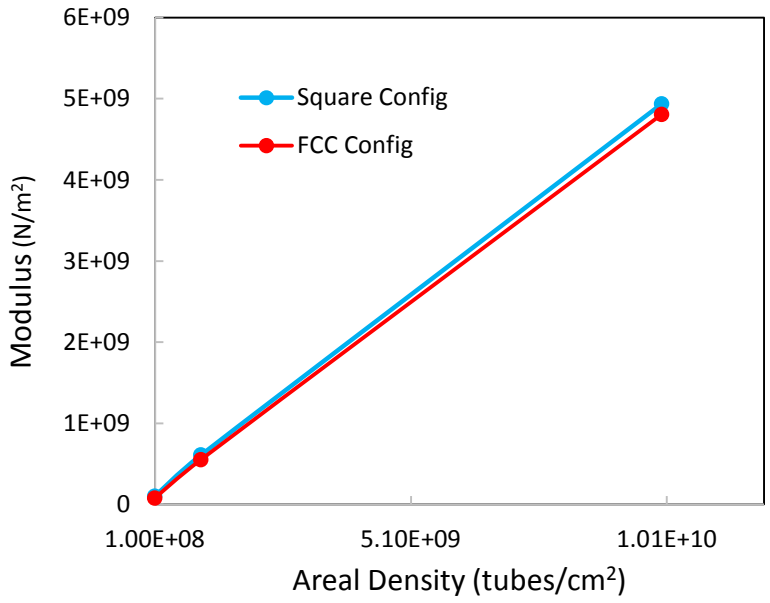

Figure 5.21. Effect of nanotube array configuration on modulus of the VA-CNT structures

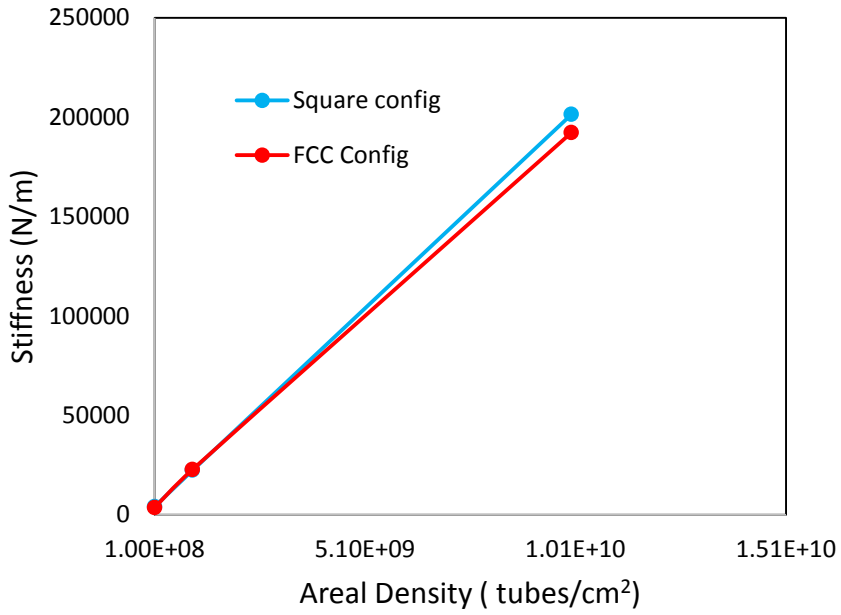

Figure 5.22. Effect of nanotube array configuration on stiffness of the VA-CNT structures

5.4 Conclusions

The structural shell modeling has been used to design and characterize the individual carbon nanotubes and aligned carbon nanotube arrays that are consisted of multi-walled CNTs. The equivalent thickness method has been used to model multi-walled CNTs. The stiffness and Young's modulus obtained from the equivalent thickness method are comparable to those obtained from the modeling of actual multi-wall structures, but at much efficient computational efforts. The VA-CNT array is constructed for a fixed area hence varying number of tubes for different densities. It is evident that the array stiffness and modulus can be tuned /customized as required by the intended application. In the aligned nanotube arrays, the modulus and stiffness are strongly dependent upon the number of walls in individual CNTs. In addition, the mechanical performance is also sensitive to the tube density.

Chapter 6.

6. Characterization and Modeling of Super-long Vertically Aligned Carbon Nanotube Arrays

6.1 Introduction

The fabrications of vertically aligned carbon nanotube arrays (VA-CNTs) are generally made by two methods: template synthesis and template-free synthesis. Terrones et al. have grown the first VA-CNTs by depositing the carbon sources in linear tracks in a silica template (Terrones et al. 1997). De Heer et al have made the carbon nanotubes through the use of an aluminum oxide micropore filter, a template used to align the nanotubes (De Heer et al. 1995) Recently, template-free synthesis has been used to produce the VA-CNTs (Bajpai et al. 2004, Ishigami et al. 2008, Chen et al. 2010). Compared to the template synthesis, the template-free synthesis is more effective in producing larger scale and taller nanotubes, so called super-long VA-CNTs. The VA-CNTs so grown can have the size as large as several square centimeters and the height as tall as several millimeters. Since the VA-CNTs can be readily integrated (grown) onto various substrates and devices, they have found a wide range of applications in areas such as the electrical interconnects (Kreupl et al. 2002), thermal interfaces (Cola et al. 2009), energy dissipation devices (Liu et al. 2008), and microelectronic devices (Fan et al. 1999). VA-CNTs can also be grown on non-planar substrates, i.e., the rounded carbon fibers. VA-CNTs on carbon fibers have had significant potentials in aerospace and space applications. They have added multi-functionality to traditional composites (Baur and Silverman 2007, Ci et al. 2008, Zhang et al. 2009), improved the fiber-matrix interface strength (Patton et al. 2009, Sager et al. 2009), and used as flow or pressure sensors on micro air vehicles (MAVs) (Zhang et al. 2010).

Compared to the VA-CNTS produced by template synthesis, the super-long VACNTs typically have much complex structure. Figure 6.1 shows the morphology of the super-long VACNT specimen examined by the scanning electron microscope (SEM).

At lower magnifications, the nanotubes are seen to well-align perpendicularly to the substrate. At higher magnification, the individual nanotubes are somewhat zigzag-like along the nanotube length with some entanglements between the nanotubes. All those features are the direct result of the template-free growth process. Results also reveal that the VA-CNTs are multiwalled (2-3 walls) carbon nanotubes and have a narrow uniform diameter distribution between 10 and 20 nm. The areal density of the VA-CNT arrays can be estimated as: $\rho=10^{10}\sim10^{11}$ tubes/cm^2 by counting the numbers of the carbon nanotubes on the substrate. The lengths of these super-long VA-CNTs are typically in the range of a few hundred to several thousand microns, as achieved by controlling the deposition time and pressure.

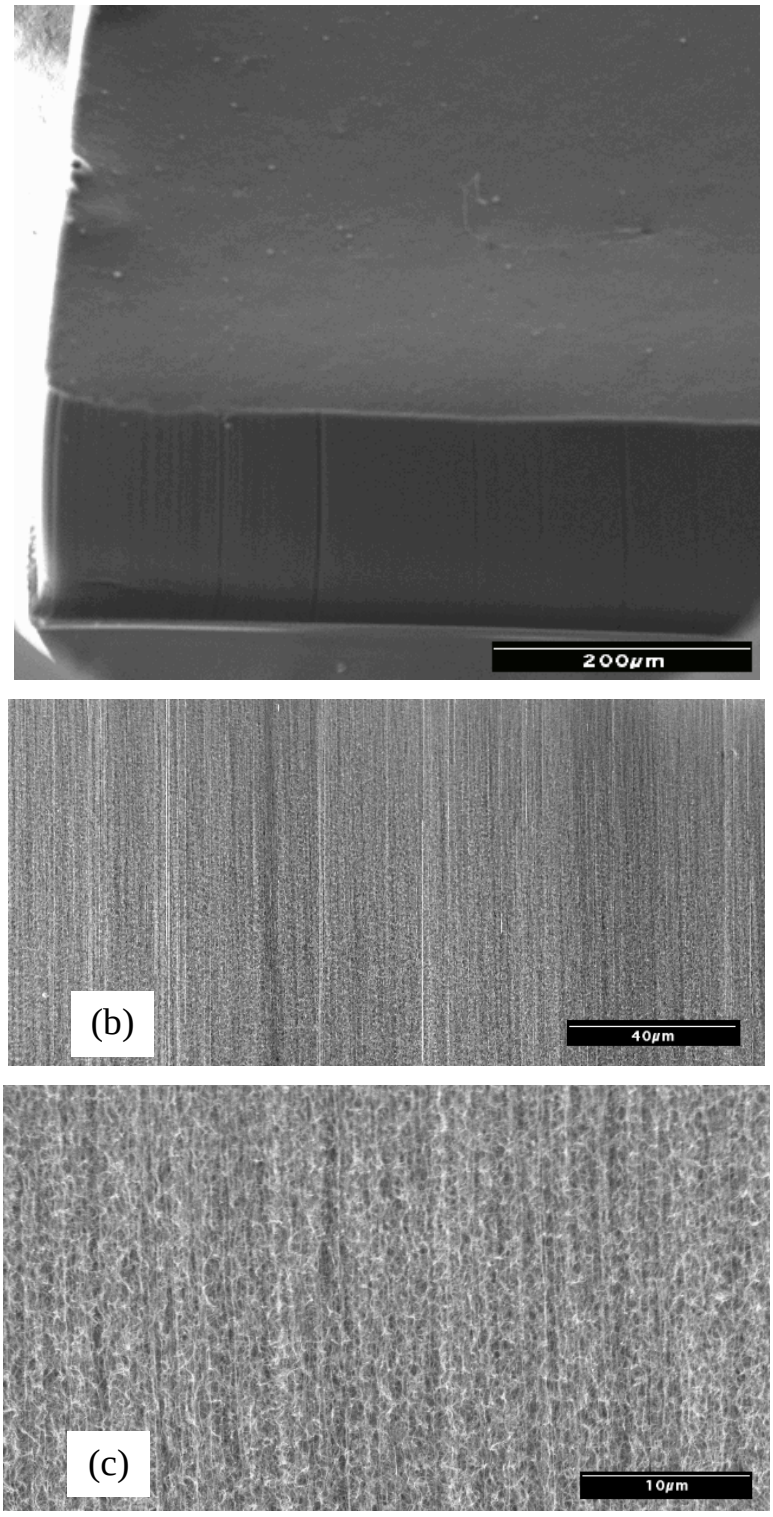

Figure 6.1. SEM images showing the morphology of the super-long vertically-aligned carbon nanotube arrays. The order of magnification increases from (a) to (c).

The mechanical properties and deformation behaviors of the super-long VA-CNTs have been investigated experimentally, mostly through the use of nanoindentation test (Qi et al. 2003, McCarter et al. 2006, Mesarovic et al. 2007, Pathak et al. 2009, Patton et al. 2009, Zhang et al. 2010). The conventional nanoindentation test is a technique for measuring mechanical properties of materials and structures in small dimensions. The depth of the indentation is typically small (a few nanometers or microns) and therefore the test is primarily used for measuring the elastic properties of materials and structures. To measure the elastic response of the VA-CNTs, an indenter of either three-face pyramidal shape (Berkovich indenter) or parabolic shape (spherical indenter) has been used to compress the specimen and then withdrawn from it. The indentation load-depth curves are obtained and then analyzed following the standard Oliver-Pharr method (Oliver and Pharr 1992). The modulus and hardness of the VA-CNT arrays have been obtained. In contrast with the extensive experimental work, little analytical or computational effort has been given towards the study of such super-long VA-CNTs, partially due to their complex microstructures.

This chapter presents the characterization and modeling of super-long VA-CNTs through experimental testing and numerical simulation. Large-displacement indentation test was developed and used to measure the elastic-plastic properties of the VA-CNT arrays. The present large displacement experiments are conducted with an in-situ nanoindenter equipped inside the chamber of a scanning electronic microscope (SEM). The technique can thus reveal both quantitative information (load-displacement) and phenomenological behaviors of the CNT arrays. A cylindrical, flat tip geometry is chosen for the indenter since the stress analysis under a tip of this form has been well established (Sneddon , Barquins and Maugis 1982).Compared to indenters of three-face pyramidal and parabolic shapes, the contact area of a cylindrical flat indenter does not change with displacement, and the extent of the stress field scales with the diameter of the indenter.

6.2 Fabrications of super-long VA-CNTs

The present VA-CNTs were synthesized by low pressure chemical vapor deposition of acetylene on planar substrates (SiO_2/Si wafers). A 10-nm thick Al layer was first coated on the wafers before the deposition of 3-nm Fe film in order to enhance the attachment of grown nanotubes on the silicon substrates. The catalyst coated substrate was then inserted into the quartz tube furnace and remained at 750^{o}C in air for 10 min, followed by pumping the furnace chamber to a pressure less than 10 mTorr. Thereafter, the growth of the CNT arrays was achieved by flowing a mixture gases of 48% Ar, 28% H_2, 24% C_2H_2 at 750^{o}C under 10~100 Torr for 10-20 min.

6.3 Principle of large-displacement indentation test

The large-displacement indentation test can be schematically described as shown in Figure 6.2. As an indenter is pushed into the material, a deformation zone is developed surrounding the indenter. The overall process resembles to the opening of a cavity in a solid and the stress required to open such a cavity can be estimated.

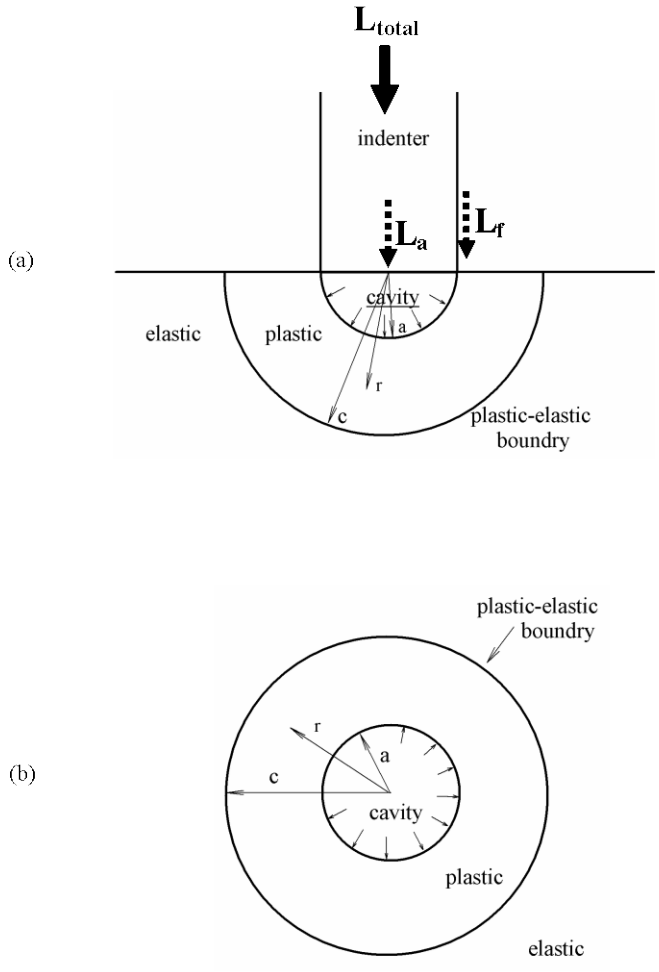

Figure 6.2. Schematic diagram showing the large-displacement indentation test. (a) Front view, (b) Top view

For blunt indenters (as opposed to sharp indenters), the cavity is typically assumed to be in cylindrical shape. The cavity starts with an initial radius a_o, and opens to a final radius a, equal to the radius of the indenter. The opening of such a cavity also expands a surrounding plastic zone from an initial radius r_o to a final radius c. The radial strain in the cylindrical polar coordinates (z, r, θ) is

$$\varepsilon_r = \ln(\frac{r}{r_o}) = \frac{1}{2} \cdot \ln(1 - \frac{a^2 - a_o^2}{r^2}) \tag{6.1}$$

Let σ_r, σ_θ be the radial and tangential stresses in the cylindrical polar coordinates. For a general elastic-plastic solid, the constitutive relationship between true stress σ and true strain ε in rectangular coordinates can be described by

$$\sigma / \sigma_y = f(\varepsilon) \tag{6.2}$$

where σ_y is the yield stress of the material. So, the stress-strain relation becomes

$$\frac{\sigma_\theta - \sigma_r}{\sigma_y} = \frac{2}{\sqrt{3}} \cdot f\left(\frac{2}{\sqrt{3}}|\varepsilon_r|\right) \tag{6.3}$$

Integrating the condition of the equilibrium, namely

$$\frac{d\sigma_r}{dr} = \frac{\sigma_\theta - \sigma_r}{r} \tag{6.4}$$

throughout the plastic region from *a* to *r*, we obtain for the pressure P on the boundary of the hollow cylinder (the value of $(-\sigma_r)$ at that point)

$$\frac{P_m}{\sigma_y} = \frac{2}{\sqrt{3}} \cdot \int_a^r f\left\{-\frac{1}{\sqrt{3}} \ln\left(1 - \frac{a^2 - a_o^2}{r^2}\right)\right\} \frac{dr}{r} \tag{6.5}$$

The above equation indicates that there exists a cavitation limit P_m as $a/a_o \to \infty$. An example solution of Equation (6.5) is shown in Figure 6.3, as calculated by using a typical yield strain of $\varepsilon_y = 0.1$ and a typical strain hardening coefficient n = 1.2 for a general elastic-plastic solid. It is seen that the ratio of P_m/σ_y reaches a constant once the indenter is fully compressed into the material. The magnitude of the ratio is bounded between 1 and 3, varying with the type of the materials.

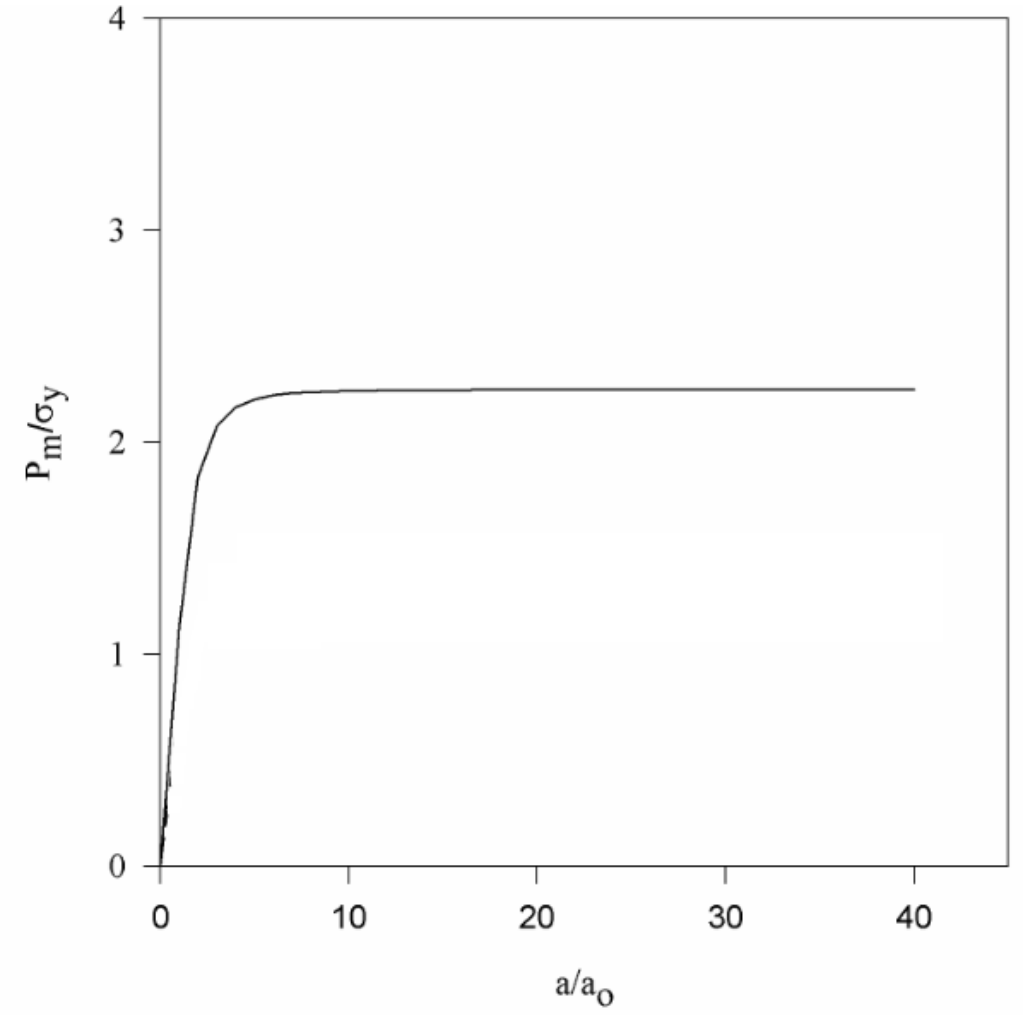

Figure 6.3. Prediction of the critical indentation stress from the cavity model. The calculation is obtained by using a typical yield strain of ε_y=0.1 and a typical strain harden coefficient n = 1.2 for a general elastic-plastic solid.

Clearly, the above equation is similar to the broadly applicable empirical relationship suggested by Tabor (Tabor 1996)

$$\frac{P_m}{\sigma_y} = C \tag{6.6}$$

where C is called the constraint factor.

Both theoretical analysis (Equation 6.5) and empirical analysis (Equation 6.6) show that the critical indentation stress (P_m) is proportional to the uniaxial yield stress (σ_y) for an elastic-plastic material. In general, the critical indentation stress beneath an indenter is greater than the uniaxial compressive yield stress of the material because of the confining pressure generated by the surrounding elastically strained material in the indentation stress field. For ductile metals, a value of $C \approx 3$ is generally considered to be appropriate (Johnson 1985, Tabor 1996). For soft polymers, the value of C becomes smaller (Wright et al. 1992, Lu and Shinozaki 1998, Lu et al. 2008);(Lu and Shinozaki 2008). For foam-like materials, the value of C generally approaches to unity, i.e., $C \approx 1$ (Wilsea et al. 1975, Olurin et al. 2000, Flores-Johnson and Li 2010). This is because the foam-like CNT arrays has a nearly zero plastic Poisson's ratio (the ratio of transverse to longitudinal plastic strain under compression). Therefore, the large indentation has resulted in very little lateral spreading of the CNT fibers under the indenter and the constraint factor becomes unity.

The critical indentation stress (P_m) can be determined experimentally through the large-displacement indentation test. As illustrated in Figure 6.2, when a cylindrical indenter of radius *a* is pressed onto a specimen, the total load (L_{total}) applied to the indenter is

$$L_{total} = L_a + L_f \tag{6.7}$$

where L_a is the axial load acting on the indenter end face and L_f the frictional load acting on the indenter side wall. The mean indentation pressure (P_m) acting on the indenter end is simply expressed as

$$P_m = L_a/\pi a^2 \tag{6.8a}$$

The frictional load (L_f) on the indenter side wall is defined by

$$L_f = 2\pi a h_c \tau \tag{6.8b}$$

where τ is the frictional shear stress and h_c the contact depth. Assume that the frictional stress is constant on the indenter wall, then the frictional load (L_f) should increase linearly with indentation depth, since the lateral surface area in contact with the material ($2\pi a\, h_c$) increases almost linearly.

Substituting Equations (6.8a) and (6.8b) into Equation 6.7 yields

$$\frac{L_{total}}{\pi a^2} = P_m + \frac{2d}{a}\tau \qquad (6.9)$$

The above equation shows that there exists a linear relationship between indentation stress and normalized displacement at large displacements. The critical indentation stress, P_m, can be determined simply by extrapolating the indentation stress-displacement curve back to zero displacement (d=0), where the frictional load (L_f) vanishes.

6.4 Experimental procedures

The large-displacement indentation tests were conducted with a custom designed in-situ nanoindenter equipped inside the SEM (FEI Sirion). The indenter used was a 100 μm diameter flat-faced cylinder, with a polished contact face. The cylindrical indenter was attached to a strain-gage based load cell, which was connected in series to a piezoelectric actuator. The piezoelectric actuator provided displacement control with sub-nanometer resolution. Resultant forces were measured through the load cell. The VA-CNT array samples were positioned on a piezoelectric positioning stage, which provided x-y-z movements with nanometer-scale resolution and with zero back-lash. The entire nanoindenter device is measured as 50 mm (width) x 50 mm (height) x 150 mm (length) and thus fits well inside the SEM chamber without disturbing the SEM's function. Instrumentation control and data acquisition were achieved by using the Labview software from National Instrument (NI).

During the test, specimens were incrementally loaded at a rate of 100 nm/sec and high resolution SEM images were acquired between displacement intervals. Load and displacement data were recorded and used to compute the indentation stress and strain. The scan images can be analyzed individually and further stitched together to produce videos and synchronized to correlate load and displacement data to the observed deformation phenomena.

6.5 Finite element modeling procedure

The deformation process of the super-long VA-CNTs was simulated using the finite element method, in which the VA-CNTs were treated as continuum solids. The commercial nonlinear finite element (FE) code ABAQUS was used (ABAQUS, 2010 - 2012). The specimen was modeled with second order, 8-node axisymmetric elements and the indenter modeled with rigid surface. For most analyses, the contact between specimen and indenter was treated as frictionless. The base of the specimen was completely constrained while the nodes along the center line constrained in the horizontal direction. A vertical described displacement was applied to the rigid surface through a reference node and the reactant force was calculated.

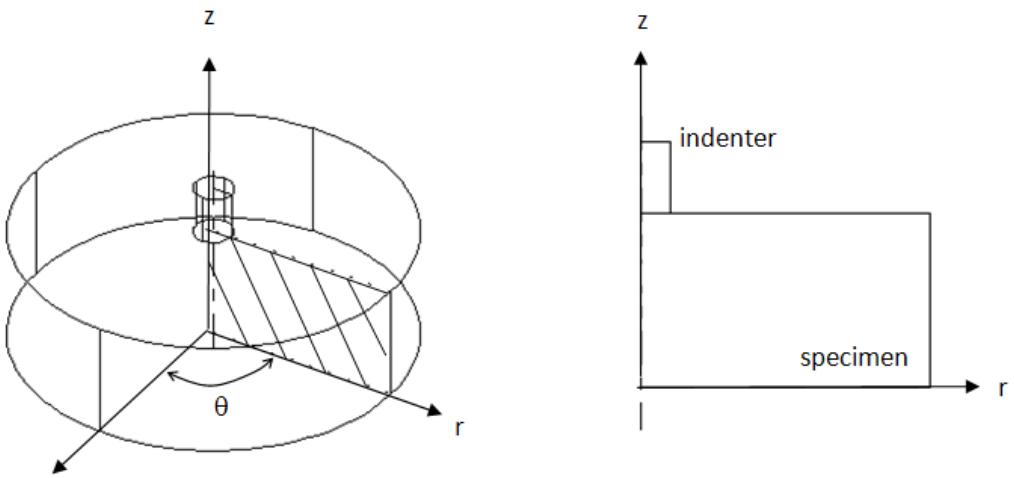

Figure 6.4. Schematic diagrams show that a 3-D indentation problem can be solved using a 2-D axisymmetric model. (Left) 3-dimensional indentation, (right) 2-dimensional axisymmetric model.

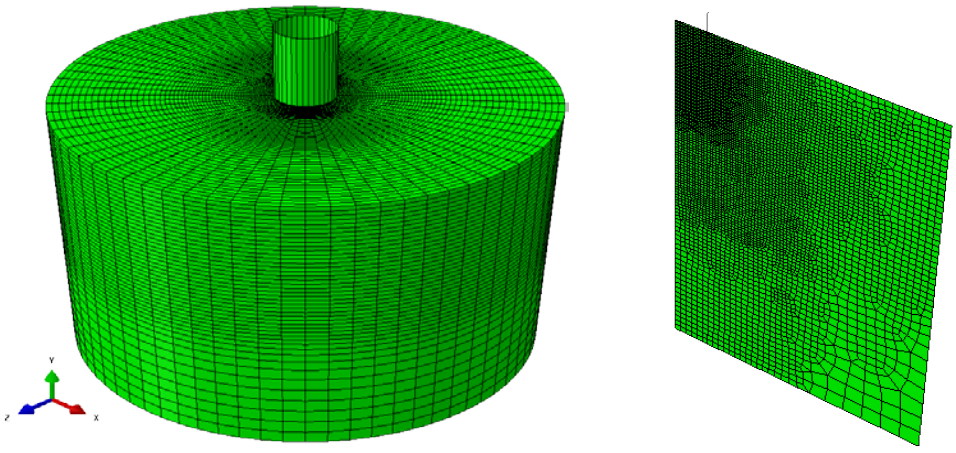

Figure 6.5. FE model setup for 3-D indentation problem showing (Left) 3-dimensional indentation model, (right) 2-dimensional axisymmetric model.

For comparative purpose, the indentation process of a dense solid was also modeled. The solid was treated as a power-law work-hardening, elastic-plastic solid, as described in detail elsewhere (Lu and Shinozaki 2008). The constitutive behavior of the power-law work-hardening, elastic-plastic solid were modeled as a piecewise linear / power-law hardening relation

$$\sigma = \begin{cases} E\varepsilon & \text{for } \sigma \le \sigma_y \\ \sigma_y (\dfrac{\varepsilon}{\varepsilon_y})^n & \text{for } \sigma > \sigma_y \end{cases} \tag{6.10}$$

where "σ" and "ε" were the applied stress and strain; "σ_y" and "ε_y" the material yield stress and strain (assuming the material was linear elastic to the yield point); "E" the Young's modulus; and "n" the strain hardening exponent describing the post-yield material behavior as a power law relation. The plasticity was modeled by a standard von Mises (J_2) flow criterion. The constitutive parameters in Equation (6.10) were obtained from experimental uniaxial stress-strain tests on the various materials.

The VACNT arrays were treated as open-cell, foam-like materials and the crushable foam plasticity model developed by Deshpande and Fleck (Deshpande and Fleck 2000) was used. The elastic part of the response is specified as linear elastic behavior, same as the dense solid (Equation (6.10)). For the plastic part of the behavior, the isotropic hardening model originally developed for metallic foams by Deshpande and Fleck (2000) was used. This model was implemented in ABAQUS as the crushable foam model, in which the yield surface is defined as

$$\sigma = \{\frac{1}{[1+(\alpha/3)^2]}[\sigma_{\text{Mises}}^2 + \alpha^2 P^2]\}^{1/2} \tag{6.11}$$

where σ_{Mises} is von Mises effective stress and P is the pressure stress. α is the shape factor of the yield surface which can be computed using the initial yield stress in uniaxial compression and the initial yield stress in hydrostatic compression.

The Arbitrary Lagrangian-Eulerian (ALE) adaptive meshing technique was used to deal with the severe distortion of elements which occurred in the large displacement indentation. The ALE method was used to allow the mesh to move independently of the underlying material during the simulated penetration, and thus prevent the analysis from terminating as a result of severe mesh distortion. These adaptive meshing procedures have been used for simulations of superplastic metal forming processes such as forging, extrusion, deep drawing, etc., which involve large amount of non-recoverable deformation (Voyiadjis and Foroozesh 1991, D. Peric 1999)

6.6 Results and discussion

6.6.1 Deformation of super-long VA-CNTs

6.6.1.1 Experimental

The indentation test is performed on an in-situ nanoindenter that is equipped inside the chamber of a SEM, and thus allows for real-time observation and video recording of the deformation process while the CNT arrays are compressed. To view the deformation process, the in-situ nanoindentation was performed at the edge of the CNT array specimen. Figure 6.6 in the following page shows the large displacement phenomenology of a CNT arrays ($t \approx 1100\ \mu m$) at various indentation stages.

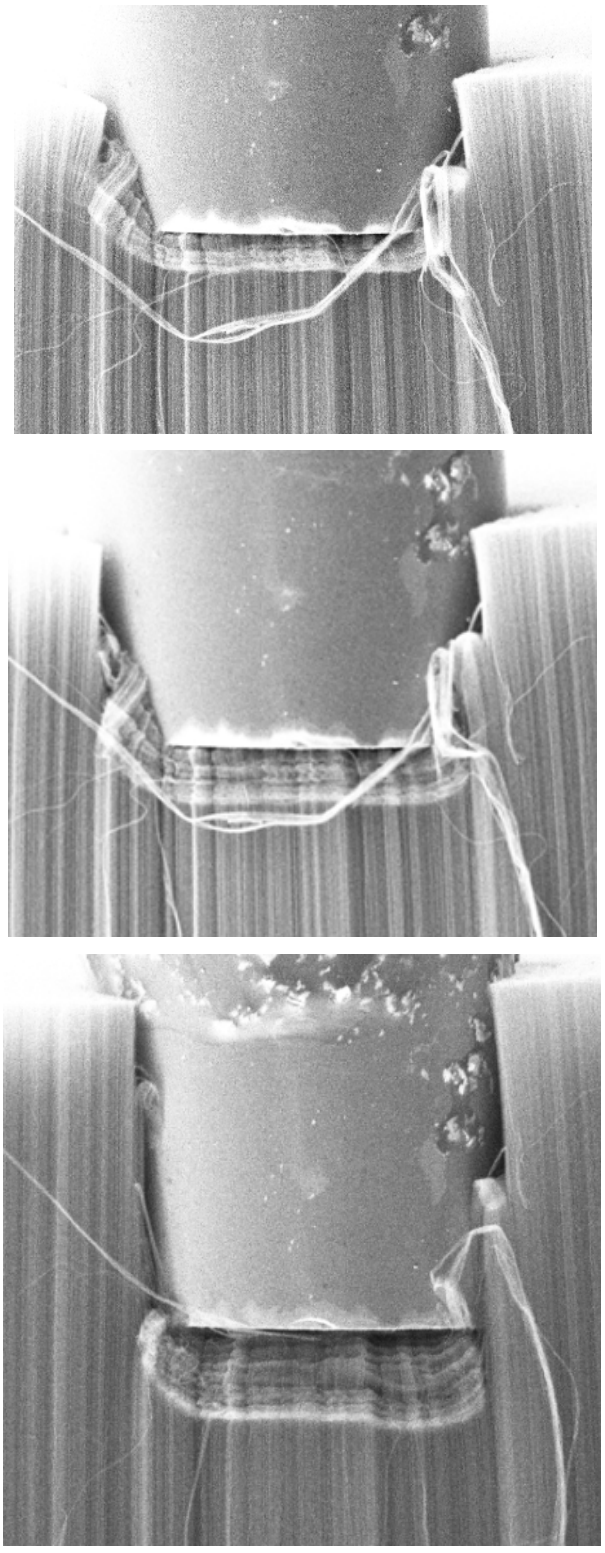

Figure 6.6. SEM images showing the development of plastic deformation in the vertically aligned carbon nanotube arrays (height ≈1100 um) under a cylindrical flat indenter.

The early stage of penetration is dominated by the elastic deformation, as revealed later by larger slopes in the load – displacement curves (Figure 6.11 and Figure 6.12). Larger slopes indicate that the CNT materials have greater stiffness initially. Further penetration of the indenter results in the plastic collapse of the carbon nanotubes beneath the indenter head (Figure 6.6). The measured stiffness thus decreases with increasing depth of indentation. Observations show that the plastic collapse of the nanotube arrays is limited in extent to the zone directly underneath the indenter face where the shear stress is large. The size of this collapsing zone is much smaller as compared to the larger, hemispherical shaped plastic zones occurred on dense, solid materials, such as polycarbonate (Wright et al. 1992) and polyethylene (Lu and Shinozaki 1998). The nanotubes outside the collapsing zone are seen to exhibit no fracture or tearing.

The series of load-drops in the stress-displacement curves are results of continuous collapsing of nanotubes as the indenter tip moves. The force required for crushing additional nanotubes is relatively small (because its volume is a small fraction of the material under load), so the measurement of the stress associated with the buckling movement are small. Therefore, the total stress at the large strain region has stayed relatively constant.

6.6.1.2 Simulation

The deformation process of the VA-CNTs was also analyzed by using the finite element method. Figure 6.7 and Figure 6.8 show the contours of the 1st principle stress (σ_1) for foam-like VA-CNTs and dense polymer, respectively. σ_1 is defined by $\sigma_1 = \frac{\sigma_r + \sigma_z}{2} + \left[\left(\frac{\sigma_r - \sigma_z}{2}\right)^2 + \tau_{rz}^2\right]^{1/2}$ and σ_r, σ_z, and τ_{rz} are the radial, normal and shear stresses in the cylindrical polar coordinates. Figure 6.9 and Figure 6.10 show the contours of the equivalent plastic strain (ε^{eq}) for foam-like VA-CNTs and dense polymer,

respectively. ε^{eq} is defined by $\varepsilon^{eq} = \sqrt{\frac{2}{3}(\varepsilon_1^2 + \varepsilon_2^2 + \varepsilon_3^2)}$ and ε_1, ε_2, ε_3, are the principal strains. For $\varepsilon^{eq} > 0$, the material has plastically deformed.

It is observed that the stress field and deformation process of VA-CNT arrays under compression are distinctly different from those of solid polymers. For a dense, solid polymer, the distribution of the stress (σ_1) under the flat indenter is in a hemispherical shape. The size (elastic-plastic boundary) of the stress field approximates the diameter of the indenter (2a, 'a' being the radius of the indenter), as illustrated by the cavity model described earlier. In contrast, the stress field (σ_1) for the foam-like VA-CNT arrays under the flat indenter is much smaller. The stress is primarily concentrated right beneath the indenter face and does not get extended to far field.

The large-displacement indentation process can be understood by the progressive developments of equivalent plastic strain (ε^{eq}). For a dense, solid polymer, the initial inelastic deformation starts near the corners of the indenter. As the depth of indentation increases, the deformed zone increases in size. After a depth of approximately half to one indenter diameter, the deformation zone becomes fully developed surrounding the indenter and then remains relatively constant in size. The diameter of the deformed zone is about twice the diameter of the indenter, again in consistence with the cavitation model. It is also seen that a conical zone directly ahead of the flat indenter tip shows little deformation. However, for the foam-like VA-CNT arrays, the equivalent plastic strain (ε^{eq}) is distributed right beneath the indenter face. The shape of this plastic zone is much narrower, as opposed to a larger, hemispherical zone occurred in the dense, solid polymers. The simulated deformation is consistent with the experimental observations (Figure 6.6). Overall results confirm that the VA-CNTs behave like low-density foams and the crushable foam plasticity model is appropriate for modeling such materials.

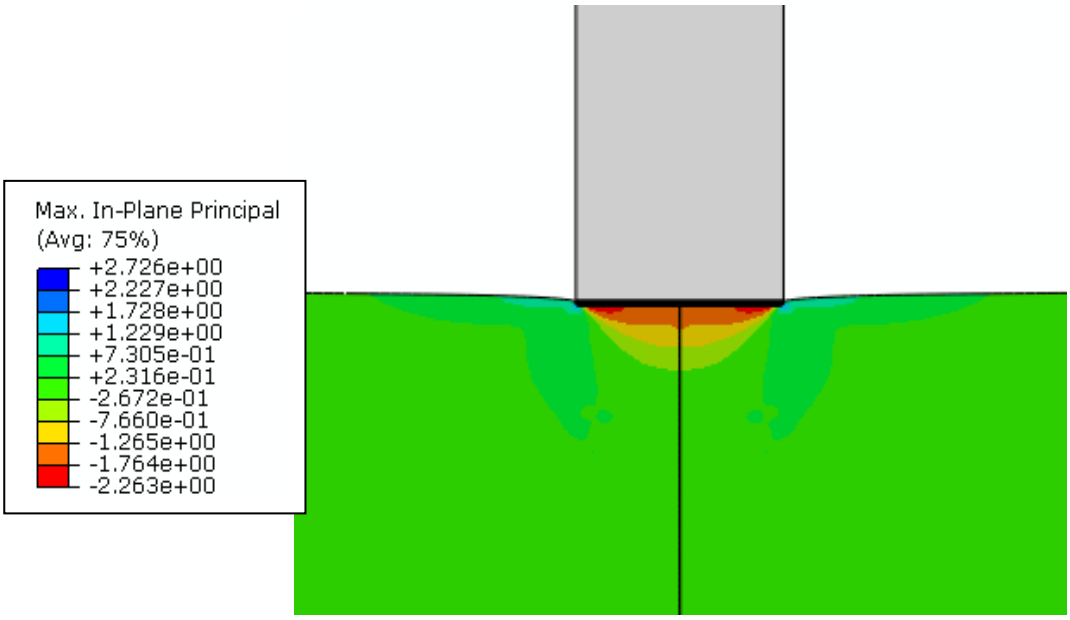

Figure 6.7. Contour of 1st principle stress in the vertically aligned carbon nanotube arrays under a flat indenter. The material is treated as an open-cell foam-like material.

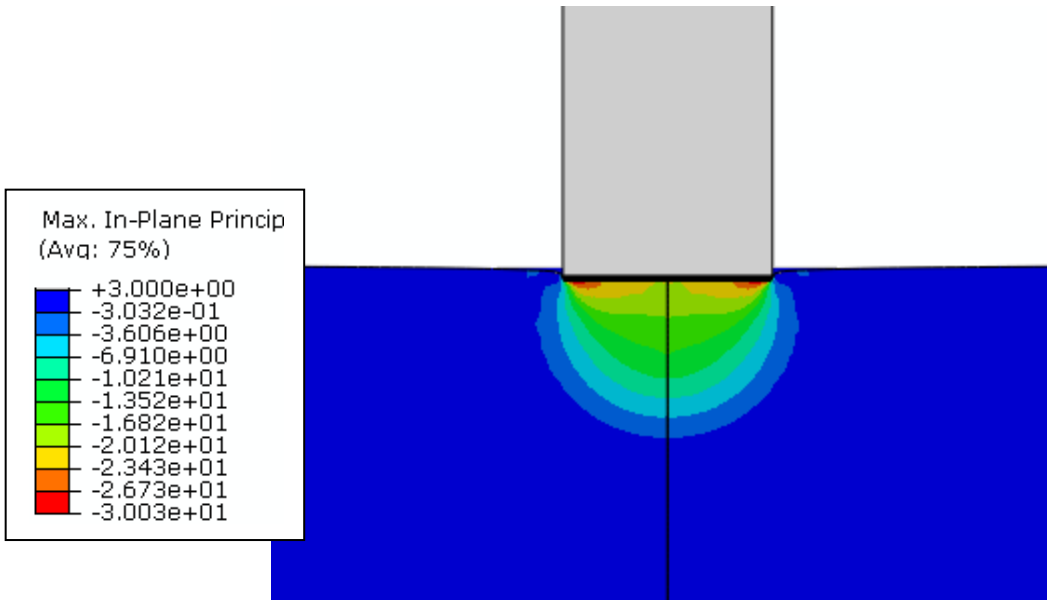

Figure 6.8. Contour of 1st principle stress in a dense, solid material under a flat indenter. The material is treated as a power-law work hardening, elastic-plastic solid.

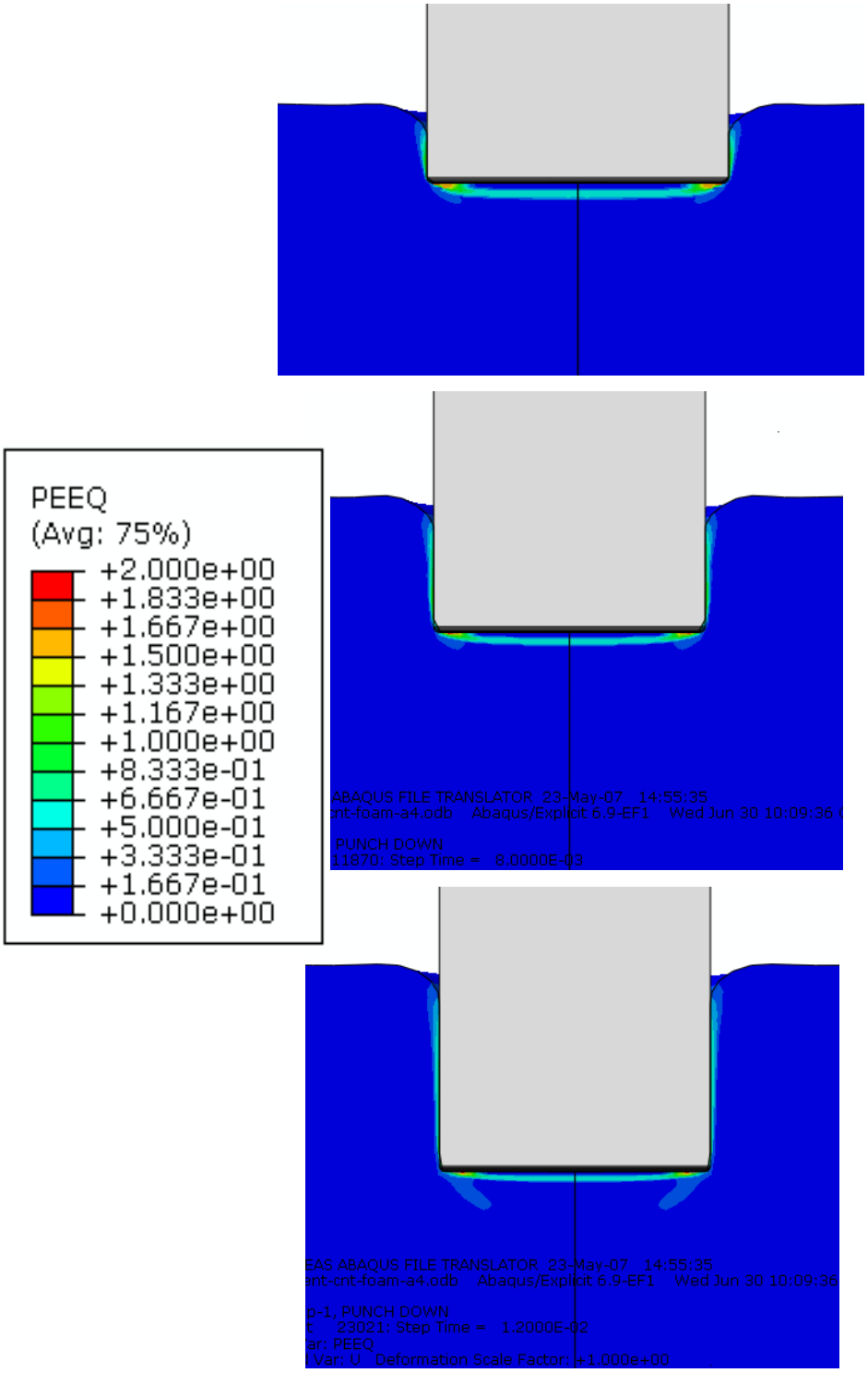

Figure 6.9. Contour of equivalent plastic strain in vertically aligned carbon nanotube arrays during large-displacement indentation. The material is treated as an open-cell foam-like material.

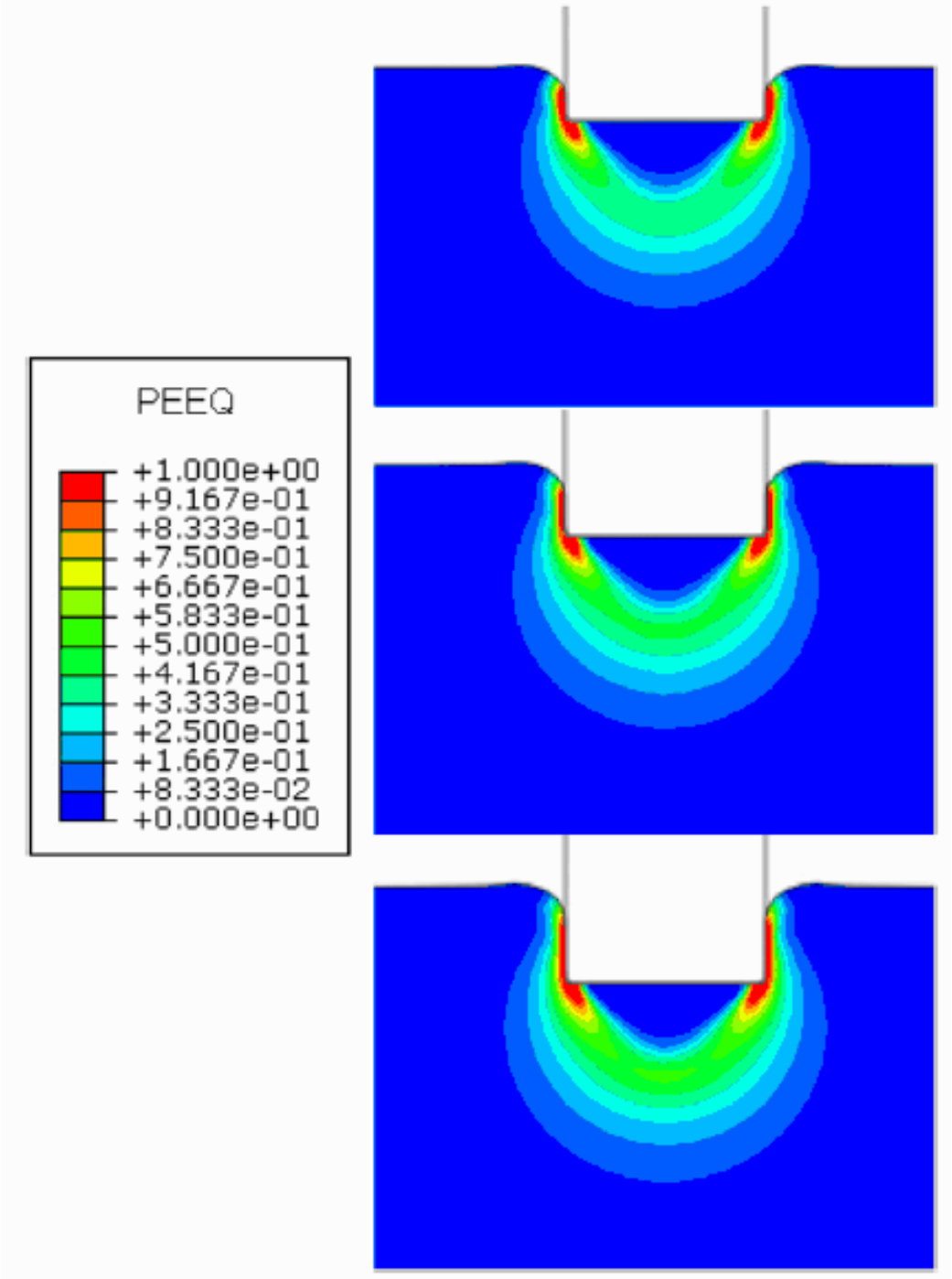

Figure 6.10. Contour of equivalent plastic strain in a dense, solid polymer during large-displacement indentation. The material is treated as a power-law work-hardening, elastic-plastic solid.

6.6.2 Stress-strain responses of VA-CNT arrays

6.6.2.1 Experimental

Figure 6.11 shows the indentation stress-displacement curves of two vertically aligned carbon nanotube arrays, with height equal to approximately 1100 μm. Results reveal that the material initially deforms elastically with the applied load on the indenter, and yields at some point as the applied load is increased. The plastic deformation field and consequently the stress field progressively change with displacement, until some steady state is achieved. The indentation of elastic-plastic solids has gained considerable attention recently, with the purpose of determining the plastic characteristics of the materials such as yield strength, work hardening rate, etc. Most of the work involves the uses of indenters of parabolic shapes, i.e., spherical and conical indenters (Mesarovic and Fleck 1999, Park and Pharr 2004). The present test has chosen a cylindrical, flat indenter. The chief advantage of this type of indenter is that the contact area remains constant during indentation, therefore the applied stress measured by the indenter at the steady state is constant. This allows the measurement of steady state deformation under the indenter, as indicated by the linear stress-displacement response at large displacements.

The plateau region indicates the plastic collapses of carbon nanotubes beneath the indenter face. Such collapse allows the strain increase while the stress stays approximately constant. A series of “load-drops” in the plateau regions is observed, which corresponds to the folding of additional carbon nanotubes. If further penetration is permitted until all folding is completed, a third region would appear: the densification region. In that region, the folding of all nanotubes under the indenter face has been completed and the compression of the folded/collapsed materials has started. As a result, the stress would start to rise sharply. Alternatively, the densification response can be observed by indenting a shorter specimen. Overall, the stress-displacement response of the VA-CNT arrays is identical to those reported on open-cell, low-density foams (Wilsea et al. 1975; Olurin et al. 2000; Flores-Johnson and Li 2010).

Following Equation 6.9, the critical indentation stress, P_m, is determined by extrapolating the large-strain indentation stress-displacement curve back to zero displacement (d=0), where P_m is the intercept. The magnitude of P_m so obtained for the present CNT arrays is approximately 6.2 MPa, from Figure 10.

For the present CNT arrays, the slopes of stress-displacement at large displacements are almost zero (Figure 6.11 and Figure 6.12), indicating that the friction shear stress (τ) acting on the indenter wall due to the elastic compression from surrounding nanotubes is negligible. Therefore, the interfacial friction between the CNT and the indenter side-wall is very small, which is constant with the finding reported by Tu et al. (Tu et al. 2003, Tu et al. 2004).

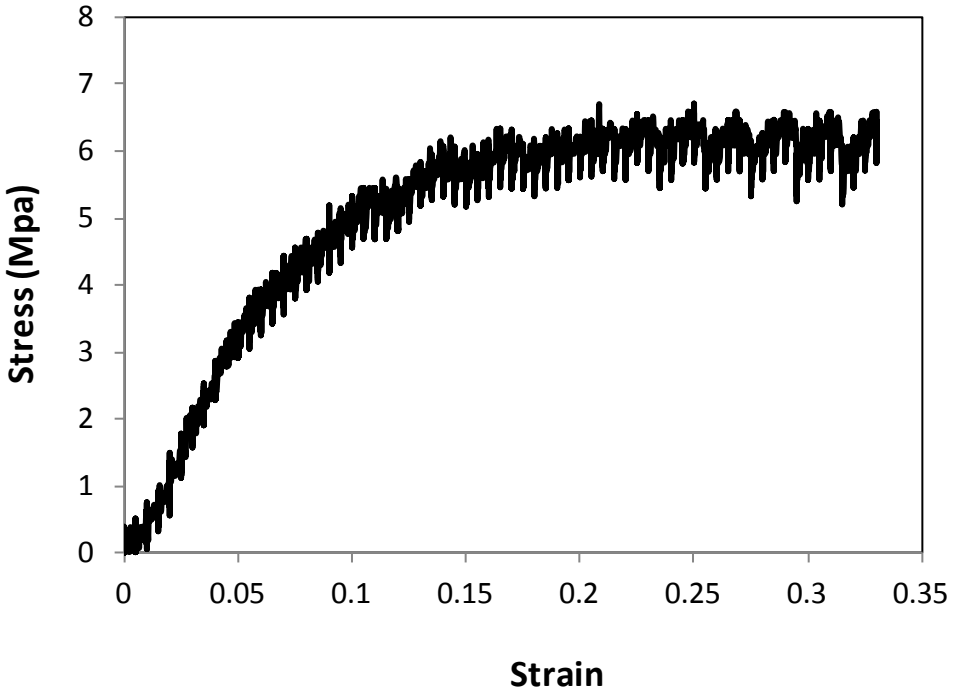

Figure 6.11. Indentation stress-strain curve of a vertically aligned carbon nanotube arrays (height ≈ 1100 μm) with cylindrical, flat-faced indenter.

6.6.2.2 Simulation

Figure 6.12 shows the indentation stress-strain response of the vertically aligned carbon nanotube arrays by using the finite element method. The calculated stress-strain curve is similar to the one measured in experiments. The bilinearity of the plots, characteristic of the measured data is seen in the finite element modeling, and is consistent with the interpretation of a largely elastic deformation field becoming largely plastic at greater penetration depths.

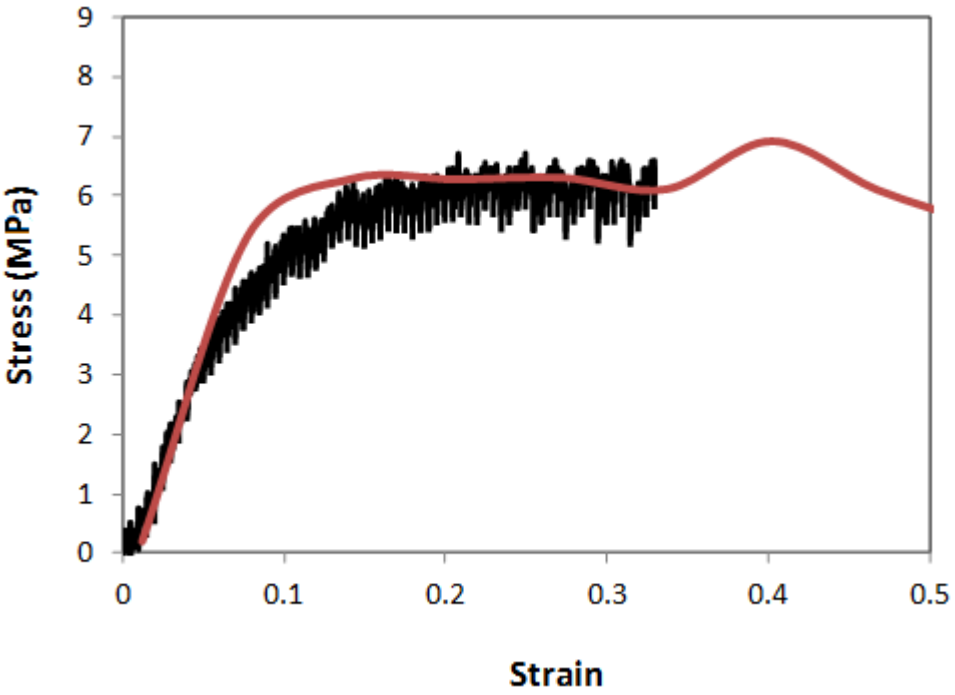

Figure 6.12. Indentation stress-strain response of the vertically aligned carbon nanotube arrays (height ≈ 1100 μm) obtained from the finite element method.

6.6.3 Effect of areal density of VA-CNT arrays

The effect of density of mechanical responses of the VACNTs is investigated. The CNT arrays were treated as open-cell foam materials. According to Gibson and Ashby(Gibson

and Ashby 1997), the relevant elastic modulus (E) and plastic yield strength (σ_y) scale with the density (ρ) for the open-cell foams:

$$E = \alpha\left(\frac{\rho}{\rho_0}\right) \tag{6.12a}$$

$$\sigma_y = \beta\left(\frac{\rho}{\rho_0}\right) \tag{6.12b}$$

where ρ_0 is the reference density and α and β are scaling coefficients.

In present study, the effect of density was examined by varying the elastic modulus and yield strength of the VACNTs as: E/E_0=1, 0.8, 0.6, 0.4 and σ_y/σ_{y0}=1, 0.8, 0.6, 0.4, where E_0 and σ_{y0} are the elastic modulus and yield strength of the original VACNTs. The stress-strain responses of the VACNTs from are shown in Figure 6.13. As the density decreases, the VACNTs become more compliance. Figure 6.14 through Figure 6.17 show von-Mises stress distribution beneath the indenter in the VA-CNT material for density ratios 0.4 (less denser), 0.6, 0.8 and 1.0(most dense). The contour plots are for identical indentation depth measured in terms of normalized strains. The results are for a normalized strain of 0.45. From these plots it may be observed that with increasing density of the material, the load carrying ability of the VA-CNT array for identical strains increases as the stress levels shown in the plot are in an increasing trend. The stresses are shown in units of in $N/\mu m^2$. Figure 6.18 through Figure 6.21 show the equivalent plastic strain distribution beneath the indenter in the VA-CNT material for density ratios 0.4, 0.6, 0.8 and 1.0 for the same identical normalized strains of 0.45.

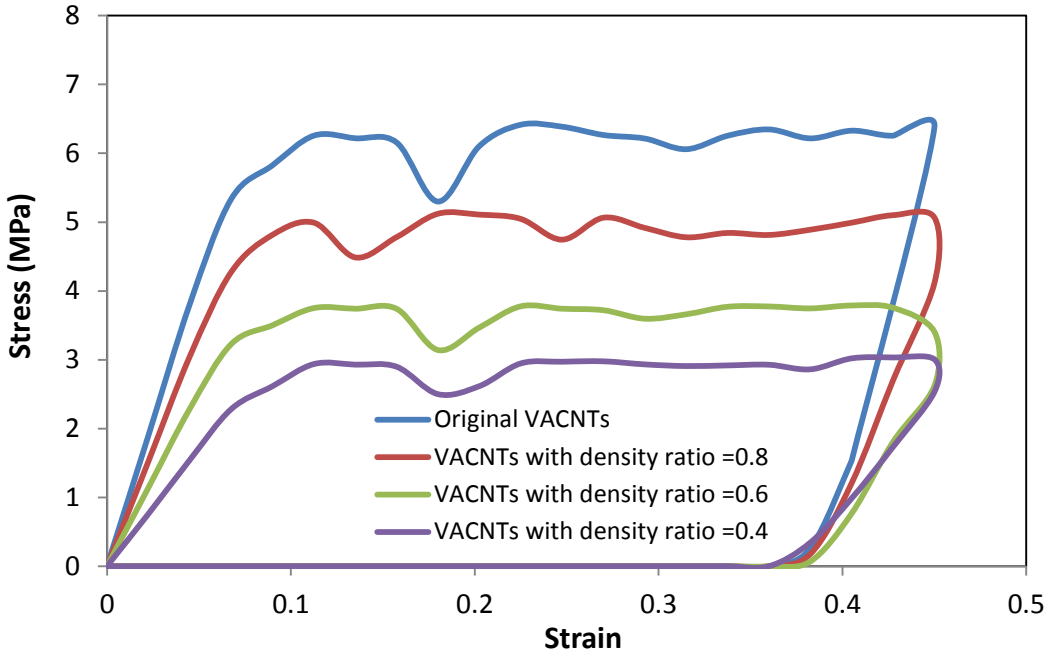

Figure 6.13. Indentation stress-strain response of the vertically aligned carbon nanotube arrays with varying densities obtained from the finite element method.

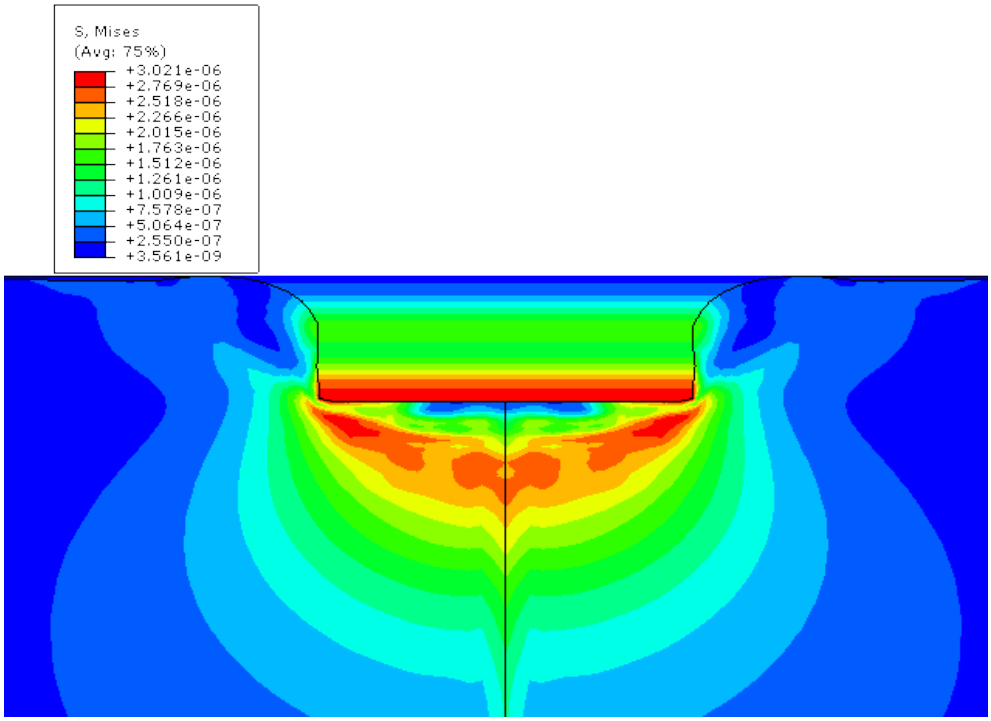

Figure 6.14. von Mises Stress for VA-CNT array corresponding to density ratio = 0.4

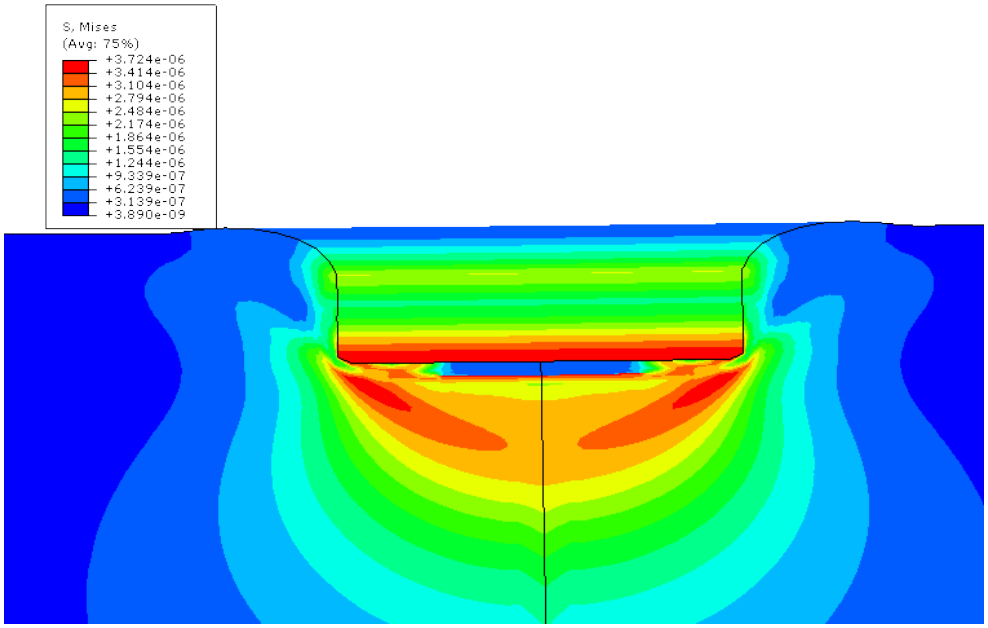

Figure 6.15. von Mises Stress for VA-CNT array corresponding to density ratio = 0.6

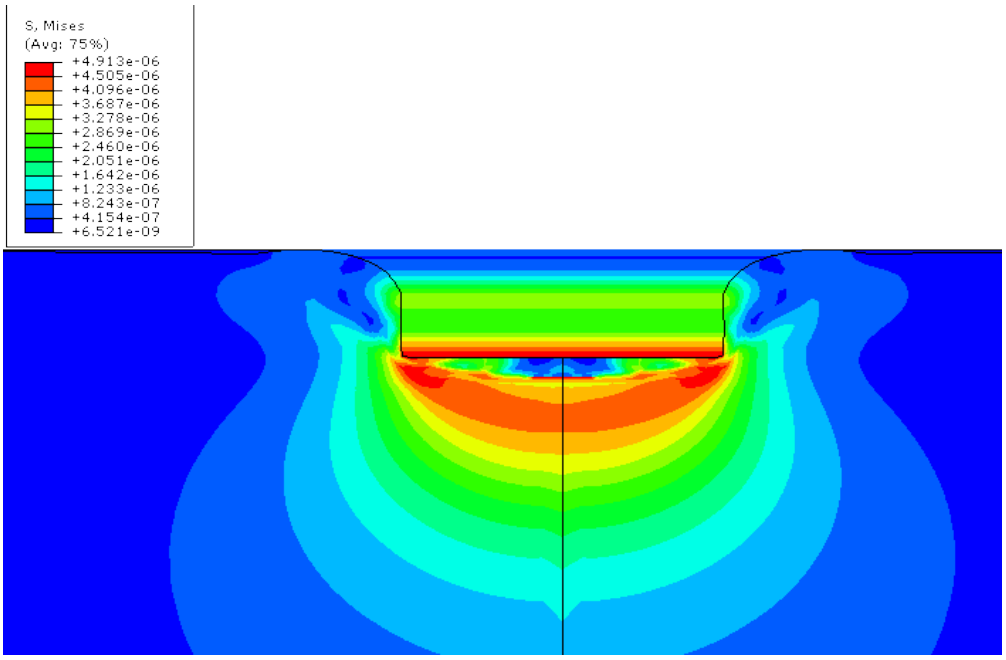

Figure 6.16. von Mises Stress for VA-CNT array corresponding to density ratio = 0.8

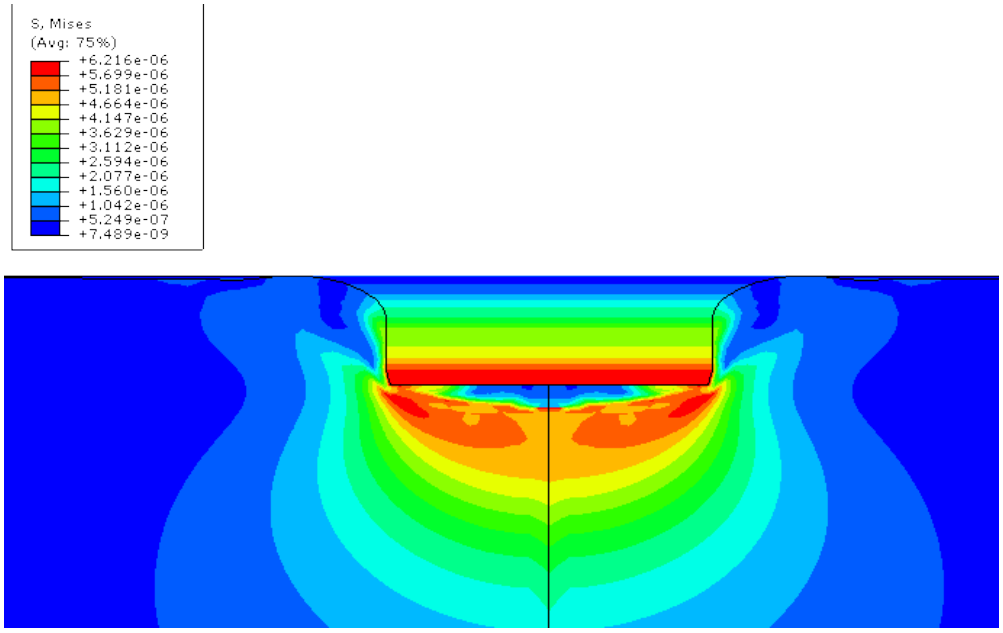

Figure 6.17. von Mises Stress for VA-CNT array corresponding to density ratio = 1.0

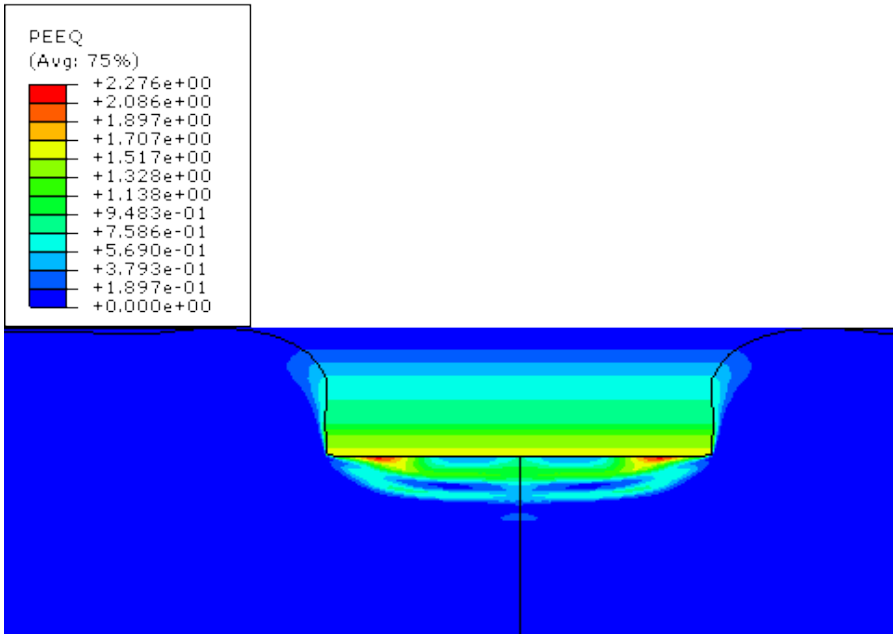

Figure 6.18. Equivalent plastic strain for VA-CNT array corresponding to density ratio = 0.4

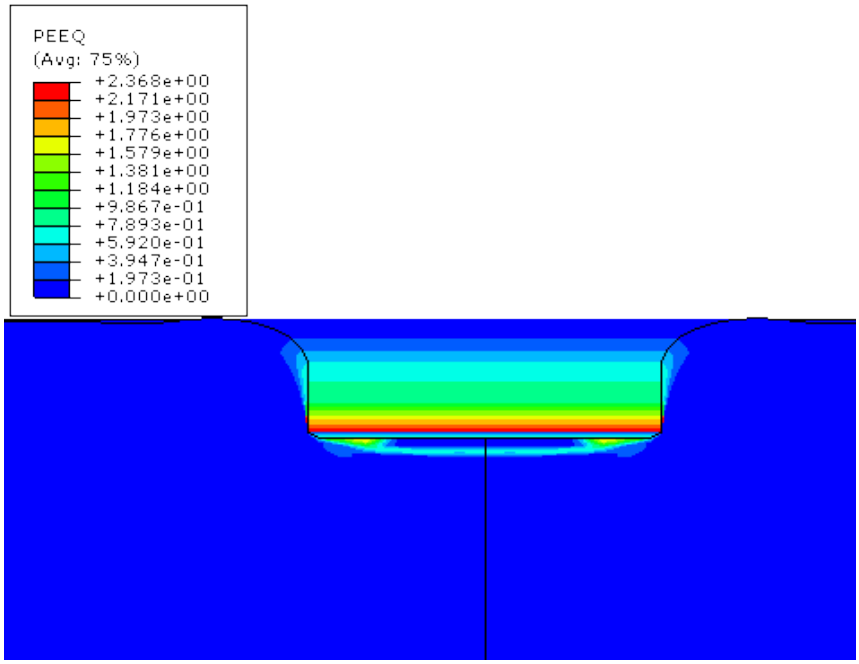

Figure 6.19. Equivalent Plastic strain for VA-CNT array corresponding to density ratio = 0.6

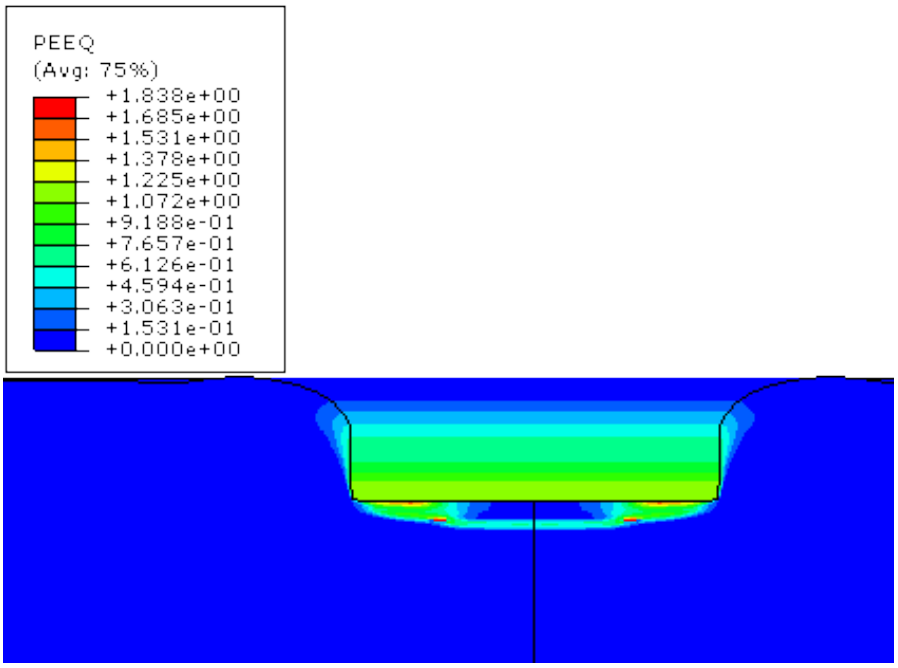

Figure 6.20. Equivalent Plastic strain for VA-CNT array corresponding to density ratio = 0.8

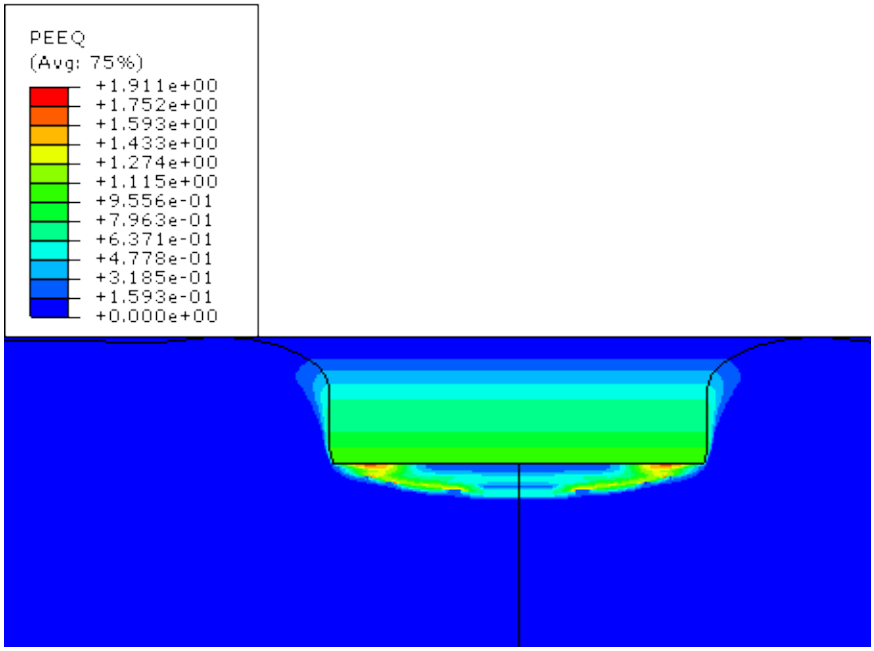

Figure 6.21.Equivalent Plastic strain for VA-CNT array corresponding to density ratio = 1.0

6.7 Conclusions

The mechanical behaviors of the vertically aligned carbon nanotube arrays (VA-CNTs) have been characterized using indentation test and finite element modeling. The large-displacement indentation test is an effective tool for measuring the elastic-plastic properties of the vertically aligned carbon nanotube arrays (VA-CNTs). Due to no lateral constraint in VACNT structures, the stress-strain responses from indentation test are identical to those from conventional axial compressive test. Both experimental and FE results show that the VA-CNTs exhibit a transient elastic deformation at small displacement and then steady sate plastic deformation at large displacement. The critical indentation stress (P_m) can be extrapolated from the indentation stress-displacement curves. The magnitude of P_m is a measure of the yield stress or collapsing stress of CNT arrays. Experiment results and finite element simulations have shown that the sizes of stress/strain zones are much smaller in foam-like VA-CNTs, as opposed to much larger, hemispherical stress/strain zones observed in the dense solid. Under the cylindrical, flat indenter, the nanotube cells collapsed plastically immediately beneath the indenter, a region of the highest stress/strain. The stress-strain responses of the VACNTs are sensitive to the densities of the materials.

Chapter 7

7. General Conclusions

Since their discoveries, carbon nanotubes have been widely studied, but mostly in the forms of 1D "individual carbon nanotube (CNT)". To date, work on the complex vertically aligned carbon nanotube arrays (VA-CNTs) is still limited. From design point of view, the existing analytical methods used to model 1D individual CNT, i.e., the classical quantum mechanics, molecular dynamics, tight binding molecular dynamics and density functional theory, would not be applicable to the modeling of VA-CNT structures due to the significant computational efforts. The overall objective of this research is to develop effective numerical modeling procedures that can be used to design, model and characterize the mechanical responses of the VA-CNTs. To achieve such goal, the Structural Mechanics approaches (beam mechanics, shell mechanics, and solid mechanics) have been used to model the VA-CNT structures.

The beam and shell mechanics are generally applicable to the VA-CNTs prepared by template synthesis methods. VA-CNTs synthesized by the use of templates are very well aligned and organized. Such materials are also highly "tunable" from the structure standpoint. The optimal performance of the VA-CNTs highly depends upon their architectures and geometric parameters, including tube height, tube diameter, nanotube array density, tube distribution pattern, among many other factors.

The structural beam elements have been first used to study the geometric parameters of the individual carbon nanotube for its mechanical properties. It is observed that the Young's modulus and shear modulus of the nanotube are sensitive to the atomic structure of the tubes, whereby the CNTs in armchair configuration exhibit higher young's modulus than the CNTs in zigzag one with increasing diameter whereas for the shear modulus the zigzag configuration exhibits higher than that of the armchair with increasing nanotube diameter. Both Young's modulus and Shear modulus generally

increase at a much steeper rate with diameter for small diameter nanotubes and then becomes stabilized for large diameter nanotubes. The Poisson's ratio computed from the values of Young's and shear moduli show that the Poisson's ratio of armchair nanotubes is higher than that of the zigzag and is sensitive for small diameters of nanotubes. The strength of the CNTs further depends upon the diameter of the C-C bonds (tube wall thickness). As the wall thickness increases, the Young's modulus of the nanotubes decreases. The modulus of the nanotubes is negligibly affected by the tube length whereas the stiffness is inversely proportional to the tube length.

The structural beam elements are further used to design and characterize the properties of aligned carbon nanotube arrays. VA-CNT structures with various densities and configurations have been constructed. Overall, the VA-CNT structures exhibit much lower modulus than the individual CNT, due to their high porosities and low densities. By increasing the nanotube array density, the modulus of VA-CNT structures are significantly improved. The individual nanotube atomic structure, i.e., zigzag versus armchair, can affect the mechanical property of the VA-CNT structure, but only at small wall thickness. The elastic modulus of the VA-CNT is again negligibly affected by the height of VA-CNTs.

In addition to the discrete beam elements, the continuum shell elements are also used to design and model the aligned carbon nanotubes structures. Based on an understanding of carbon nanotubes at the atomic/molecular level, the equivalent shell thickness and modulus in a single walled CNTs were estimated. The geometric parameters of the VA-CNT structures on its mechanical properties are thoroughly examined. For individual CNTs, the Young's modulus generally increases at a much steeper rate with diameter for small diameter nanotubes and then becomes stabilized for large diameter nanotubes. For the VA-CNTs, the modulus is strongly dependent upon the tube areal density. The higher the density, the higher the modulus. In addition, the mechanical performance is also sensitive to the tube pattern in an array. The modulus from a square packed array has a slightly higher value than that from a FCC packed one.

The structural shell modeling method is further used to design and characterize the VA-CNTs that are consisted of multi-walled CNTs. The multi-walled CNTs have been approximated as the equivalent thickness single-walled CNTs. The stiffness and Young's modulus obtained from the equivalent thickness method are comparable to those obtained from the modeling of actual multi-wall structures, but at much efficient computational efforts. The VA-CNT arrays are constructed for a fixed area hence varying number of tubes for different densities. It is evident that the array stiffness and modulus can be tuned /customized as required by the intended applications. The modulus and stiffness are strongly dependent upon the number of walls in individual CNTs. The mechanical performance is also sensitive to the VA-CNT areal density.

Another type of VA-CNTs is the so-called Super-Long VA-CNTs. Such VA-CNTs are prepared by template-free synthesis and can have the sizes as large as several square centimeters and the height as tall as several millimeters. Compared to the VA-CNTS produced by template synthesis, the super-long VACNTs typically have much complex structures, where the individual nanotubes are somewhat zigzag-like along the nanotube length with some entanglements between the nanotubes. Because of the structural complexity, these VA-CNTs have been treated as foam-like solids and modeled with solid elements.

First, the mechanical properties of such VA-CNTs are characterized by using indentation test. Due to no lateral constraint in VACNT structures, the stress-strain responses from indentation test are identical to those from conventional axial compressive test, from which the elastic and plastic properties are obtained and fed into the finite element programs. Results have shown that the sizes of stress/strain zones are much smaller in foam-like VA-CNTs, as opposed to much larger, hemispherical stress/strain zones observed in the dense solid. The deformation and stress-strain responses of the VA-CNTs are sensitive to the densities of the materials.

REFERENCES

Allen, H. G. and Bulson.P.S. (1980). Background To Buckling. Great Britain.

Bajpai, V., Dai, L. and Ohashi, T. (2004). Large-Scale Synthesis of Perpendicularly Aligned Helical Carbon Nanotubes. *J. AM. CHEM. SOC.* **126**: 5070-5071.

Barquins, M. and Maugis, D. (1982). Adhesive Contact of Axisymmetric Punches on an Elastic Half-Space-the Modified Hertz-Hubers Stress Tensor for Contacting Spheres *J. Mec. Theo. Appl.* **1**: 331–357.

Baur, J. and Silverman, E. (2007). Challenges and Opportunities in Multifunctional Nanocomposite Structures for Aerospace Applications. *MRS Bulletin* **32**(04): 328-334.

Brenner, D. W. (1990). Empirical potential for hydrocarbons for use in simulation the chemical vapor deposition of diamond films. *Physical Review B* **42**: 9458-9471.

C. N. R. Rao, R. S., B. C. Satishkumar and A.Govindaraj (1998). Large aligned-nanotube bundles from ferrocene pyrolysis. *Chemical Communications*: 1525-1526.

Cao, A., Dickrell, P. L., Sawyer, W. G., Ghasemi, N., M.N. and Ajayan, P. (2005). Super-compressible foamlike carbon nanotube films. *Science* **310**: 1307.

Chang, T. and Gao, H. (2003). Size-dependent elastic properties of a single-walled carbon nanotube via a molecular mechanics model. *Journal of the Mechanics and Physics of Solids* **51**(6): 1059-1074.

Chen, H., Roy, A., Baek, J.-B., Zhu, L., Qu, J. and Dai, L. (2010). Controlled growth and modification of vertically-aligned carbon nanotubes for multifunctional applications. *Materials Science and Engineering: R: Reports* **70**(3-6): 63-91.

Choudhary, V. and Gupta, A. (2011). Polymer/Carbon Nanotube Nanocomposites, Carbon Nanotubes -Polymer Nanocomposites. D. S. Yellampalli, InTech.

Ci, L., Suhr, J., V. Pushparaj, Zhang, X. and Ajayan, P. M. (2008). Continuous Carbon Nanotube Reinforced Composites. *NANO LETTERS* **8**(9): 2762-2766.

Cola, B. A., Xu, J. and Fisher, T. S. (2009). Contact mechanics and thermal conductance of carbon nanotube array interfaces. *International Journal of Heat and Mass Transfer* **52**(15-16): 3490-3503.

Cornwell, C. F. and Wille, L. T. (1997). Elastic properties of single-walled carbon nanotubes in compression. *Solid State Communications* **101**: 555–558.

D. Peric, M. V. J., D.R.J. Owen (1999). On adaptive strategies for large deformations of elasto-plastic solids at finite strains: computational issues and industrial applications. *Computer methods in applied mechanics and engineerlng* **176**: 279-312.

Dai, L. (2010). Controlled Growth and Modification of Aligned Carbon Nanotubes for Multifunctional Nanocomposites and Nanodevices. *IEEE*.

Dai, L., Patil, A., Gong, X., Guo, Z., Liu, L., Liu, Y. and Zhu, D. (2003). Aligned nanotubes. *Chemphyschem* **4**(11): 1150-1169.

De Heer, W. A., Bacsa, W. S., Chatelain, A., Gerfin, T., Humphrey-Baker, R., Forro, L. and Ugarte, D. (1995). Aligned Carbon Nanotube Films: Production and Optical and Electronic Properties *SCIENCE REPORTS* **268**(12): 845-847.

Deshpande, V. S. and Fleck, N. A. (2000). Isotropic constitutive models for metallic foams. *Journal of the Mechanics and Physics of Solids* **48** 1253 - 1283.

Fan, S., Chapline, M. G., Franklin, N. R., Tombler, T. W., Cassell, A. M. and Dai, H. (1999). Self-Oriented Regular Arrays of Carbon Nanotubes and Their Field Emission Properties. *Science* **283**(22): 512-514.

Flores-Johnson, E. A. and Li, Q. M. (2010). Indentation into polymeric foams. *International Journal of Solids and Structures* **47**(16): 1987-1995.

Garg, M. (2005). *Mechanics of Deformation of Carbon Nanotubes* Master of Science Massachustetts Institute of Technology.

Gates, T., Odegard, G., Frankland, S. and Clancy, T. (2005). Computational materials: Multi-scale modeling and simulation of nanostructured materials. *Composites Science and Technology* **65**(15-16): 2416-2434.

Gibson, L. J. and Ashby, M. F. (1997). Cellular Solids: Structure and Properties, Cambridge University Press.

Goze, C., Vaccarini, L., Henrard, L., Bernier, P., Hernandez, E. and Rubio, A. (1999). Elastic and mechanical properties of carbon nanotubes. *Synthetic Metals (1999)* **103**: 2500-2501.

Halicioglu, T. (1998). Stress calculations for carbon nanotubes. *Thin Solid Films* **312**: 11–14.

Hayashia, T. and Endo, M. (2011). *Composites Part B: Engineering* **42**(8): 2151-2157.

Hernandez, E., Goze, C. and Rubio, A. (1998). Elastic Properties of C and BxCyNz composite nanotubes. *Physical Review Letters* **80**: 4502-4505.

Hernandez, E., Goze, C. and Rubio, A. (1999). Elastic Properties of Single-Wall Nanotubes. *Applied Physics A. Materials Science and Processing* **68**: 287-292.

Hohenberg, P. (1964). Inhomogeneous Electron Gas. *Physical Review* **136**(3B): B864-B871.

Hutchens, S. B., Needleman, A. and Greer, J. R. (2011). Analysis of uniaxial compression of vertically aligned carbon nanotubes. *J Mech Phys Solids* **59**(10): 2227-2237.

Iijima, S. (1991). Helical microtubules of graphitic carbon. *Nature* **354**: 56-58.

Iijima, S., Brabec, C., Maiti, A. and Bernholc, J. (1996). Structural flexibility of carbon nanotubes. *The Journal of Chemical Physics* **104**(5): 2089.

Ishigami, N., Ago, H., Imamoto, K., Tsuji, M., Iakoubovskii, K. and Minami, N. (2008). Crystal Plane Dependent Growth of Aligned Single-Walled Carbon Nanotubes on Sapphire. *J. Am. Chem. Soc.* **130**(30): 9918–9924.

Ismach, A. (2008). *Epitaxial Approaches to Carbon Nanotube Organization*. Doctorate, Weizmann Institute of Science Rehovot, Israel.

Johnson, K. L. (1985). Contact mechanics, Cambridge university press.

Jorgensen, W. L., Severance, D.L. (1990). Aromatic aromatic interactions—free-energy profiles for the benzene dimer in water,chloroform, and liquid benzene. *Journal of American Chemical Society* **112** 4768–4774.

Kingston, C. T. and Simard, B. (2003). Fabrication of Carbon Nanotubes. *Analytical Letters* **36**(15): 3119-3145.

Koziol, K., Boskovic, B. O. and Yahya, N. (2010). Synthesis of Carbon Nanostructures by CVD Method. *Adv Struct Mater*: 23-49.

Kreupl, F., Graham, A. P., Duesberg, G. S., Steinhögl, W., Liebau, M., Unger, E. and Hönlein, W. (2002). Carbon Nanotubes for Interconnect Applications *Microelectronic Engineering* **64**(1-4): 399-408.

Krishnan, A., Dujardin, E., Ebbesen, T. W., Yianilos, P. N. and Treacy, M. M. J. (1998). Young's modulus of single-walled nanotubes. *Physical Review B* **B**(58): 14013–14019.

Kumar, M. and Ando, Y. (2010). Chemical Vapor Deposition of Carbon Nanotubes: A Review on Growth Mechanism and Mass Production. *Journal of Nanoscience and Nanotechnology* **10**(6): 3739-3758.

Kuncir, E. J., Wirta, R. W. and Golbranson, F. L. (1990). Load-bearing characteristics of polyethylene foam:An Examination of structural and compression properties. *Journal of Rehabilitation Research and Development* **27**(3): 229-238.

Lau, K.-T., Chipara, M., Ling, H.-Y. and Hui, D. (2004). On the effective elastic moduli of carbon nanotubes for nanocomposite structures. *Composites Part B: Engineering* **35**(2): 95-101.

Li, C. and Chou, T.-W. (2003). A structural mechanics approach for the analysis of carbon nanotubes. *International Journal of Solids and Structures* **40**(10): 2487-2499.

Li, J., Papadopoulos, C., Xu, J. M. and Moskovits, M. (1999). Highly-ordered carbon nanotube arrays for electronics applications. *Applied Physics Letters* **75**(3): 367.

Liew, K., Wong, C., He, X., Tan, M. and Meguid, S. (2004). Nanomechanics of single and multiwalled carbon nanotubes. *Physical Review B* **69**(11).

Liu, J., Zheng, Q. and Jiang, Q. (2001). Effect of a Rippling Mode on Resonances of Carbon Nanotubes. *Physical Review Letters* **86**(21): 4843-4846.

Liu, Y., Qian, W., Zhang, Q., Cao, A., Li, Z., Zhou, W., Ma, Y. and Wei, F. (2008). Hierarchical Agglomerates of Carbon Nanotubes as High-Pressure Cushions. *NANO LETTERS* **Vol. 8**(5): 1323-1327.

Logan, D. L. (2004). A First Course in the Finite Element Method. INDIA, Thomson Asia Pte Ltd.,.

Lu, J. P. (1997). Elastic Properties of Carbon Nanotubes and Nanoropes. *PHYSICAL REVIEW LETTERS* **79**(7): 1297-1300.

Lu, Y. and Shinozaki, D. M. (1998). Deep penetration micro-indentation testing of high density polyethylene. *Materials Science and Engineering A* **249**: 134-144.

Lu, Y. C., Joseph, J., Zhang, Q., Maschmann, M. R., Dai, L. and Baur, J. (2012). Large-Displacement Indentation Testing of Vertically Aligned Carbon Nanotube Arrays. *Experimental Mechanics*.

Lu, Y. C., Kurapati, S. N. V. R. K. and Yang, F. (2008). Finite element analysis of cylindrical indentation for determining plastic properties of materials in small volumes. *Journal of Physics D: Applied Physics* **41**(11): 115415.

Lu, Y. C. and Shinozaki, D. M. (2008). Characterization and Modeling of Large Displacement Micro-/Nano-Indentation of Polymeric Solids. *Journal of Engineering Materials and Technology* **130**(4): 041001.

Machida, K. (1999). Principles of Molecular Mechanics, Kodansha and John Wiley & Sons Co-publication, Tokyo.

Maiti, A. (2008). Multiscale modeling with carbon nanotubes. *Microelectronics Journal* **39**(2): 208-221.

Maschmann, M. R., Zhang, Q., Du, F., Dai, L. and Baur, J. (2011). Length dependent foam-like mechanical response of axially indented vertically oriented carbon nanotube arrays. *Carbon* **49**(2): 386-397.

McCarter, C. M., Richards, R. F., Mesarovic, S. D., Richards, C. D., Bahr, D. F., McClain, D. and Jiao, J. (2006). Mechanical compliance of photolithographically defined vertically aligned carbon nanotube turf. *Journal of Material Science* **41**: 7872–7878.

Mesarovic, S. D. and Fleck, N. A. (1999). Spherical indentation of elastic-plastic solids. *Proceedings of the Royal Society A: Mathematical, Physical and Engineering Sciences* **455**(1987): 2707-2728.

Mesarovic, S. D., McCarter, C. M., Bahr, D. F., Radhakrishnan, H., Richards, R. F., Richards, C. D., McClain, D. and Jiao, J. (2007). Mechanical behavior of a carbon nanotube turf. *Scripta Materialia* **56**(2): 157-160.

Misra, A., Greer, J. R. and Daraio, C. (2009). Strain Rate Effects in the Mechanical Response of Polymer-Anchored Carbon Nanotube Foams. *Advanced Materials* **21**(3): 334-338.

Molina, J. M., Savinsky, S.S., Khokhriakov, N.V. (1996). A tight-binding model for calculations of structures and properties of graphitic nanotubes. *Journal of Chemical Physics* **104**: 4652–4656.

Odegard, G. M., Gates, T. S., Nicholson, L. M. and Wise, K. E. (2001). Equivalent-continuum modeling of nano-structured materials. *NASA Technical Report NASA/TM* **2001**: 210863.

Odegard, G. M., Gatesb, T. S., Nicholsonc, L. M. and Wised, K. E. (2002). Equivalent-Continuum Modeling of Nano-Structured Materials. *Composites Science and Technology* **62**(14): 1869-1880.

Oliver, W. C. and Pharr, G. M. (1992). An improved technique for determining hardness and elastic modulus using load and displacement sensing indentation experiments. *Journal of Materials Research* **7**(6): 1564-1583.

Olurin, O. B., Fleck, N. A. and Ashby, M. F. (2000). INDENTATION RESISTANCE OF AN ALUMINIUM FOAM. *Scripta mater.* **43**: 983–989.

Overney, G., Zhong, W. and Tomanek, D. (1993). Structural rigidity and low-frequency vibrational modes of long carbon tubules. *Zeitschrift fur Physik D: Atoms, Molecues and Clusters* **27**: 93–96.

Pan, Z. W., Xie, S. S., Lu, L., Chang, B. H., Sun, L. F., Zhou, W. Y., Wang, G. and Zhang, D. L. (1999). Tensile tests of ropes of very long aligned multiwall carbon nanotubes. *Applied Physics Letters* **74**: 3152–3154.

Park, Y. J. and Pharr, G. M. (2004). Nanoindentation with spherical indenters: finite element studies of deformation in the elastic–plastic transition regime. *Thin Solid Films* **447-448**: 246-250.

Pathak, S., Cambaz, Z. G., Kalidindi, S. R., Swadener, J. G. and Gogotsi, Y. (2009). Viscoelasticity and high buckling stress of dense carbon nanotube brushes. *Carbon* **47**(8): 1969-1976.

Patton, S. T., Zhang, Q., Qu, L., Dai, L., Voevodin, A. A. and Baur, J. (2009). Electromechanical characterization of carbon nanotubes grown on carbon fiber. *Journal of Applied Physics* **106**(10): 104313.

Popov, V. N. and Van Doren, V. E. (2000). Elastic properties of single-walled carbon nanotubes. *PHYSICAL REVIEW B* **61**(4): 3078-3083.

Prasek, J., Drbohlavova, J., Chomoucka, J., Hubalek, J., Jasek, O., Adam, V. and Kizek, R. (2011). Methods for carbon nanotubes synthesis—review. *Journal of Materials Chemistry* **21**(40): 15872.

Prylutskyy, Y. I., Durov, S. S., Ogloblya, O. V., Buzaneva, E. V. and Scharff, P. (2000). Molecular dynamics simulation of mechanical, vibrational and electronic properties of carbon nanotubes. *Computational Materials Science* **17**(2–4): 352-355.

Qi, H. J., Teo, K. B. K., Lau, K. K. S., Boyce, M. C., Milne, W. I., Robertson, J. and Gleason, K. K. (2003). Determination of mechanical properties of carbon nanotubes and vertically aligned carbon nanotube forests using nanoindentation. *Journal of the Mechanics and Physics of Solids* **51**(11-12): 2213-2237.

Qu, L., Du, F. and Dai, L. (2008). Preferential syntheses of semiconducting vertically aligned single-walled carbon nanotubes for direct use in FETs. *Nano letters* **8**(9): 2682-2687.

Rappe, A. K., Casemit, C. J., Colwell, K. S., Goddard, W. A. and Skiff, W. M. (1992). a full periodic-table force-field for molecular mechanics and molecular dynamics simulations. *J Am Chem Soc* **114**: 10024–10035.

Ren, Z. F., Huang, Z. P., Wang, D. Z., Wen, J. G., Xu, J. W., Wang, J. H., Calvet, L. E., Chen, J., Klemic, J. F. and Reed, M. A. (1999). Growth of a single freestanding multiwall carbon nanotube on each nanonickel dot. *Applied Physics Letters* **75**(8): 1086.

Robertson, D., Brenner, D. and Mintmire, J. (1992). Energetics of nanoscale graphitic tubules. *Physical Review B* **45**(21): 12592-12595.

Ru, C. Q. (2000a). Effective bending stiffness of carbon nanotubes. *Physical Review B* **62**: 9973–9976.

Ru, C. Q. (2000b). Elastic buckling of single-walled carbon nanotube ropes under high pressure. *Physical Review B* **62**: 10405–10408.

Ru, C. Q. (2001). Axially compressed buckling of a doublewalled carbon nanotube embedded in an elastic medium. *Journal of the Mechanics and Physics of Solids* **49**: 1265–1279.

Ruoff, R. S. and Lorents, D. C. (1995). MECHANICAL AND THERMAL PROPERTIES OF CARBON NANOTUBES. *Carbon* **33**(7): 925-930.

Sager, R. J., Klein, P. J., Lagoudas, D. C., Zhang, Q., Liu, J., Dai, L. and Baur, J. W. (2009). Effect of carbon nanotubes on the interfacial shear strength of T650 carbon fiber in an epoxy matrix. *Composites Science and Technology* **69**(7-8): 898-904.

Salvetat, J. P., Briggs, G. A. D., Bonard, J. M., Bacsa, R. R., Kulik, A. J., Stockli, T., Burnham, N. A. and Forro, L. (1999). Elastic and shear moduli of single-walled carbon nanotube ropes. *Physical Review Letters* **82**: 944–947.

Sanchez-Portal, D., Artacho, E. and Soler, J. M. (1999). Ab initio structural, elastic, and vibrational properties of carbon nanotubes. *Physical Review B* **59**: 12678–12688.

Seah, C.-M., Chai, S.-P. and Mohamed, A. R. (2011). Synthesis of aligned carbon nanotubes. *Carbon* **49**(14): 4613-4635.

Sears, A. and Batra, R. (2004). Macroscopic properties of carbon nanotubes from molecular-mechanics simulations. *Physical Review B* **69**(23).

Sears, A. T. (2006). *Carbon Nanotube Mechanics: Continuum Model Development from Molecular Mechanics Virtual Experiments*. Doctor of Philosophy, Virginia Polytechnic Institute and State University.

Shen, C., Brozena, A. H. and Wang, Y. (2011). Double-walled carbon nanotubes: challenges and opportunities. *Nanoscale* **3**(2): 503-518.

Sneddon, I. N. (1946). Boussinesq's problem for flat-ended cylinder. *Mathematical Proceedings of the Cambridge Philosophical Society* **42**(01): 29-39.

Tabor, D. (1996). Indentation hardness: Fifty years on a personal view. *Philosophical Magazine A* **74**(5): 1207-1212.

Terrones, M., Grobert, N., Olivares, J., Zhang, J., Terrones, P. H., Kordatos, K., Hsu, W. K., Hare, J. P., Townsend, P. D., Prassides, K., Cheetham, A. K., Kroto, H. W. and Walton, D. R. M. (1997). Controlled production of aligned-nanotube bundles. *NATURE* **388**(3): 52-55.

Tersoff, J. (1988). New empirical approach for the structure and energy of covalent systems. *Physical Review B* **37**: 6991–7000.

Thess, A., Lee, R., Nikolaev, P., Dai, H., Petit, P., Robert, J., Xu, C., Lee, Y. H., Kim, S. G., Rinzler, A. G., Colbert, D. T., Scuseria, G. E., Tomanek, D., Fischer, J. E. and Smalley, R. E. (1996). Crystalline Ropes of Metallic Carbon Nanotubes. *SCIENCE* **273**: 483-487.

To, C. W. S. (2006). Bending and shear moduli of single-walled carbon nanotubes. *Finite Elements in Analysis and Design* **42**(5): 404-413.

Tombler, T. W., Zhou, C., Kong, J., Dai, H., Liu, L., Jayanthi, C. S., Tang, M. and Wu, S. Y. (2000). Reversible electromechanical characteristics of carbon nanotubes under local-probe manipulation. *Nature* **405**: 769–772.

Tong, T., Zhao, Y., Delzeit, L., Kashani, A., Meyyappan, M. and Majumdar, A. (2008). Height Independent Compressive Modulus of Vertically Aligned Carbon Nanotube Arrays. *NANO LETTERS* **8**(2): 511-515.

Treacy, M. M. J., Ebbesen, T. W. and Gibson, J. M. (1996). Exceptionally high Young's modulus observed for individual carbon nanotubes. *Nature* **381**(20): 678-680.

Tserpes, K. and Papanikos, P. (2005). Finite element modeling of single-walled carbon nanotubes. *Composites Part B: Engineering* **36**: 468-477.

Tu, J. P., Jiang, C. X., Guo, S. Y. and Fu, M. F. (2004). Micro-friction characteristics of aligned carbon nanotube film on an anodic aluminum oxide template. *Materials Letters* **58**(10): 1646-1649.

Tu, J. P., Zhu, L. P., Hou, K. and Guo, S. Y. (2003). Synthesis and frictional properties of array film of amorphous carbon nanofibers on anodic aluminum oxide. *Carbon* **41**(6): 1257-1263.

Tu, Z.-C. and Ou-Yang, Z.-C. (2002). Single-walled and multiwalled carbon nanotubes viewed as elastic tubes with the effective Young's moduli dependent on layer number. *Physical Review B* **65**(23).

Van Lier, G., Van Alsenoy, C., Van Doren, V. and Geerlings, P. (2000). Ab initio study of the elastic properties of single-walled carbon nanotubes and graphene. *Chemical Physics Letters* **326**: 181–185.

Voyiadjis, G. Z. and Foroozesh, M. (1991). A finite strain, total Lagrangian finite element solution for metal extrusion problems. *Computer Methods in Applied Mechanics and Engineering* **86**(3): 337-370.

Wang, J., Zhang, H., Guo, X. and Tian, M. (2011) Study of Carbon Nanotubes Based on Higher Order Cauchy-Born Rule-Synthesis, Characterization, Applications-Dr. Siva Yellampalli (Ed.).

Wang, L., Ortiz, C. and Boyce, M. C. (2011). Mechanics of Indentation into Micro- and Nanoscale Forests of Tubes, Rods, or Pillars. *Journal of Engineering Materials and Technology* **133**(1): 011014.

Wang, X. Y. and Wang, X. (2004). Numerical simulation for bending modulus of carbon nanotubes and some explanations for experiment. *Composites Part B: Engineering* **35**(2): 79-86.

Wardle, B. L., Saito, D. S., García, E. J., Hart, A. J., de Villoria, R. G. and Verploegen, E. A. (2008). Fabrication and Characterization of Ultrahigh-Volume- Fraction Aligned Carbon Nanotube-Polymer Composites. *Advanced Materials* **20**(14): 2707-2714.

Waters, J. F., Guduru, P. and Xu, J. (2006). Nanotube mechanics-Recent progress in shell buckling mechanics and quantum electromechanical coupling. *Composites Science and Technology* **66**: 1141-1150.

Waters, J. F., Guduru, P. R., Jouzi, M., Xu, J. M., Hanlon, T. and Suresh, S. (2005). Shell buckling of individual multiwalled carbon nanotubes using nanoindentation. *Applied Physics Letters* **87**(10): 103109.

Wei, B. Q., Vajtai, R., Jung, Y., Ward, J., Zhang, R., Ramanath, G. and Ajayan, P. M. (2003). Assembly of Highly Organized Carbon Nanotube Architectures by Chemical Vapor Deposition. *The Journal of Chemistry of Materials* **15**(8): 1598-1606.

Wendy, D., Cornell, Cieplak, P., Bayly, C. I., Gould, I. R., Kenneth M. Merz, J., David M. Ferguson,David C. Spellmeyer,Thomas Fox, and James W. Caldwell, a. P. A. K. (1995). A Second Generation Force Field for the Simulation of Proteins, Nucleic Acids, and Organic Molecules. *Journal of American Chemical Society. 1995, 117, 5179-5197* **117**: 5179-5197.

Wilsea, M., Johnson, K. and Ashby, M. F. (1975). Indentation of foamed plastics. *International Journal of Mechanical Sciences* **17**: 457-460.

Wong, E. W., Sheehan, P. E. and Lieber, C. M. (1997). Nanobeam Mechanics: Elasticity, Strength, and Toughness of Nanorods and Nanotubes. *Science* **277**(5334): 1971-1975.

Wright, S. C., Huang, Y. and Fleck, N. A. (1992). Deep Penetration of Polycarbonate by a Cylindrical Punch, Mechanics of Materials. **13**: 277-284.

Xu, J. and Fisher, T. S. (2006). Enhancement of thermal interface materials with carbon nanotube arrays. *Int. J. Heat Mass Transfer* **49**: 1658–1666.

Yakobson, B. I., Brabec, C. J. and Bernholc, J. (1996). Nanomechanics of Carbon Tubes: Instabilities beyond Linear Response. *Physical Review Letters* **76**(14): 2511-2514.

Yu, M. F., Files, B. S., Arepalli, S. and Ruoff, R. S. (2000). Tensile loading of ropes of single wall carbon nanotubes and their mechanical properties. *Physical Review Letters* **84**: 5552–5555.

Yu, M. F., Lourie, O., Dyer, M. J., Moloni, K., Kelly, T. F. and Ruoff, R. S. (2000). Strength and breaking mechanism of multiwalled carbon nanotubes under tensile load. *Science* **287**: 637–640.

Zhang, P., Huang, Y., Geubelle, P. H., Klein, P. A. and Hwang, K. C. (2002). The elastic modulus of single-wall carbon nanotubes:a continuum analysis incorporating interatomic potentials. *International Journal of Solids and Structures* **39**: 3893–3906.

Zhang, Q., Liu, J., Sager, R., Dai, L. and Baur, J. (2009). Hierarchical composites of carbon nanotubes on carbon fiber: Influence of growth condition on fiber tensile properties. *Composites Science and Technology* **69**(5): 594-601.

Zhang, Q., Lu, Y. C., Du, F., Dai, L., Baur, J. and Foster, D. C. (2010). Viscoelastic creep of vertically aligned carbon nanotubes. *Journal of Physics D: Applied Physics* **43**(31): 315401.

Zhou, G., Duan, W. and Gu, B. (2001). First-principles study on morphology and mechanical properties of single-walled carbon nanotube. *Chemical Physics Letters* **333**: 344–349.

Zhou, X., Zhou, J. and Ou-Yang, Z.-C. (2000). Strain energy and Young's modulus of single-wall carbon anotubes calculated from electronic energy-band theory. *PHYSICAL REVIEW B* **62**(20): 13692-13696.

VITA

Johnson Joseph

Birthdate: Feb 26 1978; Birthplace; Bangalore, Karnataka State, INDIA

Education

- Doctoral Candidate Mechanical Engineering, University of Kentucky, Lexington, KY **2013**
- M.Tech in Machine Design, B.M.S College of Engineering, Bangalore, Karnataka State, INDIA **2005**
- B.E. in Mechanical Engineering, University Visvesvaraya College of Engineering, Bangalore, Karnataka State, INDIA **2000**
- Diploma in Machine Tool Technology, S.J Polytechnic, Bangalore, Karnataka State, INDIA **1996**

Teaching, Research and Professional Experience **2010-2013**

- Teaching Assistant (Capstone Design, Lean Manufacturing, Computer Aided Design, Mechanical Vibrations, Gas Dynamics (onsite class contact)), Department of Mechanical Engineering, University of Kentucky
- Research Associate (Multiscale modeling of diastolic cardiac failure), Department of Pediatrics, University of Kentucky
- Research Assistant (Computational Design of Advanced Materials), Department of Mechanical Engineering, University of Kentucky
- Analysis Engineer (FEA/CAE), CADES Digitech Pvt. Ltd. Bangalore, India **(06-10)**

Awards

- Harrison D. Brailsford Fellowship Award, College of Engineering, University of Kentucky **2012**
- All India Council for Technical Education (AICTE), New Delhi, India, Graduate Aptitude Test in Engineering (GATE) Scholarship award **2003**

Journal Publications

1) **J. Joseph** and Y.C. Lu, “Design of Aligned Carbon Nanotubes Structures Using Structural Mechanics Modeling, Part 1: Theory and Individual Carbon Nanotube Modeling,” *Computers, Materials, & Continua* , Vol. 37, No. 1, pp. 39-57, 2013

2) **J. Joseph** and Y.C. Lu, “Design of Aligned Carbon Nanotubes Structures Using Structural Mechanics Modeling, Part 2: Theory and Individual Carbon Nanotube Modeling,” *Computers, Materials, & Continua* , Vol. 37, No. 1, pp. 59-75, 2013

3) **J. Joseph** and Y.C. Lu, "Use of Finite Element Simulation for Modeling Vertically Aligned Carbon Nanotube Arrays Based on Structural Mechanics Principles," *SAE Technical Paper* 2013-01-0645, 2013, doi:10.4271/2013-01-0645

4) Y. C. Lu, **J. Joseph**, Q. Zhang,M. R. Maschmann, L. Dai & J. Baur, **“**Large Displacement Indentation of Vertically Aligned Carbon Nanotube Arrays*”* in Book: *Challenges in Mechanics of Time-Dependent Materials and Processes in Conventional and Multifunctional Materials*, Edited by Antoun, B.; Qi, H.J.; Hall, R.; Tandon, G.P.; Lu, H.; Lu, Y.C., Springer, (2013).

5) Y. C. Lu, **J. Joseph**, Q. Zhang,M. R. Maschmann, L. Dai & J. Baur, **“**Large Displacement Indentation of Vertically Aligned Carbon Nanotube Arrays*”* *Experimental Mechanics*, Vol. 52, No.9, (2012).

6) **Joseph, J.,** Raja, S., and Lu, Y.**C.,** "Finite Element Analysis of Piezoelectric Composite Actuators," *SAE Int. J. Mater. Manuf.* 4(1):328-339, 2011, doi:10.4271/2011-01-0218.

Conference Proceedings

1) Y. C. Lu, **J. Joseph**, Q. Zhang,M. R. Maschmann, L. Dai & J. Baur, "Large-Displacement Indentation of Vertically Aligned Carbon Nanotube Arrays", Proceeding of SEM International Congress on Experimental and Applied Mechanics, Costa Mesa, California, June 11 - 14 (2012).

2) Y.C. Lu, **J. Joseph**, Q. Zhang, L. Dai, D.C. Foster, J. Baur., Large-displacement indentation of vertically aligned carbon nanotube arrays, Proceeding of International Symposium on Plasticity, Puerto Rico, January 3-9 (2012).

3) **Johnson Joseph**, S Raja and Y Charles Lu, "Finite Element Analysis of Piezoelectric Composite Actuators", *SAE World Congress*, Detroit, MI, April (2011).